Studying nonlinear optical properties of the plant light-harvesting protein LHCII

DISSERTATION

Zur Erlangung des akademischen Grades
doctor rerum naturalium
(Dr. rer. nat.)

im Fach Biophysik

eingereicht an der

Mathematisch-Naturwissenschaftlichen Fakultät I

der Humboldt-Universität zu Berlin

von

Diplom-Physiker Axel Schubert
geboren am 15.03.1970 in Jena

Präsident der Humboldt-Universität zu Berlin

Prof. Dr. Jürgen Mlynek

Dekan der Mathematisch-Naturwissenschaftlichen Fakultät

Prof. Dr. Michael Linscheid

Gutachter: 1. Prof. Dr. Bernhard Grimm, HU Berlin

2. Dr. sc. nat. Dieter Leupold, MBI Berlin

3. Prof. Dr. Gernot Renger, TU Berlin

Tag der mündlichen Prüfung: 08.03.2004

In memoriam to my grandfather,

Prof. Dr. Alfred Schubert (1915-2000).

*'Der vollkommene Weltmann wäre der,
welcher nie in Unschlüssigkeit stockte
und nie in Übereilung geriete.'*

Arthur Schopenhauer

Preface

The thesis on hand was realized in the framework of two successive research projects (Ho 1757/2-1 and Ho 1757/2-2) financed by the DFG. Both projects extended a long-standing collaboration between Prof. Paul Hoffmann, Chair for Plant Physiology at Humboldt-University Berlin, and Dr. Dieter Leupold, Max-Born Institute for Nonlinear Optics and Short-Pulse Spectroscopy Berlin. This co-operation is currently continued under the roof of SFB 429, including the participation of Dr. Heiko Lokstein and Prof. Bernhard Grimm (successor at the Chair for Plant Physiology). The unique combination of nonlinear optics and plant biology apparently embeds my studies into the present merging process between life sciences and applied physics. In spite of its high synergistic potential, these two research fields are still confronted by distinct background education, working methods and specialist terms. Accordingly, the presented work was especially shaped to reflect proper gearing between both sciences. Physical as well as biological issues with relevance for following discussions are thus explained in the introduction section. In particular, the biological system of key interest is described by an adequate physical model in Chapter 1.2.

The central objective of my thesis can be outlined as investigation of an intricate pigment-containing protein by using newly introduced laser-spectroscopic techniques. More precisely, the main light-harvesting complex of the higher plants (LHCII) is primarily studied by nonlinear polarization spectroscopy in the frequency domain (NLPF, see Chapter 2.2). These measurements were aimed to improve the interpretation of biological function in terms of physical mechanisms. The combined complexity of *both* investigated object *and* experimental method required comprehensible illustrations of their mutual interaction. This problem is addressed by simulating the nonlinear response of several heterogeneous, LHCII-like systems in NLPF experiments (see Chapter 3.1). In this way, direct 'by-eye' verification of the parameter influence on measured NLPF spectra is enabled. Accordingly, this approach facilitates intuitive understanding of the experimental results obtained for LHCII without knowing underlying physical principles in detail.

Strong sensitivity of the NLPF method to numerous physical parameters of LHCII complicated model improvements by 'just' fitting measured NLPF spectra. In other words, significant modeling was hard to achieve without knowledge about at least one part of the relevant parameter space. For that reason, all available supplementary information about molecular parameters of LHCII has been carefully summarized and further extended by own experiments. Basic absorption parameters were thus determined from reconstituted mutant samples of LHCII in co-operation with biochemists from the group of Prof. Werner Kühlbrandt, MPI Frankfurt (see Chapter 3.2). Moreover, the application of two other nonlinear laser spectroscopic techniques yielded valuable information about electronic interactions within the light-harvesting complex (see Chapter 3.3 and 3.4). These additionally determined parameters enabled finally improvements for the parameter model of LHCII by evaluating measured NLPF spectra in Chapter 3.5. The relevance of obtained information for understanding biological

functionality within the photosynthetic apparatus is conclusively drawn in Chapter 4. This section summarizes also achieved experimental and model developments from the physical point of view.

As outlined above, the presented thesis combines different experimental methods from the fields of physics and biology. Accordingly, an intense integration of my studies into the work of other collaborators became necessary. These co-operations represented in the end an inevitable basis for successful completion of the whole research project. Nevertheless, an exact distinction between contributions from the author and other co-workers to the results published in this thesis is strongly required. For that reason, each chapter in the results and discussion section explicitly lists any additional aid from other scientists.

The work presented in this thesis is partially published in the following papers:

A. Schubert, B. Voigt, D. Leupold, W. Beenken, J. Ehlert, P. Hoffmann, and H. Lokstein (1997) 'Direct observation of spectral substructure in the Q_y-absorption band of light-harvesting complex II by nonlinear polarization spectroscopy in the frequency domain at low temperature' *Biochim. Biophys. Acta*, **1321**, 195-199.

A. Schubert, A., M.A. Krikunova, H. Stiel, J. Ehlert, D. Leupold, and H. Lokstein (1998) 'Determination of the aggregate size in chlorophyll *a* oligomers by nonlinear absorption spectroscopy on the ps and fs timescale' *in:* Photosynthesis: Mechanisms and Effects, Vol. I., G. Garab (Editor), Kluwer, Dordrecht, 469-472.

A. Schubert, W. Beenken, H. Stiel, D. Leupold and H. Lokstein, (2002) 'Excitonic coupling of chlorophylls in the plant light-harvesting complex LHC-II' *Biophys. J.*, **82**, 1030-1039.

H. Rogl, R. Schödel, H. Lokstein, W. Kühlbrandt and **A. Schubert** (2002) 'Assignment of spectral substructures to pigment-binding sites in higher plant light-harvesting complex LHCII' *Biochemistry*, **41**, 2281-2287.

A. Schubert, B. Voigt, W.J.D. Beenken, J. Ehlert, D. Leupold, and H. Lokstein 'Energy equilibration in the plant light-harvesting complex LHCII studied by nonlinear polarization spectroscopy' *manuscript in preparation*.

Further relevant publications including contributions from the author:

C. Tietz, F. Jelezko, U. Gerken, S. Schuler, **A. Schubert**, H. Rogl, and J. Wachtrup (2001) 'Single molecule spectroscopy on the light harvesting complex II of higher plants' *Biophys. J.*, **81**, 556-562.

H. Lokstein, B. Voigt, **A. Schubert**, M. Krikunova, W. Beenken, K. Teuchner, J. Ehlert, K.-D. Irrgang, G. Renger, D. Leupold. (2001) 'Spectral substructure and excitonic interactions in the plant antenna complexes LHC II and CP29 as revealed by nonlinear laser spectroscopy' Proceedings of the 12th International Congress on Photosynthesis, Brisbane, Australia, CSIRO Publishing.

H. Lokstein, **A. Schubert**, B. Voigt, and D. Leupold (1998) 'Direct resolution of spectral fine-structure and ultrafast exciton dynamics in light-harvesting complex II by nonlinear polarization spectroscopy in the frequency domain' *in:* Photosynthesis: Mechanisms and Effects, Vol. I., G. Garab, editor, Kluwer, Dordrecht. 293-296.

Zusammenfassung

Ultraschnelle Energietransferprozesse zwischen den Anregungszuständen organischer Pigmentmoleküle in photosynthetischen Lichtsammelkomplexen gehören zu den schnellsten bisher untersuchten biologischen Ereignissen. Diese Vorgänge wurden insbesondere auch für den Haupt-Antennenkomplex der höheren Pflanzen (LHCII) beobachtet, der mehr als die Hälfte des pflanzlichen Chlorophylls (Chl) bindet (5 Chl *b* und 7 Chl *a* pro Monomer). Offenbar ist dieser Pigment-Protein-Komplex entscheidend für Regulationsmechanismen verantwortlich, die eine schnelle Adaptation des Photosyntheseapparats an wechselnde Belichtungsbedingungen ermöglichen. Die Struktur von LHCII ist mit einer Auflösung von 3.4 Å bekannt und erlaubt (im Prinzip) die Berechnung des Anregungsenergietransfers auf der Basis eines Förster-Mechanismus. In diesem Zusammenhang gibt es jedoch noch zahlreiche ungeklärte Fragen, die vor allem die Orientierung der Pigmente zueinander sowie deren mögliche starke (exzitonische) Wechselwirkung betreffen. Allerdings sind konventionelle spektroskopische Methoden nicht geeignet, diese Merkmale ausreichend aufzuklären. Aus diesem Grund wird in dieser Arbeit untersucht, inwieweit neuere laserspektroskopische Methoden wie die nichtlineare Polarisationsspektroskopie in der Frequenzdomäne (NLPF) zur Ermittlung unbekannter Parameter beitragen können.

Anfänglich ergaben sich besonders Fragen der Anwendbarkeit der NLPF auf solche hochkomplexen Untersuchungsobjekte sowie der Signifikanz eventuell erzielbarer Ergebnisse. Aufbauend auf einer parallel verfaßten Dissertation zu theoretischen Aspekten der NLPF-Methode [1] wurde daher ein vereinfachtes System modelliert, das die Heterogenität der individuellen Chl(e) im LHCII widerspiegelt. Die gewonnenen Resultate ließen vermuten, daß die reine Simulation von NLPF-Spektren nicht ausreicht, um eindeutige Aussagen über die Molekülparameter zu gewinnen. Um den benötigten zusätzlichen Erkenntnisgewinn zu erreichen, wurden daher Paralleluntersuchungen mit anderen laserspektroskopischen Methoden (nichtlineare Absorption mit fs-Pulsen, intensitätsabhängige NLPF, Einzelmolekülspektroskopie, Tieftemperatur-NLPF) sowie mit *in vitro* rekonstituierten Protein-Mutanten durchgeführt. Als Ergebnis konnte die Subbstruktur der Q_y-Absorptionsbande der ersten angeregten Zustände der Chl(e) für LHCII ausreichend beschrieben werden. Darüber hinaus ergaben sich Aussagen zu exzitonischen Wechselwirkungen zwischen bestimmten Chl(en), die unter anderem Einfluß auf das Energietransferverhalten haben.

Diese zusätzlichen Untersuchungen erlaubten letztendlich eine Modellierung der bei Raumtemperatur an LHCII gemessenen NLPF-Spektren. Neben dem dabei implizit gewonnenen Verständnis der nichtlinearen optischen Eigenschaften im Bereich der Q_y-Absorption ließen sich so Aussagen über bestimmte Modellparameter, besonders über die Orientierung von Übergangsdipolmomenten, ableiten. Abschließend wurde die Auswirkung der Erkenntnisse auf das Verständnis der Struktur-Funktionsbeziehungen für intra- und inter-komplexen Energietransfer erläutert.

Schlagworte: Anregungsenergietransfer, Exzitonische Wechselwirkung, lichtsammelnder Komplex LHCII, Nichtlineare Polarisationsspektroskopie.

Abstract

Ultra-fast excitation energy transfer (EET) between excited states of organic pigment molecules in photosynthetic antenna complexes belongs to the fastest observed biological processes. Such EET phenomena has been studied to a large extent for the main light-harvesting complex of the higher plants (LHCII), which appears to play an exceptional role for the regulatory function (i.e. light adaptation) of the plant photosynthetic apparatus. The structure of this pigment-protein complex – harboring more than 50 % of the total chlorophyll (Chl) content – is known with 3.4 Å resolution and reveals the binding sites of 5 Chl *b* and 7 Chl *a* per monomeric unit. Based on this structure analysis, EET calculations are (in principle) available on the molecular level under the assumption of Förster-type transfer. However, several molecular features like mutual pigment orientations and electronic interactions between their transition dipoles are still rather uncertain. Since conventional spectroscopic techniques can hardly reveal the corresponding parameters, this work was aimed at the evaluation of newly introduced laser spectroscopic techniques with respect to these questions.

In the beginning, suitability and significance of the method when applied to highly complicated structures like pigment-protein complexes were studied by modeling heterogeneous, LHCII-like absorption systems in NLPF experiments. Based on recent improvements in the NLPF theory by a parallel theoretical investigation [1], these simulations clarified the sensitivity of the NLPF method on numerous physical parameters. As a major consequence, unambiguous evaluations of NLPF measurements appear to require substantial additional information about the investigated system. Accordingly, several supplementary methods like nonlinear absorption (using fs-pulses), intensity-dependent NLPF, single-molecule spectroscopy, and NLPF at low temperatures were employed. These investigations revealed unique information about excitonic interaction between certain Chl(s), including implications for the overall EET scheme. The sub-structure model for the Q_y-absorption region of LHCII was further essentially improved by the analysis of reconstituted proteins with selectively modified Chl binding residues in the amino-acid sequence.

The sum of all complementary investigations allowed finally the evaluation of room temperature NLPF measurements of trimeric LHCII. Due to the unique selectivity of the spectra to individual transition-dipole directions, several orientation parameters have been obtained. Under this point of view, the NLPF method has indeed revealed a high potential as compared to conventional techniques like circular dichroism spectroscopy. Moreover, the understanding of nonlinear phenomena in the Q_y-absorption region of LHCII as a consequence of molecular interaction provides further knowledge for the application of other nonlinear optical experiments. Concluding, implications of the obtained results for the structure-function relationship of intra- and inter-complex EET were elucidated.

Keywords: Excitation energy transfer, Excitonic interaction, Light-harvesting complex LHCII, Nonlinear polarization spectroscopy.

Contents

Abbreviations and frequently used symbols

BChl(s)	Bacteriochlorophyll(s)
Car(s)	Carotenoid(s)
Chl(s)	Chlorophyll(s)
CD	Circular dichroism
CP	Chlorophyll-protein
EET	Excitation-energy transfer
FWHM	Full width at half maximum of transition bands
LD	Linear dichroism
LHCII	Light-harvesting complex II
LT	Low temperature (i.e., cryogenic temperatures 77 K or 4 K)
NLA	Nonlinear absorption
NLPF	Nonlinear polarization spectroscopy in the frequency domain
OD	Optical density
OG	n-octyl β-D-glucopyranoside
PSI	Photosystem I
PSII	Photosystem II
RC	Reaction center of photosystem II
RT	Room temperature (293 K)
WT	Wild type (native species without mutations)

α	Absorption coefficient
c	Speed of light
γ	Population-relaxation rate or EET rate
Γ	Phase-relaxation rate (2Γ: homogeneous linewidth)
Δ	Inhomogeneous linewidth
λ_c, ω_c	Center wavelength / frequency of transition bands
λ_p, ω_p	NLPF pump wavelength / frequency
λ_t, ω_t	NLPF probe wavelength / frequency (the index refers to test)
μ	Transition-dipole moment
n	Refractive index
σ	Absorption-cross section
T_1	Excited-state population lifetime
T_2	Dephasing time of the excited-state wavefunction (phase-relaxation time)

1   Introduction

All species of the higher plants are characterized by strongly similar organization of their photosynthetic apparatus. Considering the rules of natural selection, this functional unit must represent an uniquely effective and flexible machinery. Above all, this includes perfect adaptation to special environmental conditions (e.g., light exposure) for the numerous plant species populating different areas on earth. Furthermore, the photosynthetic apparatus needs a sufficient flexibility with respect to continuously changing radiation conditions during the yearly and daily solar circle. Last but not least, short-time variations due to different shading conditions must be balanced, for example in light spots on the ground of woods. Understanding this high flexibility and the underlying regulation mechanisms has been a long-standing challenge in life-science research [2, 3, 4]. Within the last decade, these investigations were crucially boosted by structure analyses of crystallized proteins to near atomic resolution using X-ray crystallography or electron diffraction [5, 6]. On this basis, the description of initial steps in the photosynthetic reaction chain became available on a molecular level and raised substantial interest of physicists in the topic.

Green photosynthesis serves the plants as energy supply. This task is realized by conversion of solar radiation to stored chemical energy within two major reaction sequences. The pigment-located 'light reactions' cover water cleavage into protons and molecular oxygen after an initial, photon-induced charge separation process. Accordingly, different proton concentrations appear on both sides of the photosynthetic (thylakoid) membrane. This 'proton gradient' directly drives the subsequent formation of ATP, while $NADP^+$ can be converted into NADPH due to the corresponding electro-chemical potential. In the following 'dark reactions', enzymes catalyze CO_2 fixation by using NADPH as reductant and ATP as energy source. The primary light-induced reactions of the photosynthetic process have to be performed under highly varying radiation doses. Accordingly, the respective apparatus needs protection from photo-damage under excess light conditions as well as enough efficiency during low-light phases. In fact, the overall quantum yield of the primary steps can reach an astonishing high value of 90 % under certain radiation conditions [7]. This remarkable efficiency is well above the level of any artificial solar-energetic device known today. For that reason, the investigation of underlying mechanisms has continuously fascinated scientists from in- and outside the biological research community [8, 9, 10].

Ultra-fast transfer of electronic excitation after photon absorption within light-harvesting (antenna) proteins plays a key role for this remarkable efficiency. As recently discovered in time-resolved spectroscopic studies, excitation energy transfer (EET) occurs in light-harvesting complexes of the higher plants on time scales well below one ps [11, 12, 13, 14]. Consequently, light harvesting belongs to the fastest biological processes that have been observed so far. Under this point of view, the thesis on hand attempts better understanding of ultra-fast EET in antenna proteins by refining their physical description on the molecular level.

The equivalence of *energy* and *information* transfer reveals a further interesting aspect of light-harvesting systems. Actually, EET in pigment-containing proteins corresponds to information transfer on a quantized molecular level. Antenna complexes can thus be interpreted as ultra-fast quantum-optical devices, too (cp. Appendix **A1**, p. 116). This way of looking is especially interesting, since light-harvesting proteins own 'self-organizing' capability by nature. In particular, this self-organization is not limited to protein folding of single building blocks (= antenna complexes), but covers also the formation of entire super-structures performing photosynthetic processes as *one* functional unit (= photosynthetic apparatus). These long-range arrangements are further influenced by a large number of regulatory mechanisms, which are mostly not understood today. Nevertheless, the photosynthetic apparatus can be seen as a self-organizing, quantum-optical information processor – even tough on a rudimentary level. Within the last decade, *directed* self-organization of nano-scale devices has been in the focus of numerous studies in different scientific areas [15, 16, 17, 18]. The implementation of information processing in pigment-containing proteins represents a further interesting approach to obtain such self-organizing structures with artificial functionality. Hence, the study of EET in photosynthetic proteins can also provide essential knowledge for other non-biological research fields.

1.1   The antenna complex LHCII as integral part of the photosynthetic apparatus in higher plants

The primary steps of photosynthesis in green plants are distributed among several protein complexes harbored in the thylakoid membranes of chloroplasts. These membranes divide the chloroplast volume in the form of lipid bi-layers into an aqueous inner phase (lumen) and the cytoplasmatic outer phase (stroma). The different trans-membrane protein complexes of the photosynthetic apparatus have contact to both phases and populate two distinguishable thylakoid regions. So-called Grana stacks – firmly folded thylakoid parts with directly opposing membrane surfaces – harbor predominantly Photosystem II (PSII). In contrast, the unstacked lamellar regions of the thylakoids contain mainly Photosystem I (PSI) and ATPase [19]. In the reaction center (RC) of PSII, charge separations are induced by using the energy of electronic excitations after photon absorption. With one electron removed from the primary electron donor P680, a sufficient redox potential for water oxidation exists. This potential is used at the water oxidizing complex for water cleavage into molecular oxygen and protons. Accordingly, the lumen is characterized by an excess of positive charges during light exposure, while the stroma represents a negative phase. This proton concentration difference drives ATP synthesis, which is located at ATPase complexes. Between PSII and PSI, electrons are carried via plastoquinone and cytochrome-b_6f. By using these electrons from PSII and additional energy from photo-excitation, the energy reservoir NADPH is produced in PSI.

1.1.1 About the light-harvesting function of LHCII

Within the photosynthetic apparatus of higher plants, charge separations are performed by Chlorophyll (Chl) molecules bound to the RC's in unique arrangements of molecular pairs. However, the absorption cross sections of these charge-separation units are insufficient to guarantee continuous photon absorption under natural radiation conditions. For that reason, antenna pigments are used to increase the total absorption by funnelling their additional excitation energy to the RC's. This light-harvesting mechanism is implemented by special antenna complexes containing different pigments, i.e. carotenoids (Car) and Chls (see Fig. 1.1.1).
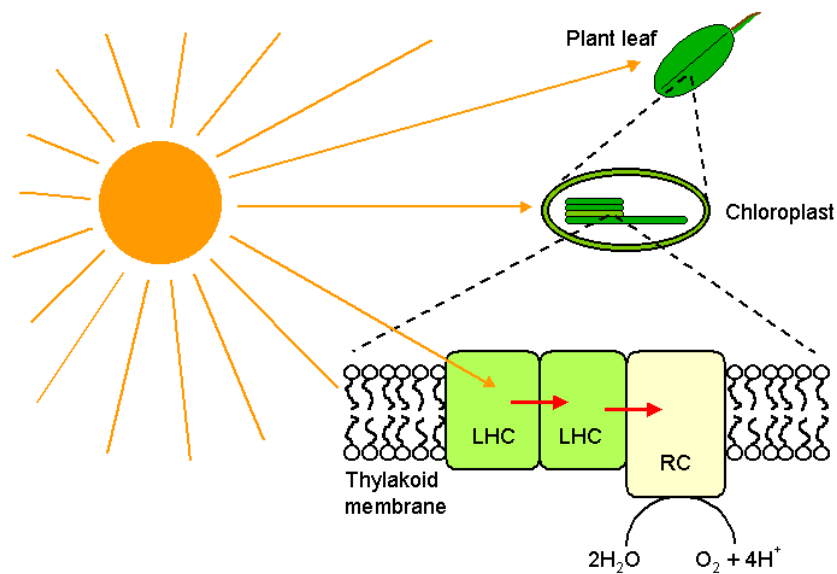
Figure 1.1.1 Schematic representation of the light-harvesting function in PSII. Chloroplasts, mainly located in leaf cells of the higher plants, contain thylakoid membranes. These thylakoids harbor the photosynthetic RCs surrounded by LHCs. Solar radiation hitting the LHCs is absorbed by attached pigments and this electronic excitation energy is transferred (probably via other LHCs) to the primary electron donor in the RC. This light-harvesting effect increases the cross section for photon-induced charge separation by far. After electron donation, the oxidized donor can induce water cleavage into molecular oxygen and protons.

Several chlorophyll-binding proteins (CP) commonly classified today as CP24, CP26, CP29, and LHCII have been identified to function as antenna proteins in PSII [20]. The arrangement of these proteins was recently investigated by negatively stained transmission electron microscopy for the PSII of *Arabidopsis thaliana* [21, 22]. A dimeric core complex with C_2-symmetry is build by two D1/D2 peptides (containing two primary electron donors) together with four core proteins (CP43 and CP47). Three of the minor antenna complexes CP24, CP26 or CP29 and two LHCII surround this assembly at rather fixed positions. Some moderately attached LHCII trimers as well as a 'lake' of less specifically bound LHCII form the outer region. It is interesting to note at this point, that LHCII shows transversal mobility within the thylakoid membrane. This allows more or less directed diffusion between locations of PSII and PSI [23]. The feature is assumed to enable regulatory function in connection with phosphorylation at the N-terminus of this trans-membrane protein [19] (cp. also the LHCII structure in Fig. 1.2.1, p. 5).

LHCII comprises the bulk antenna of the higher plant light-harvesting apparatus, harboring about 50 % of the total Chl *a+b* content in thylakoid membranes. In native environment, one finds LHCII as trimeric arrangement of proteins encoded by the genes *Lhcb1, Lhcb2,* and *Lhcb3* [24]. Several studies have addressed this structural and functional heterogeneity on the protein level [25, 26]. As a main result, *Lhcb2* appears to bind one Chl *a* molecule more than *Lhcb1* and is synthesized in larger amounts under low-light conditions [27]. Besides this, *Lhcb3* lacks the phosphorylation site at the N-terminus and might thus own reduced regulatory abilities [28]. In general, one can assume that this heterogeneity of gene products is part of the regulation mechanisms within the light-harvesting apparatus (see also Chapter 1.3).

Unfortunately, the protein heterogeneity in trimeric LHCII causes problems for exact studies of its spectroscopic properties. In particular, deviations of the Chl content complicate the interpretation of experimental results based on *one* structural model (see Chapter 1.2). Further difficulties arise from possible variations of the protein composition in different regions of the light-harvesting system: One fraction of LHCII proteins is specifically attached near the core complex. A second fraction forms the loosely bound 'lake' of LHCs around PSII in grana regions of the thylakoids. Finally, one can find LHCII together with LHCI in the lamellar, PSI containing regions of the membrane. Until now, the protein composition at different locations has not been studied in detail. For that reason, the isolation of LHCII complexes used in this work (see Chapter 2.1) was performed in a strictly supervised regime. In this way, constant protein and pigment compositions were obtained.

1.2 Constructing an adequate parameter model of LHCII

One prerequisite to comprehend EET processes in photosynthesis on a molecular level is the sufficient understanding of pigment-pigment and pigment-protein interactions. An extended theoretical framework providing mathematical descriptions for interacting molecules in protein environment has been established during the last decade [29, 30, 31, 32, 33]. On this basis, the EET processes between pigments caused by electronic dipole-dipole interactions can be simulated (see Chapter 1.3.1). Corresponding calculations require knowledge about molecular distances, involved electronic transitions, and transition-dipole orientations. Distances and orientations can be determined by structure analyses, while energy levels and environmental interactions are accessible by spectroscopic measurements. Thus, proper combination of data obtained by both experimental approaches enables (in principle) the calculation of all EET features. However, the relevant parameters can easily reach a number of several hundreds for complicated biological systems like antenna complexes. Certain simplifications are therefore required to allow useful EET calculations. Several approximations have been employed for adequate model reductions, which resulted in more or less convenient predictions of EET dynamics in different pigment-protein complexes [12, 14, 34]. Such eliminations of redundant information in the parameter

model of LHCII are discussed in the following two sections. The simplifications finally form a sufficient basis to evaluate experimental results as presented in Chapters 3.2-3.5.

1.2.1 Evaluating the LHCII structure

The structural model for LHCII obtained by electron diffraction of two-dimensional crystals reveals a trimeric arrangement of monomeric LHCII-subunits [6]. This cylindrically shaped trimer has about 90 Å diameter and 60 Å trans-membrane height. Three hydrophobic α-helices (A, B, C) connected by hydrophilic loops form the basic trans-membrane structure of each monomer. A fourth amphiphilic helix (D) is exposed to the lumen, while one protein end (N-terminus) protrudes into the stromal phase. Evaluation of the 3D electron-density map with 3.4 Å resolution indicated that 12 Chls (7 Chls *a* + 5 Chls *b*) are attached to each monomeric sub-unit (see Fig. 1.2.1). Furthermore, the location of two carotenoid molecules assigned as luteins was verified in the center of each complex near the helices A and B. The third carotenoid-binding site near helix C was not resolved in the structure, but seems to be occupied with neoxanthin (according to Croce et al. [35]). For violaxanthin, which appears in LHCII only in sub-stoichiometric amounts (cp. Table 2.1.1, p. 24), no specific binding site has been determined so far [36]. The comparison of protein sequence and structural data revealed eleven Chl-binding amino acids near nine of the twelve Chl pigments [37, 38, 39]. Apparently, the remaining three Chls (**a7**, **b1**, **b2**) are attached in a different way.

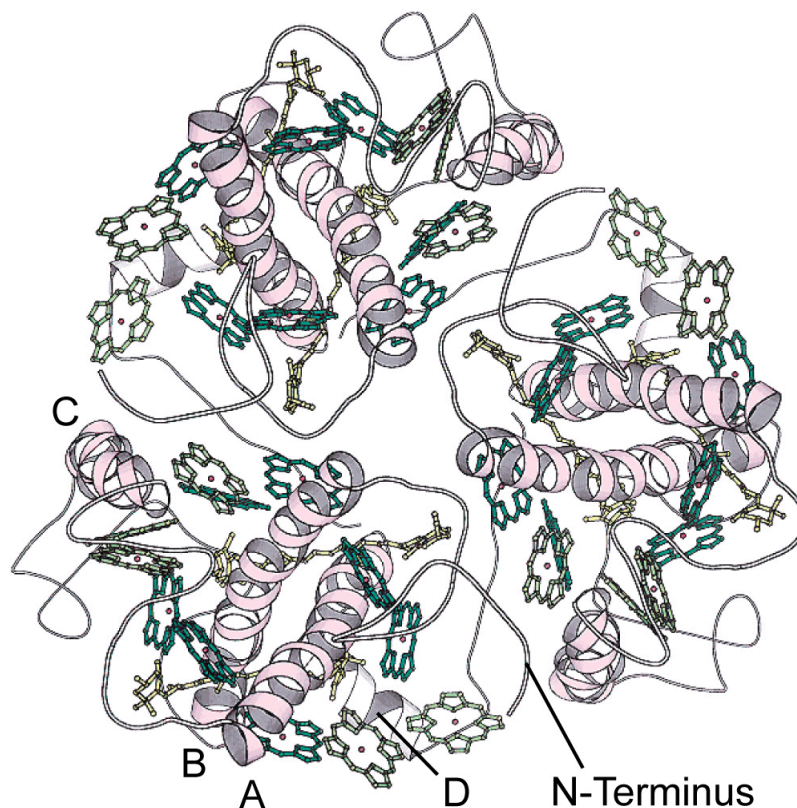**Figure 1.2.1** 3D-structural model of a trimeric LHCII complex (top view from the stromal side) as obtained by angle-dependent electron diffraction of two-dimensional protein crystals [6]. The following components are indicated: Hydrophilic trans-membrane helices A, B, C (light pink), amphiphilic helix D and hydrophilic loops (white), Chl *a* (dark green), Chl *b* (light green), and lutein (yellow).

At the current structural resolution Chls *a* and *b* are not directly distinguishable. Nevertheless, a tentative assignment basing on the necessity of effective triplet-state quenching mainly for Chl *a* and resulting proximity to lutein was suggested [6]. While occupations of several Chl-binding sites have been verified by site-directed mutagenesis [37, 38], the assignment of other sites is still a matter of debate [40]. Furthermore, actual orientations of the Chls are rather uncertain, since their phytol-chains are irresolvable at 3.4 Å resolution. Thus, atomic coordinates of Chls in the Kühlbrandt-model were obtained by fitting the nearly square porphyrin planes (cp. Fig. 1.2.4) into corresponding clouds of the electron-density map [6].
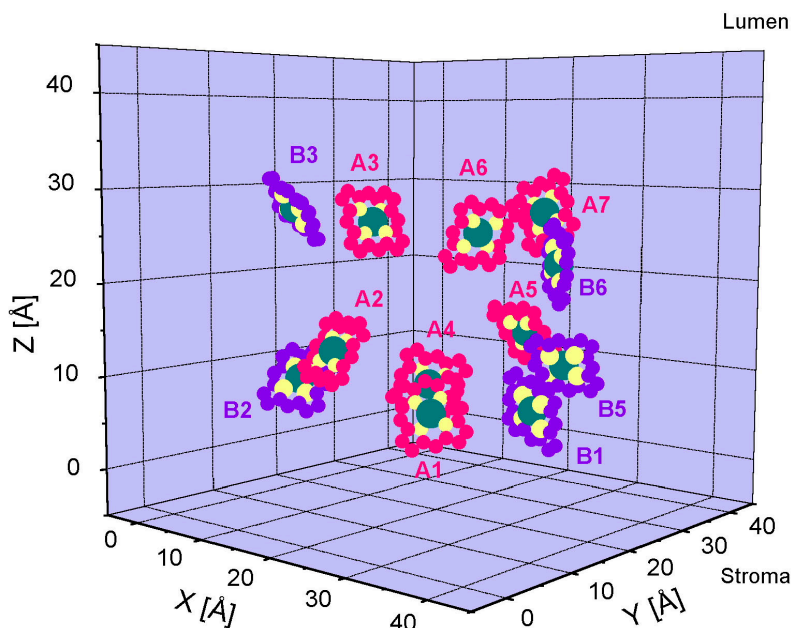
Figure 1.2.2 Atomic arrangement of the Chl *a* and *b* porphyrin planes in LHCII (viewed along the membrane). Carbon atoms are colored red (Chl *a*) and blue (Chl *b*), nitrogen atoms are yellow, and magnesium atoms are green. The atomic spheres correspond roughly to van-der-Waals radii. Atom coordinates and Chl assignments were taken from [6].

The complete structural model of LHCII according to Kühlbrandt et al. [6] contains thousands of atomic coordinates. Nevertheless, the relevant parameter number required for EET simulations can be drastically reduced. Within the LHCII complex, a majority of the protein frame has merely vanishing interactions with attached pigment molecules and can thus be neglected. In contrast, amino acids at resolved Chl-binding sites exert considerable electronic influence on the pigments. This interaction mediates the Chl-binding force and correspondingly disturbs the structure of their molecular electron orbitals slightly. In principle, the resulting shifts of Chl-transition energies can be obtained from *ab-initio* calculations [32]. However, currently available estimations show inconsistencies with the experimental findings. This may be either caused by the considerable complexity of such calculations or additional pigment-pigment interactions, which have not been considered yet (cp. Section 3.3.1). For that reason, site-specific transition energies of Chls were treated here *not* in accordance to their immediate protein vicinity. On the contrary, they were assumed as unknown parameters and additionally investigated by spectroscopic experiments as discussed in Chapter 3.2. The remaining

influence of protein environment on excited-state properties of Chls is taken into account by the transition line-shape and the refractive index **n**. In other words, explicit structure parameters of the LHCII protein frame are not required in this work.
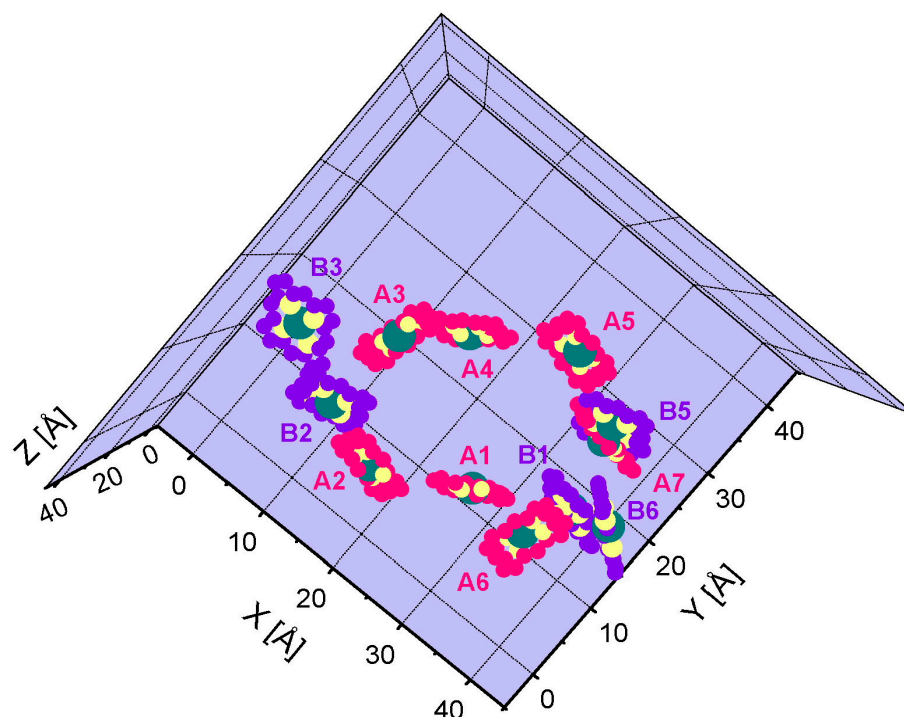
Figure 1.2.3 Atomic arrangement of Chl *a* and *b* molecular planes in LHCII (trans-membrane view from the lumenal side). Carbon atoms are colored red (Chl *a*) and blue (Chl *b*), nitrogen atoms are yellow, and magnesium atoms are green. The atomic spheres correspond roughly to van-der-Waals radii. Atom coordinates and Chl assignments were taken from [6].

A second reduction of the data set concerns Cars in LHCII, since the presented work was restricted to investigations of EET processes among the S_1-states of Chl *a* and *b*. Although Cars have their S_0-S_1 state transition in a similar spectral region like the Chls, this excitation step is spin-forbidden and shows no observable absorption. For that reason, the contributions of Cars (lutein, neoxanthin, violaxanthin) to the EET scheme were neglected as discussed in more detail below. Consequently, the structural model used in this thesis does also not include Car parameters. Nevertheless, it should be mentioned that Cars are known to play an essential role in LHCII, e.g. for light harvesting in the Soret-region, Chl-triplet quenching, excess energy dissipation, and the self-assembly ability. [41, 42, 43, 44, 45].

Summarizing all simplifications, the structural representation of LHCII was reduced here to twelve identified Chls per monomer (cp. Fig. 1.2.2, 1.2.3). This approach implies that *i*) probable EET among the S_1-states of Chls via Cars is neglected and *ii*) the protein frame is considered by spectroscopic parameters only. The obtained model still contains certain inaccuracies due to the achieved resolution in the structure analysis. As mentioned before, atomic coordinates for the Chls were obtained by fitting the electronic structure of porphyrin planes into electron-density clouds determined with 3.4 Å resolution. (For comparison: One porphyrin plane has the 'size' of about 2 x 9 x 9 Å, cp.

Fig. 1.2.4). Accordingly, the molecular planes itself are quite precisely determined, while the angular orientations within these planes remained rather uncertain.

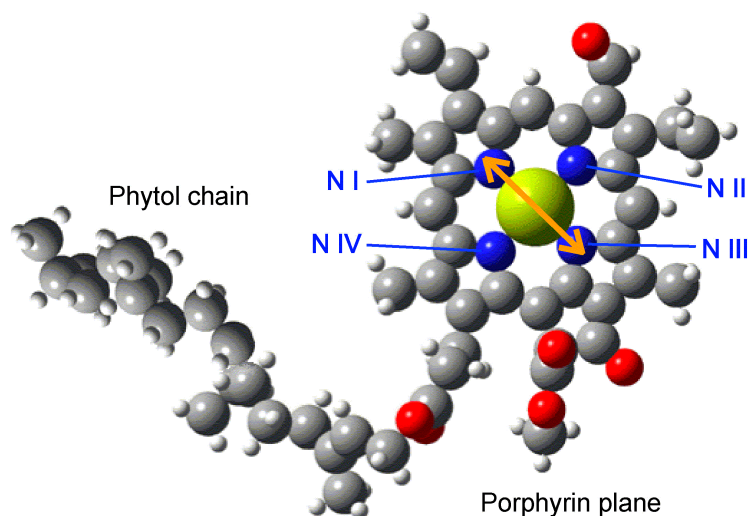**Figure 1.2.4** Atomic arrangement of Chl *b* (H - white, C - gray, O - red, N - blue, Mg - yellow). A tetrapyrrole ring forms together with a phytol chain the hydro-carbon backbone of the molecule, which contains additionally four N-atoms and one Mg-atom. Without phytol chain, the molecule represents a planar, nearly square porphyrin plane. Chl *a* looks rather similar, but has no keto-group at ring II (i.e. the oxygen atom on top is exchanged for a hydrogen atom). For both Chl species, the orientation of Q_y-transition dipoles is assumed more or less along the (N I)-(N III) diagonal (orange arrows).

Due to a nearly D_{4h}-symmetry of the porphyrins (without the phytol chain resolved), eight possible orientations are conceivable for each Chl. This results finally in two possible orientations of the molecular Q_y-transitions, since the transition dipole is assumed to be oriented along the (N I)-(N III) diagonal (see Fig. 1.2.4; cp. [14]). Although *exact* directions of Chl Q_y-dipoles in either solution or protein environment are not determined yet [46] (see also Section 3.4.2, p. 88), distinction between the two perpendicular Q_y-orientations is an essential question for the structural model of LHCII. Gradinaru et al. [14] have recently introduced the labels '0' and '1' for these two distinct orientations. While orientation '0' indicates the (N I)-(N III) axis, the '1' direction refers to the (N II)-(N IV) diagonal in the original Kühlbrandt-model [6]. Hence, each of the 12 Chl sites in the LHCII structure has to be considered with two possible transition-dipole orientations in the structural model.

As mentioned above, molecular distances and transition-dipole orientations are the key structural parameters determining inter-pigment EET (cp. also Chapter 1.3.1). Accordingly, the structural model can be finally reduced from atomic coordinates of twelve Chls to seven parameters per site (see Table 1.2.1 and Fig. 1.2.5). These values describe vector coordinates of the central Mg-atom and possible Q_y-transition dipole orientations in the form of two spatial angles, ϕ and θ. The range of both angles can be restricted to 0-180º, since two opposite directions as (N I)-(N III) and (N III)-(N I) are equivalent for EET calculations. Center-to-center distances between Chls can be directly obtained from the Mg-coordinates, ranging from 8 to 14 Å for the nearest neighbors in LHCII monomers. In contrast, the nearest neighbors of *different* monomers within a trimer – located at binding site **a4** and **a5** – are separated considerably farther (>20 Å).

For that reason, *inter*-monomeric EET does not exceed a value of 2 % of the total *intra*-complex transfer [40]. Due to this low amount, inter-monomeric transfer can be virtually neglected when compared to intra-monomeric EET. Hence, the structural data of one monomeric sub-unit represent also a sufficient model for EET calculations in the case of trimeric LHCII.

Table 1.2.1 Atomic coordinates of central Mg-atoms and possible Q_y-transition dipole orientations for Chl sites in LHCII calculated from the structure model in [6]. Possible Q_y-dipole orientations and Mg-coordinates are visualized in Fig. 1.2.5.

Chl site	Mg-coordinates [Å]			Configuration 0		Configuration 1	
	x	y	z	θ	φ	θ	φ
a1	25.004	13.248	7.154	121°	72°	35°	38°
a2	15.092	9.044	13.149	55°	80°	130°	131°
a3	8.937	21.917	25.928	132°	35°	130°	175°
a4	14.358	25.441	7.479	61°	64°	149°	33°
a5	23.62	31.441	13.749	121°	77°	47°	134°
a6	29.569	15.093	25.997	56°	34°	45°	172°
a7	29.488	26.563	27.56	114°	103°	24°	90°
b1	34.257	18.212	7.869	61°	112°	146°	84°
b2	8.038	11.062	9.264	60°	50°	128°	113°
b3	1.299	17.071	27.399	145°	33°	85°	115°
b5	31.319	27.831	11.104	50°	101°	127°	48°
b6	35.794	20.386	22.847	61°	129°	150°	124°
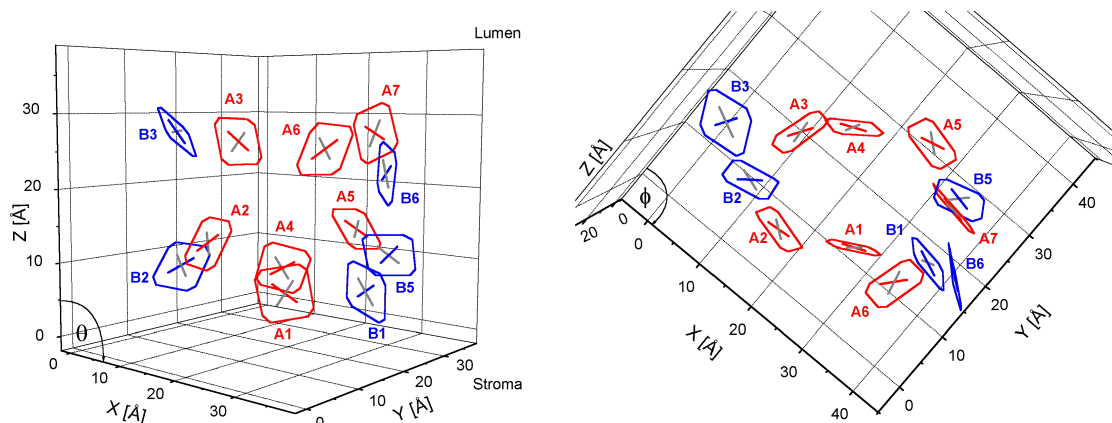
Figure 1.2.5 Reduced structural model for Chl *a* and *b* molecules in monomeric sub-units of LHCII (graphs in perspective). Molecular planes as indicated by the red (Chl *a*) and blue (Chl *b*) squares were added for convenience. Q_y-dipole orientations assumed along the (N I)-(N III) vector ('0'-direction, see text) are indicated by red bars for Chl *a* and blue bars for Chl *b*. Alternative orientations ('1'-direction) are illustrated by gray bars. Besides this, Mg-coordinates are reflected by the bar crossing points. Table 1.2.1 summarizes the underlying structure parameters. **Left panel:** View along the membrane. **Right panel:** Trans-membrane view from the lumenal side.

Table 1.2.1 contains the entire structural information required for understanding EET processes among Chl S_1-states in LHCII under the restrictions discussed above. This parameter model is further illustrated in Fig. 1.2.5. The illustration depicts that the spatial arrangement of the twelve crosses embodies all necessary structural information for EET modeling in the framework of this thesis.

1.2.2   Spectroscopic properties of LHCII

All spectroscopic features of LHCII in the visible range originate from its inherent pigments, since the protein itself absorbs in the UV-region only. The two types of attached pigments – Chls and Cars, i.e. xanthophylls – differ significantly in their excited-state properties. On one hand, both organic molecules have a π-electron backbone and therefore a rather analogous excited-state scheme. However, the first-excited state (S_1) of xanthophylls cannot be populated by single photon absorption due to a similar angular momentum as the ground state (S_0). Consequently, the Car absorption in LHCII does not interfere with S_1-transitions of Chls (cp. also Fig. 1.2.7). Although it should be mentioned that populations of Chl-triplet states (T_1) are effectively transferred to Cars [47], the NLPF experiments are not sensitive to these triplet excitations.

A schematic representation of the electronic structure of Chls relevant for absorption and relaxation processes in the visible spectral range is shown in Fig. 1.2.6. The highest occupied molecular orbital forms S_0. Due to a nearly D_{4h}-symmetry of the porphyrin plane, four excited states are formed by two pairs of virtually degenerate energy levels (Q_x, Q_y and B_x, B_y). Nevertheless, slight asymmetries break this degeneracy and result in two strong electronic transitions to Q_y (= S_1) and B_x (= S_3). In contrast, excitations to Q_x (= S_2) and B_y (= S_x) have much less transition probability and are neglected. Electronic excitations of the molecule are followed by relaxation processes combined with energy conversion until the ground state is repopulated in the thermal equilibrium. These diverse molecular relaxation channels are characterized by different kinetics (cp. Fig. 1.2.6). Vibrational relaxation takes place within some hundred fs, while radiationless internal conversion from S_3 to S_1 appears to need several ps [48]. The S_1-state fluorescence occurs within a few ns [13] and inter-system crossing is characterized by the µs to ms timescale [47]. According to these different dynamics of intra-molecular relaxation processes, EET among Chls in LHCII is mainly restricted to the S_1-states: While internal conversion depopulates S_3 almost immediately, excitations reside at S_1 about thousand times longer. Populations of T_1 are effectively transferred to Car, thus making triplet transfer among Chls less likely. For that reason, EET between S_1-states of Chls is the most relevant process that can perform the light-harvesting function of LHCII. Consequently, this work was solely directed to investigations of EET among Chl S_1-states.

Soret- and Q_y-transitions are reflected in the visible region of Chl spectra as shown in Fig. 1.2.7 (left panel). The range between 550 and 700 nm represents mainly Q_y-

absorption, while the Soret-band extends below 500 nm into the near UV-region. In contrast, almost no absorption is observable between 500 and 550 nm. The right panel in Fig. 1.2.7 enables a more detailed view into the Q_y-band structure. For Chl a, the $Q_y(0,0)$-band is centered around 665 nm, the $Q_y(0,1)$-transition peaks at 620 nm and the $Q_y(0,2)$-band has its maximum near 575 nm. Corresponding values for Chl b are 645, 595 and 550 nm. Some Q_x-absorption can be observed for both species in the region below 575 nm. While the Q_y-band of Chl a is located at about 20 nm longer wavelength when compared to Chl b, the Soret-bands are oppositely displaced (see Fig. 1.2.7, left panel).
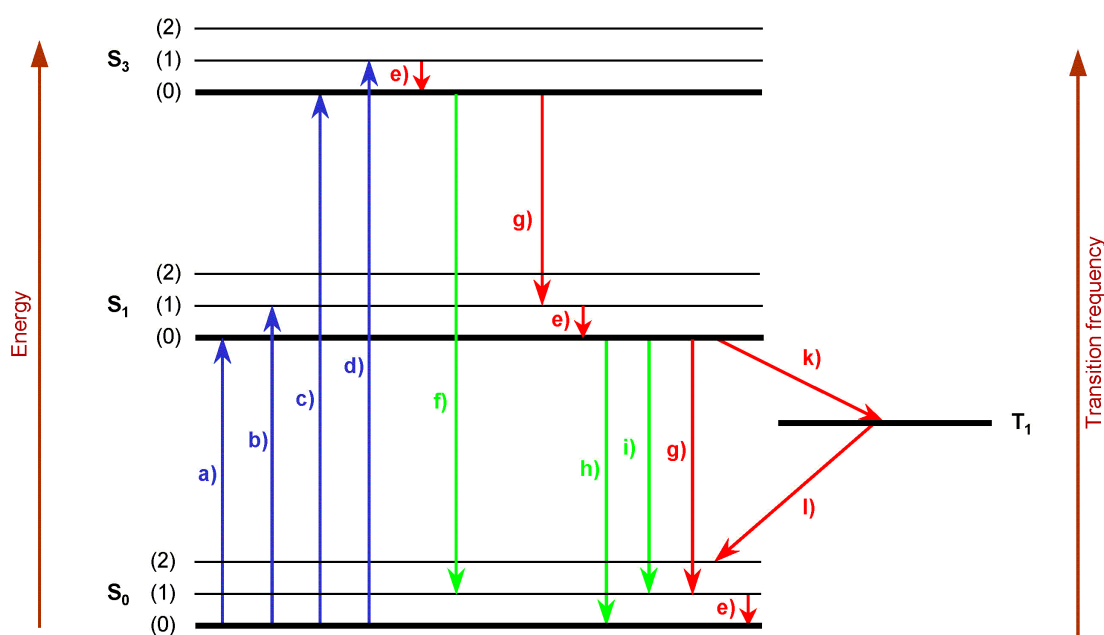
Figure 1.2.6 Possible transitions within the electronic structure of Chls (Jablonski-scheme): Photon absorptions (blue), fluorescent transitions (green), and radiationless relaxations (red). Each electronic state (S_0, S_1, and S_3) is formed by several vibrational levels (0), (1), (2)... . The rather weak Q_x-band is not considered. Different transitions are commonly distinguished as follows: **a)** $S_0(0) \rightarrow S_1(0)$: $Q_y(0,0)$-absorption; **b)** $S_0(0) \rightarrow S_1(1)$: $Q_y(0,1)$-absorption; **c, d)** $S_0(0) \rightarrow S_3$ (n): Soret-absorption; **e)** Vibrational relaxation; **f)** Ultra-weak Soret-fluorescence **g)** Internal conversion (IC); **h)** $S_1(0)$-$S_0(0)$: $Q_y(0,0)$-fluorescence; **i)** $S_1(0)$-$S_0(1)$: $Q_y(0,1)$-fluorescence; **k)** Inter-system crossing (ISC) to T_1; **l)** ISC to S_0.

To interpret the superposition of Chl a and b absorption in LHCII, one has to consider a pigment content of about 7 Chl a and 5-6 Chl b per monomer (cp. Table 2.1.1, p. 24). Furthermore, both types of molecules have different absorption strengths. The dipole strengths of the Q_y-band in Chl a (≈ 21.4 D^2 in ether solution, cp. [49]) is about for 1.5-times higher than that of Chl b [50]. (Actually, a very recent study by Knox [51] obtained somewhat higher dipole strengths for both species, but the ratio between Chl a and b is not affected by these findings.) Accordingly, the total absorption of Chl b in the Q_y-region – measured as integrated area under the spectrum – should represent a 0.53-fold contribution in comparison to Chl a. The spectra of Chl a and b are therefore compared to LHCII absorption in Fig. 1.2.7 by an adequate normalization. Although the

underlying calculation neglects possible redistributions of dipole strengths between Soret- and Q_y-bands in LHCII [52], it represents a sufficient approximation. At the first glance, one can obtain that all Q_y-transitions are shifted to longer wavelengths in LHCII. Furthermore, especially the Chl-*a* absorption is broadened in protein environment, thus resulting in a higher maximum of the molecular spectrum when compared to LHCII absorption.
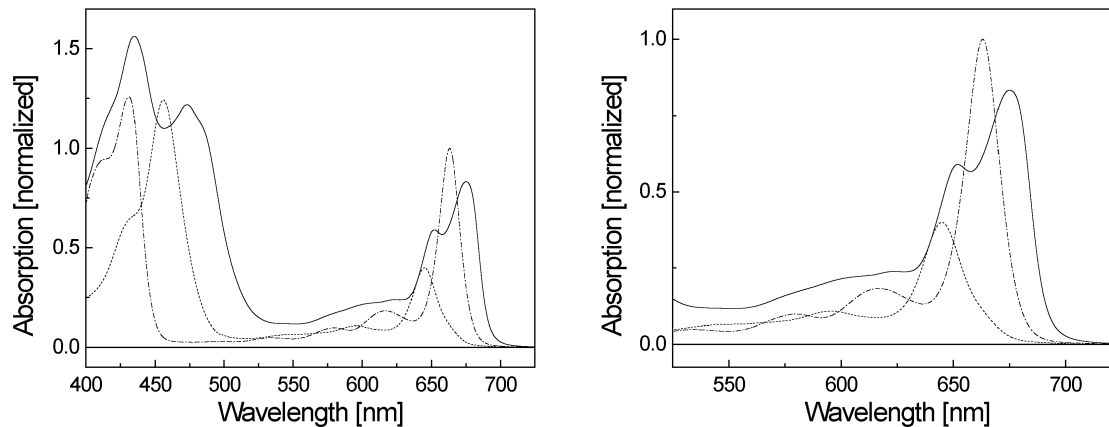

Figure 1.2.7 Left panel: Absorption profiles of the Q_y- and Soret-region of Chl *b* (dashed line) and Chl *a* (dash-dotted line) in acetone compared to LHCII in buffer/detergent solution (solid line). The Chl *a* spectrum is normalized to 1 at Q_y-maximum. In contrast, the Chl *b* spectrum is normalized to a 0.53-fold integrated area in the Q_y-region between 550 and 750 nm when compared to Chl *a*. This normalization reflects the expected contributions of both Chl species in LHCII (see text). The LHCII-absorption integral between 550 and 750 nm is normalized to equal the *sum* of Chl *a* and *b* integrals in this region. **Right panel:** Magnified Q_y-absorption region of the image in the left panel.

Proper interpretation of LHCII spectra in terms of its 12 individual Chl *a* and *b* transitions has been a long-standing challenge [40, 53, 54, 55]. In this context, the origin of spectral shifts and line-broadening mechanisms represent the crucial issues to develop an adequate sub-structure model. Spectral shifts can be caused by unique Chl environments due to the surrounding protein matrix [32] or because of electronic interactions with neighboring pigments (see Chapter 1.3.1). Accordingly, the Q_y-band of LHCII is formed by superposition of several overlapping sub-bands, which are characterized by slightly shifted transition energies. In this case, spectral broadening must not reflect an increased width of individual transitions, but results from heterogeneity among their center wavelengths, λ_c. One indication for the nature of spectral sub-structure in LHCII can be obtained by studying the absorption at low temperatures (see Fig. 1.2.8). At 4 K, the spectrum clearly shows two distinct bands in the Chl *a* region, one band around 660 nm, and two weak bulges at 645 and 640 nm. This observable heterogeneity is commonly referred to as 'spectral forms' of Chls in LHCII, thus describing pigments with individual first-excited state transition energies [56, 57]. Other recent studies have also addressed spectral heterogeneity in the Soret-band [41, 58], where the absorption of Cars overlapping with Chl *b* absorption had to be further considered (see the shoulder near 490 nm in Fig. 1.2.7, left panel).
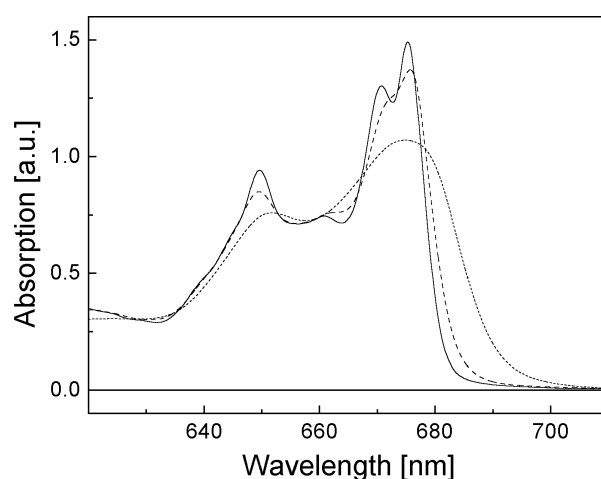
Figure 1.2.8 Absorption spectra (main Q_y-transition band) of isolated trimeric LHCII recorded at 4 K (solid line), 120 K (dashed line), and 293 K (dotted line).

Adequate theoretical descriptions of Chl-transition bands are a main prerequisite for modeling the LHCII absorption sub-structure. This mathematical representation must take into account that the individual molecular transitions have no exactly determined transition energies. On the contrary, their energy levels vary on different timescales due to interactions with the environment. Several mathematical approaches have been used to obtain comprehensive descriptions of all possible interactions in condensed matter [30, 33]. Unfortunately, the resulting expressions contain numerous variable parameters and most of these values are not directly accessible by experimental measurements. It should be further mentioned that a sub-structure model is required in this thesis to evaluate nonlinear optical properties of LHCII. According to the theoretical framework developed for this purpose [1], a simpler mathematical description was necessary.

Consequently, Chl bands are approximated by Voigt-profiles, thus reflecting homogeneous and inhomogeneous broadening mechanisms. This approximation implies that principally two timescales are considered for molecular interaction with the environment. Homogeneous broadening refers to phase relaxation of the electronic states on timescales faster than other excited-state dynamics. These variations result from coupling of molecular states to vibrational modes of the surrounding protein matrix. In contrast, inhomogeneous broadening describes quasi-stationary differences in the pigment-protein interactions because of environmental differences for each individual Chl. This distinction between two broadening mechanisms is of essential importance for understanding the nonlinear response in NLPF experiments (see Chapter 2.2.3). In particular, the homogeneous part describes properties of *one single* transition, while the inhomogeneous contribution summarizes a molecular *ensemble*.

Additionally, the number of vibrational levels considered in the Q_y-absorption model has to be chosen. Several authors have recently included five distinct Chl bands [12, 59], thus describing the complete set of observable transitions ($Q_y(0,0)$, $Q_y(0,1)$, $Q_y(0,2)$, $Q_x(0,0)^*$, and $Q_x(0,1)$ according to [60]. However, modeling of the main $Q_y(0,0)$-

---

* The $Q_y(0,2)$- and $Q_x(0,0)$-transitions are assumed to overlap almost completely.

absorption region of LHCII between 625 and 700 nm (see Fig. 1.2.7, right panel) does not necessarily require this complete set of bands. On the other hand, the $Q_y(0,1)$-transition of Chl *a* clearly overlaps with the $Q_y(0,0)$-transition of Chl *b*. Hence, each Q_y-transition is approximated in the framework of this thesis by *two* bands, thus reflecting $Q_y(0,0)$- and $Q_y(0,1)$-absorption. A basic parameter set describing the corresponding Voigt-profiles for molecular Chl *a* in solution is summarized in Table 1.2.2 and further illustrated in Fig. 1.2.9.

Table 1.2.2 Two-band approximation of the $Q_y(0,0)$- and $Q_y(0,1)$-transitions of Chl *a* and *b* in acetone solution. The underlying Voigt-profiles are characterized by λ_c, absorption coefficient α, homogeneous width 2Γ and inhomogeneous width Δ. Indicated α parameters take into account the 0.68-fold dipole strength of Chl *b* when compared to Chl *a*. The model for Chl *a* is compared to a measured spectrum in Fig. 1.2.9.

	Chl *a*		Chl *b*	
	$Q_y(0,0)$	$Q_y(0,1)$	$Q_y(0,0)$	$Q_y(0,1)$
λ_c [nm]	663.2	617	645.1	595
α [a. u.]	1	0.46	0.68	0.49
2Γ [nm]	10	34	15	46
Δ [nm]	11	11	11	11
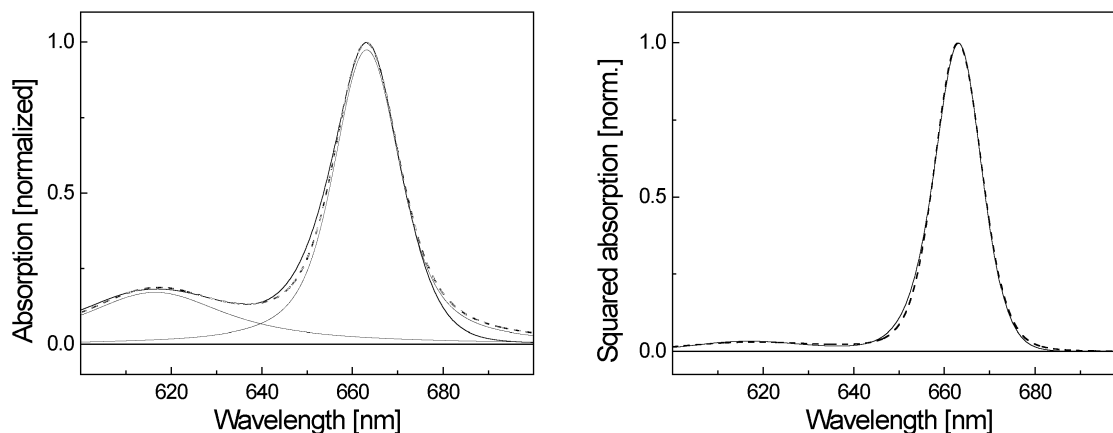
Figure 1.2.9 Left panel: Chl-*a* absorption profile in acetone between 600 and 700 nm (solid line). The spectrum is approximated by one Voigt-profile for each of the (0,0)- and (0,1)-transitions (thin lines) using parameters from Table 1.2.2. Superposition of the two bands results in the dashed line. **Right panel:** Squared curves of the measured and simulated spectra from the left panel.

Some minor differences between theoretical description and measured spectrum are observable in the red wing of the Q_y-band in Fig. 1.2.9 (left panel). However, it should be mentioned that NLPF spectra are related to *square* values of the absorption line shape as discussed below especially in Sections 2.2.3 and 3.1.1. Accordingly, deviations between theoretical model and measured spectrum are only relevant on the level of squared values as shown in Fig 1.2.9 (right panel). The differences between measured spectra and the two-band model can be obviously neglected in the whole range from 600 to 700 nm. Hence, the approximation of two Voigt-profiles per electronic transition

represents a sufficient compromise between parameter reduction and adequate mathematical description. This approach has been therefore employed to establish an absorption sub-structure model for LHCII in Chapter 3.2 and to evaluate NLPF spectra in Chapter 3.5.

Last but not least, some relevant characteristics of LHCII fluorescence (see Fig. 1.2.10) are shortly described in the following. Obviously, almost all emission originates from Chl *a*, i.e. when considering the ~10 nm shift of Chl absorption in LHCII. This observation is related to fast and effective EET from Chl *b* to Chl *a* within the complex as discussed in more detail in Chapter 1.3.1. Furthermore, LHCII fluorescence is slightly narrower than Chl-*a* emission in solution (see Fig. 1.2.10, right panel), while Chl *a* absorption is somewhat broader in LHCII. Spectral heterogeneity of (slightly narrower) bands in LHCII is again the most plausible origin of this feature. A minor contribution to the LHCII fluorescence between 640 and 660 nm is most probably related to 1-3 % emission from Chl *b*. The extent of this contribution corresponds well to the expected population distribution between S_1-states of Chl *a* and *b* in the thermal equilibrium. It should be further mentioned that molecular fluorescence spectra look highly similar after excitation in either the Soret- or Qy-region. This behavior reflects that excitations of S_3-states relax radiationless to fluorescent S_1-state within a few ps (see above). Hence, the emission spectrum features in both cases mainly contributions from $Q_y(0,0)$- and $Q_y(0,1)$-transitions (maximum at ~685 and ~735 nm, respectively). On the other hand, highly sensitive two-photon excited fluorescence spectra can indeed reveal the minimal fraction of Soret-emission as recently shown in [61].
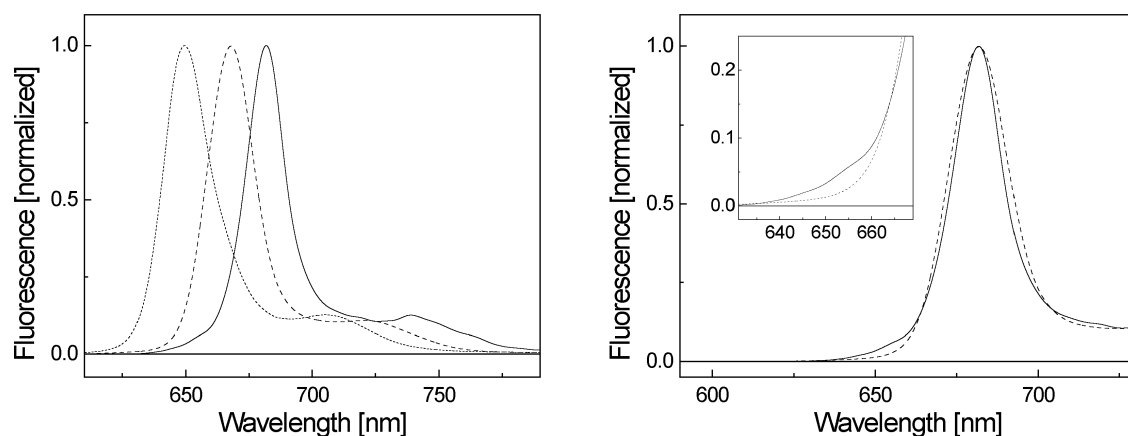
Figure 1.2.10 Left panel: Normalized RT fluorescence spectra of Chl *b* (dotted line) and Chl *a* (dashed line) in acetone compared to LHCII in buffer/detergent solution (solid line). Excitation wavelengths were 460 nm (Chl *b* and LHCII) and 420 nm (Chl *a*). **Right panel:** Chl *a* emission spectrum from the left panel shifted by 14 nm to longer wavelength (dashed line) in comparison to LHCII emission from the left panel (solid line). Differences in the area between 640 and 660 nm are shown in more detail in the inset.

1.3 Physical description and biological function of excitation energy transfer and regulation in LHCII

Regarding effective EET as one major task of the photosynthetic antenna system in higher plants, dipole-dipole interactions between Chls function as the key mechanism. This transfer can be modeled in two different regimes distinguishing between weak or strong electronic interaction among the pigment molecules. The first case results in Förster-type EET [62, 63], which is known to enable transfer times as fast as some hundred fs [12]. However, strong coupling among pigments causing 'excitation delocalization' over several molecules may further increase the EET efficiency [64]. The formation of such delocalized states, also known as 'exciton' formation, was observed among bacteriochlorophyll (BChl) pigments in photosynthetic antenna complexes of purple bacteria [65, 66, 67]. According to theoretical calculations [31, 68, 69, 70], delocalization can be expected in the case of Chls for inter-molecular distances of at least ≤ 12 Å. Since center-to-center distances to the nearest neighbor range between 8 and 11 Å in LHCII, the possible existence of excitonic states became an extensively discussed topic.

To begin with, excitonic interaction is presumably reflected by the considerably increased optical activity [40]. Compared to monomeric Chl in solution, circular dichroism (CD) spectra of LHCII reveal a rotational strength that may be hardly explained without considering excitonic interactions [71]. However, the CD spectrum of LHCII has not been consistently modeled so far, and several different models have been proposed [64, 72, 73, 74]. Furthermore, the excited-state energy levels are commonly shifted in comparison to monomeric Chl in the case of excitonic coupling. Nevertheless, this effect might overlap with spectral shifts originating from Chl interactions with the protein environment [32]. Thus, spectral shifts due to exciton formation are hard to identify in heterogeneous spectral sub-structures like for LHCII. A last significant feature of excitonic coupling is that light-induced bleaching of one exciton state affects the spectral distribution of the other one. Accordingly, the occurrence of satellite holes in non-photochemical hole-burning experiments at 4 K has been taken as indicative of excitonic coupling [54]. Unfortunately, this effect cannot be sufficiently distinguished from burn-induced alterations in the protein matrix.

The discussion above reveals a high uncertainty about possible excitonic interactions among Chls in LHCII due to the shortcomings of conventional spectroscopic methods. Consequently, the nature of EET among Chl S_1-states in LHCII remains a still unresolved question. The following section describes Förster-type and excitonic EET to gain some basic insight into both mechanisms. This comparison aids the comprehension of experimental investigations in Chapter 3.3 and 3.4 as well as the theoretical analysis of NLPF spectra in Chapter 3.1.

1.3.1 Energy transfer in LHCII: Förster-type hopping or exciton relaxation?

Radiationless energy transfer depicts the exchange of excitations between different electronic states. This process is generally directed from excited states with higher energy to those with lower energy (= 'downhill') by dissipating excess energy via vibrational relaxation. Nevertheless, thermal fluctuations of the excited-state energies can also enable 'uphill' transfer to levels with higher electronic energy. Although the probability for uphill transfer decreases with increasing gaps between the energy levels, the basic mechanism is independent from the transfer direction. Hence, 'uphill'- and 'downhill'-transfer are not explicitly distinguished in the following. Förster-type and excitonic EET are compared in Fig. 1.3.1 within the electronic structure of two uncoupled Chls (left panel) and a strongly coupled Chl dimer (right panel).

Förster-type EET

Excitonic EET
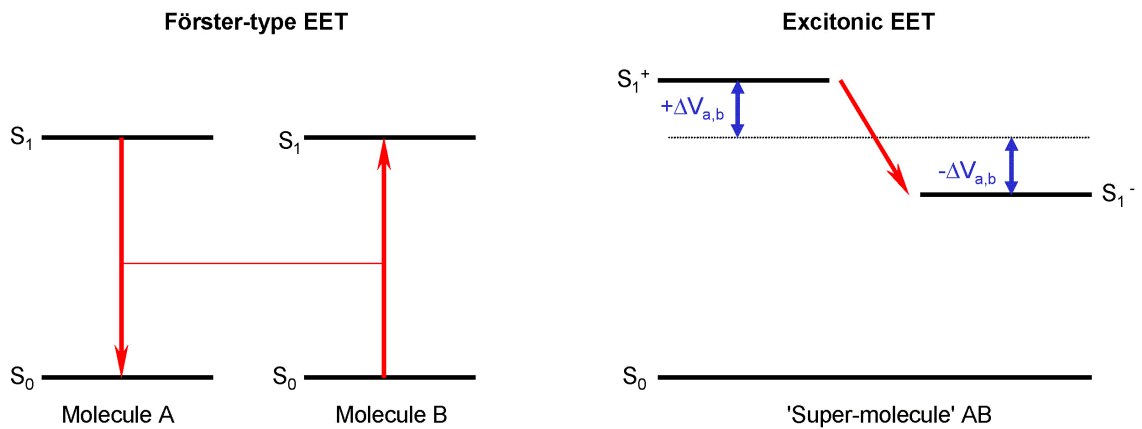
Figure 1.3.1 EET mechanisms on the molecular level of electronic ground and excited states. **Left panel:** Förster-type EET between the S_1-states of molecules A and B, corresponding to radiationless ground-state repopulation at molecule A and simultaneous excited-state population at molecule B. The excitation exchange is induced by dipole-dipole interaction between the molecular transition dipoles. **Right panel:** EET among excitonic states formed by strongly interacting molecules A and B. Due to strong electronic coupling between both molecular transition dipoles, a common ground state is formed together with two exciton states S_1^+ and S_1^-. These states are shifted by V_{AB} with respect to the initial molecular levels. (An additional, absolute shift of all electronic states due to van-der-Waals interaction can be subtracted). Within the excitonic level structure, EET occurs rather in the form of relaxation between exciton states than as EET between different molecules.

Förster-transfer between uncoupled Chls occurs because of dipole-dipole interaction between the transition-dipole moments of neighboring molecules A and B. The corresponding transfer rate $\gamma_{A,B}$ depends on inter-molecular distances, $\vec{r}_{AB}$, the geometrical arrangement of transition dipoles, κ, the refractive index **n** of the medium, and spectral overlaps $C_{A,B}$ between donor A and acceptor B according to (cp. [40])

$$\gamma_{A,B} = \frac{C_{AB} \cdot \kappa^2}{n^4 \cdot \vec{r}_{AB}^6} .$$ (1)

In Eq. 1, the factor κ depends on the unit vectors of the transition dipoles, $\hat{\mu}_{A/B}$, and unit vectors of molecular distances, $\hat{r}_{AB}$, according to $\kappa = \hat{\mu}_A \cdot \hat{\mu}_B - 3(\hat{\mu}_A \cdot \hat{r}_{AB})(\hat{\mu}_B \cdot \hat{r}_{AB})$. Spectral overlaps $C_{A,B}$ correspond to overlapping areas under the donor emission and acceptor absorption spectrum. They can be roughly estimated for Chls *a* and *b* in

solution by comparison of Figs. 1.2.7 and 1.2.10 in the previous chapter. The following values $C_{A,B}$ were calculated in [14] for transfer channels between both Chls types in LHCII: $C_{a,a} \approx 30$ ps^{-1} nm^6, $C_{b,b} \approx 15$ ps^{-1} nm^6, and $C_{b,a} \approx 10$ ps^{-1} nm^6. In principle, these values further deviate for each individual pair of Chls due to the exact λ_c of their transitions [75]. However, the resulting differences of ± 30 % are quite moderate within one Chl species. For that reason, EET is modeled in this work by using the constant overlap integrals above without considering exact transition wavelengths. This approximation enabled further considerable simplifications for simulations of NLPF spectra in Chapter 3.5. Finally, it should be mentioned that the estimated value of $C_{a,b} \approx$ 1 ps^{-1} nm^6 is in good agreement with the negligible Chl *b* fluorescence observed for LHCII (see inset in Fig. 1.2.10).

Proper determination of the refractive index **n** plays a further crucial role for correct calculations of Förster-rates [76]. Various recent studies investigated **n** for Chls in protein environment, mostly resulting in values of ~1.6 [40, 77]. However, several closely neighboring Chls in LHCII or the ones on the surface do not feature *any* in-between protein parts. Electro-magnetic screening of dipole-dipole interactions in the order of **n** = 1.6 is thus hardly conceivable for these molecules. Under the assumption of water molecules shielding the Chls (**n** $\approx$ 1.3), the calculations of $\gamma_{A,B}$ would become about three times higher. Moreover, the presumption of pure vacuum filling the space between two neighboring Chls (**n** = 1) results in six-fold increased $\gamma_{A,B}$. Apparently, this problem should be investigated with more care in the future to obtain more precise calculations of EET rates.

Strong coupling between Chls can cause the formation of excitonic states as observed within the B850 ring of the antenna complex LH2 of purple bacteria [65, 66]. Certainly, it should be mentioned that the excitonically coupled BChls in LH2 have *i*) moderately higher transition-dipole moments than Chls, *ii*) nearly constant distances of about 8.5 Å, and *iii*) almost parallel orientations of nearest-neighbor transition dipoles due to a ring-like arrangement [5]. In contrast, Chls in LHCII feature much less order as outlined in Section 1.2.1. Nevertheless, calculation of the coupling strength[*] V_{AB} according to [40],

$$V_{AB} = \frac{5.04 \cdot f_I^2 \left| \mu_A \right| \left| \mu_B \right| \kappa^2}{\sqrt{n} \cdot r_{AB}^3} \quad , \tag{2}$$

results in considerable interaction energies for at least some Chl-pairs (f_I: local field correction). This calculation is less influenced by uncertainties about **n**, but it depends on the still unknown Chl-transition dipole orientations in LHCII (cp. Section 1.2.1). Accordingly, calculated inter-molecular coupling strengths as summarized for example in [40] represent only an incomplete picture at the present state of knowledge. On the other hand, most conventional spectroscopic methods are inappropriate to reveal (or exclude) excitonic coupling in LHCII. For that reason, this discussion is continued further below based on new experimental data as obtained in Chapter 3.3 and 3.4.

---

[*] In the case of excitonic coupling in dimers, V_{AB} is directly related to the split between S_1-energy levels as indicated in Fig. 1.3.1 (right panel).

Besides a split of energy levels induced by excitonic coupling (see Fig. 1.3.1, right panel), the transition probability can be redistributed between exciton states. This redistribution depends on geometrical orientations of the involved molecular transition dipoles. In the case of excitonically coupled Chl *a/a* homodimers, any distribution up to two-fold probability in either the S_0-S_1^+- or S_0-S_1^--transition is possible. In contrast, a maximum value of 1.7-fold increased transition probability for the S_0-S_1^--transition can be estimated in the case of Chl *a/b* heterodimers due the lower dipole moment of Chl *b*. Three different cases of excitonic redistribution are shown in Fig. 1.3.2 to exemplify the influence on resulting absorption spectra.
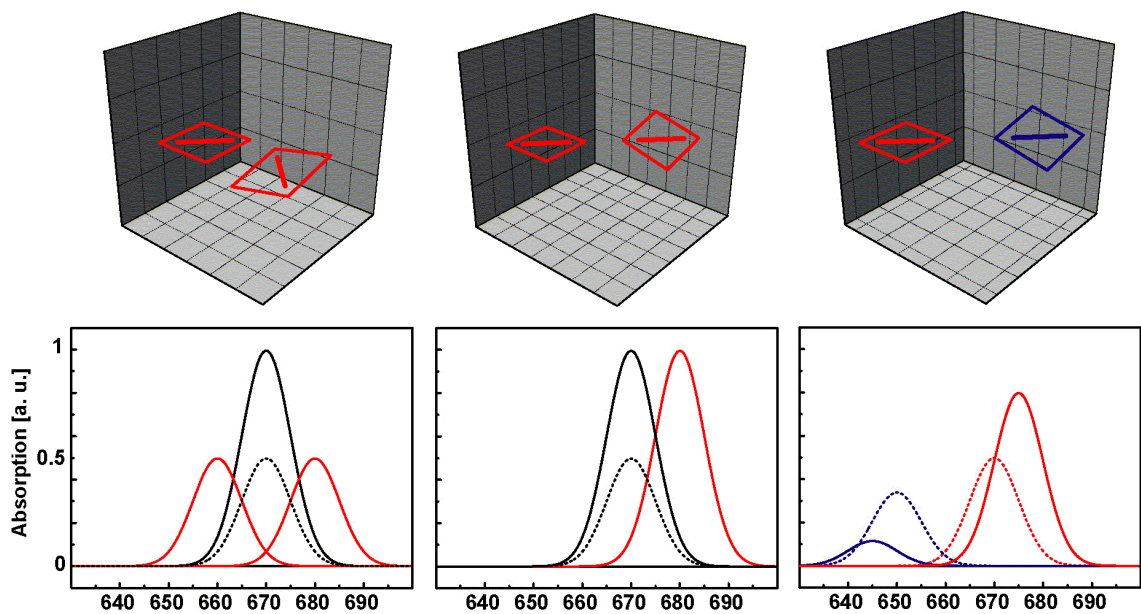
Figure 1.3.2 Redistribution of transition probability between excitonic states of electronically coupled Chl-dimers in dependence on transition-dipole orientations. Different arrangements are shown in the upper 3D-graphs (squares: Chl planes, bars: transition dipoles). Simulated absorption spectra in the lower graphs indicate corresponding distributions of transition probability among the S_0-S_1^+ and S_0-S_1^- transitions (cp. Fig. 1.3.1, right panel). **Left panel:** In-plane arrangement with 90°-orientation between two Chl-*a* dipoles. The molecular S_0-S_1 transition is assumed at 670 nm (black dashed line). Without coupling, the absorption spectrum of both Chls results in one transition band (black solid line). In the case of excitonic coupling the transition probability is equally distributed between S_0-S_1^+- and S_0-S_1^- transitions (red lines). **Center panel:** Exact 'in-line' orientation of two Chl-*a* dipoles. The uncoupled case is similar to the graph in the left panel. However, *all* transition probability is concentrated in the S_0-S_1^- transition (red line) for coupled dimers. **Right panel:** Nearly 'in-line' orientation between one Chl *a* and one Chl *b* dipole. The spectra without coupling are simulated by dashed lines (Chl *a*: red, Chl *b*: blue). In the case of exciton formation, redistribution results in transition bands as indicated by the solid lines.

In contrast to Förster-transfer, excitonic EET does not necessarily refer to spatial movements of excitations under the classical point of view. Moreover, the transfer corresponds to spectral relaxation among delocalized states, since excitations cannot be assigned to one individual molecule any longer (cp. Fig. 1.3.1, right panel). This delocalization is caused by exciton-state formation as superposition of former individual molecular orbitals, including formation of a common ground state [78]. A better insight into this mechanism can be obtained by comparing possible EET pathways for uncoupled molecules and excitonic sub-units within pigment-protein complexes (see

Fig. 1.3.3). Without coupling, excitations are always located at one specific molecule after initial photon absorption. Accordingly, EET occurs as Förster-type hopping process along an energetically determined molecular pathway until the next antenna or RC protein is reached. In contrast to this, EET among excitonic sub-units is less specifically localized at individual molecules. However, the average distances between most of the Chls in LHCII are too large to expect coupling among all pigments [79]. Hence, the transfer between excitonic sub-units will occur again by Förster-type hopping.
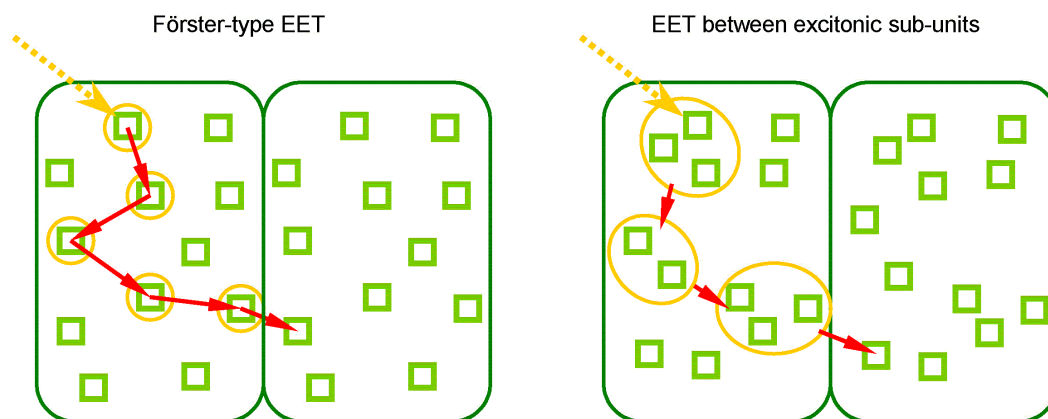
Figure 1.3.3 Two conceivable EET mechanisms within the pigment-containing protein complex LHCII. Dark-green boxes indicate the outer protein boundaries, while light-green squares represent the individual Chls. Photon absorption is indicated by dotted arrows. Excitations are illustrated by orange circles/ellipses and EET is shown as sequence of red arrows. **Left panel:** Förster-type EET **Right panel:** Coherent EET among excitonic sub-units formed by two or three Chls.

As mentioned at the beginning of this chapter, several experimental techniques have been used to investigate excitonic interactions in LHCII or other plant antenna proteins. Nevertheless, the question of possible excitonic coupling has not been solved so far. On the other hand, EET among the Q_y-bands of Chls can be quite efficient even in the case of Förster-type transfer [12]. Accordingly, the LHCII structure and observed EET rates have not been brought together in a physically congruent model yet. For example, certain features in transient absorption spectra of the highly related antenna complex CP29 are hard to explain by pure Förster transfer [75]. In the opinion of the author, this problem is mainly related to *i)* uncertainties about actual Chl *a* or *b* assignments to several binding sites, *ii)* an exact reflection of the refractive index **n** in-between two closely neighboring Chls, and *iii)* general ambiguity about dipole orientations of Chl Q_y-transitions in LHCII. Accordingly, the thesis on hand tackled some of these problems by new experimental approaches, thus offering a complement to the existing 'zoo' of spectroscopic techniques. To improve the comparability of obtained results with other studies, an initial EET scheme is presented in Table 1.3.1. This scheme presumes pure Förster-transfer between all Chl-binding sites according to Eq. 1 and reflects the theoretical approach commonly used in recent publications [12, 40, 75]. All required geometrical parameters κ^2 and $\vec{r}_{AB}$ as summarized in Table 1.3.2 can be directly obtained from the structural data shown in Table 1.2.1 (p. 9). Different modifications of the scheme in Table 1.3.1 as suggested by other authors and by the studies on hand are then discussed in Chapter 3.5.

Table 1.3.1 Approximated EET rates $\gamma_{A,B}$ [ps^{-1}] among Chl S$_1$-states in LHCII as calculated for Förster-transfer (see Eq. 1, **n** = 1.6). The left column indicates the donor sites, while the first row names the acceptor sites. All underlying geometrical parameters are summarized in Table 1.3.2. In contrast to results presented in Chapter 3.2 and 3.5, the Chl assignment is assumed according to the original Kühlbrandt model [6] (Chl *a*: red, Chl *b*: blue). Deviations from this presumed Chl occupancy could be directly considered in the scheme below by adapting the different overlap factors C$_{A,B}$ in Eq. 1. All dipole orientations were supposed in 0-direction (cp. Table 1.2.1, p. 9). Other orientations require adaptations of the corresponding geometrical factor κ^2 as summarized in appendix **A2**. EET rates >10% of the maximum value are shown in bold, and rates lower than 0.01 ps^{-1} are neglected.

	a1	a2	a3	a4	a5	a6	a7	b1	b2	b3	b5	b6
a1	X	**1.15**	-	0.02	0.1	0.08	0.01	0.17	0.01	-	-	-
a2	**1.15**	X	-	0.2	~0*	0.27	-	-	**0.45**	-	-	-
a3	-	-	X	0.06	0.22	-	0.04	-	-	0.09	-	-
a4	0.02	0.2	0.06	X	**0.95**	-	-	-	-	-	0.01	-
a5	0.1	~0*	0.22	**0.95**	X	-	0.34	-	-	-	0.32	-
a6	0.08	0.27	-	-	-	X	**0.98**	-	-	-	-	0.02
a7	0.01	-	0.04	-	0.34	**0.98**	X	-	-	-	0.01	0.14
b1	1.69	-	-	0.02	0.015	-	0.015	X	0.02	-	**1.18**	0.01
b2	0.12	**4.5**	0.01	0.01	0.01	-	-	0.02	X	0.03	-	-
b3	-	0.01	**0.94**	-	-	-	-	-	0.03	X	-	-
b5	-	-	-	0.12	**3.2**	0.015	0.12	**1.18**	-	-	X	**0.48***
b6	-	-	0.01	0.01	-	0.25	**1.38**	0.01	-	-	**0.48***	X

* These values indicate possible errors for the parameters calculated in [40].

Table 1.3.2 Geometrical parameters of Q$_y$-dipoles for all determined Chl sites in LHCII. Numbers in the upper-right half indicate distances r_{AB} [Å] between approximated point-dipoles located at the Mg-coordinates. The lower-left half contains geometry factors κ^2 under the assumption of '0'-orientation for all transition dipoles (cp. Chapter 1.2.1, only pairs with distances <25 Å are considered). Chl *a*/*b* pairs with closest distances are highlighted by bold numbers.

	a1	a2	a3	a4	a5	a6	a7	b1	b2	b3	b5	b6
a1	x	12.3	26.2	16.2	19.4	19.5	24.8	**10.5**	17.2	31.4	16.4	20.3
a2	0.72	x	19.2	17.4	24.0	20.3	26.9	21.9	**8.3**	21.4	25.0	25.5
a3	-	0.03	x	19.6	21.3	21.7	21.1	31.3	19.9	**9.2**	27.5	27.1
a4	0.07	1.02	0.46	x	12.7	26.1	25.2	21.2	15.8	25.3	17.5	26.8
a5	1.0	0.05	3.6	0.72	x	21.3	15.8	18.0	26.0	29.9	**8.9**	18.8
a6	0.78	3.35	0.009	-	0.03	x	11.6	19.0	27.6	28.4	20.9	**8.8**
a7	-	-	0.44	-	0.88	0.42	x	21.9	32.2	29.7	16.6	**10.0**
b1	1.25	0.001	-	0.79	0.26	0.02	0.75	x	27.2	38.3	10.6	15.2
b2	1.83	**0.84**	0.56	0.10	-	-	-	-	x	20.3	28.8	32.3
b3	-	0.07	**0.31**	-	-	-	-	-	0.07	x	35.8	35.0
b5	0.03	-	-	2.12	**0.94**	0.39	1.59	0.64	-	-	x	14.6
b6	0.003	-	-	-	0.12	**0.07**	**0.78**	0.05	-	-	1.64	x

The calculated rates in Table 1.3.1 allow an estimation of major EET pathways in LHCII as determined by the underlying Chl arrangements (see Table 1.3.2). These structural data reveal 11 pairs of Chls with less than 15 Å distance, 32 pairs with

distances between 15 and 25 Å, and 23 pairs with more than 25 Å separations. A rough distinction between strongly interacting, weakly interacting and nearly non-interacting pairs corresponds to these three classes. In particular, the EET rates of pairs with 10, 15, or 25 Å distance reflect a ratio of about 1000/100/1 when assuming equal dipole orientations. Interestingly, all Chl *b* sites are connected by substantial EET to at least one Chl *a* site. This feature explains the rather low Chl *b* contribution to LHCII fluorescence as mentioned in the previous section (cp. Fig. 1.2.10). EET between Chls with more than 25 Å distance can be neglected due to the extremely low values. For all other pigments, the geometrical factor κ^2 further determines the rate calculation. Hence, these values are added to Table 1.3.2 for Chl pairs with distances <25 Å under the assumption of '0'-orientation of their transition dipoles. Additionally, a complete set of parameters κ^2 considering *all* possible combinations of '0'- and '1'-orientations can be found in the appendix **A2**.

1.3.2   Mechanisms for energy-transfer regulation

The regulation of EET efficiency under different environmental conditions is one of the most important tasks in higher plants due to their immobile population of continental surfaces. Other photosynthetic organisms populate habitats with less radiation fluctuation (low-light areas in the deeper sea) or are able to react to illumination changes by movements. The time interval of possible radiation changes between fractions of a second to months requires regulation mechanisms with a comparably widespread dynamic range. However, the timescale observable in spectroscopic experiments [3, 80, 81, 82, 83] is in the focus of interest here (without ignoring the biological relevance of slower regulatory function). In principle, EET regulation is enabled by increased light-harvesting efficiency under low-light conditions and, vice-versa, dissipation of excess energy at high light exposure. Nevertheless, radiation fluctuations cover a large intensity range, and no single mechanism can perform sufficient regulation alone. On the contrary, light adaptation represents a stepwise sequence of several distinct, rather different mechanisms. Interestingly, the antenna complex LHCII has been found to play an essential role within this regulation scheme [44, 45, 82, 84, 85].

In general, optical excitation is converted within the photosynthetic apparatus by three basic mechanisms. Besides re-emission, the energy can be consumed in the RC to induce charge separations or dissipated as thermal excitation (heat). The last two processes occur radiationless and lower in this way the total fluorescence yield. Accordingly, charge separations result in so-called photochemical fluorescence quenching [86, 87], while thermal dissipation results in non-photochemical quenching [88, 89]. Intrinsic EET regulation in higher plants is performed by such non-photochemical quenching mechanisms [3, 43, 90]. However, the exact molecular mechanism(s) for this process are not identified yet. Interestingly, the formation of LHCII aggregates *in vitro* is known to result in considerable fluorescence lifetime and quantum yield decrease [91, 92]. Possible origins of this quenching are electronic coupling of pigments or the formation of charge-transfer states, thus resulting in

increased rates for internal conversion. A corresponding lifetime shortening can be observed in the case of excitonically coupled Chl dimers as discussed in Section 3.3.1. Accordingly, the question of possible excitonic coupling among Chls in LHCII becomes essentially important for its regulation capabilities. It was further observed that xanthophylls play a substantial role for the ability of excess-energy dissipation [93]. Nevertheless, it is still unknown if this effect is related to structural influences of xanthophyll binding on LHCII aggregation [81] or directly caused by other effects [43].

Highly effective non-photochemical quenching is the first choice for protection from excess radiation. On the other hand, also low-light conditions require photosynthetic regulation, since the light reactions are performed in the two separated photosystems. PSII functions in this context as photon-driven proton generator as well as electron donator [94]. The more photons are absorbed, the more electrons are donated to PSI. If the electron-consuming reactions at PSI are too slow, the electron excess would steadily increase. However, NADPH formation at PSI is also a light-induced reaction, and its efficiency can be improved by enhanced absorption. Accordingly, a unique regulation mechanism adapts the antenna-cross sections of PSII and PSI by re-allocation of LHCII between both systems [95]. Phosphorylation at the N-terminus of LHCII proteins is expected to influence their allocation in either grana regions (mainly PSII) or lamellar thylakoids (mainly PSI) [19]. With the phosphorylation process involved, the reaction time of this mechanism is considerably slower than non-photochemical quenching. However, photon energy is not dissipated in this case, but *re*distributed between both photosystems. This makes the regulation process perfectly suited also for low-light conditions.

Finally, it should be mentioned that variation of the LHCII protein composition can also regulate the light-harvesting efficiency. In particular, *Lhcb2* appears to bind one Chl *a* molecule more than *Lhcb1* and it is found with increased amounts in plants grown under low-light conditions [27]. It can be assumed that additional Chls increase the EET efficiency and allow in this way an adaptation to reduced light exposure. Certainly, the reaction time of this process is considerable longer than for other mechanisms described above and of less relevance for the work presented here. On the other hand, regulation on this genetic level impressively demonstrates the unique adaptation abilities of the higher plant photosynthetic apparatus by combination of completely different approaches.

2   Materials and Methods

2.1   Isolation and Characterization of LHCII samples

Due to different growth and isolation conditions, possible variations in protein and pigment compositions can occur in LHCII preparations. For that reason, native LHCII samples used in this work have been prepared under the highest achievable control of all parameters. Furthermore, the isolation process was closely related to the procedures used for sample preparation in [6] to ensure comparability with the available structural data. In detail, trimeric LHCII was purified and characterized in collaboration with Dr. H Lokstein (HU Berlin) by following a slightly modified procedure according to Krupa et al. [96]. Pea plants (*Pisum sativum L.*) were grown on vermiculate from seed at 20º under continuous white-light exposure of ~300 µmol quanta m^{-2} s^{-1}. The plants were kept in the dark for 12 h prior to harvest to enable reversion of the xanthophyll cycle as well as starch reduction. Tissue of selected leafs was homogenized in 200 ml chilled buffer *A* (50 mM Tricin, 0.4 M Sorbitol, pH 7.8), filtered through cheese cloth and centrifuged for 5 min at 5.000 g. The obtained pellets of thylakoid membranes were re-suspended in buffer *B* (20 mM Tricin, pH 7.8) and the Chl *a+b* concentration was adjusted to 0.8 mg/ml as confirmed according to [97, 98]. Triton X-100 (0.7 %) was added to a final concentration of 0.7 % to solubilize the thylakoid membranes.

After incubation for 30 min at room temperature (RT), the suspension was centrifuged for 40 min at 30.000 g to separate solubilized thylakoid proteins. From the supernatant, LHCII precipitation was induced by $MgCl_2$ (20 mM) and KCl (100 mM) treatment and stirring for one hour. Aggregated fractions of LHCII were separated by 10 min centrifugation on sucrose pads (25 ml 0.5 M sucrose and 50 mM Tricin, pH 7.8) at 10.000 g. The sediments, re-suspended in buffer *B*, were again adjusted to 0.8 mg/ml Chl *a+b* and Triton X-100 was added to obtain a Triton/Chl ratio of 10:1 (w/w). A second precipitation was induced with analogous $MgCl_2$- and KCl-treatment and subsequent centrifugation on sucrose pads for 40 min at 30.000 g. The obtained pellets of purified LHCII were twice washed by re-suspension in buffer *B* and 5 min centrifugation at 40.000 g. Finally, aliquots containing 1 ml of final preparations were shock-frozen in liquid nitrogen (77 K) and stored at the same temperature. For spectroscopic measurements, trimeric LHCII was obtained from thawed samples by addition of 1.2 % *n*-octyl β-D-glucopyranoside (OG) at 110 µg/ml Chl *a+b* concentration. The pigment content of LHCII isolates was determined by HPLC analysis as indicated in Table 2.1.1.

Table 2.1.1 Pigment content per LHCII trimer as obtained by HPLC analyses of isolated samples. The obtained Chl-*a/b* ratio corresponds to ~1.3.

Pigment	Chl *a*	Chl *b*	Lutein	Neoxantin	Violaxantin
Content in LHCII	21.0±0.6	16.5±0.6	6	2.7±0.3	1.0±0.1

[*] Two lutein molecules per LHCII monomer were assumed as internal standard for Chl quantification.

Further sample characterization has been performed for the following reason: During cation-induced aggregation, partial contamination of LHCII aggregates by minor antenna complexes cannot be completely excluded. Since LHCII harbors proportionally more Chl *b* than CP24 or CP29, any content of these proteins is reflected in the total Chl *a/b* ratio. Accordingly, Chl-*a/b* ratios of 7:5 or less indicate high concentrations of LHCII. However, verification of minor CP fractions below 5 % via the pigment composition is impractical due to the exactness of this method. For that reason, the protein content has been additionally analyzed by poly-acryl amide gel electrophoresis (using sodium-dodecyl sulfate as charge carrier, SDS-PAGE). Gels containing 12% acryl amide were run at 100 V for 45 min and subsequently silver-stained. Besides the dominating *Lhcb*-fraction with 27-28 kD weight, the results commonly indicate some residual protein content near ~65 kD (see Fig. 2.1.1). These residues are assumed to represent trimeric LHCII complexes, since SDS treatment denatures the protein. However, explicitly *no* other proteins were observed in the gels (Fig. 2.1.1), thus indicating a purity of better than 99 %. Under this point of view, the sample quality represents a reliable basis for studying physical properties of LHCII *in vitro*.
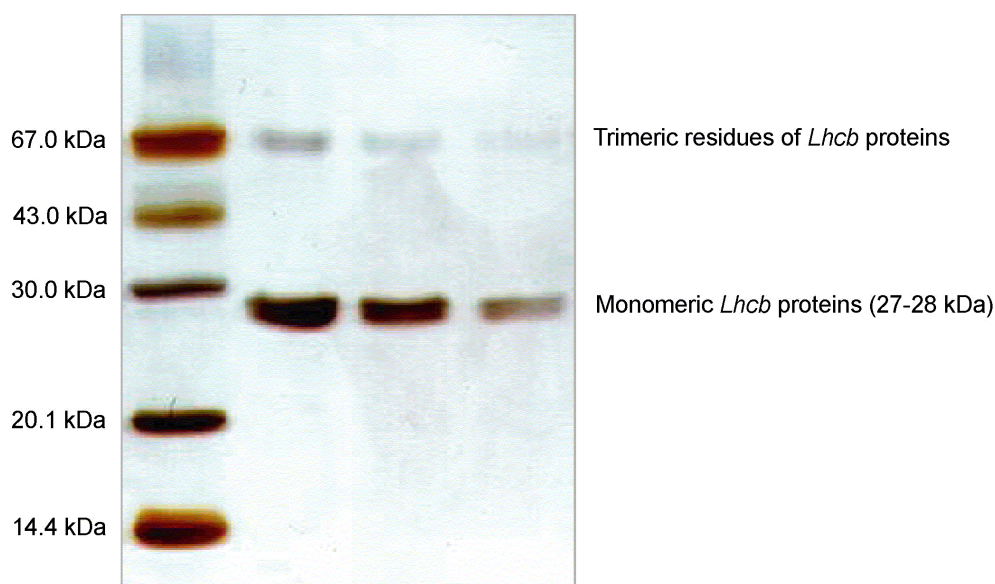

Figure 2.1.1 Sample purity after LHCII isolation verified by silver-stained SDS-PAGE (running from top to bottom). The left lane shows marker proteins of different sizes. Three other lanes were run at different LHCII concentrations, thus revealing an overwhelming content of 27-28 kD proteins (*Lhcb 1,2*). The weak band around 65 kD can be assigned to residues of trimeric LHCII, while other Chl proteins (CP24, CP26, CP29, CP43, or CP47) are clearly absent.

Besides biochemical characterizations, absorption and fluorescence spectroscopy were employed to monitor sample intactness. In this way, long-term stability, functional integrity and aggregation state could be sufficiently controlled. Strong laser fields as applied in nonlinear spectroscopic experiments are expected to cause partial photo-damage. Hence, a corresponding photo-bleaching was frequently tested by monitoring the absorption spectrum. If any sample degradation was detected via reduced optical density in the Q_y-maximum, new samples were prepared. Degradation of the protein can be further observed by fluorescence measurements, since intact LHCII complexes show only emission from the Chl *a* region (see Fig. 1.2.10). Hence, the observation of any

Chl *b* fluorescence after excitation in the Soret-band indicates separation of Chls from the protein matrix or at least disturbed functional integrity.

To ensure preparation of LHCII samples in their native *trimeric* arrangement, additional spectroscopic measurements were employed. After the isolation process, the proteins are aggregated and trimerization must be induced by detergent treatment. However, low detergent concentrations may result in partially remaining aggregates, while high amounts can denature the complex. In the first case, the fluorescence-quantum yield is lowered because of excitation quenching (cp. Section 1.3.2). On the other hand, degradation of the protein complexes becomes observable by Chl *b* fluorescence as mentioned above. Accordingly, the evaluation of fluorescence-emission spectra can be used to determine proper detergent concentrations as reported in [92]. The obtained results are compared to NLPF measurements of LHCII samples with varying detergent content (see Section 3.5.3). In this way, the existence of trimeric LHCII was confirmed at concentrations of 1.2 % OG in Tricin-buffer solution.

2.2   Measuring the nonlinear optical response of LHCII

Applications of nonlinear spectroscopic methods on multi-pigment systems like LHCII are a great challenge with respect to proper interpretation of the obtained experimental data. Former investigations of LHCII were mainly concentrated on time-resolved measurements using ps- and fs-laser pulses [11, 13, 99, 100, 101, 102], CD and fluorescence studies [30, 53, 71, 103, 104, 105] as well as Raman spectroscopy [106, 107]. Moreover, the application of single-molecule spectroscopy on light-harvesting complexes opened a new approach to study such systems [108, 109]. Other methods like hole-burning spectroscopy [54, 110] have been applied especially at cryogenic temperatures. Nevertheless, these conventional methods are not suited to reveal specific physical parameters. For example, the excited-state dynamics of pigment molecules in protein environment resulting from electron-phonon coupling are hard to observe in time-resolved experiments. In contrast, three-pulse photon-echo counting studies can detect this interaction. The signal originates in this case from third-order nonlinearity in the system [111]. Recent experimental applications of this technique resulted in further theoretical improvements [112, 113]. In this way, the understanding of nonlinear optical properties in condensed-phase multi-level systems was essentially increased [63]. These theoretical developments built also a firm basis to improve the NLPF theory (cp. [1]), which was essentially required in the thesis on hand.

The NLPF method has two major advantages when compared to conventional spectroscopic techniques. First, the method is sensitive to possible excitonic interactions within the investigated system. This feature is discussed with respect to experimental results in Chapters 3.4 and 3.5. On the other hand, NLPF spectra allow *simultaneous* evaluation of several physical parameters, i.e. EET rates and molecular transition-dipole orientations. Hence, the method represents an ideal complement to former attempts of evaluating *different* measurements in *one* model for the investigated pigment-protein

complex [72, 114]. This unique feature of NLPF spectra surely justifies the required theoretical effort, which has been achieved by the parallel work of Beenken [1]. A short introduction into the NLPF theory relevant for this thesis can be found below. The evaluation of additionally performed nonlinear absorption (NLA) measurements did not require theoretical extensions, but it was based on previously published calculations [65]. Nevertheless, underlying principle and experimental setup are also briefly outlined in the following section to ensure comprehensibility.

2.2.1 Experimental and theoretical aspects of nonlinear absorption

In this work, NLA-experiments have been applied to investigate excitonic coupling via the observation of redistributed transition probability. As illustrated in Fig. 1.3.2 (p. 19), excitonic interaction can result in absorption bands with either increased or decreased transition probability $|\vec{\mu}|^2$. Corresponding changes of the absorption coefficient α ($\alpha = C_0 \cdot |\vec{\mu}|^2$, $\vec{\mu}$: transition-dipole moment, C_0: constant) are reflected by the spectral absorption-cross section $\sigma(\omega)$. Furthermore, environmental influence on molecular transitions may also effect $\sigma(\omega)$, in particular, by the transition bandwidth 2Γ. Hence, $|\vec{\mu}|^2$ can be determined by measuring the maximum value $\sigma(\omega_c)$ at λ_c and simultaneous estimation of Γ. Investigations of intensity-dependent transmission, better known as NLA, allow the determination of $\sigma(\omega_c)$. This general approach has been used before in experiments with ps-laser pulses to study the extent of excitonic delocalization in bacterial light-harvesting complexes LH2 [115]. Since heterogeneity among Chl-absorption bands in LHCII and ultra-fast EET among their excited states complicate the evaluation of such studies on the ps-time scale, NLA-measurements using fs-laser pulses are presented in this work for the first time. In addition, the comparability of measurements in both time regimes was demonstrated (see Section 3.3.1). The general setup employed in both experiments differs mainly by the laser systems used.
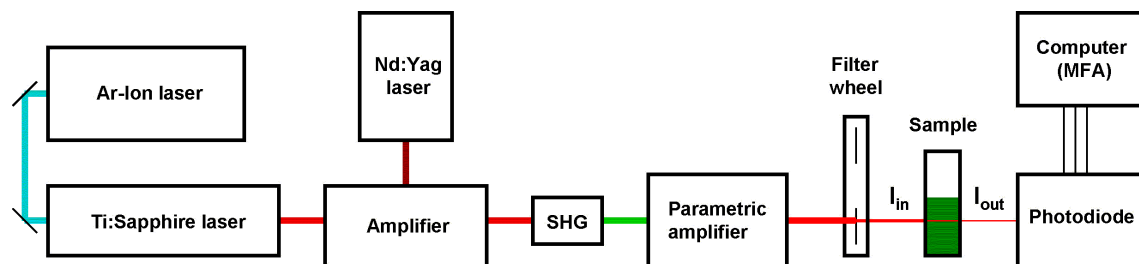
Figure 2.2.1 NLA setup used for measurements with 120-fs pulses (see text for details). Distinct colors of the laser beams illustrate different steps of wavelength conversion. Intensity-dependent transmission is measured by the ratio of incident (I_{in}) and transmitted (I_{out}) light intensities.

Pulses of 400 ps duration in the range between 640 and 680 nm were generated by a nitrogen-laser pumped dye laser as described before [116]. The fs-laser system (CPA 1000, CLARK-MXR Inc., Dexter, MI, USA) consisted of an Ar-ion laser pumped Ti:Sapphire oscillator with 1 kHz repetition rate and a Nd:YAG pumped regenerative amplifier (see Fig. 2.2.1). The fundamental was transformed to 400 nm by second-

harmonic generation. Subsequently, a parametric amplifier was used to generate pulses in the range from 600 to 700 nm. Pulse durations of about 120 fs were monitored by frequency-resolved optical gating analysis (FROG). The laser beam was focused in both time regimes onto a 1-mm rotating sample cuvette (Hellma, Mühlheim, Germany) as ~30 μm spot. This led to maximum photon flux densities of $2 \cdot 10^{16}$ and $4 \cdot 10^{18}$ photons per cm^2 and pulse for the fs- and ps-pulses, respectively.

Intensity-dependent transmission curves T(I) were recorded by measuring the transmission $T = I_{in}/I_{out}$ (see Fig. 2.2.1) for different incident light intensities. Fitting and parameter evaluation were performed by using the software package CALE [117], which is based on a rate-equation system for the specific energy-level scheme. This model included absorption from ground to first-excited states and one further absorption at the same wavelengths to higher excited states (S_0, S_1, and S_3 in the case of molecular Chl, cp. Fig. 1.2.6, p. 11). It should be explicitly mentioned that this approach does *not* distinguish between transitions of monomeric molecules or exciton states of coupled molecules. Relevant time constants in this model are the lifetimes of both excited states (see Chapter 1.2.2). Accordingly, a quasi-instantaneous approach could be used to fit NLA data obtained with 120 fs pulses, since lifetimes longer than 1 ps are insignificant in this case.

The intensity-dependent transmission T(I) can be expressed as (see [118])

$$T(I) = \int I(t) \exp\left[c\left(\sigma_{10}^{abs}\left(n_1(t) - n_0(t)\right) + \sigma_{x1}^{abs}\left(n_x(t) - n_1(t)\right)\right)d\right]dt \, / \int I(t)\,dt \,. \tag{3}$$

Ground and excited state populations $n_i(t)$ are described by the following system of differential equations

$$\frac{dn_i(t)}{dt} = \sum_j \sigma_{ij}^{abs}\left(n_j(t) - n_i(t)\right)I(t) \tag{4}$$

with the initial conditions $n_i(t_0) = \delta_{i0}$. I(t) is the incident time-dependent light intensity, which was approximated here as a Gaussian-shaped pulse. Particle densities and optical path lengths in the sample are represented by c and d, respectively. σ_{ij} is the absorption cross section of transitions from state j to i and was assumed to equal the corresponding cross section for stimulated emission from i to j. The spatial distribution of I(t) is considered by the photon-transport equation (cp. [117]). In a quasi-instantaneous approach as used for fs-experiments, the NLA curve depends only on σ_{ij}.

In contrast to this, the application of ps-pulses requires consideration of internal-conversion rates, thus resulting in a rate-equation system as previously described [117].

2.2.2 Nonlinear polarization spectroscopy: Experimental setup

The higher-order polarizability of transparent media can be investigated by wave-mixing processes between intense light fields. Numerous three- and four-wave mixing techniques applied to solid-state crystals [119, 120], molecular ensembles in the gas

phase [121, 122] or condensed matter [123, 124] are reported. The NLPF method corresponds to such a wave-mixing process, too. Within the initially isotropic sample, optical birefringence is induced by photon absorption from an intense, linearly polarized laser field (pump field, $\vec{E}_P$). This birefringence is then probed by polarization rotation of a second, also linearly polarized laser field (probe field[*], $\vec{E}_t$). The resulting field vector perpendicular to $\vec{E}_t$ represents the signal field $\vec{E}_s$. It is related to the other two fields by third-order polarization $P_s^{(3)}$ induced in the medium (cp. Eq. 5 and 6 below). All fields are further characterized by their frequencies ω_P, ω_t and ω_s, which are related to corresponding wavelengths λ_P, λ_t and λ_s by $\omega = c/2\pi \cdot \lambda$. Employing the geometrical arrangement shown in Fig. 2.2.2, NLPF signals can be directly detected as $\left|\vec{E}_s\right|^2$ behind the analyzer.
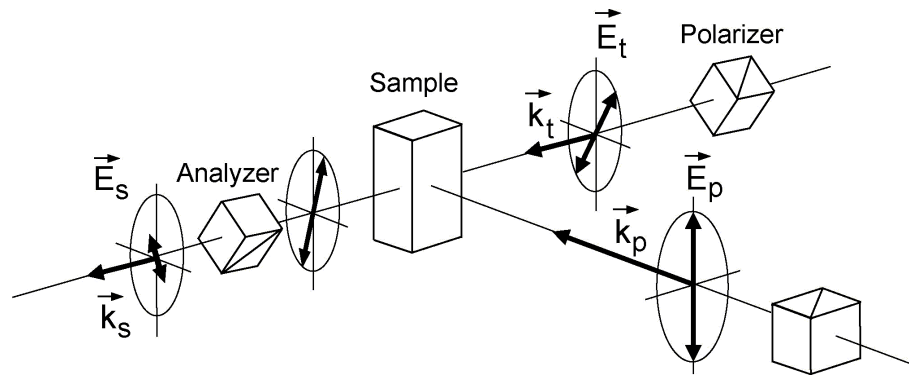

Figure 2.2.2 Experimental principle of the NLPF method under consideration of electrical field and propagation vectors. The probe field spreads along $\vec{k}_t$ in perpendicular direction to the pump field ($\vec{k}_P$), while the corresponding field vectors ($\vec{E}_t$ and $\vec{E}_P$) enclose an angle of 45°. Third-order polarization induced within the sample results in a signal field $\vec{E}_s$ with perpendicular orientation to $\vec{E}_t$ and the same propagation vector ($\vec{k}_s$) as the probe field. Due to perpendicular orientation of polarizer and analyzer, only $\vec{E}_s$ can pass through to the detection system.

While theoretical aspects of the NLPF method are explained in more detail further below, the formation of $\vec{E}_s$ is described macroscopically at this point. For this purpose, the field vector $\vec{E}_t$ is presumed as superposition of one component parallel to $\vec{E}_P$ (= $\vec{E}_t^{\parallel}$) and one perpendicular vector $\vec{E}_t^{\perp}$ (cp. Fig. 2.2.2). $\vec{E}_t^{\perp}$ is commonly absorbed in the sample without any influence of $\vec{E}_P$. In contrast to this, $\vec{E}_t^{\parallel}$ cannot be absorbed by *those* molecules, which have been previously excited via the pump field. On the contrary, photons of $\vec{E}_t^{\parallel}$ can induce stimulated emission by electronic interaction with these excited molecules. Hence, the component $\vec{E}_t^{\parallel}$ is stronger after passing the medium, while $\vec{E}_t^{\perp}$ is partly absorbed. Final superposition of both vectors yields a rotation of the initial field vector $\vec{E}_t$. This rotation is detected by measuring the component perpendicular to $\vec{E}_t$ behind the analyzer. Accordingly, the NLPF signal originates in

---

[*] To distinguish the indices of **p**ump and **p**robe field, the latter is named E_t under the meaning of 'test' field.

equal parts from ground state bleaching (by reduced $\vec{E}_t^{\parallel}$ -absorption) as from excited-state population (by stimulated $\vec{E}_t^{\parallel}$ -emission).

In all NLPF experiments, the arrangement shown in Fig. 2.2.2 has been employed. Perpendicular orientation of wave vectors $\vec{k}_t$ and $\vec{k}_P$ was recently suggested by Voigt et al. [125] to eliminate disadvantageous scattering effects of the co-linear setup used before [123]. Within this fixed geometry, NLPF signals can be detected in dependence on wavelength and intensity variations of $\vec{E}_t$ and $\vec{E}_P$. In the framework of this thesis, the first case was carried out by measuring 'NLPF pump spectra' under variation of λ_P at different, but fixed λ_t (cp. [126]). In principle, the measurement of 'NLPF probe spectra' with varying λ_t at fixed λ_P is also possible, but has not been carried out so far because of experimental difficulties. Besides this, the intensity-dependence of NLPF signals is only relevant with respect to $\left| \vec{E}_P \right|^2$, since the theoretical description in Chapter 2.2.4 is based on the assumption $\left| \vec{E}_t \right|^2 << \left| \vec{E}_P \right|^2$. Accordingly, NLPF pump spectra were also recorded at different pump-field intensities.
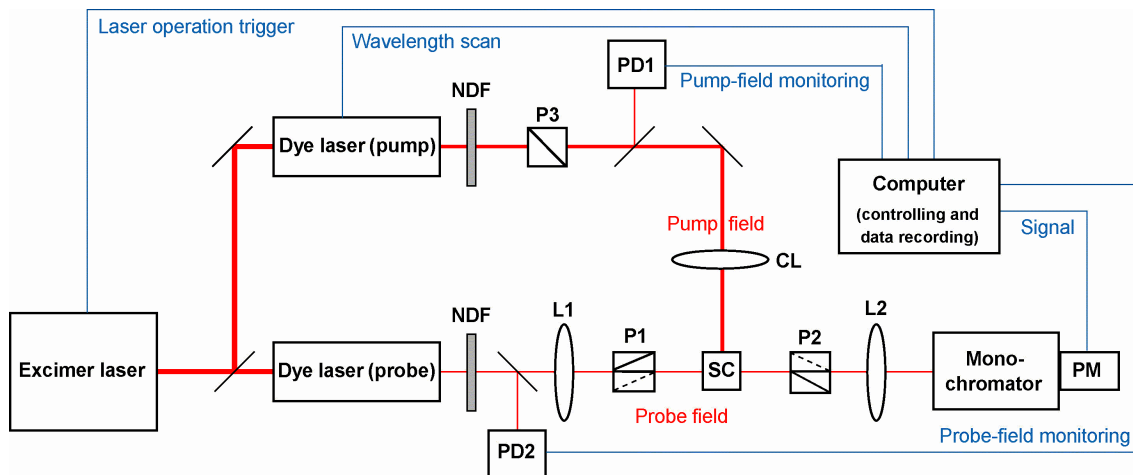

Figure 2.2.3 Experimental setup employed for NLPF measurements. The following abbreviations are used: NDF - neutral density filter, P: polarizer, L: (convex) lens, CL: cylindrical lens, PD: photo diode, SC: sample cuvette, PM: photo-multiplier. Mirrors and beam splitters are not explicitly named. Propagation of different laser beams is shown by red lines and electrical signal controlling is indicated by blue connections. For exact laser-field orientations, cp. Fig. 2.2.2 (P1: Polarizer, P2: Analyzer).

All measurements of NLPF spectra has been performed using a similar setup as shown in Fig. 2.2.3. Two dye lasers (LAS 100, Laser Analytical Systems, Berlin, and LPD 3000, Lambda Physik, Göttingen) simultaneously pumped by 15 ns pulses of a XeCl-excimer laser (LPX 100, Lamda Physik) provided laser beams for the pump and probe field, respectively. The range of λ_p (1.5 pm spectral bandwidth) was tuned between 630 and 700 nm according to the amplification profile of the used laser dye (DCM in DMSO). Intensity variations were achieved by neutral-density filters and monitored by a pyro-electrical radiation detector (PEM 100, Lasertechnik Berlin) at sample location. Polarization of the light fields according to Fig. 2.2.2 was assured by two conventional polarizers, while the analyzer (Glan-Thompson polarization prism PGL0.6, Bernhard Halle & Nachf., Berlin) is characterized by an extremely sensitive on/off ratio of better than 10^{-7}.

Intensity fluctuations were monitored by two photo-diodes using partial reflections from the corresponding light paths. A convex lens focused the probe beam with about 50 μm diameter into the sample cuvette (5x5x50 mm, Hellma 111.57-QS). The perpendicularly propagating pump field was shaped by a cylindrical lens to a 5 mm x 150 μm focus in the same plane. Different wavelengths of the signal field $\vec{E}_s$ were selected by a grating-monochromator (Carl Zeiss, Jena). Before signal recording in the processing unit, photons were amplified by a photo-multiplier (Hamamatsu R636-200). NLPF spectra as shown for example in Fig. 3.1.1 (p. 41) were measured by stepwise scanning of the pump laser (typically 0.2 nm steps). Ten subsequently recorded spectra were averaged to obtain values for median and error range after correction for probe-laser fluctuations. These spectra have been additionally corrected for the amplification profile of the laser dye, which was measured by using the PEM as intensity detector. Evaluation of these NLPF spectra was then performed according to the theoretical basis explained in the next section.

2.2.3 Nonlinear polarization spectroscopy: Wavelength dependence

The initially described NLPF theory [123, 127, 128, 129] was recently extended by the studies of Beenken [1] to facilitate investigations of biological systems like pigment-protein complexes. This development was considerably influenced by experimental results obtained for LHCII (this work) as well as for other antenna complexes [130, 131]. Certainly, a short introduction into the theoretical modeling is an inevitable basis to evaluate the presented experimental results. For that purpose, relevant equations of the NLPF theory from [132] are briefly discussed in the following.

According to notations used in Fig. 2.2.2, the interacting electric fields in NLPF experiments are distinguished as pump field $\vec{E}_P$, probe field $\vec{E}_t$, and resulting signal field $\vec{E}_s$. In lowest order, the signal field $\vec{E}_s$ is generated by third-order polarization $P_s^{(3)}$ in the medium. Under the restriction $\left|\vec{E}_t\right| << \left|\vec{E}_P\right|$ and for $\omega_s = \omega_t$, this polarization is determined as

$$\vec{P}_s^{(3)} = \chi_{sppt}^{(3)}(-\omega_t, \omega_p, -\omega_p, \omega_t) \left|\vec{E}_p\right|^2 \vec{E}_t \tag{5}$$

The index *sppt* in Eq. 5 indicates that only this *one* element of the third-order susceptibility tensor contributes to the signal. Cubic terms of incident fields remain zero due to the applied vector orientations, i.e. $\vec{k}_s = \vec{k}_t$ and $\vec{k}_s \perp \vec{k}_P$ (cp. Fig. 2.2.2). Correspondingly, NLPF spectra recorded by detecting the signal-field intensity $\left|\vec{E}_s\right|^2$ under variation of ω_p and at fixed ω_t feature the line shape

$$S(\omega_p) \;=\; \left|s(\omega_p, \omega_t)\right|^2 \;=\; C \cdot \left|\chi_{sppt}^{(3)}(-\omega_t, \omega_p, -\omega_p, \omega_t)\right|^2 . \tag{6}$$

Equation 6 indicates that measured NLPF pump spectra recorded under variation of ω_P correspond to *squared* line-shape functions $s(\omega_P, \omega_t)$. Elements of the third-order susceptibility tensor $\chi^{(3)}$ can be calculated by solving the equations of motion for the

systems density operator. These equations depend strongly on the physical model used to describe the absorbing species and were solved earlier for isolated two-level systems [127, 129]. However, the experimental data in this work could not be evaluated satisfactory based on such simple models. Hence, this theory was extended to consider possible excitonic coupling, EET, and mutual orientations of the involved transition dipoles [132]. The resulting mathematical expressions for $s(\omega_p, \omega_t)$ are summarized in the following without entering the fundamental level of density-matrix calculations.
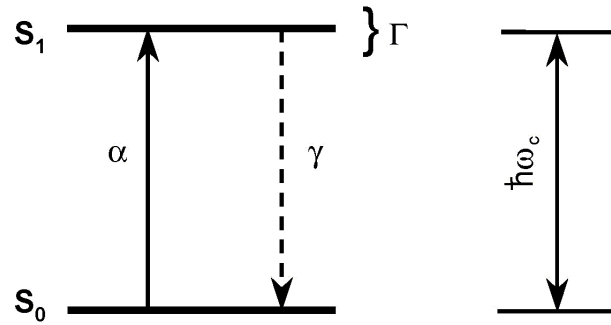
Isolated two-level systems

Figure 2.2.4 Two-level system with electronic excitation and relaxation processes between ground state S_0 and first-excited state S_1 (cp. Fig. 1.2.6, p. 11). The parameters α and γ characterize absorption and relaxation processes, respectively (α: absorption coefficient, γ: excited-state population relaxation rate, $\hbar\omega_c$: transition energy). The dephasing rate Γ reflects homogeneous broadening of the excited state, thus resulting in a Lorentzian line shape of the absorption band with 2Γ FWHM (see Fig. 2.2.5).

The two-level system illustrated in Fig. 2.2.4 facilitates the simplest description of an absorbing species by electronic transitions between ground state S_0 and excited state S_1. In spite of its simplicity, this basic model is highly useful to explain different terms appearing in NLPF equations. Following detailed density-matrix calculations in [123], the NLPF line-shape function of a two-level system (cp. Fig. 2.2.4) corresponds to

$$s(\omega_p, \omega_t) = \frac{i}{\Gamma - i\omega_{tc}} \left(\frac{2}{\gamma} \frac{2\Gamma}{\Gamma^2 + \omega_{pc}^2} + \frac{2}{\gamma + i\omega_{pt}} \left(\frac{1}{\Gamma - i\omega_{tc}} + \frac{1}{\Gamma + i\omega_{pc}} \right) \right) . \tag{7}$$

The detuning frequencies are defined as $\omega_{pc} = \omega_p - \omega_c$, $\omega_{tc} = \omega_t - \omega_c$, and $\omega_{pt} = \omega_p - \omega_t$. Since ω_{tc} has a constant value for fixed ω_t, two major parts can be distinguished in the line shape of Eq. 7. The first term in brackets describes a Lorentzian at center frequency ω_c with the linewidth 2Γ (FWHM). The second part, mainly contributing for $\omega_p \approx \omega_t$ yields a peak at center frequency ω_t with the FWHM γ. Due to the origin of their bandwidths,

$$\Gamma = 1/T_2 \qquad \text{and} \qquad \gamma = 1/T_1 , \tag{8}$$

the two features are assigned as T_2-peak and T_1-peak in the following (T_1: excited-state population lifetime; T_2: dephasing time of the excited-state wavefunction). Two unique features of the NLPF signal are reflected by the pre-factor $2/\gamma$ in Eq. 7. First, excited-state population relaxation with the rate γ reduces NLPF signal amplitudes as

considered by the corresponding denominator. Furthermore, the factor 2 indicates that excited-state populations contribute twice to NLPF spectra due to a ground state bleaching *and* stimulated emission signal. Figure 2.2.5 illustrates typical absorption and NLPF spectra of two-level systems.
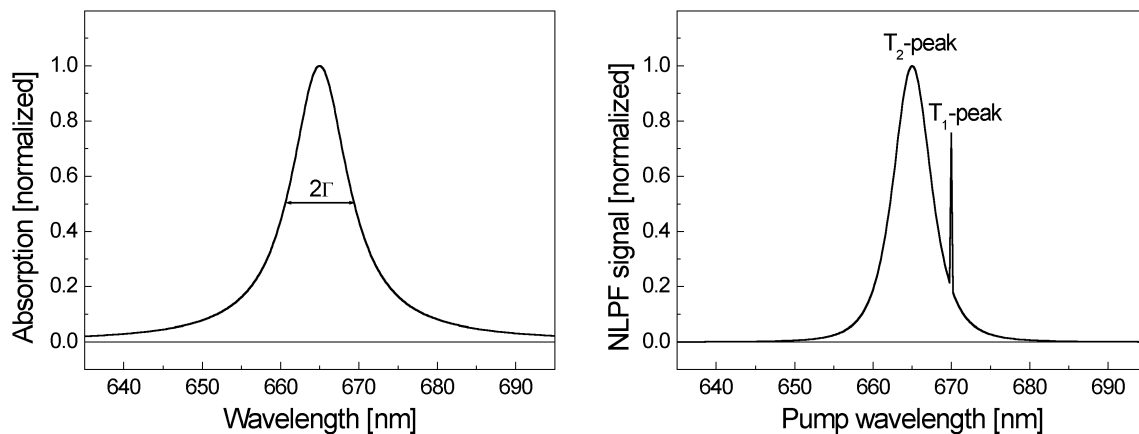

Figure 2.2.5 Simulated absorption and NLPF spectrum of a two-level system as shown in Fig. 2.2.4 using the following parameters: $\omega_c = 15040$ cm^{-1} ($\lambda_c \approx 665$ nm), $\Gamma = 100$ cm^{-1}, and $\gamma^{-1} = 50$ ps (α is an arbitrary value for normalized spectra). **Left panel:** The absorption band represents a Lorentzian with ~9 nm FWHM (corresponding to $2\Gamma = 200$ cm^{-1}) centered at 665 nm. **Right panel:** The broad T_2-peak of NLPF spectra has its maximum at the same wavelength, but it is shaped like a *square* Lorentzian (~5.4 nm FWHM). The T_1-peak is centered at λ_t (670 nm) and has a FWHM of $1/\gamma \approx 0.1$ cm^{-1} (~4.5 pm).

Equation 7 reflects the NLPF line-shape function of a single two-level system. Additionally, this equation describes ensembles of molecules in the case of identical transition parameters and without any interaction among them. This theoretical model is stepwise extended below to *i*) molecular ensembles with deviating transition parameters, *ii*) EET among excited states, *iii*) excitonic interactions, and *iv*) variable orientations of transition dipoles. Exact calculations for these models can be found in [1]. This study revealed that the linewidth of T_1-peaks in multi-level systems are predominantly determined by excited states with the *smallest* γ. In the case of first-excited Chl states in LHCII (smallest $\gamma \approx (3.5$ ns$)^{-1}$, see [13]), the FWHM can thus be estimated as ~0.05 pm. Since this value is far below the experimental resolution obtained with the applied laser bandwidths (>1 pm), T_1-peaks contain virtually no information. Consequently, all NLPF line-shape functions are reduced to T_2-terms in the following. Nevertheless, it should be mentioned that complete calculations including both peaks might be relevant for other investigated systems [126].

Molecular ensembles

The first theoretical extension considers different molecular species absorbing at distinct center frequencies. In particular, this property can reflect a countable number of molecules attached to different binding sites within a protein matrix (heterogeneous sub-structure). On the other hand, statistical distributions of molecular absorption bands are also conceivable (inhomogeneous broadening). Both cases are illustrated with respect to their center-frequency distributions in Fig. 2.2.6.
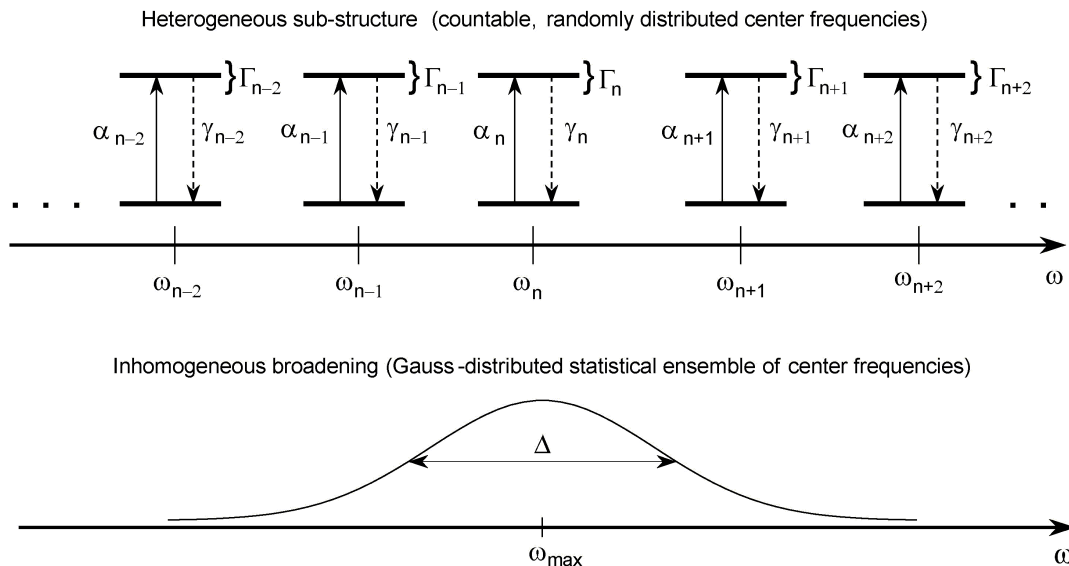
Heterogeneous sub-structure (countable, randomly distributed center frequencies)

Inhomogeneous broadening (Gauss-distributed statistical ensemble of center frequencies)

Figure 2.2.6 Two different distributions of center frequencies for multiple two-level systems.

For **n** countable transitions (see Fig. 2.2.6), the NLPF line-shape function can be calculated by summing up **n** different T_2-terms from Eq. 7:

$$S_{het}(\omega_p, \omega_t) = \sum_n \alpha_n^2 \, \frac{2}{\gamma_n} \, \frac{i}{\Gamma_n - i\omega_{tn}} \, \frac{2\Gamma_n}{\Gamma_n^2 + \omega_{pn}^2} \quad . \tag{9}$$

Certainly, the detuning frequencies in Eq. 7 must be substituted by $\omega_{Pn} = \omega_p - \omega_n$ and $\omega_{tn} = \omega_t - \omega_n$ for each transition. Any interactions among the different two-level systems are neglected at this point. The coefficients α_n are weighting factors representing different transition-dipole moments $\vec{\mu}_n$ and/or different molar concentrations c_n of the distinguished species:

$$\alpha_n \propto \sqrt{c_n} \left| \vec{\mu}_n \right|^2 . \tag{10}$$

Equation 9 represents the NLPF line-shape function for ensembles of distinct molecules in a protein structure like the Chls in LHCII. Since each molecule is described by its individual set of transition parameters $\alpha_n, \omega_n, \gamma_n$, and Γ_n, this allows distinction between the two Chl species *a* and *b*. It should be pointed out again, that the index **n** in Eq. 9 counts the *excited* states of *different* molecules, $S_1^1, S_1^2, \ldots S_1^n$.

In the next step, Eq. 9 can be extended to statistical distributions of center frequencies for molecules with identical transition-dipole moments $\vec{\mu}$ by substituting concentration factors c_n in Eq. 10 with a concentration distribution $c(\omega)$:

$$\alpha(\omega) \propto \sqrt{c(\omega)} \left| \vec{\mu} \right|^2 . \tag{11}$$

The distribution function $c(\omega)$ reflects slightly different environments for the individual members of a molecular ensemble with otherwise *identical* parameters. This inhomogeneous broadening commonly results in Gaussian distributions of molar concentrations around the center frequency ω_{max} with a FWHM Δ (cp. Fig. 2.2.6):

$$c(\omega) = \frac{n_0}{\Delta\sqrt{\pi/2}} \exp\left\{\frac{-2(\omega - \omega_{max})^2}{\Delta^2}\right\} \ . \tag{12}$$

Accordingly, NLPF line-shape functions can be calculated for such statistical ensembles by substituting the summation over index **n** with a frequency integral $d\omega$. Detuning frequencies ω_{pc} and ω_{tc} are correspondingly substituted by frequency-dependent terms $\omega_p - \omega$ and $\omega_t - \omega$, respectively:

$$s_{inh}(\omega_P, \omega_t) = \int \alpha^2(\omega) \frac{2}{\gamma} \frac{i}{\Gamma - i(\omega_t - \omega)} \frac{2\Gamma}{\Gamma^2 + (\omega_p - \omega)^2} \ d\omega . \tag{13}$$

Equation 13 describes inhomogeneous broadening among transitions characterized by equal properties γ, Γ, and μ. In contrast to this, Eq. 9 contains the line-shape function of heterogeneous sub-structures featuring *different* parameters γ_n, Γ_n, and μ_n. Consequently, a combination of both cases can be realized by introducing frequency-dependent coefficients for each of the **n** distinct transitions,

$$\alpha_n(\omega) \propto \sqrt{c_n(\omega)}\left|\vec{\mu}_n\right|^2 . \tag{14}$$

This results in the line-shape function

$$s_{inh+het}(\omega_p, \omega_t) = \int \sum_n \alpha_n^2(\omega) \frac{2}{\gamma_n} \frac{i}{\Gamma_n - i(\omega_t - \omega)} \frac{2\Gamma_n}{\Gamma_n^2 + (\omega_p - \omega)^2} \ d\omega . \tag{15}$$

for heterogeneous distributions of inhomogeneously broadened transitions. Comparison of Eq. 9 and 15 reveals a generally applicable approach to describe additional spectral inhomogeneity in a heterogeneous system of countable transitions. This is realized by introducing frequency-dependent coefficients $\alpha_n(\omega)$ and subsequent integration over the frequency space

$$s_{inh+het}(\omega_p, \omega_t) = \int s_{het}(\omega_p - \omega, \omega_t - \omega) \ d\omega . \tag{16}$$

For that reason, inhomogeneous broadening is not explicitly considered any further in the following sections. All line-shape functions discussed below can be easily extended to inhomogeneous distributions of center frequencies by numerical integration according to Eq. 16. For more details, e.g., additional inhomogeneity in the relaxation rates, see the parallel work of Beenken [1].

Incoherent EET

In contrast to ensembles of isolated two-level systems, EET influences the correlation between heterogeneously distributed transition bands. Without EET, only those transitions that were *directly* excited by the pump-field can induce polarization rotation of the probe field. (This is mathematically reflected by the same index **n** for ω_{P_n} and ω_{t_n} in Eq. 9.) However, a different correlation is obtained for incoherent EET from one excited state to another excited state, $S_1^m \rightarrow S_1^n$ (cp. Fig. 1.3.1, left panel, p. 17). In this case, the probe field detects ground-state depopulation at transition **n** (S_0^n) also after excitation of transition **m** ($S_0^m \rightarrow S_1^m$). Hence, S_1^m and S_1^n are correlated in dependence

on the EET rate between them. This behavior can be introduced into the NLPF line-shape function by extending ground-state relaxation rates γ_n from Eq. 9 to a matrix of generalized relaxation rates, $\hat{\gamma}$. The matrix elements γ_{nm} describe EET rates from excited states S_1^m to S_1^n within an ensemble of countable transitions. Furthermore, all diagonal elements γ_{nn} summarize the total S_1^n-depopulation rates, which corresponds to inverse excited-state population lifetimes (cp. Eq. 8):

$$\gamma_{nn} = -\gamma_n - \sum_{m \neq n} \gamma_{mn} = 1/T_1^n \quad (m = 1...n) \tag{17}$$

Resulting correlations between all possible pairs of transitions can be considered by additional summation over terms with *different* indices, ω_{pm} and ω_{tn}:

$$s(\omega_p, \omega_t) = \sum_{n,m} \alpha_n \frac{i}{\Gamma_n - i\omega_{tn}} \beta_{nm} \frac{2\Gamma_m}{\Gamma_m^2 + \omega_{pm}^2} \alpha_m. \tag{18}$$

Correlation factors β_{nm} are used to weight the different contributions in dependence on the mutual EET rates. Accordingly, the corresponding pump-probe correlation matrix $\hat{\beta}$ is defined by

$$\sum_n \beta_{mn} \cdot \gamma_{nl}^{eet} = 2\delta_{ml} \quad (m = 1...n; l = 1...n). \tag{19}$$

This determination equation reflects the total depopulation rates defined in Eq. 17 as well as correct summation of donated and accepted excitations. According to Eq. 18, the line-shape function shows contributions from probing transition **n** while pumping transition **m** if the matrix element β_{nm} is $\neq 0$. The factor 2 in Eq. 19 considers again the two-fold dependence of the NLPF signal on induced excited-state population (due to ground-state bleaching *and* stimulated emission).

Excitonic coupling (coherent EET)

The influence of excitonic coupling between molecular transitions on NLPF line-shape functions is discussed in the following. For that purpose, all indices used for summation over different states must be redefined. In previous equations, **m** and **n** distinguish different excited states of heterogeneously distributed transitions. At this point, they are used to label different states in an excitonic level structure. Following the example of an excitonic dimer in Fig. 1.3.1 (right panel, p. 17), the indices **n** = 1 and **n** = 2 would thus refer to the exciton states S_1^- and S_1^+, respectively. (Excitonic coupling between more than two molecules results in the formation of more than two exciton states and can be correspondingly described by using higher numbers of the index **n**.) EET within the excitonic level structure is then summarized in a similar γ-matrix as shown in Eq. 17, now containing different rates of *coherent* (excitonic) EET.

With this index substitution, the NLPF line-shape of **n** excitonic transitions resulting from coupling of **n** molecules yields a similar expression as shown in Eq. 18. Nevertheless, the β-matrix must be redefined as

$$\sum_n \beta_{mn} \cdot \gamma_{nl}^{hom} = \delta_{ml} + 1 \quad (l \neq 0).$$

(20)

The difference between Eq. 19 and 20 is related to the common ground state of excitonic states. Accordingly, each excitation of *one* state within an excitonic level structure bleaches also the ground state of *all* other transitions. This behavior results in the constant '1' at right side of Eq. 20 instead of factor 2 before the δ-operator.

In contrast to 'heterogeneous sub-structures', excitonic level structures connected by coherent EET are referred to in the following as 'homogeneous sub-structures'. Consideration of both sub-structure types within *one* expression of the NLPF line-shape function requires consistent labeling of the different involved states. Hence, the indices **n** and **m** count from now on all excited states in the system. They can either represent the excited states of uncoupled molecules *or* the excitonic states of – probably multiple – excitonic sub-units. In other words, **n** and **m** indicate either the first excited state S_1^i of molecule **i** *or* the state S_1^j in an excitonic manifold of **j** states. Correspondingly, the matrix element γ_{nm} contains incoherent or coherent EET rates from excited state **m** to excited state **n** and diagonal elements according to Eq. 17. The determination equation of the β-matrix changes to

$$\sum_n \beta_{mn} \cdot \gamma_{nl}^{mix} = \begin{cases} 2 \text{ for } m = l \\ 1 \text{ for } m \neq l, \text{ and } m,l \text{ homogeneously coupled} \\ 0 \text{ for } m \neq l, \text{ and } m,l \text{ not homogeneously coupled.} \end{cases}$$

(21)

Finally, combination of Eq. 17, 18 and 21 yields a complete mathematical description for NLPF line-shape functions of 'mixed sub-structures'.

Transition-dipole orientations

The last theoretical extension considers mutual orientations of transition-dipole moments. This is required to reflect the distribution of Chl orientations found in LHCII (cp. Table 1.2.1 and Fig. 1.2.5, pp. 9). Apparently, each pair of transition-dipole vectors μ_n and μ_m encloses a certain angle ϕ_{nm} independently from its origin (molecular or excitonic). Detailed calculations in [132] resulted in a corresponding geometrical factor, which includes orientation averaging for randomly oriented samples:

$$g_{nm} = \frac{1 + 3 \cos 2\phi_{nm}}{4}.$$

(22)

This leads to the following expression for line-shape functions considering the pair-wise dipole orientations:

$$s(\omega_p, \omega_t) = \sum_{n,m} \alpha_n \frac{2}{\gamma_n} \frac{i}{\Gamma_n - i\omega_{tn}} \beta_{nm} g_{nm} \frac{2\Gamma_m}{\Gamma_m^2 + \omega_{pm}^2} \alpha_m.$$

(23)

The geometrical factor in Eq. 22 assumes values between $g_{nm} = 1$ for $\phi_{nm} = 0°$ and $g_{nm} = 0$ for $\phi_{nm} = 54.5°$ ('magic' angle) as further discussed in Section 3.1.5.

Equation 23 represents the complete NLPF line-shape function for mixed absorption sub-structures including EET rates and transition-dipole orientations. It should be further mentioned again that additional inhomogeneous broadening can be included by integration over the resulting frequency distribution according to Eq. 16. Hence, the theoretical descriptions above represent a proper basis for simulations of NLPF spectra measured on Chl-containing antenna proteins. In the framework of this thesis, these equations are used to interpret measurements in the Q_y-absorption region of isolated trimeric LHCII. To enhance the comprehensibility of expressions above, Chapter 3.1 illustrates the detailed influence of different parameters on NLPF spectra by numerous simulations. In this way, further understanding of the contained information is obtained without concentrating on underlying theoretical details.

2.2.4 Nonlinear polarization spectroscopy: Intensity dependence

General calculations describing NLPF signals in the presence of intense pump fields have been formerly presented by Marcano and Golding [133] as well as Beenken and May [134]. The results are extended in the following to reflect spectral heterogeneity and EET processes like for Chls in LHCII. The adaptation has been achieved in close co-operation with Wichard J. D. Beenken and was previously published by the author in [118]. On this basis, the interpretation of intensity-dependent NLPF spectra measured with trimeric LHCII became available as discussed in Chapter 3.3.

The NLPF-signal dependence on probe frequency ω_t, pump frequency ω_p, and pump-field intensity $I_p(\omega_p)$ can be expressed as

$$S(\omega_t, \omega_p, I_p) \propto \left| \int_0^\pi d\theta \, \sin^5\theta \int_0^{2\pi} d\phi \, \cos^2\phi \, \cos 2\phi \sum_{ij} \zeta_{ij}(\omega_t)\left(n_i(I_p, \omega_p) - n_j(I_p, \omega_p)\right) \right|^2 \quad (24)$$

with $\mathrm{Re}\{\zeta_{ij}(\omega)\} = \sigma_{ij}(\omega)/2$, $\mathrm{Im}\{\zeta_{ij}(\omega)\} = \sigma_{ij}(\omega)\left(\omega - \omega_{ij}\right)/2\Gamma_{ij}$ [134]. The integrals average over randomly oriented dipoles (sample representation) characterized by angles ϕ and θ. The population probabilities n_j are determined by the following system of equations:

$$\sum_j \left(\gamma_{ij} + \sigma_{ij}(\omega_p)I_p \sin^2\theta \, \cos^2\phi\right) n_j = 0, \qquad \sum_j n_j = 1. \quad (25)$$

Energy relaxation rate and cross section of the transition from state j to i are named γ_{ij} and $\sigma_{ij}(\omega_p)$, respectively. Diagonal elements γ_{ii} and $\sigma_{ii}(\omega_p)$ are calculated by

$$\gamma_{ii} = -\sum_j \gamma_{ji} \, ; \; (i \neq j) \qquad \text{and} \qquad \sigma_{ii}(\omega_p) = -\sum_j \sigma_{ji}(\omega_p) \, ; \; (i \neq j). \quad (26)$$

Adequate modeling of the investigated species LHCII was based on the description of EET processes in a simple donor-acceptor (D-A) pair. This approach is generalized below to multiple D-A schemes including branched energy transfer. D and A can be represented by two-level systems (see Fig. 2.2.7), if the higher excited-states are not saturated (because of lifetimes much shorter than the ground-state recovery time,

see [132]). This assumption has been verified for Chls due to the short lifetimes of their higher-excited singlet states (cp. Section 1.2.2).
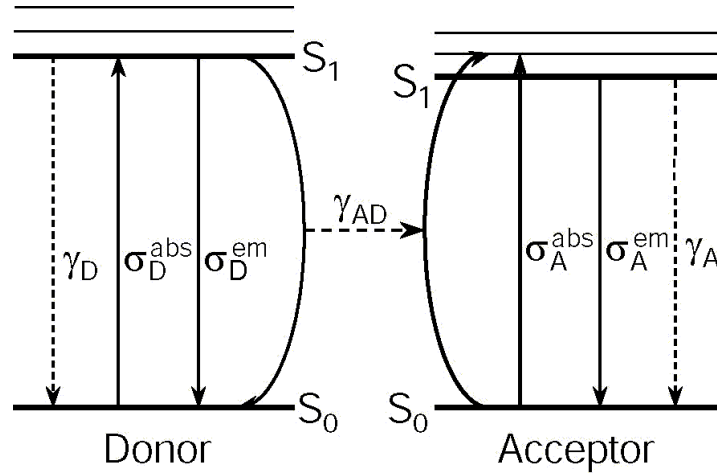

Figure 2.2.7 Basic term scheme employed for the description of intensity-dependent NLPF (as applied to LHCII in this work). γ_{AD} is the EET rate between Donor (D) and Acceptor (A), while γ_D and γ_A are energy relaxation rates. Parameters σ^{abs} and σ^{em} indicate the corresponding absorption and emission cross sections.

For the system in Fig. 2.2.7, the required matrices for Eq. 24-26 can be expressed as follows:

$$\hat{\sigma}(\omega) = \begin{pmatrix} -\sigma_A^{abs}(\omega) - \sigma_D^{abs}(\omega) & \sigma_A^{em}(\omega) & \sigma_D^{em}(\omega) & 0 \\ \sigma_A^{abs}(\omega) & -\sigma_A^{em}(\omega) - \sigma_D^{abs}(\omega) & 0 & \sigma_D^{em}(\omega) \\ \sigma_D^{abs}(\omega) & 0 & -\sigma_A^{abs}(\omega) - \sigma_D^{em}(\omega) & \sigma_A^{em}(\omega) \\ 0 & \sigma_D^{abs}(\omega) & \sigma_A^{abs}(\omega) & -\sigma_A^{em}(\omega) - \sigma_D^{em}(\omega) \end{pmatrix} \quad \text{(a)}$$

$$\text{and} \quad \hat{\gamma} = \begin{pmatrix} 0 & \gamma_A & \gamma_D & 0 \\ 0 & -\gamma_A & \gamma_{AD} & \gamma_D + \gamma_{annihil} \\ 0 & 0 & -\gamma_D - \gamma_{AD} & \gamma_A + \gamma_{annihil} \\ 0 & 0 & 0 & -\gamma_A - \gamma_D - 2\gamma_{annihil} \end{pmatrix}. \quad \text{(27 b)}$$

The first, second and third row in Eq. 27 represent processes that populate (+) or depopulate (–) ground and excited states of acceptor (A) and donor (D), respectively. The fourth row indicates excitation of both, D and A. These different processes indicate absorption of the acceptor $\left(\sigma_A^{abs}(\omega)\right)$ and the donor $\left(\sigma_D^{abs}(\omega)\right)$, stimulated emissions to their ground states $\left(\sigma_A^{em}(\omega), \sigma_D^{em}(\omega)\right)$, and energy relaxation (γ_A, γ_D). EET from D to A is represented by the rate γ_{AD}. EET rates measured in LHCII are significantly higher than the fluorescence decay rate, which corresponds here to the energy relaxation rate of acceptors. Hence, the approximation $\gamma_{AD} \gg \gamma_A \approx \gamma_D$ can be introduced in the further calculation. The fourth column of matrix $\hat{\gamma}$ contains the excitation-annihilation rate $\gamma_{annihil}$. It describes a rate for the generation of doubly excited states after simultaneous excitation of D and A and subsequent relaxation into single-excited states [70, 135]. Resulting from fast EET and short lifetimes of higher excited Chl states in LHCII, this annihilation rate is considerably higher than the relaxation rates of first-excited states.

Hence, the approximation $\gamma_{annihil} \gg \gamma_A \approx \gamma_D$ can be also introduced in the following. Finally, the model is restricted to intensities lower than the donor saturation threshold, which is much higher than that of the acceptor due to annihilation and fast EET: $\gamma_{annihil}, \gamma_{AD} \gg \sigma_D^{abs} \cdot I \approx \sigma_D^{em} \cdot I$. Including all these approximations, the combination of Eq. 24-27 yields the intensity-dependent NLPF signal

$$S(\omega_t, \omega_p, I_p) \propto \left| \int_0^\pi d\theta \, \sin^5\theta \int_0^{2\pi} d\phi \, \cos 2\phi \, \zeta_A(\omega_t) \frac{\sigma_A^{abs}(\omega_p) + \sigma_D^{abs}(\omega_p)}{\gamma_A} \right.$$
$$\left. \times \left(\frac{15}{13}\eta(\omega_t, \omega_p) + \frac{1}{1 + \xi(\omega_p)I_p \sin^2\theta \cos^2\phi} \right) I_p \sin^2\theta \cos^2\phi \right|^2 \tag{28}$$

with the saturation parameter

$$\xi(\omega_p) = \frac{\sigma_D^{abs}(\omega_p) + \sigma_A^{abs}(\omega_p) + \sigma_A^{em}(\omega_p)}{\gamma_A} . \tag{29}$$

The saturation parameter is the value of interest to verify experimental results in Chapter 3.4, since it allows determinations of absolute cross sections if γ_A is known. A second parameter,

$$\eta(\omega_p) = \frac{13}{15} \frac{\sigma_D^{abs}(\omega_p)}{\sigma_A^{abs}(\omega_p) + \sigma_D^{abs}(\omega_p)} \times \frac{\gamma_A}{\gamma_{AD}} , \tag{30}$$

contains the ratio γ_A/γ_{AD} and allows verification of the employed approximation $\gamma_{AD} \gg \gamma_A$. Evaluating the integrals for orientation averaging, intensity-dependent NLPF signals can be described by

$$S(\omega_t, \omega_p, I_p) \propto \left| \eta(\omega_t, \omega_p)\xi(\omega_p)I_p + \frac{3}{\xi(\omega_p)I_p} - \left(1 + \frac{3}{\xi(\omega_p)I_p}\right) \frac{\arctan\sqrt{\xi(\omega_p)I_p}}{\sqrt{\xi(\omega_p)I_p}} \right|^2 . \tag{31}$$

This result can be easily extended to systems with more than one donor substituting σ_D^{abs} by a sum of cross-sections in Eq. 29. Considering more than one acceptor species (not unlikely for antenna complexes), summation over several σ_A^{abs} and σ_A^{em} can also be introduced. However, in this case the overall fluorescence decay rate has to be multiplied with the number of probed terminal acceptors (N_A), which corresponds to the effective number of EET branches. Using the reasonable approximation of similar fluorescence decay rates for every acceptor, the saturation parameter yields

$$\xi(\omega_P) = \frac{\sum_D \sigma_D^{abs}(\omega_P) + \sum_A \sigma_A^{abs}(\omega_P) + \sum_A \sigma_A^{em}(\omega_P)}{N_A \cdot \gamma_{fd}} . \tag{32}$$

In other words, the quantity $\xi(\omega_P)$ is correlated with the combined absorption and emission cross-sections 'per terminal state of the EET chain'.

3 Results and discussion

3.1 Modeling the NLPF signal of heterogeneous absorption systems like LHCII requires substantial additional information

Based on theoretical descriptions in the previous chapter, the influence of different molecular parameters on NLPF spectra is discussed in the following. To provide comprehensive understanding of parameter interactions in complicated multi-pigment systems like antenna complexes, a sizeable number of simulations became necessary. Without this detailed analysis, the later evaluation of measured spectra (see Chapter 3.5) would be rather ambiguous. General correlations between different molecular parameters and the line shape of NLPF spectra are similar for several types of higher plant antenna proteins, i.e. CP24, CP26, CP29, and LHCII. On the other hand, these complexes differ by the number of 7-14 attached Chls *a/b* [136]. Fortunately, a sufficient discussion of all relevant parameter correlations can be obtained even under the assumption of only seven Chls. On this basis, NLPF measurements of LHCII are evaluated in Chapter 3.5 by model extension to the necessary number of transition bands. In a similar way, the following results can also be adapted to recent [41, 131] and future NLPF experiments with other antenna proteins. Besides this, comparison of different simulations below enables a comprehensible perception of rather distinct parameter effects on NLPF spectra, even without advanced theoretical knowledge.
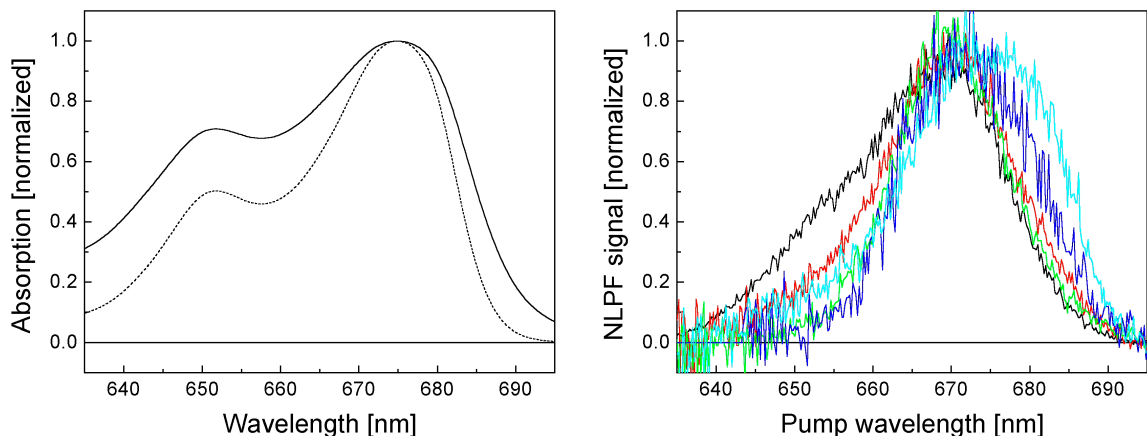
Figure 3.1.1 Left panel: Absorption spectrum of LHCII (solid line) and squared absorption (dashed line). **Right panel:** NLPF spectra of trimeric LHCII measured at λ_t = 645 nm (black), 655 nm (red), 665 nm (green), 675 nm (blue), and 685 nm (cyan).

NLPF spectra of LHCII obtained at five different λ_t are initially shown in Fig. 3.1.1 (together with the corresponding absorption spectrum). These experimental results are discussed in detail in Chapter 3.5, but allow at this point a first impression of actually measured spectra. Since NLPF signals depend on square modules of the NLPF line-shape function (cp. Eq. 6, p. 31), a squared absorption spectrum is also included in Fig. 3.1.1 (left panel).

3.1.1 The effect of heterogeneous absorption sub-structures on NLPF spectra

Table 3.1.1 describes a heterogeneous absorption sub-structure consisting of seven similar, homogeneously broadened transition bands. Their parameters are chosen to reflect the conditions of Chls in antenna complexes and are stepwise refined below. In particular, slightly distinct λ_c indicate deviating environments of the individual attached Chls (see Chapter 3.2 below). Simulated NLPF pump spectra of this model as obtained by using the theoretical descriptions in Section 2.2.3 (especially Eq. 6 and 9, pp. 31) are shown in Fig. 3.1.2. Equal fluorescence decay rates $\gamma_{fd} = (3.5 \text{ ns})^{-1}$ were assumed for each transition at this stage as well as for all simulations in the following. Since different absorption bands show clearly distinct contributions in dependence on λ_t, the pump-probe character of NLPF measurements is apparent at the first glance.

Table 3.1.1 Transition parameters used for simulating absorption and NLPF spectra in Fig. 3.1.2.

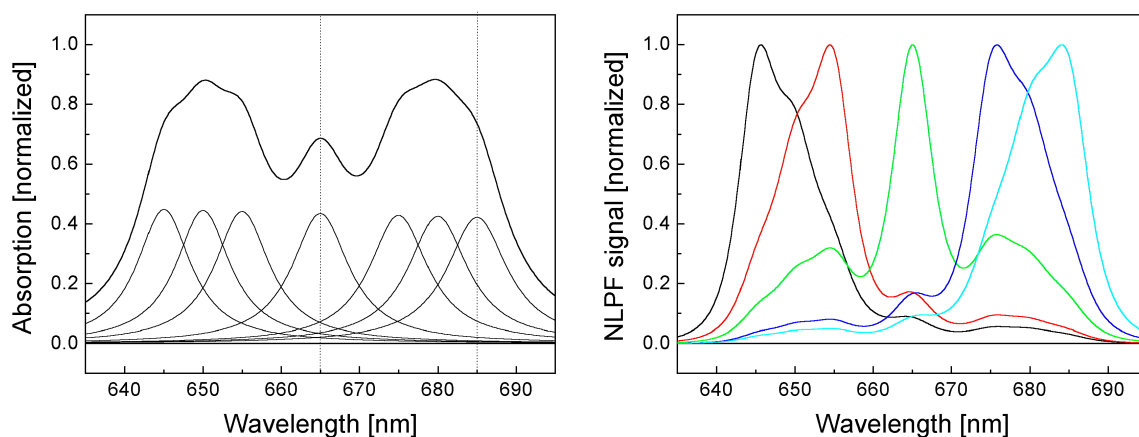| λ_c [nm]	645	650	655	665	675	680	685
α	1	1	1	1	1	1	1
2Γ [cm^{-1}]	200	200	200	200	200	200	200

Figure 3.1.2 Left panel: Combined absorption spectrum (thick line) of a heterogeneous absorption sub-structure consisting of seven sub-bands (thin lines) according to Table 3.1.1. (The vertical dashed lines indicate two different λ_t, which have been used to construct the line-shape in Fig. 3.1.3.) **Right panel:** Simulated NLPF pump spectra of the absorption sub-structure from Table 3.1.1 for $\lambda_t = 645$ nm (black), 655 nm (red), 665 nm (green), 675 nm (blue), and 685 nm (cyan).

The rather low complexity of the model above allows a detailed view into the origin of NLPF signals as further demonstrated in Fig. 3.1.3. In this graphic, different contributions of distinct sub-bands to the NLPF line-shape are illustrated for two λ_t (665 and 685 nm). One should remember in this context that measured NLPF pump *spectra* (λ_t fixed, λ_p tuned) correspond to square modules of NLPF *line-shape functions* (see Chapter 2.2.3). Accordingly, the NLPF pump spectra simulated in Fig. 3.1.2 correspond to *squared* line-shape functions from Fig. 3.1.3.
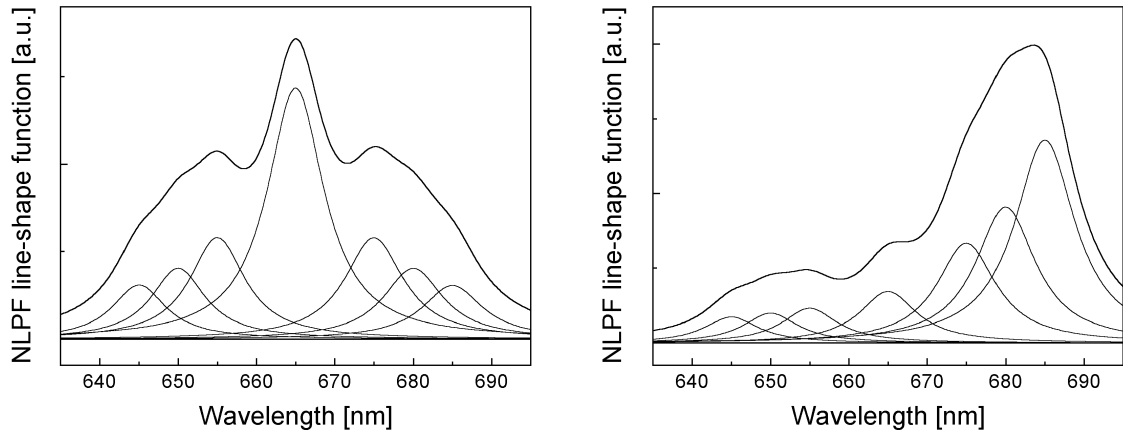
Figure 3.1.3 Simulated contributions of the seven sub-bands from Table 3.1.1 to the NLPF line-shape function as obtained by a simplified mathematical approach (see text). **Left panel:** $\lambda_t = 665$ nm, **Right panel:** $\lambda_t = 685$ nm.

In heterogeneous sub-structures, all transitions absorb photons from external fields in dependence on their absorption-cross section $\sigma(\lambda)$ as reflected by the sub-band amplitudes at λ. Accordingly, the combined absorption spectrum represents a pure summation of all sub-bands (see Fig. 3.1.2, left panel). In NLPF experiments, the pump field *excites* all sub-bands in a similar way. (Notably, this feature is represented by the last term $2\Gamma_n/\Gamma_n^2 + \omega_{Pn}^2$ in Eq. 9, p. 34, which describes the Lorentzian line-shape of each homogeneously broadened absorption band.) However, corresponding ground-state depletions are *probed* at λ_t, and the absorption-cross section $\sigma(\lambda_t)$ of each band becomes thus also relevant. This behavior is described by a complex term $i/\Gamma_n - i\omega_{tn}$ in Eq. 9. Since this complex factor can be hardly visualized, it is approximated at this stage by a real expression. In particular, the relative absorption values at λ_t were obtained for each band from Fig. 3.1.2 and their square root applied to scale the sub-bands in Fig. 3.1.3. This approximation nicely illustrates NLPF line-shape functions as superposition of contributions from different sub-bands in dependence on their absorption at λ_t.

Table 3.1.2 Transition parameters used for simulating absorption and NLPF spectra in Fig. 3.1.4.

λ_c [nm]	645	650	655	665	675	680	685
α	1	1	1	1	1	1	1
2Γ [cm^{-1}]	200	200	200	200	200	200	200
Δ [cm^{-1}]	120	120	120	120	120	120	120

In the next step, the sub-structure model is extended by including additional inhomogeneous broadening for each band.[*] Fig. 3.1.4 shows simulated absorption and NLPF spectra of a heterogeneous sub-structure consisting of seven bands with parameters according to Table 3.1.2. Apparently, the additional inhomogeneous widths

---

[*] Heterogeneous absorption systems consisting of only inhomogeneously broadened transitions are not further considered, since they would just result the (infinitesimal small) T_1- peak at λ_t.

smooth both the absorption and NLPF spectra, but the right panel reveals the underlying spectral heterogeneity much better (cp. especially $\lambda_t = 665$ nm). This feature of NLPF line-shapes was expected to simplify the sub-structure analysis for complicated heterogeneous absorption systems like antenna complexes. Nevertheless, a strong overlap between different bands can mask this enhanced spectral resolution.
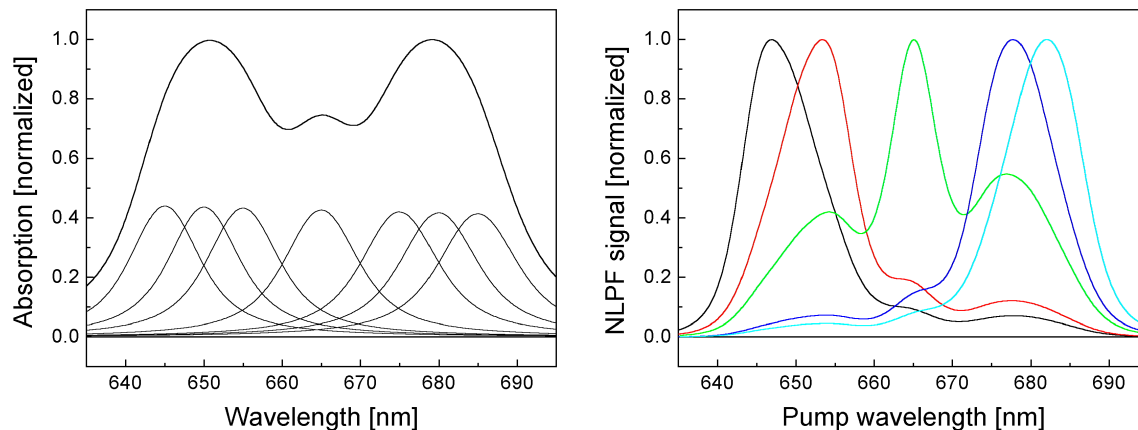

Figure 3.1.4 Left panel: Simulated absorption spectrum (thick line) of a heterogeneous absorption sub-structure consisting of seven sub-bands (thin lines) with parameters as shown in Table 3.1.2. **Right panel:** Simulated NLPF pump spectra of the heterogeneous model from the left panel for $\lambda_t = 645$ nm (black), 655 nm (red), 665 nm (green), 675 nm (blue), and 685 nm (cyan).

In the next simulation, a less symmetric model (Table 3.1.3) describing bands with non-equidistant λ_c is depicted. This modification, resulting in less symmetric spectra (Fig. 3.1.5), represents Chls at different binding sites more realistically (cp. Chapter 3.2). The loss of symmetry in NLPF spectra due to shifted λ_c is again most obviously for $\lambda_t = 665$ nm. It is further interesting to note that modest band shifts of some transitions result in considerable changes of both, the absorption and NLPF spectra. This behavior is important with regard to sub-structure models obtained by other authors (cp. Chapter 3.2). Furthermore, the high sensitivity of NLPF spectra on minor changes in the underlying sub-structure model is illustrated at this point (cp. Fig. 3.1.4 and 3.1.5).

Table 3.1.3 Parameters used for simulating absorption and NLPF spectra in Fig. 3.1.5.

λ_c [nm]	645	651	655	665	671	677	682
α	1	1	1	1	1	1	1
2Γ [cm^{-1}]	200	200	200	200	200	200	200
Δ [cm^{-1}]	120	120	120	120	120	120	120

Two reasons require additional parameter variations in the regular sub-structure models considered so far. The spectral region above 660 nm can be mainly attributed to Chl a absorption, while Chl b absorbs at shorter wavelengths (cp. the 20 nm separation of Q_y-absorption maxima for both Chl species in solution, Fig. 1.2.7, p. 12). Chl b is further known to have only 70 % of Q_y-transition probability when compared to Chl a [50]. Hence, the absorption coefficients α should reflect the proper values for each species. Taking this into account, the three short-wavelength transitions in Table 3.1.4

are now assumed to represent Chl *b*, while the other bands correspond to Chl *a*.[*] The distinction between both species has further consequences for their homogeneous linewidth, since $Q_y(0,0)$-transitions of Chl *b* are slightly broader than for Chl *a* (cp. Table 1.2.2, p. 14). Accordingly, higher values of 2Γ are further assumed for the 'Chl *b*'-species in Table 3.1.4.
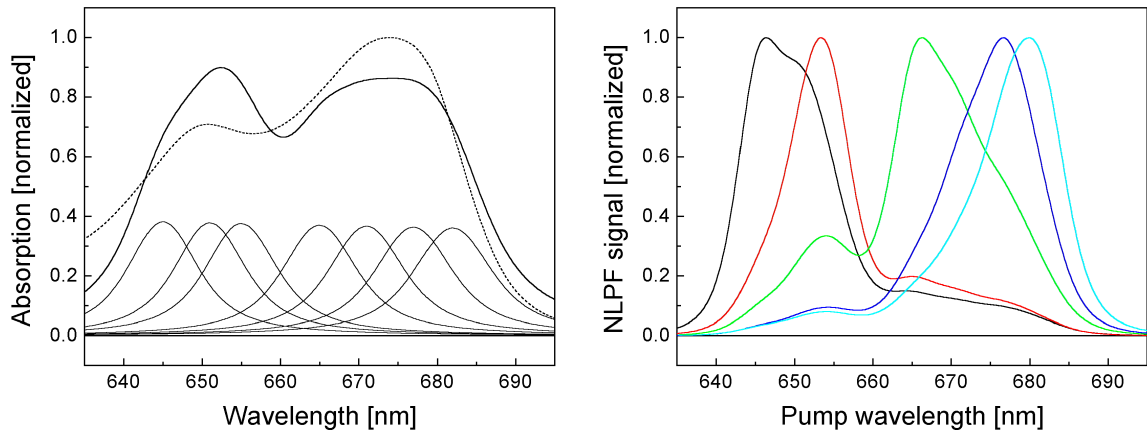

Figure 3.1.5 Left panel: Simulated absorption spectrum (thick line) of a heterogeneous absorption sub-structure consisting of seven sub-bands (thin lines) with parameters as shown in Table 3.1.3. An absorption spectrum of LHCII is added for comparison (dashed line). **Right panel:** Simulated NLPF pump spectra of the heterogeneous band structure from left panel for λ_t = 645 nm (black), 655 nm (red), 665 nm (green), 675 nm (blue), and 685 nm (cyan).

The resulting absorption spectrum in Fig. 3.1.6 reflects basic features of the measured LHCII absorption, since increased Γ and reduced α lower the significance of the short-wavelengths bands. This decreased relative contribution becomes more significant in the NLPF spectra due to a quadratic dependence of NLPF signals on absorption coefficients α (see Eqs. 6 and 9 in Section 2.2.3). However, in measured NLPF spectra of LHCII the Chl *a* bands are even stronger reflected, especially for short λ_t (cp. Fig. 3.1.1). This observation indicates a strong influence of further parameters on NLPF spectra. While the simulations have described so far only the *superposition* of different Chl bands, any *interactions* among the pigments were neglected. Accordingly, the model is extended below to reflect additional interaction parameters. To enhance the comparability of all simulations, the underlying absorption sub-structure is not varied any further, but fixed to the model established in Table 3.1.4 (cp. Fig. 3.1.6).

Table 3.1.4 Transition parameters used for simulating absorption and NLPF spectra in Fig. 3.1.6.

λ_c [nm]	645	651	655	665	671	677	682
α	0.7	0.7	0.7	1	1	1	1
2Γ [cm^{-1}]	300	300	300	200	200	200	200
Δ [cm^{-1}]	120	120	120	120	120	120	120

---

[*] The Chl *a/b* ratio of 4:3 corresponds roughly to the ratio found in LHCII (7:5).
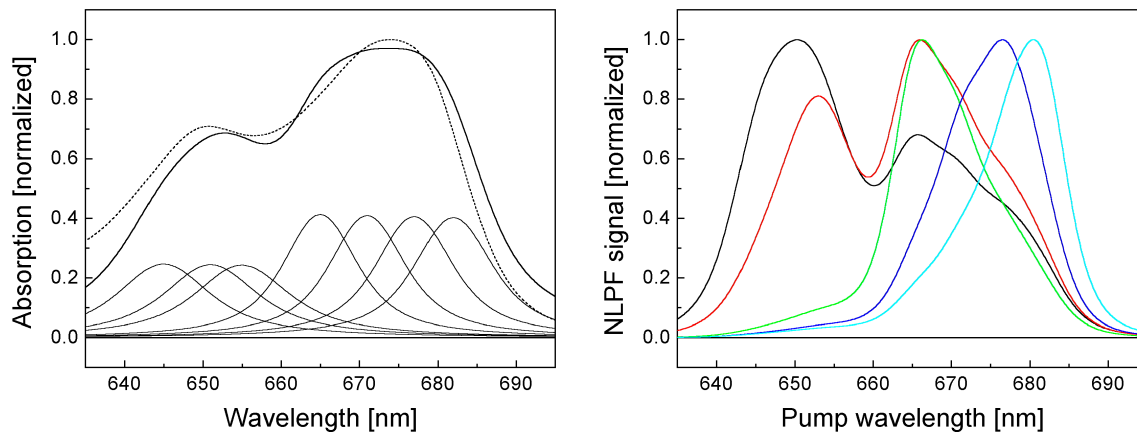
Figure 3.1.6 Left panel: Simulated absorption spectrum (thick line) of a heterogeneous absorption sub-structure consisting of seven sub-bands (thin lines) with parameters as shown in Table 3.1.4. An original LHCII absorption spectrum (dashed line) is added for comparison. **Right panel:** Simulated NLPF pump spectra of the heterogeneous band structure from the left panel for $\lambda_t = 645$ nm (black), 655 nm (red), 665 nm (green), 675 nm (blue), and 685 nm (cyan).

3.1.2   The effect of excitonic coupling among Chls on NLPF spectra

The phenomenon of excitonic coupling, resulting in transition band shifts and redistributed transition probability, is described in Chapter 1.3.1. Unfortunately, reliable calculations of coupling effects in LHCII have not been accomplished so far due to uncertainties about Chl arrangements within the complex (cp. Chapter 1.2.1). For that reason, the investigation of excitonic interaction is still an experimental challenge. It will be demonstrated below that excitonic coupling is strongly reflected in NLPF spectra because of the creation of common ground states in this case. Moreover, possible redistributions of transition probability are *not* included at this stage, since this would require modifications of the underlying sub-structure model. In other words, NLPF spectra are analyzed in the following with respect to excitonic coupling for geometries similar to the left panel in Fig. 1.3.2 (p. 19). Nevertheless, the identification of excitonic interaction for other geometrical arrangements *including* redistribution of transition probability is certainly possible by a combined analysis of absorption and NLPF spectra (cp. Section 3.1.6).

Excitonic coupling in different dimeric units is illustrated in Fig. 3.1.7. The left panel depicts formation of one Chl *a* and one Chl *b* homodimer, while spectra in the right panel reflect the influence of coupling in a Chl *a*/*b* heterodimer. In both cases, NLPF spectra are essentially characterized by increased contributions of the excitonic bands. For example, the Chl *b* dimer is reflected by a stronger left wing in the NLPF spectrum for $\lambda_t = 655$ nm as obvious by comparison of Fig. 3.1.6 (right panel) and Fig. 3.1.7 (left panel). Similarly, the Chl *a* dimer results in an enhanced amplitude around 670 nm for $\lambda_t = 685$ nm when comparing the same graphs.
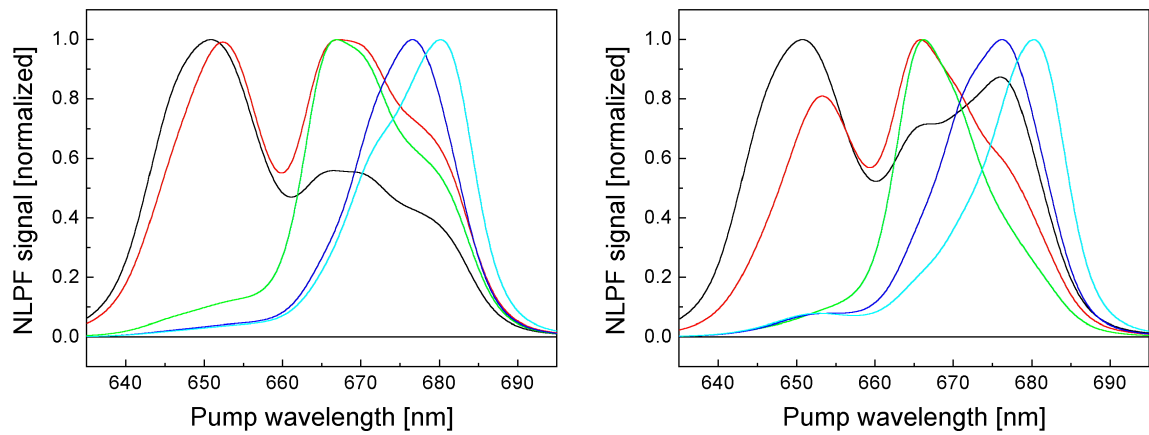
Figure 3.1.7 Simulated NLPF spectra with λ_t = 645 nm (black), 655 nm (red), 665 nm (green), 675 nm (blue), and 685 nm (cyan) for the sub-structure from Table 3.1.4 (p. 45) considering additional formation of excitonic dimers. **Left panel:** One Chl *b* dimer with transitions at λ_c = 645 and 655 nm and one Chl *a* dimer with transitions at λ_c = 671 and 682 nm. **Right panel:** One Chl *a/b* dimer with transitions at λ_c = 651 and 677 nm.

The observable effect is exclusively related to *common* ground state creation for strongly coupled Chls (cp. Fig. 1.3.1, p. 17) as explained for the Chl *b* dimer with excitonic transitions at λ_c = 645 and 655 nm. In this case, ground state depletion can be probed at λ_t = 645 nm after excitation of either the *same* exciton transition with $\lambda_P \approx 645$ nm or the *other* exciton transition with $\lambda_P \approx 655$ nm. Certainly, the additional ground state depletion can be also detected in the opposite case, λ_t = 655 nm and $\lambda_P \approx 645$ nm. This behavior is mathematically represented by an additional summand '1' in the complex factor β_{ij} from Eq. 20 (p. 37). However, the detailed theoretical discussion of the resulting spectra is more complicated, since λ_t and λ_P do usually not coincide with λ_c as assumed in the example above. On the other hand, this chapter was aimed to provide basic understanding of NLPF spectra in complicated multi-level systems *without* detailed knowledge of the mathematical background. Accordingly, readers with deeper theoretical interest are referred to the parallel work of Beenken [1].

Enhanced contributions of excitonic transitions are also observed for the Chl *a/b* heterodimer as shown in the right panel of Fig. 3.1.7. The coupling results in an increased contribution of the 677 nm band for λ_t = 645 nm. Moreover, (rather small) maxima around 651 nm are observable for λ_t = 675 and 685 nm when compared to Fig. 3.1.6 (right panel). Although the second feature is less obvious, it may indeed provide substantial information about coupling in measurements with adequate sensitivity. Interestingly, the NLPF spectrum for λ_t = 655 nm is barely influenced by excitonic coupling. This behavior originates from the intricate λ_t-dependency of NLPF signals as indicated in Eq. 9 (p. 34). To illustrate these correlations at least by some means, NLPF *probe* spectra are simulated for five different λ_P in Fig. 3.1.8. It should be noted that NLPF probe spectra have not been measured in this work. However, such simulations are quite helpful at this stage to clarify the effect of excitonic interactions on NLPF spectra. Apparently, the two models with/without excitonic coupling in Fig. 3.1.8 show only minor differences in the NLPF probe spectra for λ_P = 655 and 672 nm. In contrast, NLPF signals of the exciton model are twice as intense around 680 nm for λ_P = 645 and 655 nm. A similar increase is observed around 648 nm for λ_P = 675 and 685 nm. In other

words, the significance of excitonic interaction in NLPF *pump* spectra depends mainly on the relative distribution of excitonic transition wavelengths with respect to λ_t. Accordingly, excitonic contributions to the NLPF signal may also vanish completely for certain λ_t.
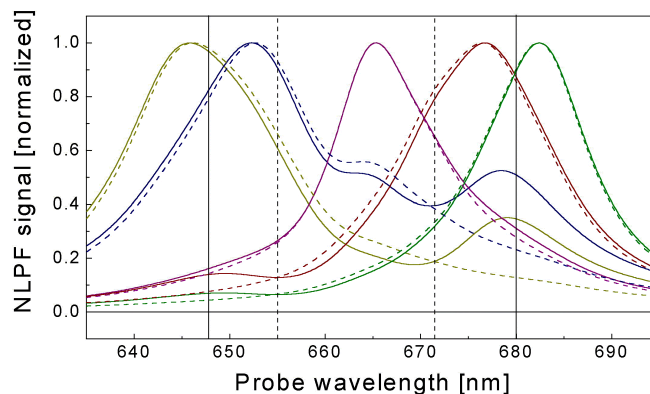

Figure 3.1.8 Simulation of the NLPF signal in dependence on λ_t (NLPF *probe* spectra) for λ_P = 645 nm (gold), 655 nm (navy), 665 nm (purple), 675 nm (wine), and 685 nm (olive). Dotted lines: Band structure model according to Table 3.1.4 (p. 45) without excitonic coupling. Solid lines: Band structure model according to Table 3.1.4 including a Chl-*a*/*b* dimer with excitonic transitions at 651 and 677 nm. Two vertical solid lines (648 and 680 nm) specify λ_t with the strongest difference between both models, while vanishing differences are indicated by dashed vertical lines (655 and 672 nm).

The simulations in Fig. 3.1.9 finally extend the model to more complicated systems of excitonic interactions, i.e. the formation of *three* different Chl-*a*/*b* dimers. Comparison of the left and right panels indicates that interacting Chl pairs with transitions at different λ_c clearly result in distinct NLPF spectra. According to this, the NLPF method has indeed the potential to analyze excitonic interactions in strongly heterogeneous systems. However, it should be noted again that additionally redistributed transition probability affects also the absorption sub-structure. Excitonic transitions might thus be reflected in the coupling parameter (β_{ij}) *and* in the α-parameters of each sub-band. Hence, it became essentially important in this work to study possible exciton formation *prior* to the evaluation NLPF measurements (see Chapter 3.3 and 3.4).
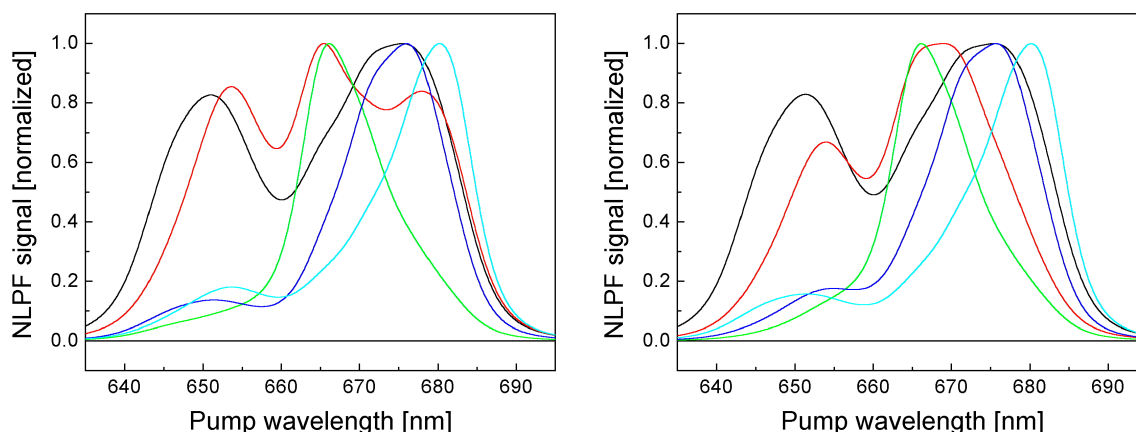
Figure 3.1.9 Simulated NLPF spectra of a heterogeneous absorption sub-structure according to Table 3.1.4 (p. 45) considering the formation of different excitonically coupled dimers. λ_t = 645 nm (black), 655 nm (red), 665 nm (green), 675 nm (blue), and 685 nm (cyan). **Left panel:** Three Chl-*a*/*b* dimers with transitions at 645/671 nm, 651/677 nm and 655/682 nm. **Right panel:** Three Chl-*a*/*b* dimers with transitions at 645/682 nm, 651/677 nm and 655/671 nm.

3.1.3 The effect of Chl-Chl energy transfer on NLPF spectra

Incoherent EET between two-level systems is described in Chapter 1.2 as combination of two simultaneous transitions $S_1 \rightarrow S_0$ for the *donor* and $S_0 \rightarrow S_1$ for the *acceptor*. In NLPF experiments, ground-state depletion induced by the pump field is thus repopulated for donor transitions on the timescale of EET. If this transfer is considerably faster than other relaxation processes, only those transitions that function as acceptors show significant ground-state depletion. Consequently, excitations of donor transitions are not probed directly, but via the acceptor states. Thus, the ratio between EET times $T_{\mu\nu}$ and the fluorescence lifetime $\tau_{fd} = 1/\gamma_{fd}$ becomes a significant parameter in NLPF spectra. For example, donor transitions of Chls in LHCII connected by EET rates faster than 1 ps^{-1} contribute thousand times less to ground-state depletion ($\gamma_{fd} \approx 1/3.5$ ns, cp. [13]). At the same time, moderate variations of $T_{\mu\nu}$ are less significant in NLPF spectra as long as $T_{\mu\nu} << \tau_{fd}$. It should be further noted that excitonic coupling is *not* considered at this stage, but EET is assumed as Förster-type hopping (cp. Chapter 1.3.1). All EET schemes in this section contain transfer rates $\gamma_{\mu\nu}$ [ps^{-1}], which correspond to transfer times $T_{\mu\nu}$ according to $\gamma_{\mu\nu} = 1/T_{\mu\nu}$. In contrast to this, EET rates employed for numerical simulations and mathematical descriptions of NLPF spectra, i.e. the β-matrix in Eq. 19 (p. 36), are defined by $\gamma_{\mu\nu}$ [cm^{-1}] $= 1/2\pi \cdot c \cdot T_{\mu\nu}$ (c: speed of light in cm/s).

Table 3.1.5 EET rates $\gamma_{\mu\nu}$ [ps^{-1}] used to simulate NLPF spectra in Fig. 3.1.10 and 3.1.11 (donor transitions: left column, acceptor transitions: top row). Values in red indicate random distributions of 'downhill' EET rates between various transitions and were considered for simulations in Fig. 3.1.10 and 3.1.11. Values in blue indicate 'uphill' transfer for the three bands with lowest transition energies (end of the EET chain) and have been *additionally* considered for simulations in Fig. 3.1.11. In the latter case, the lower-right sub-matrix indicates formation of an acceptor 'pool', wherein excited states continuously exchange their excitation energy.

λ_c [nm]	645	651	655	665	671	677	682
645	x	1	0.3	0	0.2	5	3
651	0	x	0.5	2	10	0.1	0.1
655	0	0	x	0	0	2	0.5
665	0	0	0	x	0.03	0	2
671	0	0	0	0	x	0.3	0.5
677	0	0	0	0	0.2	x	1.5
682	0	0	0	0	0.3	0.5	x

NLPF simulations for different EET schemes are inspired by the emission properties of LHCII (see Chapter 1.2.2). This emission originates (to a large extent) from only a few (or one) Chl *a* absorbing at the red edge of the Q_y-absorption region. This observation can only be explained by efficient EET to these final state(s). A corresponding EET schemes is approximated by random distributions of transfer rates between different excited states as shown in Table 3.1.5. Values in red indicate downhill

EET to *one* final state with $\lambda_c = 682$ nm. The resulting NLPF spectra are shown in Fig. 3.1.10. In contrast, NLPF spectra in the case of partial back-transfer and corresponding formation of an acceptor 'pool' are simulated in Fig. 3.1.11 (cp. values in blue in Table 3.1.5).
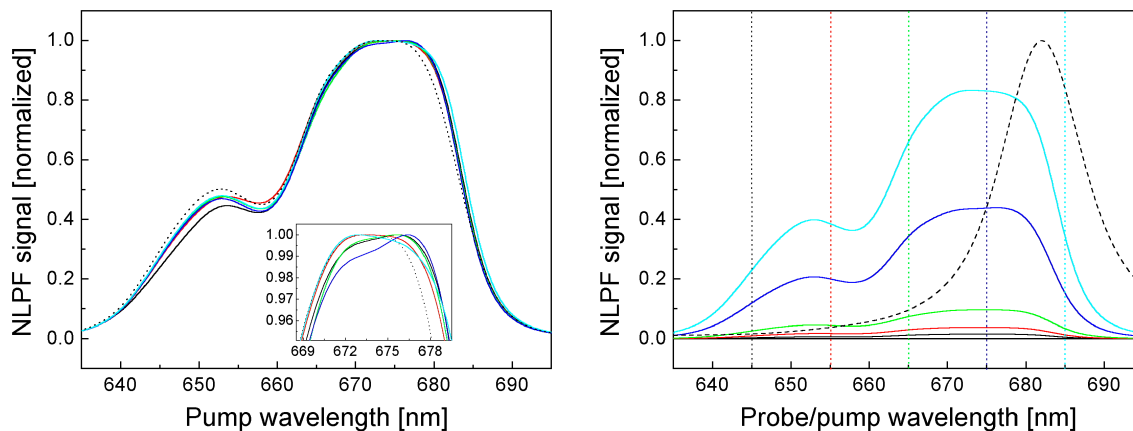

Figure 3.1.10 Left panel: Simulated NLPF pump spectra of the absorption sub-structure from Table 3.1.4 (p. 45) considering 'randomly' distributed EET rates according to the values in red in Table 3.1.5 (values in blue were assumed 0). $\lambda_t = 645$ nm (black), 655 nm (red), 665 nm (green), 675 nm (blue), and 685 nm (cyan). The dotted line corresponds to the squared absorption spectrum of all sub-bands (cp. Fig. 3.1.6, left panel, p. 46). **Right panel:** The dashed line shows a NLPF *probe* spectrum for $\lambda_P = 675$ nm simulated for the same parameters as used in the left panel. Since all normalized NLPF spectra have nearly identical values at $\lambda_P = 675$ nm, the NLPF probe spectrum can be used to calibrate relative signal amplitudes. Thus, each spectrum is normalized at $\lambda_P = 675$ nm to the value obtained for different λ_t from the NLPF probe spectrum (i.e., from the crossing point of the dashed spectrum with the vertical dotted lines for each λ_t).

NLPF spectra in Fig. 3.1.10 (left panel) do not depend on λ_t and essentially resemble a squared absorption spectrum. Minor differences result from partial inhomogeneous broadening and are not further discussed. The origin of lost λ_t-selectivity can be directly obtained from unidirectional EET to the final acceptor state. Since all other excited states return shortly after pump-field excitation to S_0 (due to fast EET processes), only the transition at 682 nm can be actually probed by the probe field. Accordingly, the simulation of a NLPF *probe* spectrum for this EET scheme represents exactly the shape of the acceptor sub-band with $\lambda_c = 682$ nm. (Compare the dashed line in the right panel of Fig. 3.1.10 with the corresponding sub-band in the left panel of Fig. 3.1.6, p. 46). Since, furthermore, *each* excitation induced at *any* transition arrives rapidly at the final acceptor, all NLPF spectra resemble more or less squared absorption curves.

In contrast to vanishing λ_t-selectivity, the signal amplitudes of NLPF spectra certainly vary in dependence on the precise absorption strengths of the acceptor band at λ_t. This is demonstrated by simulating relative amplitudes of the NLPF spectra at different λ_t in Fig. 3.1.10 (right panel). A NLPF *probe* spectrum calculated for $\lambda_P = 675$ nm is used to estimate the amplitudes of NLPF pump spectra, which depend significantly on λ_t. It should be further mentioned that intermediate EET stages on the pathway to the final acceptor have *no* effect on NLPF signals – as long as they are fast in comparison to τ_{fd}. For example, an EET scheme with direct $651 \rightarrow 682$ nm transfer as single channel results in identical NLPF spectra and amplitudes like a two-step scheme according to

$651 \rightarrow 665 \rightarrow 682$ nm. In contrast, equilibration among more than one acceptor state due to 'uphill' EET (cp. Section 1.3.1) changes the relative signal amplitudes as illustrated in Fig 3.1.11.
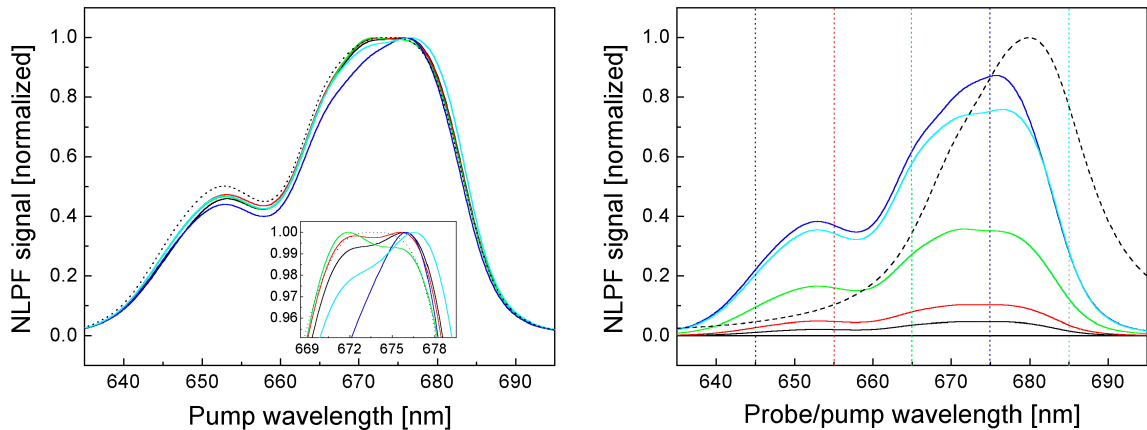

Figure 3.1.11 Left panel: Simulated NLPF pump spectra of the absorption sub-structure from Table 3.1.4 (p. 45) considering 'randomly' distributed EET rates according to Table 3.1.5 (values in red *and* blue). λ_t = 645 nm (black), 655 nm (red), 665 nm (green), 675 nm (blue), and 685 nm (cyan). The dotted line corresponds to the squared absorption spectrum of all sub-bands (cp. Fig. 3.1.6, left panel, p. 46). **Right panel:** The dashed line shows a NLPF spectrum for λ_P = 675 nm simulated by using the same parameters. Since all normalized NLPF spectra in the left panel have nearly identical values at λ_P = 675 nm, the NLPF probe spectrum can be used to calibrate relative signal amplitudes. In particular, each spectrum is normalized at λ_P = 675 nm to the value obtained for the corresponding λ_t from the NLPF probe spectrum (i.e., from the crossing point of the dashed spectrum with vertical dotted lines for each λ_t).

Bi-directional EET among excited states at the end of the EET chain results in an acceptor 'pool', and excitations induced by the pump field are continuously exchanged therein. Accordingly, the NLPF *probe* spectrum (right panel in Fig. 3.1.11) represents a superposition of all three 'pool' transitions from Table 3.1.4. The relative contribution of each band is determined by its ratio of accepted and donated excitations, which corresponds directly to the ratio of summarized 'uphill' and 'downhill' rates. Hence, the actual shape of NLPF probe spectra is highly sensitive to the EET distribution, while NLPF pump spectra reflect this information only in the order of some percent (see the inset in Fig. 3.1.11, left panel). Relative signal amplitudes calculated in Fig. 3.1.10 and 3.1.11 (right panels) further illustrate the differences between NLPF probe spectra in dependence on the acceptor state(s). Apparently, the highest amplitude is obtained for λ_t = 675 nm in Fig. 3.1.11 (acceptor pool) in contradiction to λ_t = 685 nm in Fig. 3.1.10 (one acceptor). With no doubt, the determination of absolute amplitudes would thus improve the sensitivity of the NLPF method on EET rates. However, neither absolute NLPF signals nor NLPF probe spectra have been experimentally investigated in the framework of this thesis. On the contrary, the discussion of both features was added at this stage to enhance the comprehensibility of different EET parameter correlations.

A different picture must be drawn if one of the acceptors is isolated from all other acceptor states, thus functioning as 'dead end' in the EET chain. This situation might occur for Chl *a* that has only Chl *b* as closest neighbors. The excited state of this Chl *a* can be populated by EET from the respective Chls *b* due to sufficient spectral overlap, but back transfer is highly unlikely (see Section 1.3.1). Hence, the corresponding Chl *a*

would function as excitation 'trap'. Two different cases of excitation trapping are modeled in Table 3.1.6 and the corresponding NLPF spectra are simulated in Fig. 3.1.12.

Table 3.1.6 EET rates $\gamma_{\mu\nu}$ [ps^{-1}] used to simulate NLPF spectra in Fig. 3.1.12 (donor transitions: left column, acceptor transitions: top row). The lower-right sub-matrix indicates a pool of acceptor states. To model an excitation trap at the 671 nm transition, all values in *red* and *green* were assumed 0 in the left panel of Fig. 3.1.12. To model as excitation trap at the 682 nm transition, all values in *blue* and *green* were assumed 0 in the right panel of Fig. 3.1.12.

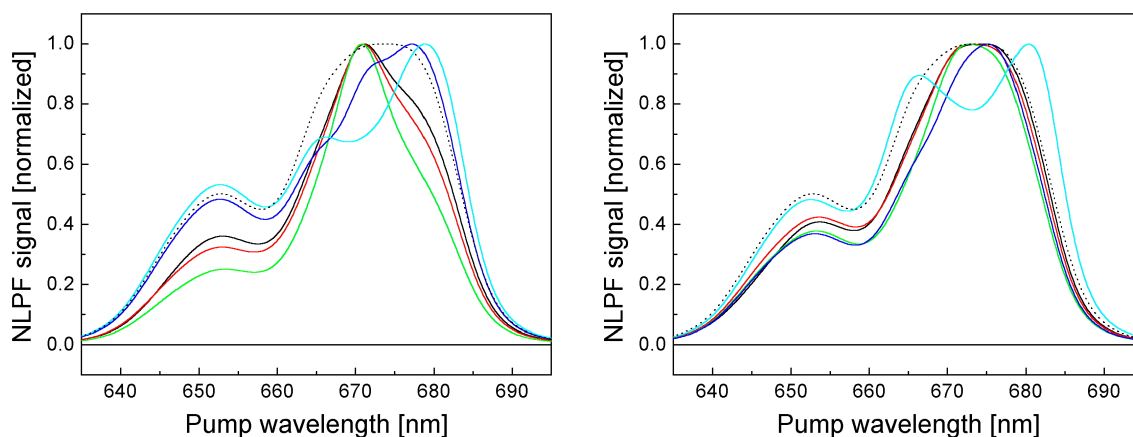| λ_c [nm]	645	651	655	665	671	677	682
645	x	1	0.3	0	0.2	5	3
651	0	x	0.5	2	10	0.1	0.1
655	0	0	x	0	0	2	0.5
665	0	0	0	x	0.03	0	2
671	0	0	0	0	x	0.3	0.5
677	0	0	0	0	0.2	x	0.7
682	0	0	0	0	0.3	0.5	x

Figure 3.1.12 Simulated NLPF pump spectra of the absorption sub-structure from Table 3.1.4 (p. 45) considering the EET scheme in Table 3.1.6. λ_t = 645 nm (black), 655 nm (red), 665 nm (green), 675 nm (blue), and 685 nm (cyan). The dotted line corresponds to the square of a combined absorption spectrum of all sub-bands (cp. left panel in Fig. 3.1.6, p. 46). **Left panel:** Values in red and green from Table 3.1.6 were assumed 0 (the 671 nm band functions as excitation trap). **Right panel:** Values in blue and green from Table 3.1.6 were assumed 0 (the 682 nm band functions as excitation trap).

Simulations of excitation-trapping states in Fig. 3.1.12 result in significantly changed NLPF spectra. The origin of these differences can be analyzed with respect to the exact EET pathways through the system. For example, the formation of a trapping state at 671 nm (left panel) reduces the contributions of the 645, 655 and 682 nm bands to the spectra obtained at short λ_t. This decrease originates from disconnection of the corresponding bands from the 671 nm transition (see Table 3.1.6), which is mainly probed at shorter λ_t. In contrast, the 671 nm band itself is suppressed for λ_t = 685 nm, since it has no EET to the mainly probed transition in this case. Comparison of the spectra simulated for different trapping states indicates that NLPF measurements allow the detection of such features. Nevertheless, excitation trapping is not expected for

trimeric LHCII samples as investigated in this thesis. On the other hand, trapping state formation might be observable in future measurements of intact photosystems.

Comparison of Figs. 3.1.10-3.1.12 indicates that NLPF spectra enable an interesting view into intrinsic mechanisms of excitation energy equilibration. Nevertheless, corresponding evaluations of actually measured spectra can become rather ambiguous because of the high number of different parameters determining the NLPF signal. This complexity is illustrated by the next two simulations, which *combine* the influence of EET with the effects from excitonic coupling as discussed in Section 3.1.2.
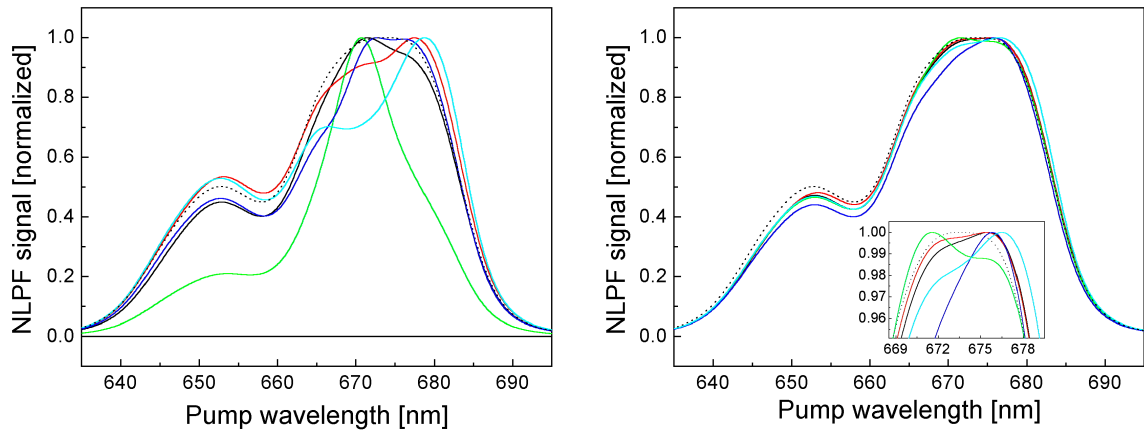

Figure 3.1.13 Simulated NLPF pump spectra of the absorption sub-structure from Table 3.1.4 (p. 45) considering EET *and* excitonic interactions. λ_t = 645 nm (black), 655 nm (red), 665 nm (green), 675 nm (blue), and 685 nm (cyan). Dotted lines correspond to squared absorption spectrum of all sub-bands (cp. left panel in Fig. 3.1.6, p. 46). **Left panel:** EET scheme as used for the left panel in Fig. 3.1.12 (excitation trap for the transition at 671 nm). Chl *a/b*-dimer formation as employed for the simulations in Fig. 3.1.9 (three dimeric units with transitions at 645/671 nm, 651/677 nm and 655/682 nm). **Right panel:** EET scheme as used for Fig. 3.1.11 (Excitation equilibration among three acceptor states without trapping). Chl *a/b*-dimer formation as employed for the simulations in Fig. 3.1.9 (three dimeric units with transitions at 645/671 nm, 651/677 nm and 655/682 nm).

Both simulations in Fig. 3.1.13 must be compared on one hand to Fig. 3.1.9 (left panel, p. 48), where the same exciton structure is modeled *without* EET. Apparently, EET has the strongest influence on the spectral shape as mostly obvious by the different Chl *b* and Chl *a* contributions in Fig. 3.1.9 and 3.1.13. Furthermore, excitonic interactions are observable if a trapping state exists as obtained by comparison of Fig 3.1.13 (left panel) with Fig. 3.1.12 (left panel). Especially the spectra for λ_t = 645 and 655 nm show noticeable differences in dependence on possible dimer formation. In contrast, excitonic coupling might *not* be reflected in NLPF spectra in the case of energy equilibration among acceptor states *without* excitation trapping (cp. Fig. 3.1.13, left panel, and Fig. 3.1.11, right panel). The observable differences between excitonically coupled and uncoupled transitions vanish, because coherent and incoherent EET rates are both contained in the β-matrix with similar weighting (see Eq. 21, p. 37). Thus, both types of transfer are indistinguishable if all excitations end finally at the same acceptor state(s). One can finally conclude that effects of excitonic coupling are either observable or imperceptible in NLPF spectra in dependence on the underlying EET scheme. This phenomenon reveals the highly intricate correlations between different parameters in the NLPF spectra of a multi-level absorption system. Consequently, the establishment of a

partial parameter model *before* the evaluation of NLPF measurements might strongly improve the methods significance as further discussed in Section 3.1.6.

3.1.4 The effect of higher vibrational states on NLPF spectra

The Q_y-absorption region of Chls was briefly analyzed in Chapter 1.2.2 (see Table 1.2.2, p. 14, and Fig. 1.2.9). For Chl *a*, one can observe a (0,0)-band with $\lambda_c \approx 665$ nm as well as additional higher vibrational transitions $Q_y(0,x)$ in organic solvents. From Fig. 1.2.7 (p. 12) one can further obtain that the $Q_y(0,1)$-band of Chl *a* overlaps to some extent with the $Q_y(0,0)$-band of Chl *b*. This overlap might be even stronger in LHCII, where the Chl *a* absorption is shifted by up to 15 nm to longer wavelengths. For that reason, the possible influence of Chl (0,1)-transitions in NLPF spectra is further analyzed.

A convenient approach to consider (0,1)-transitions in the absorption model above is the assumption of seven additional bands. Their parameters can be estimated from the values in Table 1.2.2 (p. 14) and result in seven pairs of (0,0)- and (0,1)-bands as summarized in Table 3.1.7. Inhomogeneous broadening of the higher vibrational bands is neglected because of their considerably broader homogenous linewidth. Furthermore, it must be reflected in the parameter model that each (0,1)-transition depopulates the same ground state as the corresponding (0,0)-transition. This is achieved in the same way as for excitonically coupled transitions by adapting the respective terms in the β-matrix according to Eq. 20 (p. 37).

Table 3.1.7 Transition parameters of additional (0,1)-bands used to for the simulation of absorption and NLPF spectra in Fig. 3.1.14. (Further parameters of the (0,0)-transitions can be found in Table 3.1.4, p. 45).

(0,0)-transition: λ_c [nm]	645	651	655	665	671	677	682
(0,1)-transition: λ_c [nm]	595	601	605	619	625	631	636
(0,1)-transition: α	0.49	0.49	0.49	0.46	0.46	0.46	0.46
(0,1)-transition: 2Γ [nm]	41	41	41	34	34	34	34

The EET scheme for additional (0,1)-transitions can be reduced to intra-band relaxation from $S_1(1)$ to $S_1(0)$, since this process is known to occur within a few ps (see Section 1.2.2). Strictly speaking, $S_1(1)$ states may also participate in EET to neighboring molecules, if the EET rates are fast in comparison to vibrational relaxation.[*] However, results obtained in the previous section clearly indicate that *exact* pathways of excitations through the system are irrelevant for NLPF spectra – as long as all EET rates are significantly higher than γ_{fd}. Accordingly, NLPF line shapes are identical for EET either between two $S_1(1)$-states and subsequent relaxation to $S_1(0)$ or between two $S_1(0)$-

---

[*] The spectral overlap between $S_1(1)$-transitions is quite large because of their considerable bandwidth.

states after initial vibrational relaxation. The same time, $S_1(0) \rightarrow S_1(1)$ back-transfer is nearly impossible because of the large energy gap. Finally, an overall EET scheme for seven (0,0)-transition bands and corresponding (0,1)-transitions can be sufficiently approximated by the values in red in Table 3.1.8. All other rates in the lower right sub-matrix are identical to the values used for Fig. 3.1.12 (left panel) and enable thus comparison with these spectra.

Table 3.1.8 EET rates $\gamma_{\mu\nu}$ [ps^{-1}] used to simulate NLPF spectra in Fig. 3.1.12 (donor transitions: left column, acceptor transitions: top row, λ_c in nm). Values in red indicate vibrational relaxation within the first-excited electronic states. The lower-right sub-matrix is identical to the EET scheme from Table 3.1.6 as used for the simulations in Fig. 3.1.12 (left panel).

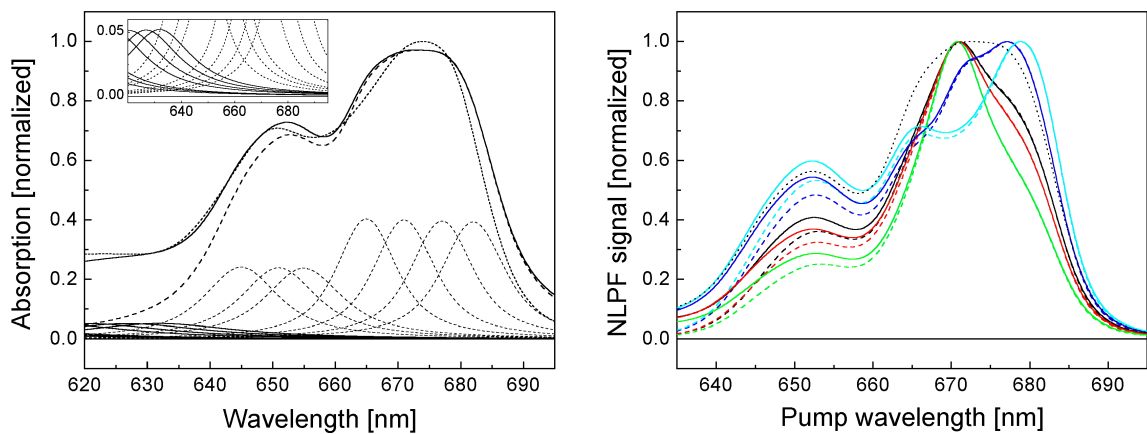| λ_c	595	601	605	615	621	627	632	645	651	655	665	671	677	682
595	x	0	0	0	0	0	0	1	0	0	0	0	0	0
601	0	x	0	0	0	0	0	0	1	0	0	0	0	0
605	0	0	x	0	0	0	0	0	0	1	0	0	0	0
615	0	0	0	x	0	0	0	0	0	0	1	0	0	0
621	0	0	0	0	x	0	0	0	0	0	0	1	0	0
627	0	0	0	0	0	x	0	0	0	0	0	0	1	0
632	0	0	0	0	0	0	x	0	0	0	0	0	0	1
645	0	0	0	0	0	0	0	x	1	0.3	0	0.2	5	3
651	0	0	0	0	0	0	0	0	x	0.5	2	10	0.1	0.1
655	0	0	0	0	0	0	0	0	0	x	0	0	2	0.5
665	0	0	0	0	0	0	0	0	0	0	x	0.03	0	2
671	0	0	0	0	0	0	0	0	0	0	0	x	0	0
677	0	0	0	0	0	0	0	0	0	0	0	0	x	0.7
682	0	0	0	0	0	0	0	0	0	0	0	0	0.5	x

Figure 3.1.14 Left panel: Absorption sub-structure considering seven (0,0)-transitions (thin dashed lines) with parameters from Table 3.1.4 (p. 45) and seven (0,1)-transitions (thin solid lines) from Table 3.1.7. Thick lines indicate the resulting total absorption (dashed: superposition of (0,0)-transitions; solid: superposition of (0,0)- *and* (0,1)-transitions). An original LHCII absorption spectrum is further added (dotted line), while the inset shows (0,1)-bands in higher magnification. **Right panel:** Solid lines illustrate NLPF spectra of the absorption sub-structure from the left panel considering an EET scheme according to Table 3.1.8. For comparison, dashed lines show NLPF spectra from Fig. 3.1.12 (left panel), which considered only seven (0,0)-bands and an EET scheme according to Table 3.1.6 (p. 52) with a trapping state at the 671 nm transition. λ_t = 645 nm (black), 655 nm (red), 665 nm (green), 675 nm (blue), and 685 nm (cyan). The dotted line is the squared absorption spectrum of *all* sub-bands from the left panel.

Extension of the (0,0)-substructure model in Table 3.1.4 (p. 45) with seven (0,1)-transitions from Table 3.1.7 is illustrated in Fig. 3.1.14 (left panel) by the resulting absorption spectra. Although higher vibrational bands have only ~15% amplitude in comparison to (0,0)-transitions, their influence in the blue part of the Q_y-region is noticeably. In particular, the LHCII absorption is much better reflected in the range between 620 and 650 nm. On the other hand, NLPF spectra of this model in Fig. 3.1.14 (right panel) show only slightly increased amplitudes. This behavior reflects again the dependence of NLPF line shapes on *squared* absorption coefficients (cp. Eq. 23 and 6 in Section 2.2.3). One can finally conclude that higher vibrational transitions are necessary to establish an adequate model for LHCII absorption spectra, but their influence on NLPF spectra is only moderate.

The low impact of (0,1)-transitions on NLPF spectra makes their influence for evaluating measured spectra rather insignificant. For that reason, higher vibrational bands are approximated in the following by superposition to *one* band as indicated in Fig. 3.1.15 (left panel).
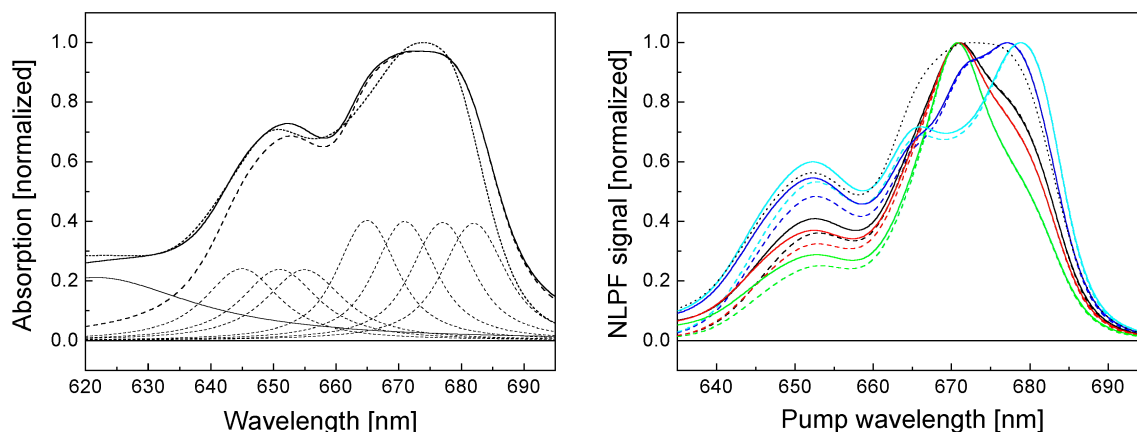

Figure 3.1.15 Left panel: Absorption sub-structure considering seven (0,0)-transitions (thin dashed lines) with parameters from Table 3.1.4 (p. 45) and *one* additional band (thin solid line) summarizing the seven (0,1)-transitions from Table 3.1.7. The additional band is approximated by the following parameters: λ_c = 622 nm, α = 2.1, and 2Γ = 980 cm^{-1}. Thick lines indicate the resulting absorption spectra (dashed: superposition of (0,0)-transitions; solid: superposition of seven (0,0)-transitions *and* the additional band). An original LHCII absorption spectrum is further added (dotted line). **Right panel:** Solid lines illustrate NLPF spectra of the absorption sub-structure from the left panel considering an EET scheme according to Table 3.1.6 with additional transfer rates (1 ps^{-1}) from the 622 nm band to *each* $S_1(0)$-state. For comparison, dashed lines show NLPF spectra from Fig. 3.1.12 (left panel), which considered only seven (0,0)-bands and an EET scheme according to Table 3.1.6 (p. 52) with a trap state at the 671 nm transition. λ_t = 645 nm (black), 655 nm (red), 665 nm (green), 675 nm (blue), and 685 nm (cyan). The dotted line corresponds to the squared absorption spectrum of *all* sub-bands from the left panel.

All (0,1)-transitions from Table 3.1.7 are summarized in Fig. 3.1.15 to one (virtual) transition, which enables a correct description of the short-wavelength part in the absorption spectrum. Accordingly, the combined absorption spectrum looks similar to the profile in Fig. 3.1.14 (left panel). The proper representation of this band in NLPF spectra requires an adaptation of the EET scheme in Table 3.1.8. This is achieved by introducing fixed EET rates (= 1 ps^{-1}) from this single band to *each* of the seven (0,0)-transitions. Resulting NLPF spectra (see Fig. 3.1.15, right panel) show a highly similar shape when compared to simulations with seven separate (0,1)-bands (Fig. 3.1.14, right

panel). In other words, the effect of higher vibrational transitions on NLPF spectra can be efficiently included by superposition into one band and corresponding EET rates to all $S_1(0)$-states.

3.1.5   The effect of Chl orientation on NLPF spectra

In Section 1.2.1, the orientations of Chl transition dipoles in LHCII are discussed with respect to the available structure data as summarized in Table 1.2.1 (p. 9). The satisfactory identification of their exact geometrical arrangement is a matter of continuing debate in the recent literature [14, 40, 72]. NLPF measurements are expected to be highly sensitive on these individual dipole directions, since the signal results from two interacting light beams with well-defined field orientations (cp. Fig. 2.2.2, p. 29). Indeed, the individual Chl orientations are reflected in the mathematical description of NLPF line-shape functions according to Eq. 22 and 23 (p. 37). Hence, the NLPF method might provide an adequate tool to determine transition-dipole orientations in multi-level systems like LHCII. Particularly, it should enable a distinction between the two possible (perpendicular) orientations of Chl dipoles summarized in Table 1.2.1 (p. 9).

In the simulations above, parallel dipole orientations were assumed for *all* transitions. The resulting NLPF spectra are now compared to simulations for certain dipole orientations, i.e. randomly distributed directions of the dipoles assigned to each absorption band. Figure 3.1.16 (left panel) illustrates spectra of the sub-structure model from Table 3.1.4 (p. 45) under additional consideration of dipole orientations according to Table 3.1.9. Interestingly, comparison of this graph to Fig. 3.1.6 (right panel, p. 46) reveals identical spectra in both cases of either parallel or random dipole orientations. This behavior can be directly explained by analyzing Eq. 23 (p. 37). If EET or excitonic coupling are not considered in the parameter model, non-vanishing matrix elements of the correlation factor β_{nm} exist only for $n = m$. However, the geometry factors g_{nm} has a constant value '1' in these cases – independently from actual dipole orientations. In other words, the geometrical arrangement has no effect on NLPF spectra, as long as different transitions are not correlated by EET or excitonic coupling via the β-matrix. A similar effect can be obtained from Eq. 23, if two transitions enclose the 'magic angle' of 54°. Since g_{nm} vanishes in this case, the corresponding correlation factor β_{nm} is not reflected in the NLPF spectrum (cp. again Eq. 23, p. 37). Accordingly, the spectra in left panel of Fig. 3.1.16 would also reproduce the case of excitonic coupling between any Chls, as long as each pair of transition dipoles encloses the 'magic angle'.

The simulation in Fig. 3.1.16 (right panel) is based on a model with randomly distributed transition-dipole orientations and three excitonically coupled dimers. Comparison with the left panel of Fig. 3.1.9 (p. 48) clarifies the orientation effect on NLPF spectra, since *parallel* orientation for *all* transition dipoles was assumed in that graph. The effect is most obvious in the spectral region between 660 and 680 nm for $\lambda_t = 645$ or 655 nm and can be briefly explained as follows. Since two transitions share the same ground state in the case of dimeric coupling, ground-state depopulation induced at

one transition can be also probed via the second transition. The probability for probing one of these two transitions depends on their dipole orientation with respect to the probe field. Accordingly, this probability can be reduced for the second transition in dependence on actual geometrical arrangements of both dipoles. In other words, the effect of excitonic coupling on NLPF spectra varies with the geometry factor g_{nm}, if the dipole orientations of excitonic transitions are non-parallel.

Table 3.1.9 Transition-dipole orientations (spatial angles θ and φ) used for simulations of NLPF spectra in Fig. 3.1.16, 3.1.17, and 3.1.18. The top row indicates the corresponding transition bands.

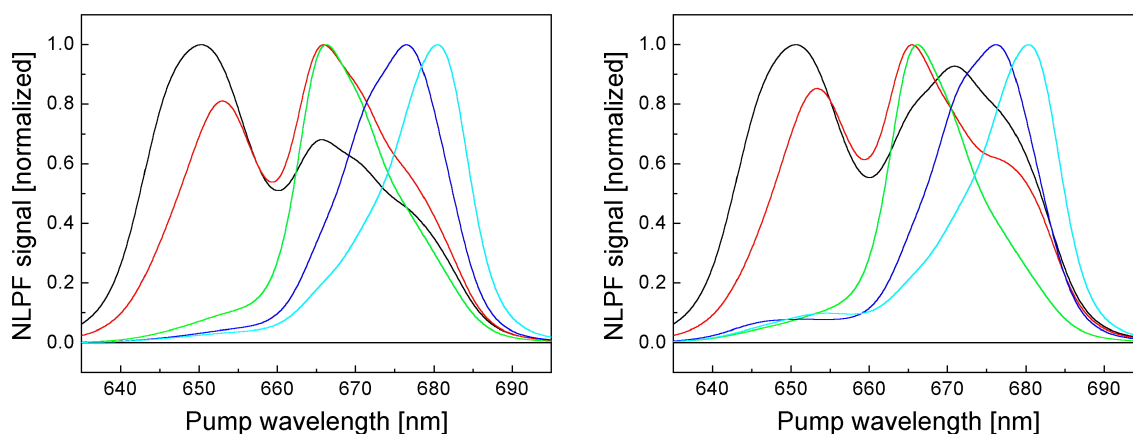| λ_c [nm]	645	651	655	665	671	677	682
θ	70°	45°	10°	0°	75°	20°	40°
φ	35°	65°	50°	90°	15°	0°	10°

Figure 3.1.16 Simulated NLPF spectra of a heterogeneous absorption system with seven bands as described in Table 3.1.4 (p. 45) considering dipole orientations of the transition dipoles according to Table 3.1.9. λ_t = 645 nm (black), 655 nm (red), 665 nm (green), 675 nm (blue), and 685 nm (cyan). **Left panel:** No excitonic coupling or EET among the excited states. **Right panel:** No EET among the excited states, but formation of three dimeric units with transitions at 645/671 nm, 651/677 nm and 655/682 nm.

This feature is further clarified in Fig. 3.1.17 (left panel) by simulating the same exciton model from Fig. 3.1.16 (right panel) with different dipole orientations according to Table 3.1.10. Again, deviations are most apparent in the region between 660 and 680 nm for λ_t = 645 or 655 nm. Additionally, dashed lines in the left panel of Fig. 3.1.17 show NLPF spectra for a model with the same dipole orientations from Table 3.1.10, but different excitonic interactions. These curves clearly deviate from the solid-line spectra because of their distinct underlying coupling scheme. Consequently, it can be stated that combinations of excitonic coupling and individual dipole orientations are significantly reflected in NLPF spectra.

Combined effects of EET and dipole orientations on NLPF spectra are further illustrated in Fig. 3.1.17 (right panel). The employed parameters correspond to dipole orientations in Table 3.1.9 and the EET scheme from Table 3.1.6 (fast relaxation to the two lowest transitions and one trapping state with λ_c = 671 nm). A comparison of NLPF spectra for this EET scheme with the same EET model under the assumption of *parallel* dipole orientations (left panel in Fig. 3.1.12, p. 52) reveals a major decrease in the short-

wavelength region. These reduced contributions between 640 and 660 nm occur because excitations of donor states can only probed via the acceptor(s) (see above). If the acceptor(s) dipole orientation(s) are different, not all of the initially induced excitations are detected by the probe field. 'Magic angle'-orientation between a donor/acceptor pair would thus suppress the donor contribution to NLPF spectra *completely*. Accordingly, it has to be stated that combinations of effective EET rates with rather random dipole orientations might reduce the information yield in NLPF spectra. In particular, Chl *b* molecules connected by fast EET to the Chl *a* region can be much weaker reflected. Furthermore, actual EET rates are barely distinguishable as long as they are considerably higher than γ_{fd}. For that reason, the determination of EET rates by NLPF measurements was *not* attempted in the framework of this thesis. On the contrary, EET rates were included in the evaluation of measured spectra (see Chapter 3.5) by calculating their values based on the actually employed structural model.

Table 3.1.10 Dipole orientations (spatial angles θ and φ) of the transition dipoles used for simulated NLPF spectra in the **left** panel of Fig. 3.1.17. The top row indicates the corresponding transition bands.

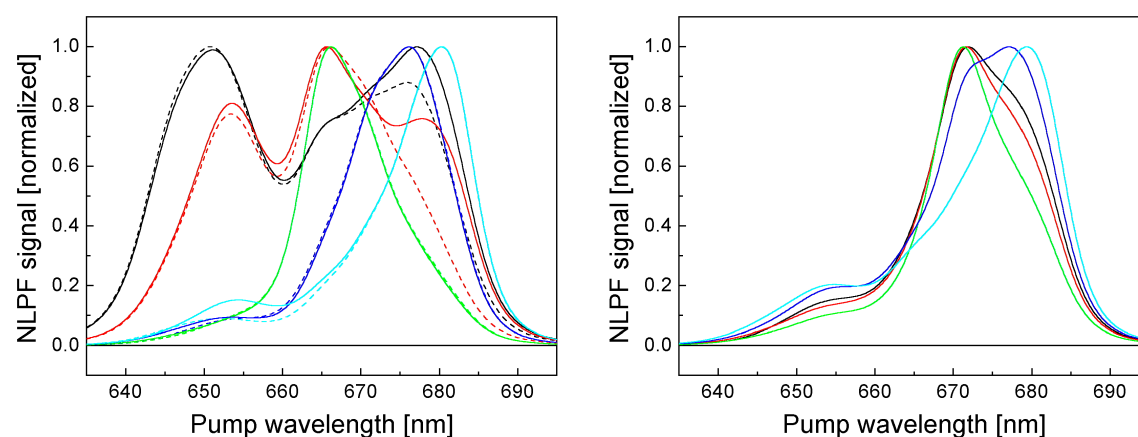| λ_c [nm]	645	651	655	665	671	677	682
θ	40°	10°	45°	130°	0°	165°	40°
φ	20°	110°	90°	25°	75°	50°	80°

Figure 3.1.17 Simulated NLPF spectra of a heterogeneous band structure with seven sub-bands as described in Table 3.1.4 (p. 45) for different dipole orientations. λ_t = 645 nm (black), 655 nm (red), 665 nm (green), 675 nm (blue), and 685 nm (cyan). **Left panel:** No EET among the excited states, but formation of three dimeric units with transitions at 645/671 nm, 651/677 nm and 655/682 nm (solid lines) as well as 645/682 nm, 651/677 nm and 655/671 nm (dashed lines). Transition-dipole orientations are assumed according to Table 3.1.10. **Right panel:** No excitonic coupling, but EET rates according to Table 3.1.6 (p. 52, values in red and green assumed 0). Transition-dipole orientations were simulated according to Table 3.1.9.

The last simulations in this section are intended to visualize combined effects of *all* parameters introduced above on NLPF spectra. In Fig. 3.1.18 (left panel), the seven absorption bands from Table 3.1.4 (p. 45) are combined with the EET scheme from Table 3.1.6 (p. 52), dipole orientations from Table 3.1.9 (p. 58) and excitonic coupling of three heterodimers (transitions at 645/671 nm, 651/677 nm and 655/682 nm). Comparison with both panels in Fig. 3.1.17 reveals that the combination of EET rates

and random dipole orientations primarily determines the shape of NLPF spectra. Nevertheless, excitonic coupling within the dimeric units is also reflected in the spectral shape, although these features are less obvious (compare especially the spectrum for $\lambda_t = 655$ nm around 680 nm in left panel of Fig. 3.1.18 and right panel of 3.1.17). Finally, one can state that NLPF spectra are indeed sensitive to combined effects of EET, dipole orientations and excitonic coupling even in intricate multi-level absorption systems. Thus, the evaluation of measured spectra will in principle allow the determination of corresponding parameters as further discussed in the summary of this chapter.

Last but not least, the simulation in Fig. 3.1.18 (right panel) illustrates the effect of additional (0,1)-transitions in the case of a combined parameter model. Slightly higher contributions to the NLPF signal resulting from higher vibrational bands can be observed in the region between 640 and 660 nm when compared to the left panel. Moreover, the spectra simulated with the full model of seven (0,1)-bands (dashed lines) are nearly identical to the reduced model with one combined (0,1)-band (solid lines). Hence, the superposition of higher vibrational transition to one band can be seen as a satisfactory approximation for the evaluation of measured NLPF spectra in this work. In this way, the blue edge of absorption spectra can be described correctly, while the efficiency of NLPF simulations is increased by the reduced band number.
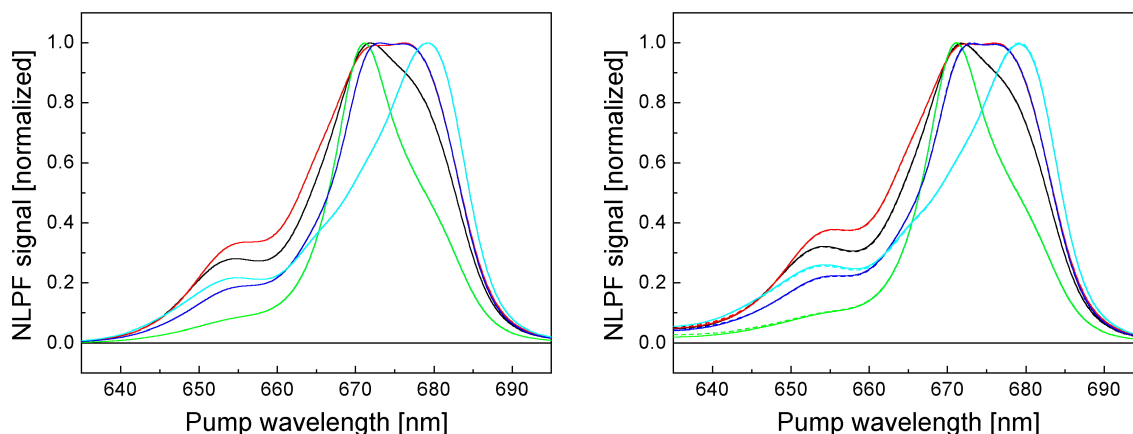

Figure 3.1.18 Simulated NLPF spectra of a heterogeneous absorption system with seven sub-bands as described in Table 3.1.4 (p. 45). The underlying EET scheme was assumed according to Table 3.1.6 (p. 52; red and green values 0). The employed dipole orientations are shown in Table 3.1.9 (p. 58) and three heterodimers with transitions at 645/671 nm, 651/677 nm and 655/682 nm were supposed. **Left panel:** Spectra simulated for seven (0,0)-bands without higher vibrational transitions. **Right panel:** Dashed lines: Spectra simulated for seven (0,0)- and seven (0,1)-transitions (Table 3.1.7, p. 54) connected by EET rates shown in Table 3.1.8 (p. 55). (0,1)-transitions were assumed parallel to the respective (0,0)-transition. Solid lines: Seven (0,0)- and *one* virtual transition summarizing all seven (0,1)-bands. (Solid and dashed lines are almost identical.)

3.1.6 Summary

In this chapter, several physical parameters describing basic properties of Chls in LHCII and related antenna complexes were investigated with respect to their effect on NLPF signals. The obtained features are briefly summarized in the following and discussed with respect to the ability of evaluating *measured* NLPF spectra. For that purpose, the parameters are again distinguished in 5 groups: 1) (0,0)-band parameters (λ_c, α, 2Γ, and Δ); 2) (0,1)-band parameters (λ_c, α, 2Γ); 3) Excitonic coupling terms; 4) EET rates ($\gamma_{\mu\nu}$); 5) Transition-dipole orientations (θ and φ).

Apparently, the first two classes essentially determine the absorption spectrum and they are accordingly reflected in NLPF spectra. Nevertheless, comparison of simulations in Fig. 3.1.6 (right panel) with spectra in Fig. 3.1.18 reveals that the markedness of these parameters might be strongly superimposed by other effects. In particular, the Chl *b* region and (0,1)-bands are much weaker pronounced in NLPF spectra, if EET and random dipole orientations are included in the model. Hence, the NLPF method turned out to be less suited to study the absorption sub-structure of LHCII than initially expected.[*] The *simultaneous* determination of absorption and interaction parameters by solely evaluating NLPF spectra would thus become a highly ambiguous attempt. Nevertheless, this conundrum can be overcome by studying the absorption sub-structure *in advance* to NLPF simulations as described Chapter 3.2. Accordingly, the dependence of NLPF spectra on the remaining three groups of interaction parameters is depicted in the following under the assumption of a previously established sub-structure model.

In Fig. 3.1.19, the NLPF spectra of graph **A** are simulated for the seven-band model of Table 3.1.4 (p. 45) considering random dipole orientations from Table 3.1.9 (p. 58). Interestingly, these spectra are strikingly similar to simulations for parallel dipole orientations, since the dipole directions do not affect NLPF signals in the absence of other interactions (cp. Fig. 3.1.6, right panel, p. 46). Graph **B** illustrates EET effects on NLPF spectra, which commonly result in reduced λ_t-selectivity and suppressed contributions of the short-wavelength bands (EET scheme according to Table 3.1.6, p. 52). The effect of excitonic interaction (graph **C**) is primarily simulated for coupling in excitonic sub-units like Chl *a*/*b* heterodimers. Apparently, the coupling is hardly resolvable for longer λ_t like 675 and 685 nm, but evident for shorter λ_t as 645 and 655 nm.

The combined effect of random dipole orientations and EET (graph **D**) indicates a further reduction of the Chl *b* contribution in NLPF spectra. For certain orientations (i.e., the 'magic angle'), those transition bands that are connected by fast 'downhill' EET to other excited states can even vanish completely. Besides this, the combination of dipole orientations and excitonic coupling in graph **E** causes moderate, but still resolvable deviations in NLPF spectra. The combined effect of EET and excitonic coupling in

---

[*] A different picture must be drawn for low temperature applications of the method, which could indeed reveal basic spectral features in Section 3.5.3.

graph **F** results also in clearly different spectra. Finally, the combination of all three parameter sets results in the NLPF spectra in graph **G**. Obviously, the effects of EET, dipole orientations and excitonic coupling show all a significant impact on the spectral shape even in this case.
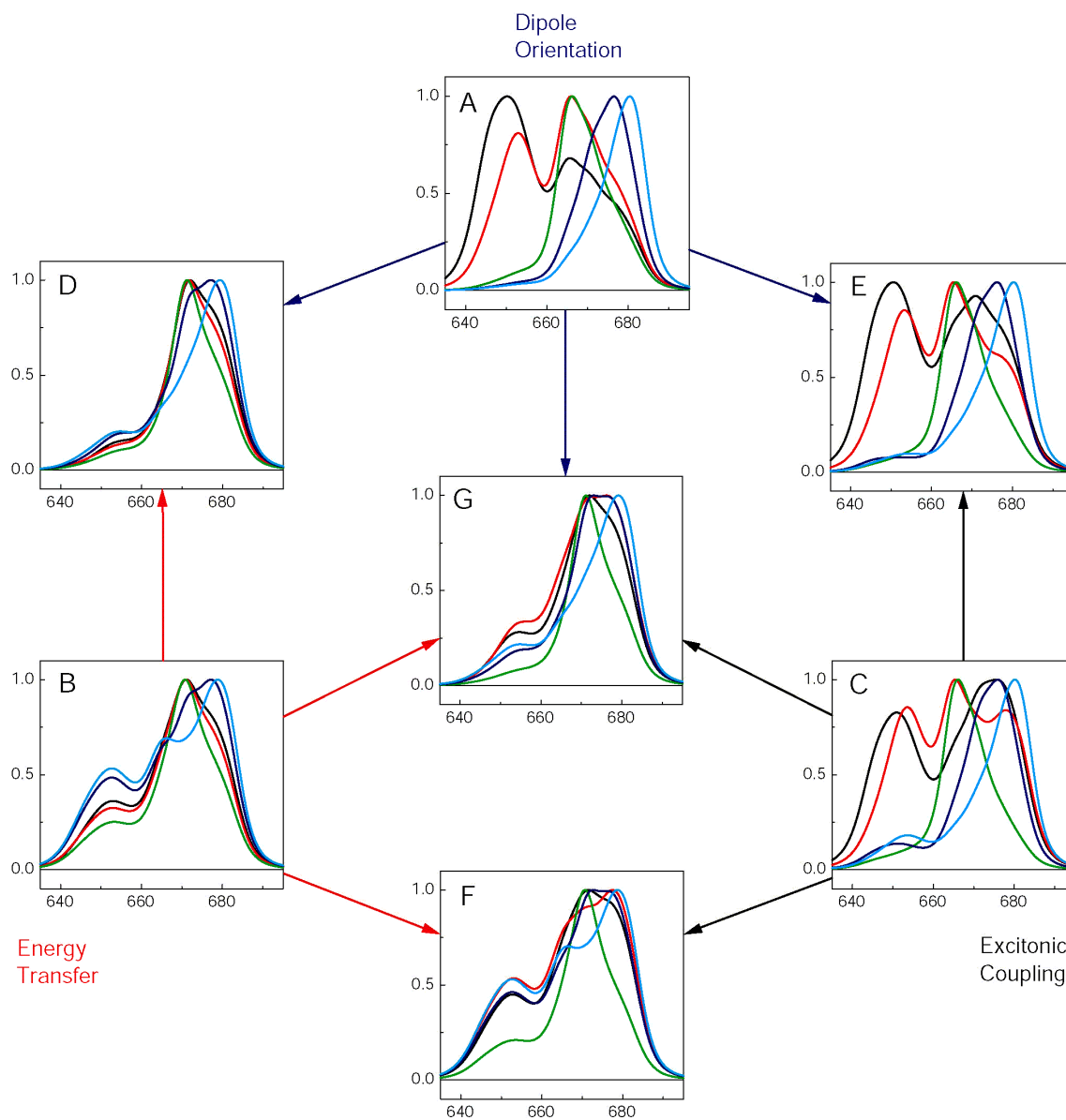

Figure 3.1.19 Summarizing overview of NLPF spectra simulated in this chapter based on the seven-band model in Table 3.1.4 (p. 45) by considering the effects of following parameters: *i*) Random dipole orientations (according to Table 3.1.9, p. 58). *ii*) Randomly distributed EET rates (Table 3.1.6, p. 52). *iii*) Excitonic coupling in three heterodimers with transitions at $\lambda_c = 645/671$ nm, 651/677 nm, and 655/682 nm. (**A**) Only dipole orientations; (**B**) Only EET rates; (**C**) Only excitonic coupling; (**D**) Dipole orientations and EET; (**E**) Dipole orientation and excitonic coupling; (**F**) EET and excitonic coupling; (**G**) Excitonic coupling, dipole orientations, and EET. Graph (**A**) is further identical to NLPF spectra of the sub-structure model without any other additional parameters.

From comparison of Fig. 3.1.19 with the experimental results in Fig. 3.1.1 (p. 41) one can obtain, that *measured* spectra of LHCII show a high similarity to simulations in graph **D**. This observation gives a strong hint that EET and dipole orientations basically determine these spectra. Thus, excitonic coupling among Chls does either not exist in LHCII or it is suppressed in the NLPF spectra due to specific cases of transition-

probability redistribution or dipole orientations. To resolve this question, the manifestation and extent of excitonic coupling is supplementary studied in Chapters 3.3 and 3.4 by using other nonlinear spectroscopic techniques. The combination of results obtained there with the sub-structure model established in Chapter 3.2 forms a sufficient starting point for the evaluation of NLPF measurements in Chapter 3.5. The required significance for parameter determinations was finally obtained by fixing the EET rates to values calculated according to Eq. 1 (p. 17) on the basis of available structural data.

3.2 Obtaining additional information, Part I: Substructure analysis using LHCII mutants with selectively removed Chl-binding sites

This chapter addresses the origin of Chls spectral heterogeneity in LHCII causing the intricate absorption sub-structure within the Q_y-band. The most common assumption is that spectral heterogeneity results from slightly different environments of each Chl within the protein matrix. In fact, most of the Chls are in close distance to certain amino-acid side chains, which form Chl-binding sites by providing ligands for Mg^{++}-binding. In this context, theoretical calculations revealed considerable differences in the Q_y-transition energy of attached Chls in dependence on the side-chain type [32]. Besides this, several studies investigating the extent of spectral heterogeneity in LHCII revealed up to eleven sub-bands by using different experimental approaches [53, 56, 71, 137, 138]. Nevertheless, no commonly accepted sub-structure model could be established by application of these techniques. Fortunately, LHCII is one of the very few membrane proteins that can be refolded *in vitro* from its components [139, 140]. On this basis, a general assignment of LHC absorption regions attributed to Chl *a* or Chl *b* could be recently presented [141]. Direct correlation of Chls at individual binding sites with distinct spectral sub-bands by studying recombinant LHCII mutants with selectively modified binding sites has also been attempted [37, 38]. The latter work resulted in a sub-structure model as shown in Table 3.2.1, which assumes mixed occupation at certain binding sites with both Chl *a* and Chl *b* (promiscuity).

Table 3.2.1 Occupation of Chl binding sites and corresponding $Q_y(0,0)$-bands according to Remelli et al. [38]. Binding sites are named by using the nomenclature of Kühlbrandt et al. [6].

	a1	a2	a3	a4	a5	a6	a7	b1	b2	b3	b5	b6
Chl *a*	100	100	50	100	100	50	0	100	0	50	0	0
Chl *b*	0	0	50	0	0	50	100	0	100	50	100	100
λ_c (Chl *a*)	679	681	662.5	674	674	678.5	-	679.5	-	665	-	-
λ_c (Chl *b*)	-	-	650	-	-	652	652	-	644	650	652	652

A comparison of simulations based on the parameter set of Remelli et al. [38] with measured LHCII absorption spectra in Fig. 3.2.1 clearly indicates the incompleteness of this model. Discrepancies are apparent under the assumption of 12 nm bandwidth as well as for 16 nm, while the first number represents the most favored value in the recent literature [40, 55]. Due to noticeable deviations in Fig. 3.2.1, the sub-structure from Table 3.2.1 turned out to be unacceptable for evaluating NLPF spectra in this thesis. In particular, the observed error would be further increased in NLPF spectra because of the quadratic dependence of NLPF signals on the absorption parameters (cp. Section 2.2.3).

Certainly, several sub-structure models suggested by other authors [53, 55, 56] fit better to the measured absorption spectra, but these models are not based on the full information that is available today. On the other hand, the experimental approach of studying mutant LHCII samples with selectively modified binding-sites is indeed highly promising for understanding the heterogeneity in LHCII. Those Chls, which originally

occupy the altered binding sites in native proteins, can be expected to be absent in the mutant complex (see below). Accordingly, the corresponding band must vanish in the absorption spectrum.
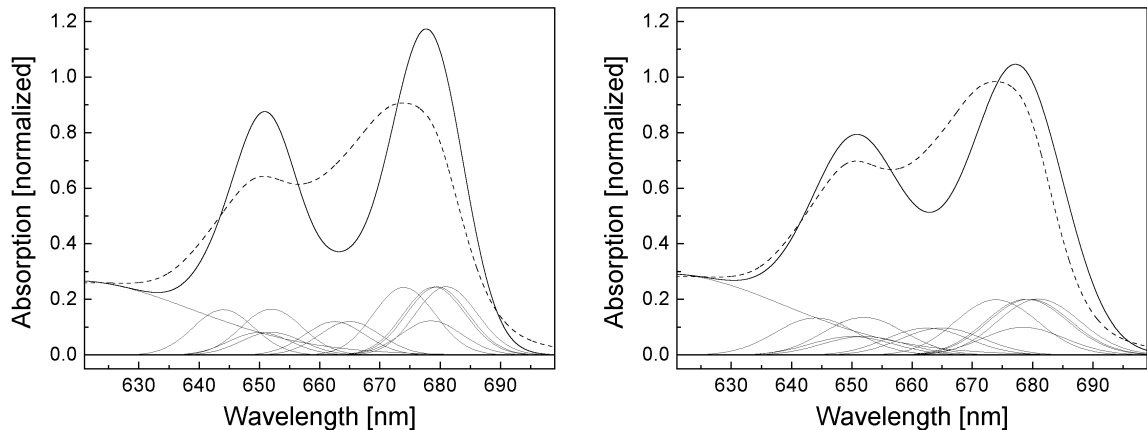

Figure 3.2.1 Simulation of the Q_y-absorption region (solid lines) according to the sub-structure model of Remelli et al. [38] (thin lines, see Table 3.2.1). Measured absorption spectra of LHCII are added (dashed lines). The bands were simulated by Gaussians with 12 nm (**left panel**) and 16 nm (**right panel**) FWHM and following α-parameters: 100 % Chl *a*: α = 1; 100 % Chl *b*: α = 0.7; 50 % Chl *a*: α = 0.5; 50 % Chl *b*: α = 0.35. (Please note that sub-bands with identical parameters are superposed in the illustration.)

In this context, the origin of deviations between the sub-band model above and measured absorption spectra becomes especially interesting. One reason for possible misinterpretation is exemplified in Fig. 3.2.2 by using the seven-band model from Table 3.1.4 (p. 45). In the left panel, the loss of one transition band for mutant samples with one modified binding site is simulated. However, the simultaneous spectral shift of a further band (5 nm blue-shift of the band absorbing at $\lambda_c = 682$ nm) in the right panel changes the difference spectrum completely.
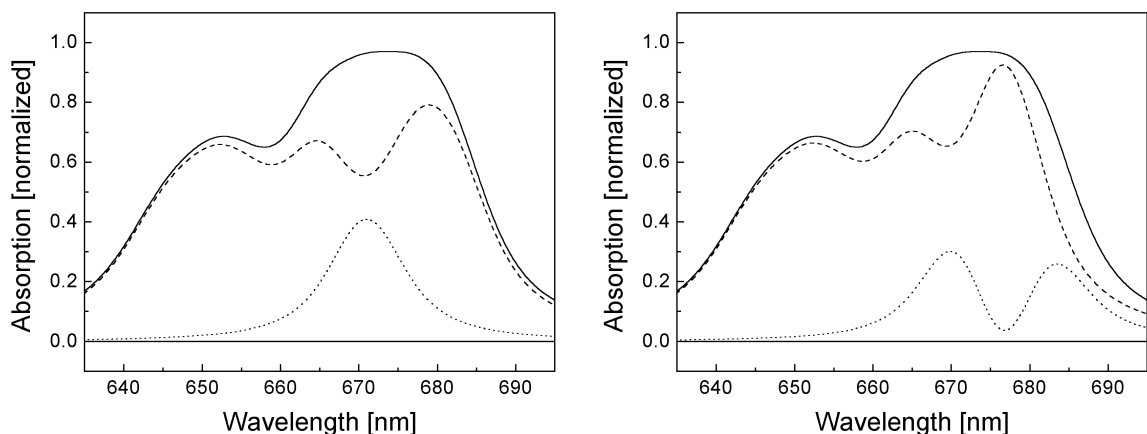

Figure 3.2.2 Illustration of possible artifacts in analyses of the Q_y-band sub-structure by using mutant LHCII. The solid line shows the total absorption of the seven-band model from Table 3.1.4 (page 45). In the **left** panel, the dashed line indicates the total absorption of the same model, but with one band ($\lambda_c = 671$ nm) removed. In the **right** panel, the same band was removed, but the band with $\lambda_c = 682$ nm was additionally shifted to 677 nm. From the two difference spectra (dotted lines) one can conclude that the additional shift causes an impression of *two* missing bands.

The probability of such accompanying shifts in samples with removed Chls is not unlikely. Each lack of the (rather large) Chl molecules at their original location can induce instabilities in the whole protein frame, thus leading to at least slight structural changes. These changes can cause spectral shifts also for other, not necessarily neighboring pigment molecules. Hence, the proper interpretation of results from mutation analyses can be rather complicated, especially for samples lacking more than the one Chl from the modified binding site. Consequently, the studies presented in this chapter were aimed to a straightforward interpretation of investigations of mutant LHCII. The main focus was set on advantageous features of absorption spectra at low temperature and a restriction to the most reliable mutants. The results have been partly published in [142][*].

3.2.1 Absorption spectra at low temperature

Recently, the refolding of LHCII into native-like trimers has been achieved by a simple one-step procedure [143]. This procedure was later used to generate specifically modified recombinant species of LHCII with individual Chl binding sites removed by site directed mutagenesis [37]. A selection of the mutants described there (i.e., the species with modified binding sites **b3**, **b6**, **a2** and **a5** according to the nomenclature in [6]) was employed together with reconstituted WT and isolated, native LHCII for LT and RT absorption studies. The reconstituted samples were provided and analyzed by H. Rogl (MPI Frankfurt) following the procedures in [37]. Native LHCII was purified from pea similarly to the description above in Chapter 1.1. For low temperature absorption measurements, glycerol was added to the samples yielding a final concentration of 67 % (v/v) and the samples were cooled to 4 K in about 30 min. A slow cooling rate was used at ~120 K to avoid cracking of the sample. 4 K absorption spectra of trimeric LHCII were recorded in close collaboration with Drs. R. Schödel, H. Lokstein (HU Berlin) and H. Rogl (MPI Frankfurt) on a Shimadzu UV-2101PC photometer equipped with a liquid-helium cooled Oxford cryostat. Glass cuvettes with a light path of 1 mm were used and spectra were recorded with a resolution of 0.5 nm at a bandwidth of 2 nm. For mutant **a5** the band corresponding to the monomeric LHCII was taken directly from the sucrose density gradient and glycerol was added to 67 % (v/v). The absorption was measured at 77 K in a plastic cuvette with 10 mm light path placed in a liquid-nitrogen cooled holder in co-operation with W. Rühle (Uni Mainz). WT spectra were normalized to identical Q_y-band areas on the wavenumber scale to ensure conservation of the total transition probability at different temperatures. Mutant samples were scaled to the WT areas using factors reflecting the altered Chl contents (see Table 3.2.2). For the Q_y-transition probability of Chl *a* as compared to Chl *a*, a factor of 0.68 was assumed [50].

---

[*] H. Rogl and A. Schubert contributed in equal parts to this publication as explicitly noted on the front page of the paper.

Absorption spectra of five different recombinant forms of LHCII were recorded at cryogenic temperatures. Four of these were trimers (WT and mutants **b3**, **a2**, **b6**) which were obtained in concentrations suitable for investigation at 4 K. However, refolding of the mutant complex lacking the binding site for Chl **a5** yielded only monomers, which were less stable and could not be concentrated to the required density. Therefore, the monomeric mutant complex **a5** was investigated at 77 K and compared to refolded monomeric WT at the same temperature. The 4 K and 77 K absorption spectra are shown in Fig. 1. The spectra are normalized to represent the amount of attached Chl obtained from pigment analysis (Table 3.2.2). Absorption changes are consistently confined to relatively narrow spectral regions. Difference spectra calculated in relation to the refolded WT complex indicate that one Chl band is lacking in each of the mutant forms. For mutants **a2** and **a5** the missing bands are located in the spectral region characteristic of Chl *a* Q_y-absorption, while mutant **b6** obviously lacks a pigment absorbing in the Chl-*b* region. This is consistent with the results of the pigment analysis by HPLC (see Table 3.2.2).
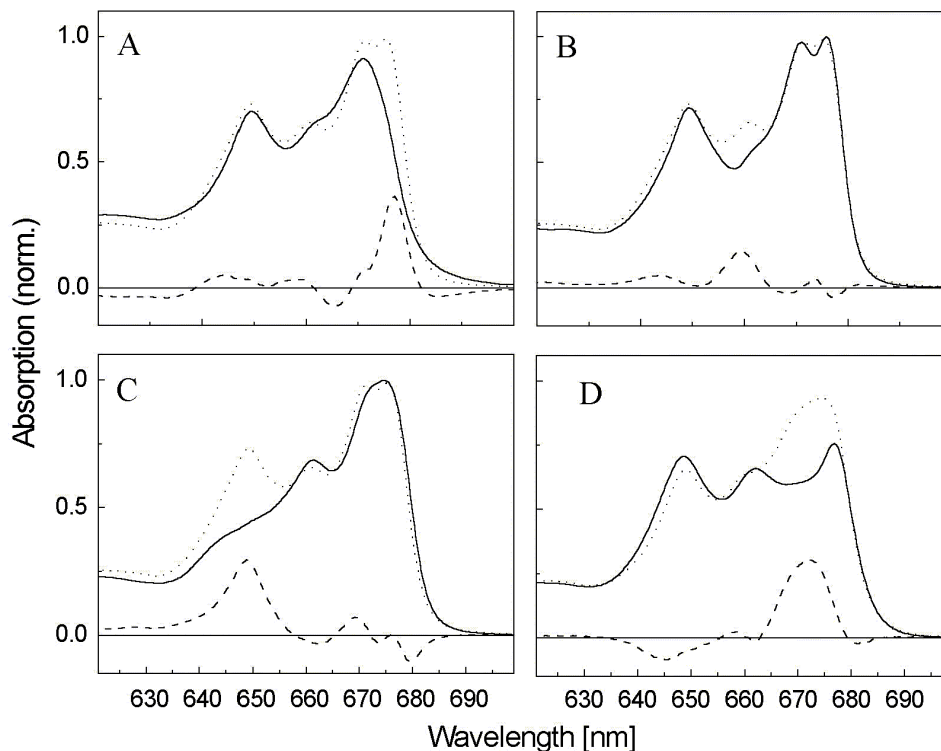

Figure 3.2.3 Absorption spectra at 4 K of LHCII mutants **a2** (A), **b3** (B), **b6** (C) as compared to trimeric WT and monomeric mutant **a5** compared to monomeric WT at 77 K (D). The spectra correspond to WT (dotted line), mutants (solid line), and the difference between WT and mutants (dashed line).

Mutant **b3** obviously lacks the Chl absorbing at $\lambda_c = 659$ nm with a bandwidth of 6.9 nm FWHM (Fig. 3.2.3, **B**), which is roughly half way between the regions characteristic for Chl *a* and Chl *b* [141]. The assignment of this pigment to Chl *a* [37] was deduced from pigment analysis (Table 3.2.2). The obtained λ_c is in agreement with RT spectroscopic data of monomeric complexes with partial occupancy of site **b3** [38].

The absorption difference spectrum between mutant **a2** and WT (Fig. 3.2.3, **A**) is characterized by one missing band centered at 676 nm and 5.2 nm FWHM. Chl **a2**

appears to represent one of the terminal states in the EET pathway of LHCII as suggested previously [37, 38]. A similar conclusion was reached for the homologous monomeric antenna complex CP29 from maize [144]. Since no ultra-fast EET from this spectral region has been observed [14], the FWHM of the transition at 4 K must be determined by environmental effects only. Accordingly, the revealed bandwidth must correspond to pure inhomogeneous broadening of about 5 nm, confirming an earlier estimation obtained by hole-burning spectroscopy [110].

Table 3.2.2 Chlorophyll contents of the native and *in-vitro*-refolded LHCII as obtained by HPLC.

	Mutation site	Chl *a* content	Chl *b* content
Native trimeric LHCII	-	7.0[*]	5.5[*]
Refolded trimeric WT	-	6.9	6.4
Trimeric Mutant **b6**	Q131A	+ 0.3	- 1.9
Trimeric Mutant **b3**	H212A	- 0.6	+ 0.1
Trimeric Mutant **a2**	N183A	- 0.8	+ 0.2
Monomeric refolded WT	-	6.3	6.2
Monomeric refolded Mutant a5	H68A	- 0.8	+ 0.2

* Two lutein molecules per LHCII monomer were assumed as internal standard for Chl quantification.

Mutant **b6** is characterized by decreased absorption predominantly in the Chl *b* region around 650 nm (Fig. 3.2.3, **C**). This observation is in good agreement with previous studies of monomeric LHCII and the homologous protein CP29 [38, 144]. The comparatively large area of the missing band probably reflects a lack of more than one Chl *b* in this complex, as suggested also by the pigment analysis (Table 3.2.2). Since only one binding site was modified in this mutant, the additional loss of Chl *b* must be due to cooperative effects on adjacent Chl binding sites [38]. The main band in the difference spectrum, however, is located at 649 nm with 8.6 nm FWHM.

Mutant **a5** forms only monomers. Different mutations in this particular binding site confirm this finding [39]. Although monomers are generally less robust than trimeric LHCII, mutant **a5** was sufficiently stable for absorption measurements at 77 K. The pigment analysis indicates the lack of about one Chl *a* per monomer when compared to refolded monomeric WT LHCII. The difference spectrum between mutant **a5** and WT at 77 K is characterized by a missing band in the Chl *a* region around 672 nm with 9.8 nm FWHM (Fig. 3.2.3, **D**). It can be assumed that this large bandwidth is not an inherent feature of this binding site but rather results from perturbations of the environment of this Chl in the less stable monomeric complex. It is well known that absorption spectra of LHCII monomers can differ significantly from those of trimers, depending on the preparation method [53]. Therefore, the data obtained of monomeric complexes are omitted from the detailed discussion below. The well-resolved missing bands of all 4 mutant complexes, however, clearly support the following conclusions:

Summarizing the observations above, a 'one site – one sub-band' model is the most suitable approximation for the description of the Q_y-absorption region of LHCII. The

results provide clear evidence that each binding site is predominantly occupied by either Chl *a* or by Chl *b* in all four mutants. Mixed occupancy can be excluded, as it would result in two distinct missing bands in both the Chl *a* and the Chl *b* regions of the absorption difference spectrum. Mixed occupancy of binding site **b3** with 50 % each of Chl *a* and Chl *b* was postulated in the above-mentioned earlier study by Remelli et al. [38]. However, this complex was monomeric and refolded at an elevated Chl *a/b* ratio of 2.3, while the trimers used here were refolded at Chl *a/b* ratio of 1.35 [37] corresponding to the Chl distribution in native LHCII. It is known that some Chl binding sites in LHCII can be forced to accept either Chl *a* or Chl *b* under non-physiological conditions [141]. Hence, the mixed occupancy at binding site **b3** reported in [38] may be due to the significantly higher level of Chl *a* present during refolding, or to the fact that monomers rather than trimers were used.
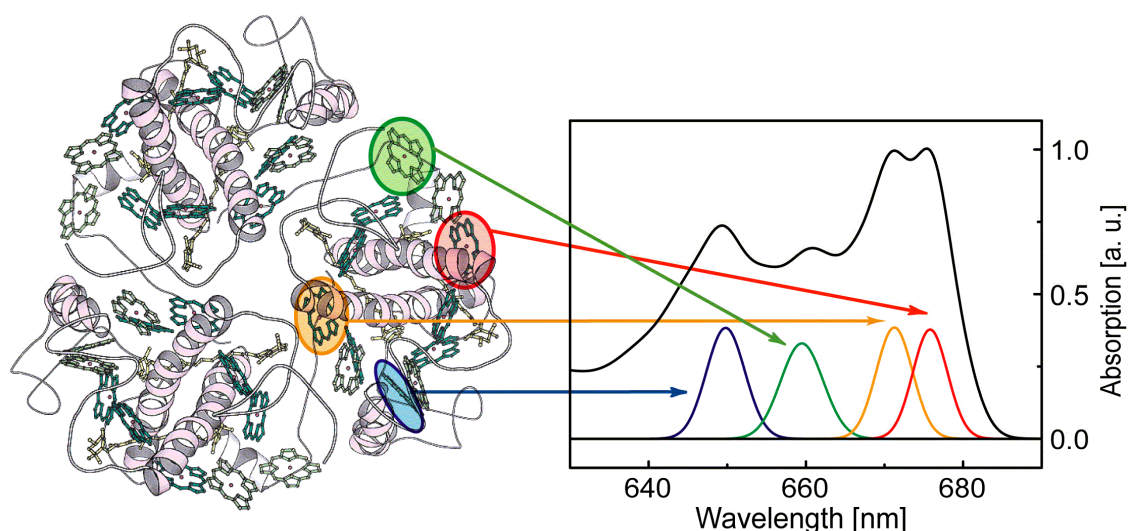

Figure 3.2.4 Assignment of spectral chlorophyll forms to the corresponding binding sites in the 3D structure of LHCII. Chl **b6** – blue, Chl **b3** – green, Chl **a5** – yellow, Chl **a2** – red. The LHCII trimer is viewed from the stromal side.

As all four main spectral bands of LHCII could be assigned to specific Chl binding sites, the following points are implicated relating to the structure and function of LHCII (Fig. 3.2.4). First, the assignment of absorption bands to individual pigments provides a firm base for better understanding of the absorption spectrum of LHCII and its sub-bands. Second, a three-dimensional map of the chromophores with their corresponding spectral features is indispensable for a description of the ETT process. This process must account for the spectral, spatial and temporal evolution of the excitation energy once an LHCII molecule has absorbed a photon.

In the following discussion, a model to describe the high-resolution spectra obtained at 4 K is developed. Several previous attempts to deconvolute the Q_y-absorption region of LHCII into sub-bands have been reported [53, 56]. Auxiliary techniques such as linear or circular dichroism and Stark spectroscopy have been employed by others to identify sub-bands [55, 137]. Some bands were identified by hole-burning studies at cryogenic temperature [110]. Nevertheless, the exact number of transitions necessary to

describe the absorption spectrum of LHCII could not be provided by these investigations. At room temperature, modeling of LHCII absorption has been shown to require at least six separate transitions [56]. At 77 K, eleven forms were found by the techniques summarized in [53]. More recent studies were based on eight to twelve Chl bands [12, 55]. However, no commonly accepted sub-structure model of LHCII has been established so far.

A reasonable choice of the physical absorption-band parameters plays a key role in this regard, since even the simplest approach of Gaussian deconvolution requires at least three parameters per band (λ_c, Δ, α). In this regard, essential information is now provided by this site directed mutation analysis. As pointed out above, one can directly observe at least four unambiguous, nearly Gaussian-shaped sub-bands that can be used as guide points for further sub-band analysis. Moreover, the FWHM of the terminal fluorescent transition at the red edge of the LHCII absorption spectrum is determined to 5.2 nm. The total FWHM represents a convolution of contributions from homogeneous and inhomogeneous broadening. Inhomogeneous broadening results from quasi-static heterogeneity in the environment of pigments occupying homologous binding sites in different LHCII molecules. Homogeneous broadening at 4 K is due to fast energy relaxation processes. Accordingly, the FWHM of the band at 676 nm represents pure inhomogeneous broadening, as it is located at the end of the EET chain where no fast energy relaxation occurs.

From the above considerations one can deduce that inhomogeneous broadening for Chl transitions in LHCII is about 5 nm, since the different pigments have statistically similar environments. However, EET times in the 100 fs range have been measured in other regions of the Q_y-band [12, 14, 112]. The corresponding transitions are therefore additionally broadened by up to 3 nm (see Chapter 1.2.2). As a result one expects sub-bands with a total FWHM of 4 to 9 nm, with the narrowest bands at the red edge of the absorption spectrum. The fact that all three difference bands in trimeric LHCII conform to these values strongly suggests a general limitation of the transition bandwidths to a range between 4 and 9 nm.

Hence, sub-band analysis was performed assuming Gaussian-shaped bands with the restrictions of broadening as outlined above. These restrictions, together with the four sub-bands directly observed at 676, 672, 659, and 649 nm, considerably improved the reliability of our sub-structure analysis. The number of sub-bands was increased stepwise until a satisfactory fit was obtained. This procedure requires *at least* 10 bands (with their respective parameters listed in Table 3.2.3). One additional band was used to take into account contributions from higher vibrational transitions of Chl *a* that overlap with the absorption of Chl *b* in the region below 640 nm (cp. Fig. 3.2.5 and Table 3.2.3). A marginal difference between the measured spectra and the fit can be observed on the red edge of the Q_y-band. It most probably reflects a deviation of the real band shapes from the assumed Gaussian shape. Strikingly, the absorption strengths of the transitions at 671 and 676 nm are 1.5-2 times higher than the others (see Fig. 3.2.5 and Table 3.2.3). This is most likely due to the superposition of two bands with similar λ_c. On the other hand, excitonic interactions between Chls can lead to the formation of absorption bands

with increased transition-dipole strength (see Chapters 3.3 and 3.4). As mentioned above, one cannot distinguish between these two possibilities by the analysis of the absorption spectrum. We note, however, that the double dipole strength in each of these two bands results in a total of 12 transitions, in complete agreement with the 3D structure [6].

Clearly, the same 10-band model holds for refolded WT and for native LHCII. This interpretation implies that the slightly increased Chl *b* content of refolded LHCII (see Table 3.2.2) does not indicate an additional Chl *b* at a specific binding site, as no additional sub-band is observed in the corresponding spectrum. Rather this difference seems to be due to peripherally, non-specifically attached Chl *b* from the refolding process, which is therefore not present in the isolated native LHCII. Another, more significant difference between refolded WT and native LHCII is the different height of the two bands centered at about 671 and 676 nm. In the case of the band centered at 671 nm this can be explained by a 15 % smaller FWHM of the band in native LHCII, since the areas are of the same magnitude for both preparations (see Table 3.2.3). The difference may relate to a slightly higher inhomogeneity of Chl binding sites in refolded LHCII or originate from the different lipid/detergent environment of the two complexes (i.e. specifically bound thylakoid lipids versus synthetic lipids). By contrast, the area of the 676 nm band that is about 20 % larger in native LHCII corresponds to an actual increase in transition probability. The occupancy of this peripheral Chl binding site or its lipid and detergent environment may be responsible for this behavior. Variations in excitonic interaction strengths are another explanation. This decrease in height of the 676 nm band in refolded LHCII had also been observed by others in samples prepared by a different method [145]. Notably, this is the only appreciable difference in the spectral properties between native and refolded LHCII. Good evidence for the integrity of refolded WT complexes is given by 2D crystals, which have the same space group and unit cell dimensions as those from native LHCII, and were indistinguishable at the obtained resolution of 15 Å (cp. [140]).
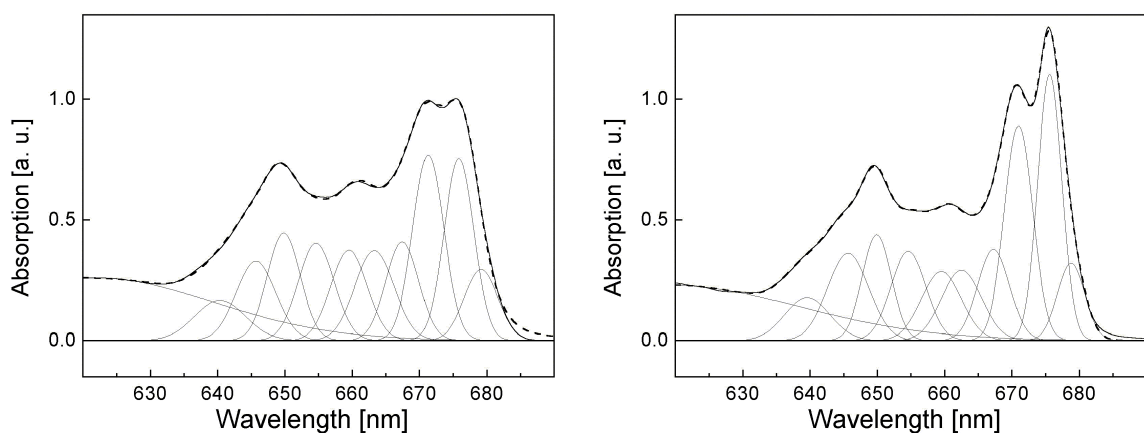

Figure 3.2.5 Fit of the 10-sub-band model from Table 3.2.3 as applied to refolded WT (**left panel**) and native (**right panel**) LHCII at 4 K: Measured spectra (solid line), fitted absorption spectra (dashed line), and resolved sub-bands (thin lines).

In the following the sub-band model of Table 3.2.3 is briefly discussed in the context of earlier studies performed at 4 and 77 K with native LHCII preparations. Data recorded at these two temperatures are comparable, since temperature dependence of the band positions below 100 K is negligible (< 1 nm, see Fig. 3.2.6). There are two significant deviations, which exceed the uncertainty range of 1.5 nm. First, in the vicinity of the resolved transition at 671 nm other studies have suggested two bands (at 671 and 673 nm, see [53]). This may indicate that the intense band at 671 nm in our model indeed represents two different, but strongly overlapping transitions. Second, the band around 659 nm, which is absent in mutant **b3**, has not been observed in previous studies. Most probably this band was not resolved due to the overlap with the transition at 663 nm (cp. Fig. 3.2.5).

Table 3.2.3 Spectral substructure analysis for refolded WT and native LHCII. Ten sub-bands (Gaussian profiles) were identified by λ_c [nm], FWHM Δ [nm] and relative area α. The area values were yielded in arbitrary units from the fitting program by using normalized spectra (Fig. 3.2.5) as input.

	Refolded WT LHCII at 4 K									
λ_c	622.0*	640.0	645.4	649.8	654.6	659.4	663.2	667.6	671.2	675.6	678.8
α	4.88	0.51	1.02	1.05	1.05	0.98	1.06	1.06	1.51	1.60	0.80
Δ	45.6	8.6	7.6	6.0	6.4	6.4	6.4	5.6	5.2	5.2	5.8
	Native LHCII at 4 K									
λ_c	620.0*	639.8	645.6	649.8	654.4	659.4	663.0	667.6	670.8	675.4	678.4
α	3.8	0.70	1.02	0.90	1.01	0.98	0.77	0.97	1.48	2.00	0.73
Δ	39.6	8.6	7.2	5.0	6.4	6.8	6.4	5.2	4.4	4.6	5.8

* This Gaussian band summarizes higher vibrational (0,1)-transitions of Chl *a* interfering with the (0,0)-transitions of Chl *b*. It does not represent any (0,0)-transition of a Chl molecule.

3.2.2 Studying the temperature dependence

Absorption spectra obtained at 4 K are ideal for studying the spectral sub-structure of refolded and native LHCII. However, understanding the light-harvesting function of LHCII under physiological conditions requires information about its absorption properties at RT. In order to provide this information, the temperature dependence of peak positions and FWHM of the resolved bands was examined (Fig. 3.2.6). As expected, all difference spectra are characterized by an increasing FWHM of the main bands with temperature. This can be attributed to enhanced homogeneous broadening due to stronger coupling of the pigments with their protein environment. The band centered at 676 nm broadens to about 11 nm at RT. Assuming temperature-independent inhomogeneous broadening, the homogeneous bandwidth can be deduced as $2\Gamma = 215$ cm^{-1} ($\approx$ 9 nm). An unexpected feature is the significant red shift with increasing temperature of the two bands at 659 and 676 nm by 3.5 and 5 nm, respectively. It has been speculated earlier that a broadening of the red edge of the LHCII spectrum is due to the appearance of new spectral bands during the transition from 10 K to RT [55]. However, Fig. 3.2.6 (**A**) strongly suggests that this behavior

originates from the considerable shift of the spectral sub-bands in this region. By comparison, the Chl-*b* band at 650 nm shifts only by 1 nm, indicating that the temperature dependent shift of different sub-bands is variable. Hence, the extrapolation of spectral features from 4 K to RT turns out to be more complex than anticipated (see below).
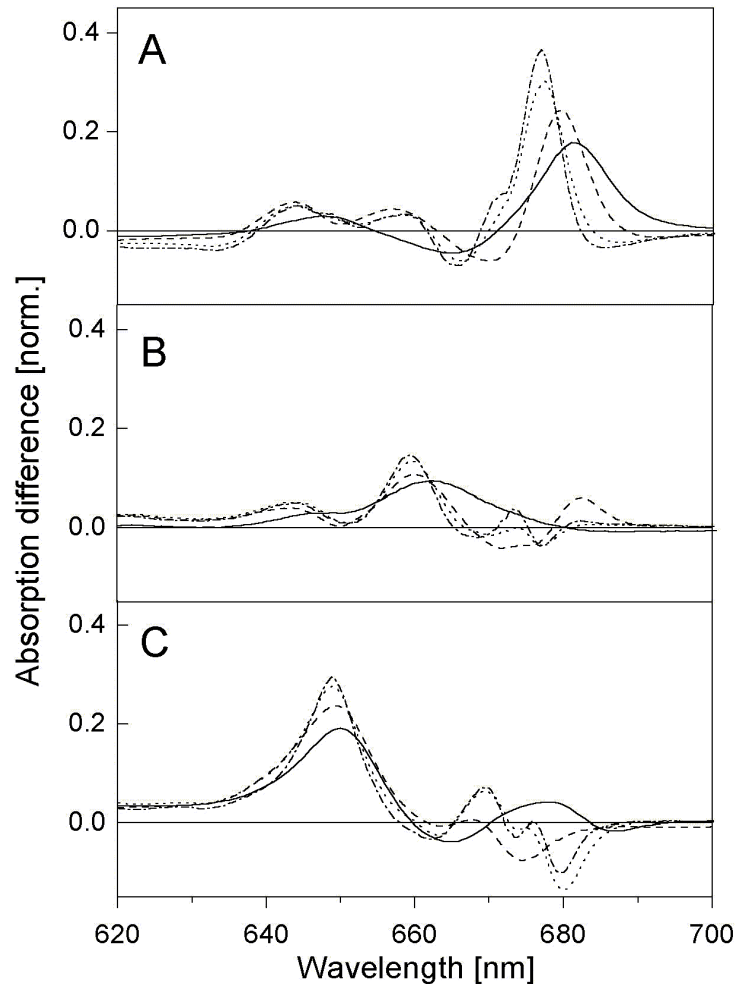

Figure 3.2.6 Absorption difference spectra (WT *minus* mutant) for trimeric LHCII mutants **a2** (A), **b3** (B), and **b6** (C) at 293 K (solid line), 150 K (dashed line), 77 K (dotted line), and 4 K (dot-dashed line).

For comparison of data obtained at different temperatures one has to consider these highly variable band shifts. The 676 nm-band shift was further related to that of the fluorescence maximum in a temperature range between 4 K and 293 K for native LHCII (Fig. 3.2.7, right panel). Around 100 K, the data indicate a switch of the terminal emitting state: Below this temperature, the 678 nm band represents the end of the EET chain. At higher temperature, the 676 nm band becomes the lowest energetic transition as a consequence of its large temperature-dependent shift to longer wavelengths. Interestingly, the fluorescence maximum follows above 100 K exactly the absorption-band shift of the 676-nm transition, but not below. Obviously, the fluorescence originates from distinct transitions at different temperatures. For that reason, results obtained in LT experiments like hole-burning spectroscopy [54, 110] or line-narrowing fluorescence measurements [105, 146] should be compared to RT data with due care.

Interestingly, temperature dependent shifts of the *minor* bands in each absorption difference spectrum (Fig. 3.2.6) do not follow a regular pattern.   Hence, mixed occupancy of the respective modified binding sites can be sufficiently *excluded* as origin of these features. On the contrary, it seems more likely that the minor difference bands reflect temperature effects on the protein structure. With no doubt, the lack of individual Chls in the LHCII mutants will cause local changes of the protein structure, which may in turn give rise to minor spectral differences. Such protein distortions comprise most probably a complex temperature dependence, since the structural arrangement follows an intricate energetic equilibration. Consequently, the minor spectral features show an indistinct dependence on temperature variations.
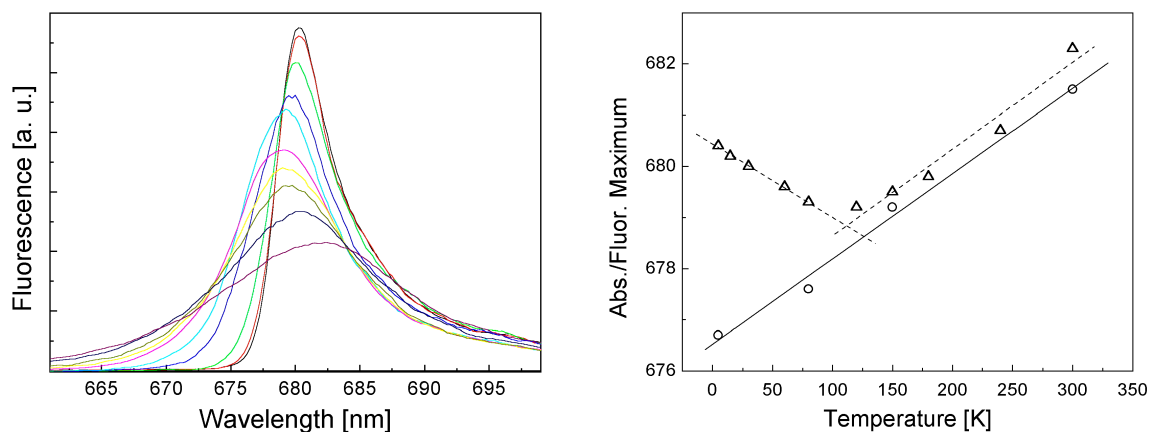

Figure 3.2.7 Left panel: Fluorescence spectra of LHCII (not normalized) at different temperatures: 4 K (black), 15 K (red), 30 K (green), 60 K (blue), 80 K (cyan), 120 K (magenta), 150 K (yellow), 180 K (dark yellow), 240 K (navy), and 293 K (purple). **Right panel:** Temperature dependent shift of the LHCII fluorescence maximum (as obtained from the left panel, triangles) compared to the temperature dependent shift of the Chl **a2**-absorption maximum (as obtained from panel A in Fig. 3.2.6, circles).

3.2.3   Implications for the room temperature absorption spectrum

Temperature dependent shifts of λ_c (i.e., different shifts for distinct bands) hamper the straightforward development of a sub-structure model by scaling the LT results to RT. On the other hand, observed changes of the bandwidths follow comprehensible mechanisms of increasing homogeneous broadening, thus providing useful parameters also for RT models. The bandwidth in Fig. 3.2.6 (**A**) corresponds to ~5 nm at 4 K and ~10 nm at 293 K. A homogeneous widths $2\Gamma \approx 9$ nm can thus be obtained by assuming Voigt-profiles at RT (see Chapter 1.2.2) and temperature-independent inhomogeneous broadening ($\Delta \approx 5$ nm). Accordingly, the variation of band parameters can be reasonably limited to $\Delta = 4\text{-}6$ nm and $2\Gamma = 8\text{-}13$ nm for the RT absorption model. (The latter value considers again the possibility of additional broadening of up to ~3 nm due to ultra-fast EET.)

Considering the bandwidth limitations at RT, the establishment of a sub-structure model for native LHCII is attempted in the following on the basis of determined LT parameters. Unfortunately, the observed variable band shifts prevent straightforward scaling between the two temperatures and raise the question of additional restrictions. Since the structure of LHCII reveals five Chl *b* and seven Chl *a* [6], respective

contributions (including the 0.68-fold transition probability of Chl *b*) should be also reflected in the absorption sub-structure (see Chapter 1.2.2, i.e. Fig. 1.2.7, p. 12). A sub-band model as obtained by fitting the LT spectrum under this additional limitation is illustrated in Fig. 3.2.8 (left panel). Except one modification, the resulting λ_c are fully comparable to the model in Table 3.2.3 (see Fig. 3.2.5, right panel) considering an error range of ±1 nm for each λ_c. In particular, the 663 nm band has to be shifted to 656 nm, since otherwise the differences between Chl *a* and Chl *b* regions cannot be balanced out. The remaining slight deviations in the Chl *b* region indicate that the 'half' Chl *b* apparent in the pigment analysis of native LHCII (see Table 3.2.2, p. 68) must be further included. This additional 0.5 Chl *b* (when compared to the structure analysis [6]) reflects either heterogeneity between the *Lhcb* proteins or an unspecific bound pigment, which is partly removed during isolation. The absorption band of this molecule is expected to comprise strong inhomogeneity due to a much less defined environment, but it contributes to the total Chl-*b* absorption with ~10 %. Accordingly, the consideration of this additional absorption by an inhomogeneously broadened band in Fig. 3.2.8 (right panel) yields a better fit, while all other parameters remain nearly unchanged. The result is illustrated in Fig. 3.2.8 (right panel) and parameter values are summarized in Table 3.2.4.

Table 3.2.4 Sub-structure model of the LHCII absorption spectrum obtained by restricting the model to adequate α-parameters for Chl *a* and *b*, respectively (see text). Ten Gaussian sub-bands are identified by λ_c [nm], Δ [nm] and relative area α [a.u.], thus reflecting the 12 Chls observed in the LHCII structure due to two-fold values for α in column 11 and 12. The band in the first column ($\lambda_c = 625$ nm) summarizes higher vibrational (0,1)-transitions of Chl *a* interfering with the (0,0)-transitions of Chl *b*. The band in the second column ($\lambda_c = 654$ nm) considers 0.5 unspecific bound Chl *b* per LHCII monomer.

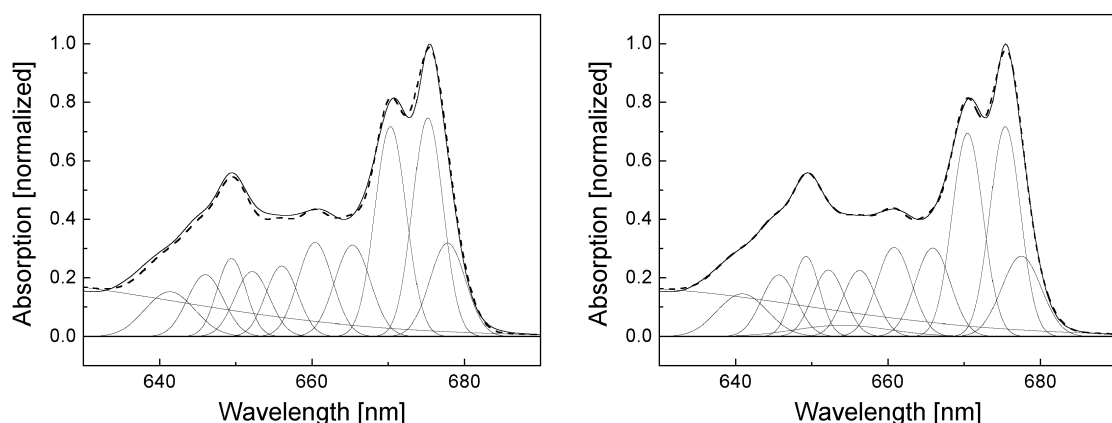| λ_c	625.0	654.0	640.8	645.7	649.2	652.4	656.3	660.8	665.9	670.4	675.4	677.5
α	6.28	0.35	0.7	0.7	0.7	0.7	0.7	1	1	2	2	1
Δ	58.3	14.7	7.6	5.3	4.1	5.0	5.0	5.4	5.4	4.8	4.6	6.1

Figure 3.2.8 Fit of the sub-band model from Table 3.2.3 as applied to native LHCII at 4 K under the additional restriction of 0.68-times lower contributions of the Chl *b*. Measured spectra (solid line), fitted absorption spectra (dashed line), and resolved sub-bands (thin lines). **Left panel:** 10 sub-bands taking into account 5 Chl *b* and 7 Chl *a*. **Right panel:** 10 sub-bands taking into account 5 Chl *b* and 7 Chl *a* and one additional sub-band considering the contribution of 0.5 Chl *b* according to the pigment analysis. Considering the two bands with double amplitudes, the both models reflect 12 Chls identified in the LHCII structure.

Together with the limitations for homogeneous and inhomogeneous bandwidths above, the sub-structure model in Table 3.2.4 represents a firm base to scale LT parameters to RT conditions. In particular, 2Γ was assumed to be variable 8 and 13 nm (in 1 nm steps), while Δ was approximated as a constant value for each band (5 nm). An unambiguous fit of the absorption range between 620-690 nm is obtained, if the four λ_c determined from mutant samples are fixed within intervals of ±1 nm. Hence, the resulting model (Table 3.2.5 and Fig. 3.2.9) represents a highly confident absorption sub-structure of LHCII, which is essentially required to evaluate NLPF spectra further below (see Chapter 3.5).

Table 3.2.5 Sub-structure model of the LHCII absorption spectrum at RT obtained by extending the ten-band model determined at 4 K (cp. Table 3.2.8) to 293 K (see text). Ten sub-bands (Voigt-profiles) are identified by λ_c [nm], Δ [nm], 2Γ [nm], and α [a.u.]. The Lorentzian band in the first column with $\lambda_c = 618$ nm summarizes higher vibrational (0,1)-transitions of Chl *a* interfering with the (0,0)-transitions of Chl *b*. The Voigt-profile in the second column ($\lambda_c = 655$ nm) considers 0.5 Chl *b*, which is expected to be unspecific attached per LHCII monomer.

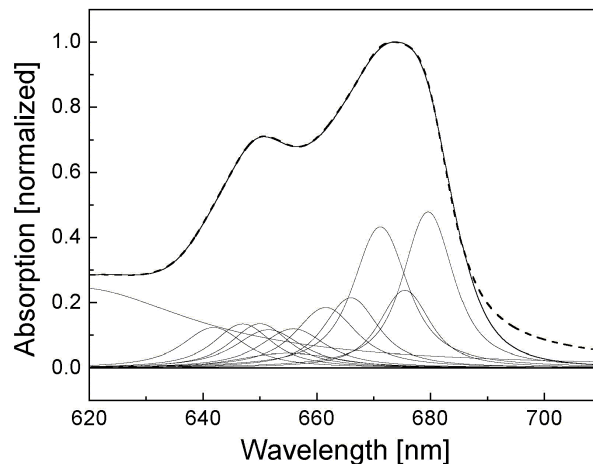| λ_c	618.0	655.0	641.8	647.0	650.0	651.5	655.9	661.6	666.0	671.2	675.5	679.6
α	6.2	0.35	0.7	0.7	0.7	0.7	0.7	1	1	2	1	2
2Γ	50	12	11	10	10	12	10	11	9	9	8	8
Δ	-	15	5	5	5	5	5	5	5	5	5	5

Figure 3.2.9 Simulation of the Q_y-absorption spectrum of native LHCII (RT) as obtained by extending the ten-band model determined at 4 K (Table 3.2.4 and Fig. 3.2.8) to 293 K (Table 3.2.5): Measured spectra (solid line), fitted absorption spectra (dashed line), and resolved sub-bands (thin lines).

As a major advantage of the presented sub-structure model, it contains a clear distinction between homogeneous and inhomogeneous broadening. The underlying mathematical description by a Voigt-profile with bandwidth parameters Δ and 2Γ is necessary for the evaluation of NLPF spectra (see Section 3.1.1). In contrast to this, deviations of the actual linewidths from an ideal Voigt-profile at RT (cp. Section 1.2.2) cause slight differences in the red edge of the Q_y-band. However, corrections of this additional error can only be achieved by rather extensive mathematical expressions for the exact line shape of Chls in protein environment [30, 33]. Since these descriptions require a higher number of parameters per band, their application is rather unsuitable for

the sub-structure analysis of spectral heterogeneity in LHCII. Furthermore, the NLPF theory has not been extended to such comprehensive mathematical expressions, yet (see i.e. [1]).

It should be further mentioned that deviations from the exact band shape – resulting from the description by Voigt-profiles – are barely reflected in NLPF spectra. In particular, deviations between measured and modeled absorption in Fig 3.2.9 are hardly resolvable in squared spectra (Fig. 3.2.10, left panel). Due to a *quadratic* dependence of the NLPF signal on the absorption profile of each band, the underlying deviations are thus sufficiently reduced.

Last but not least, the above introduced summation of all higher vibrational transitions to one Lorentzian band is evaluated. For that purpose, Fig. 3.2.10 (right panel) compares the band in the first column from Table 3.2.5 with (0,1)-transitions calculated in a similar way as performed in Section 3.1.4 (from the parameters obtained for Chl in solution, Table 1.2.2, p. 14). Since the superposition of expected vibrational bands (dashed line) resembles satisfactorily the Lorentzian from Table 3.2.5 (solid line), this simplification represents a nearly exact approximation. As a result, the absorption spectrum can be correctly described in the range of Chl *b* (0,0)-bands overlapping with Chl *a* (0,1)-bands, too. The same time, the number of bands considered in the model is significantly reduced (to one half). This is of main importance for an efficient evaluation of NLPF spectra, since the usability of the one-band approximation was also proved for NLPF simulations in Section 3.1.4.
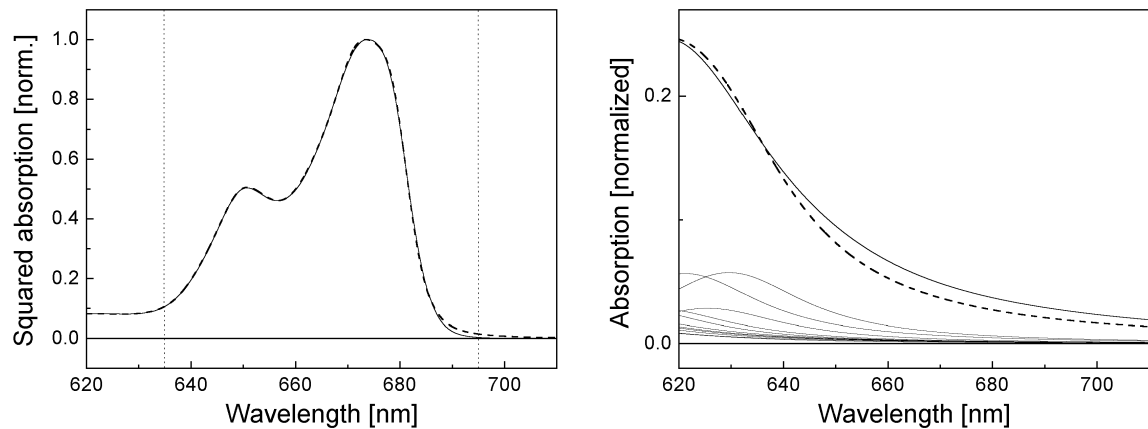

Figure 3.2.10 Left panel: Squared values of the measured (solid line) and simulated (dashed line) absorption spectra in Fig 3.2.9. The dotted lines indicate the accessible spectral range for the NLPF measurement (see text). **Right panel:** Comparison of the broad band approximating all vibronic (0,1)-transitions (first column in Table 3.2.5, solid line) to the calculated contribution of the vibronic bands (thin lines), which are superposed to the dashed line.

3.2.4 Summary

Concluding, the sub-structure in Table 3.2.5 is briefly compared to models developed by other authors in previous studies. The first attempts of sub-structure analyses for LHCII were performed by Gaussian decomposition and resulted in different numbers of

bands [56, 138]. Additional interpretation of certain features in LD and CD as well as LT absorption spectra ended in a comprehensive model with 10-11 bands [53]. The exact number of 5 Chl *b* and 7 Chl *a* identified in the structure (and corresponding transition probabilities) were later considered for sub-structure modeling by Trinkunas et al. [12]. In the same work, higher vibrational bands were also included, but with a rather extensive parameter set. In contrast to this, the evaluation of absorption spectra obtained from mutant LHCII with specifically removed Chl-binding sites [37, 38] allowed the assignment of several Chls to certain sub-bands. Unfortunately, these attempts did not result in a congruent sub-structure model. Accordingly, this experimental approach was used here in a modified manner. In particular, *i)* only mutants yielding the highly stable, *trimeric* form of LHCII were considered for the sub-structure analysis, *ii)* mutants lacking both Chl *a* and *b* or with ambiguous determination of the removed Chl have been excluded, and, *iii)* the sub-structure analysis was extended to LT spectra showing much higher resolution than the RT absorption. The observed temperature dependence of λ_c and 2Γ was employed to scale the LT model to RT conditions, thus basically improving earlier attempts [55, 56]. Besides this, the sub-structure model obtained here explicitly includes the difference between inhomogeneous and homogeneous broadening. Correct distinction between these two contributions is essential for evaluating NLPF spectra (see Chapter 3.1.1). Hence, Table 3.2.5 represents the most convenient sub-structure model for the discussion of NLPF measurements in 3.5. In this part, further improvements of the parameter set are discussed with respect to results obtained in the following Chapters 3.3 and 3.4 from investigating possible excitonic interactions in LHCII. In particular, the origin of the two bands with double amplitude from either excitonic coupling or superposition of strongly overlapping transitions is elucidated.

3.3 Obtaining additional information, Part II: Nonlinear absorption with fs-pulses

Experimental and theoretical aspects of the nonlinear absorption technique are outlined in Chapter 2.2.1 with respect to direct determinations of the transition probability $\left|\vec{\mu}\right|^2$. The method has been earlier applied to study excitonic coupling in bacterial antenna complexes using ps-laser pulses [65]. Nevertheless, EET processes in LHCII on time scales down to about one hundred fs [13, 147] complicates the evaluation of experimental data considerably. Hence, different NLA investigations using fs-pulses as well as ps-pulses are reported in this Chapter. First, the method is evaluated by comparison of monomeric Chl in solution and an excitonically coupled model system in Section 3.3.1 as previously reported [148]. Subsequently, section 3.3.2 describes the results obtained from LHCII measurements as partly published in [118].

3.3.1 Application to model systems: Evaluation of the method

Nishigaki et al. [32] have recently interpreted the red-shift of the Q_y-absorption band in LHCII when compared to molecular Chl solutions by pure pigment-protein interactions. In particular, *ab-initio* calculations describing Chls in the environment of their respective protein-binding site reveal indeed slightly different S_0-S_1 transition energies. This results in varying shifts of the individual $Q_y(0,0)$-transitions (15 nm spread among λ_c for Chl *a*) and is expressed by the broader and red-shifted Q_y-band in LHCII. Interestingly, the shift calculated for the Chl at binding-site **a2** (Asparagin-residue) resulted in $\lambda_c \approx 670$ nm. On the other hand, the analysis of mutant **a2** with the corresponding binding site removed (see Section 3.2.2) clearly shows that the corresponding Chl absorbs around 680 nm. Accordingly, excitonic coupling could be the origin of the observed discrepancy. The formation of exciton states with nearly all transition probability in the long-wavelength transition due to special geometrical arrangements appear as simple red shift in absorption spectra (see Fig. 1.3.2, p. 19). Accordingly, *in-vitro* aggregates of Chls showing similar shifts have received longstanding attention as model systems for understanding pigment organization *in vivo*. Dimers of Chls are of particular interest, since they are the simplest conceivable objects to study excitonic interactions between pigments. According to this, comparison of dimeric and monomeric Chl in solution can be used as excellent proof of the applicability of an experimental method to determine excitonic interactions.

The formation of Chl-*a* aggregates in aqueous dimethyl sulfoxide (DMSO) has been extensively investigated by Uehara et al. [149, 150]. In particular, a species formed in 50 % DMSO/buffer and absorbing at 685 nm was reported to represent Chl dimers. Since absorption and fluorescence spectra of this species do not depend on Chl *a* concentration when varied over two orders of magnitude, the presence of residual monomers or higher aggregates is rather improbable. A similar preparation method was employed here to obtain dimeric Chl in solution. Chl *a* was isolated under assistance of

Dr. H. Lokstein (HU Berlin) according to the procedure described by [151] and purified by paper chromatography. Aggregation was induced at 45 µM Chl concentration in 50 % buffered aqueous DMSO (cp. [150]) and monomers were obtained in 100 % DMSO. In the NLA experiment, the sample transmission is registered in dependence on incident light intensity in a single beam set-up as described above (Section 2.2.1). Experiments with the ps-system were performed under partly assistance of Dr. H. Stiel (MBI Berlin). The fs-laser system was run in the fs-application lab at MBI Berlin, where Dr. F. Noack assisted the experiments by laser operation. Dr. H. Stiel and Dr. B. Voigt (MBI Berlin) were involved in the design of the experimental setup.
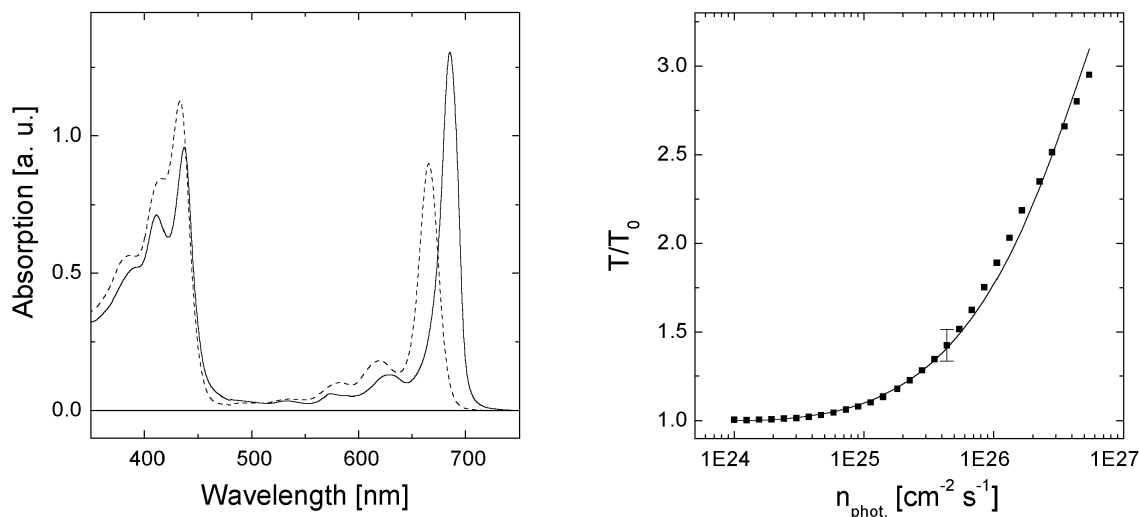

Figure 3.3.1 Left panel: Absorption spectra of monomeric (dashed line) and aggregated (solid line) Chl *a* (c = 45 µM, d = 2 mm). The total area under the absorption curve keeps unchanged during aggregation, while the complete Q-absorption band (500-750 nm) is increased by 19 %. Due to the lower contributions of the higher vibronic transitions in the aggregates, the area of the $Q_y(0,0)$-transition is increased by 29 %. **Right panel:** NLA curves of Chl-*a* monomers obtained with 400-ps pulses at 665 nm. The solid line represents the best fit to the data (see Table 3.3.1).

Quantitative aggregation of Chl *a* was assessed by the absorption spectrum as shown in Fig. 3.3.1 (left panel). The Q_y-absorption of the aggregates is shifted by about 20 nm to longer wavelength. In general, excitonic interactions in linear aggregates lead to a *split* of the monomer excited states. However, if the Q_y-transition dipoles are arranged more or less 'in line', the transition-dipole moment to the upper states can vanish completely (cp. Fig. 1.3.2 in Section 1.3.1). As a result, the absorption appears to be red-shifted. To fit NLA curves of both, Chl *a* monomers and aggregates, a three-level (S_0, S_1, S_2) model with the following parameters was used (cp. Section 2.2.1): σ_{ij}, σ_{ji} absorption and induced emission cross sections (j < i), γ_{ij} corresponding relaxation rates from level i to level j. The origins of the three levels differ in both species. They represent ground state, first and second excited state in case of the monomer and common ground state, one-exciton and two-exciton state for the aggregates. Since the fluorescence spectra are barely red-shifted when compared to absorption for aggregates as well as for monomers, it was assumed $\sigma_{ij} = \sigma_{ji}$. Inter-system crossing to triplet states was neglected due to the short pulse durations. NLA of the monomeric sample was measured with 400-ps pulses at the absorption maximum

(665 nm) as shown in Fig. 3.3.1 (right panel). Fitting was carried out with γ_{10} fixed at the observable fluorescence decay rate of $[5\ ns]^{-1}$.

The obtained molecular parameters are shown in Table 3.3.1. The resulting σ_{ij} are in nice quantitative agreement with earlier results as obtained on the ns timescale [152]. NLA of the Chl *a* aggregates was recorded at the respective absorption maximum (685 nm) with two different pulse durations (Fig. 3.3.2). Fitting of the fs-data was insensitive to the value of γ_{10}, since this relaxation process is considerable longer than the pulse duration and thus it was fixed at 50 ps. From evaluation of the ps measurements, however, γ_{10} could be directly obtained as about hundred times larger than the corresponding value of monomeric Chl. This corresponds well to the observed steady state fluorescence quenching of two orders of magnitude.
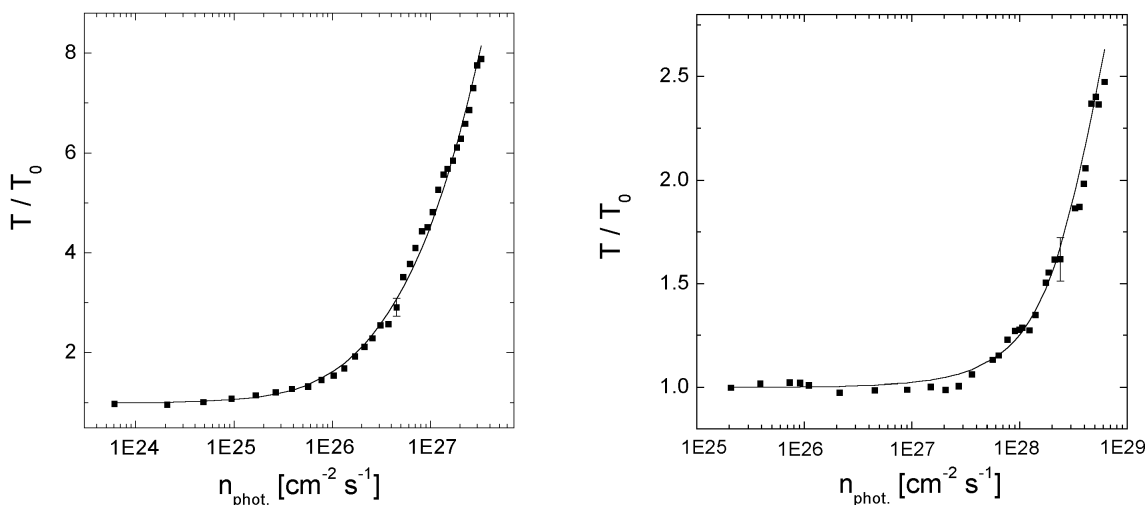

Figure 3.3.2 NLA curve of Chl-*a* aggregates obtained at 685 nm excitation with 400-ps pulses (**left panel**) and 120-fs pulses (**right panel**). Solid lines represent the best fits to the data according to the values in Table 3.3.1, one average error bar is added for each curve.

The absorption-cross sections of Chl aggregates are about three to four times larger than those of monomers. Taking into account that the homogeneous linewidth of the aggregates is roughly 3/5 that of monomers (cp. Fig. 3.3.1, left panel), the transition dipole moment appears to be increased by a factor of 2.5 to 3. As further indicated in Fig. 3.3.1 (left panel), about one third of the enhanced oscillator strength in the $Q_y(0,0)$-absorption band is transferred from the Soret-region because of hyperchromic effects (cp. [52]). Thus *at least* a coupling of **two** transition-dipole moments must be assumed: If the corresponding transition dipoles are oriented 'in line', the long-wavelength transition has two-fold transition probability (see Chapter 1.3). Hence, considering the interpretation of the Chl species absorbing around 685 nm as dimeric molecules [150] based on Raman-spectroscopic results, the 'in-line' dimer appears to be the most probable arrangement of the aggregate.

Notably, the determination of absorption-cross sections with fs-pulses yields almost identical results as obtained with ps-pulses. This behavior was expected, since the employed systems do *not* feature any ultra-fast processes on the sub-ps timescale like EET in antenna complexes, Nevertheless, the investigation of complicated systems like

LHCII requires simplifications in the model, which can only be applied in the fs-regime. Under this point of view, the results above demonstrate the general feasibility of NLA experiments for the determination of excitonic coupling even in the case of biological complexes characterized by ultra-fast excited-state dynamics.

Table 3.3.1 Excited-state parameters obtained from fitting the NLA curves in Fig. 3.3.1 (right panel) and Fig. 3.3.2.

	Pulse length	λ_{ex}	σ_{10} [cm^2]	σ_{21} [cm^2]	γ_{10} [ns]$^{-1}$	γ_{21} [ps]$^{-1}$
Aggregates	120 fs	685 nm	$9.5 \cdot 10^{-16}$	$1.1 \cdot 10^{-15}$	20*	~ 1.0
Aggregates	400 ps	685 nm	$9.3 \cdot 10^{-16}$	$9.6 \cdot 10^{-16}$	50	~ 1.0
Monomers	400 ps	665 nm	$3.0 \cdot 10^{-16}$	$4.3 \cdot 10^{-16}$	0.2*	~ 1.0

* Parameters that were fixed during the fit procedure.

3.3.2   Application to LHCII: Evidence for excitonic coupling

The theoretical modeling of NLA experiments allows certain simplifications, if all excited- state dynamics occur on time scales considerably longer than the pulse length (see Section 2.2.1). Accordingly, application of the NLA technique using 120-fs pulses at the red edge of the Q_y-absorption band of LHCII enables a straightforward evaluation of the obtained results: The fastest energy relaxation or transfer processes observed in the covered spectral region are well above 1 ps [12]. Hence, incoherent EET dynamics can be ignored completely. Moreover, a possibly unresolved relaxation among exciton states (coherent EET) can also be excluded, since in the case of efficient excitonic coupling the upper exciton bands are not sufficiently populated due to their spectral separation. On the other hand, the spectral width of the 120 fs-pulse (6 nm, FWHM) increases the error range in the spectrally integrating NLA experiment and favors its application in regions of moderate absorption changes. The most reasonable compromise between these two requirements was established by applying fs-pulses at a central wavelength of 680 nm (see Fig. 3.3.3 , left panel).

The measurements were performed with the single beam set-up previously described (see Section 2.2.1) in the fs-application lab at MBI Berlin and assisted by Dr. F. Noack (laser operation). LHCII samples used for the experiments have been prepared and characterized under assistance of Dr. H. Lokstein (HU Berlin) according to the descriptions in Chapter 2.1. The NLA curve measured on trimeric LHCII (1.2 % *n*-octyl β-D-glucopyranoside at 110 μg/ml Chl *a+b*) is shown in Fig. 3.3.3 (right panel). Being able to neglect the EET dynamics, the obtained NLA curve in can be evaluated on the basis of a single three-level model without the considaration of rate constants (cp. Section 2.2.1). The corresponding fit yields a ground-state absorption-cross section of $1.3(\pm 0.2) \times 10^{-15}$ cm^2 at 680 nm for LHCII (and $1.5(\pm 0.2) \times 10^{-15}$ cm^2 for excited state absorption). This value is about four times that of monomeric Chl *a* in diethyl-ether solution (3.1×10^{-16} cm^2 at peak wavelength, cp. [49]). For evaluation of NLA data obtained at wavelengths shorter than 680 nm (not shown) one would have to consider

EET on time scales of the laser-pulse duration - even employing 120 fs pulses [12]. Several attempts of summarizing measured EET rates in an overall scheme were recently made [14, 112], but no generally accepted model has been established so far. Hence, the analysis of NLA data obtained at shorter wavelengths is much less straightforward and was omitted.
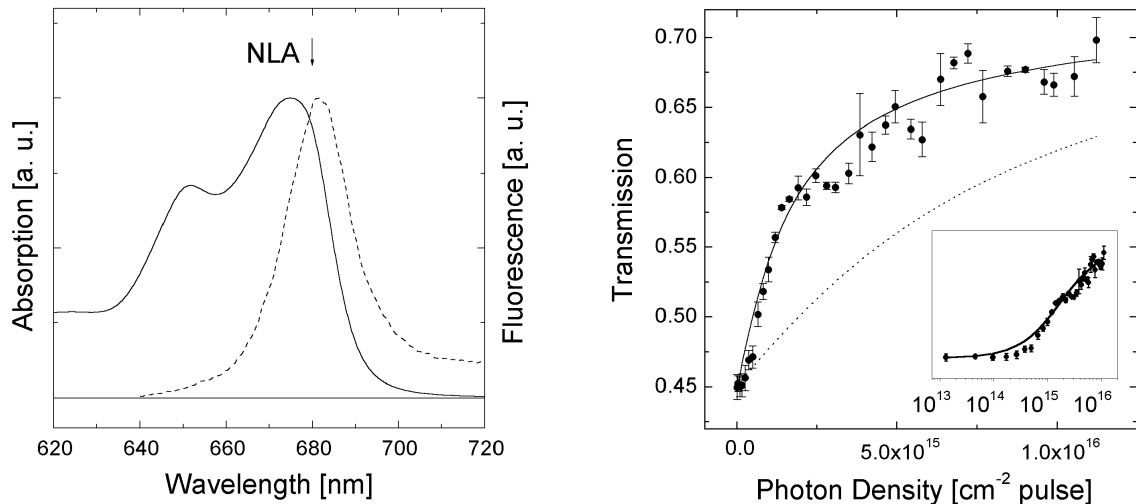

Figure 3.3.3 Left panel: Normalized absorption and fluorescence spectra of trimeric LHCII. The arrow indicates the excitation wavelength of the fs-NLA experiment. **Right panel:** NLA curve of trimeric LHCII obtained at 680 nm excitation with 120-fs pulses. The solid lines represents the best fits to the data according to values mentioned in the text. The dashed line shows a similar simulation under the assumption of monomeric Chl-*a* molecules in solution.

The four-fold increase of the absorption-cross section shows a high similarity to the results obtained for the aggregates with dimeric coupling among Chls in Section 3.3.1. They can be therefore interpreted as the strongest hint for excitonic coupling in LHCII so far. However, the exact determination needs a detailed evaluation with respect to transition bandwidths and hyperchromic effects. This is discussed in Section 3.4.2 under consideration of further experimental results obtained by the study of intensity-dependent NLPF spectra, which allowed the determination of the *emission*-cross section. Notably, both techniques rely on complementary attempts in the theoretical handling of the underlying systems dynamics: while NLA with fs-pulses represents a quasi-instantaneous approach, the model used to interpret intensity-dependent NLPF data is based on the assumption of quasi-stationary conditions after completion of the fast EET processes.

3.4   Obtaining additional information, Part III: Studying the NLPF intensity dependence in the fluorescence region of LHCII

3.4.1   Experimental results

NLPF spectra of LHCII obtained at different λ_t with low pump-beam intensities are presented and discussed in Chapter 3.5. In contrast to this, the following section is focused on *intensity-dependent* NLPF spectra recorded with λ_t fixed in the spectral region of LHCII fluorescence (685 nm, see Fig. 3.4.1). LHCII samples were prepared and characterized similar to the procedures described in Chapter 1.1 (assistance: Dr. H. Lokstein) and trimeric samples (1.2 % *n*-octyl β-D-glucopyranoside at 110 µg/ml Chl *a+b*) were used for the experiments. The intensity-dependent NLPF spectra were recorded applying the setup described in Chapter 2.2.2.
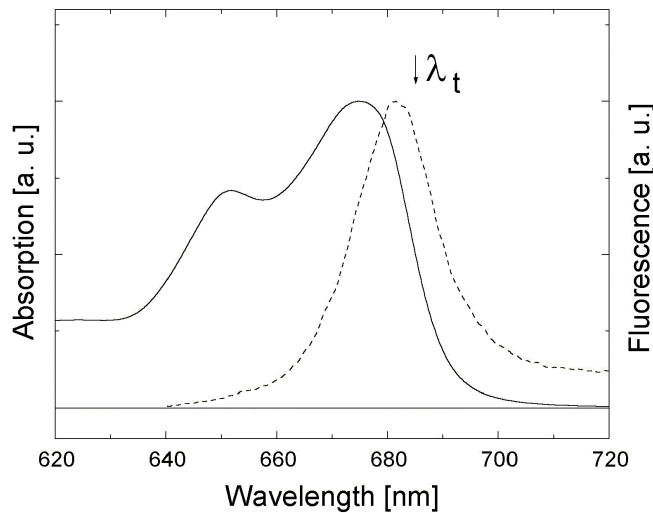

Figure 3.4.1 Normalized absorption and fluorescence spectra of trimeric LHCII. The arrow indicates λ_t as used for intensity-dependent NLPF experiments.

The pump wavelength was tuned across the main Chl-*a* emission region (670 - 690 nm), which overlaps strongly with the red absorption edge. NLPF spectra recorded at different pump beam intensities are presented in Fig. 3.4.2 (left panel). Each curve is the average of 10 repetitive measurements, additionally smoothed by averaging over 15 neighboring data points. The distribution of data points before smoothing is shown for curve **d**. For the employed pump-beam intensities see legend of Fig. 3.4.2. For each value of λ_p, the intensity dependence of the NLPF signal was extracted from curves **a** to **g**. This is illustrated in Fig. 3.4.2 (right panel) for $\lambda_p = 678$ nm (corresponding to the dashed line in Fig. 3.4.2, left panel).

In agreement with the knowledge about EET processes in LHCII [12, 13, 14] the model for evaluation of the spectra can be based on the assumption that all excitations are transferred to the fluorescent state(s) on a time scale significantly shorter than the fluorescence lifetime. Thus, unknown intermediate steps in the EET scheme can be

neglected and the system can be described in a generalized donor/acceptor model. As deduced in Section 2.2.4, the intensity dependence of the NLPF signal for probing the fluorescent state (acceptor) is determined by Eq. 31 (p. 40), depending on only two parameters $\xi(\omega_p)$ and $\eta(\omega_p, \omega_t)$. The reciprocal value of the saturation parameter $\xi(\omega_p)$ indicates the point at which the NLPF signal starts to deviate from the initial quadratic intensity dependence. The large number of Chls in LHCII requires the consideration of several donors and acceptors and, possibly, branched EET between them. Therefore the model was extended resulting in Eq. 32 (p. 40) for the saturation parameter, which can also be expressed as

$$\xi(\omega_p) = \frac{\sigma^{abs}(\omega_p)}{N_A \cdot \gamma_{fd}} + \frac{\sigma^{em}(\omega_p)}{N_A \cdot \gamma_{fd}}, \tag{33}$$

The cross section $\sigma^{abs}(\omega_p)$ does not necessarily reproduce the steady-state absorption spectrum of LHCII. Rather, $\sigma^{abs}(\omega_p)$ comprises the absorption of the *probed* acceptor(s) and of *those* donors that confer their excitation energy to them (cp. Eq. 32, p. 40). Analogously, the cross section $\sigma^{em}(\omega_p)$ may not reflect the entire fluorescence spectrum but only the emission of the *probed* acceptor state(s). The fluorescence decay rate γ_{fd} has to be multiplied by the number of fluorescent species N_A if the EET path branches to more than one acceptor. The second parameter $\eta(\omega_p)$ is determined by the ratio between γ_{fd} and the EET rates according to Eq. 30 (p. 40). Thus $\eta(\omega_p)$ is ideally suited to verify the assumption of EET being much faster than the fluorescence decay.
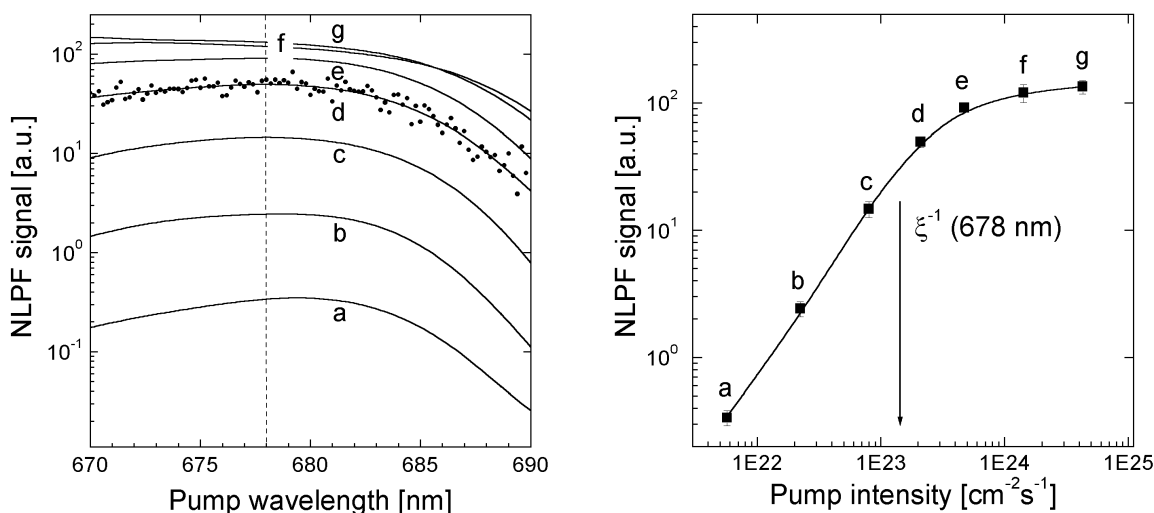

Figure 3.4.2 Left panel: NLPF spectra of trimeric LHCII probed at 685 nm for different pump-field intensities: $5.7 \cdot 10^{21}$ (**a**), $2.3 \cdot 10^{22}$ (**b**), $8.0 \cdot 10^{22}$ (**c**), $2.1 \cdot 10^{23}$ (**d**), $4.7 \cdot 10^{23}$ (**e**), $1.4 \cdot 10^{24}$ (**f**) and $4.3 \cdot 10^{24}$ (**g**) photons cm^{-2} s^{-1}. Solid lines represent smoothed spectra (see text), dots indicate original distribution of the data belonging to curve **d**. NLPF signal values as obtained at $\lambda_P = 678$ nm (vertical dashed line) are used to demonstrate the intensity dependence in the right graph. **Right panel:** Intensity dependence of the NLPF signal of trimeric LHCII probed at 685 nm and pumped at 678 nm as obtained from the figure to the left. The pump-beam intensities correspond to the values **a**) - **g**) given in the legend above. The solid line is the result of the fit (for parameters see text). The obtained ξ-value is visualized by an arrow.

NLPF saturation curves are fitted according to Eq. 31 (p. 40) to obtain values of $\xi(\omega_p)$ and $\eta(\omega_p)$. For the curve in Fig. 3.4.2 (right panel) the fit yields the following parameters: $\xi = 8.4 \cdot 10^{-24}$ cm$^2\cdot$s, $\text{Re}\{\eta \cdot \xi\} = 2.7 \cdot 10^{-26}$ cm$^2\cdot$s and $\text{Im}\{\eta \cdot \xi\} \approx 0$. The very low value of η implies that the EET rates γ_{AD} are significantly higher than the fluorescence decay rate γ_A according to Eq. 30 (p. 40). Plotting ξ versus λ_p, a 'ξ - spectrum' was generated (Fig. 3.4.3, left panel).

A recent study on the bleaching behavior and fluorescence polarization of single complexes demonstrated that each of the three subunits in trimeric LHCII is characterized by its own terminal acceptor state(s), thus suggesting a mainly independent EET path for each monomer ([109], cp. Fig. 3.4.4, p. 91). Hence, the subunits of the trimer can be expected to act independently in the NLPF experiment and modeling has to account for the contributions of 7 Chl *a* and 5 Chl *b* comprising a monomeric subunit of LHCII [6]. According to this, the contribution of $\sigma^{abs}(\omega_p)$ to the ξ-spectrum is estimated as follows: Assuming that all donor species absorbing between 670 and 690 nm transfer their excitation energy to the probed acceptor(s), $\sigma^{abs}(\omega_p)$ as used in Eq. 3 equals the actual absorption-cross section in this range. The total transition-dipole strength of one LHCII monomer yields $|\vec{\mu}_{LHC}|^2 = 7|\vec{\mu}_{Chla}|^2 + 5|\vec{\mu}_{Chlb}|^2 \approx 10.5|\vec{\mu}_{Chla}|^2$ (considering $\vec{\mu}_{Chlb} \approx 0.83\,\vec{\mu}_{Chla}$, [50]). Scaling the area under the Q_y-absorption spectrum of LHCII to the 10.5-fold of the area under the absorption cross section spectrum of Chl *a* (3.1x10^{-16} cm^2 at maximum, [49]) yields $\sigma^{abs}(674\text{nm}) = 1.7(\pm0.3)$x10^{-15} cm^2. This result can be used to scale the LHCII absorption spectrum between 670 and 690 nm to approximate values of $\sigma^{abs}(\omega_p)$.

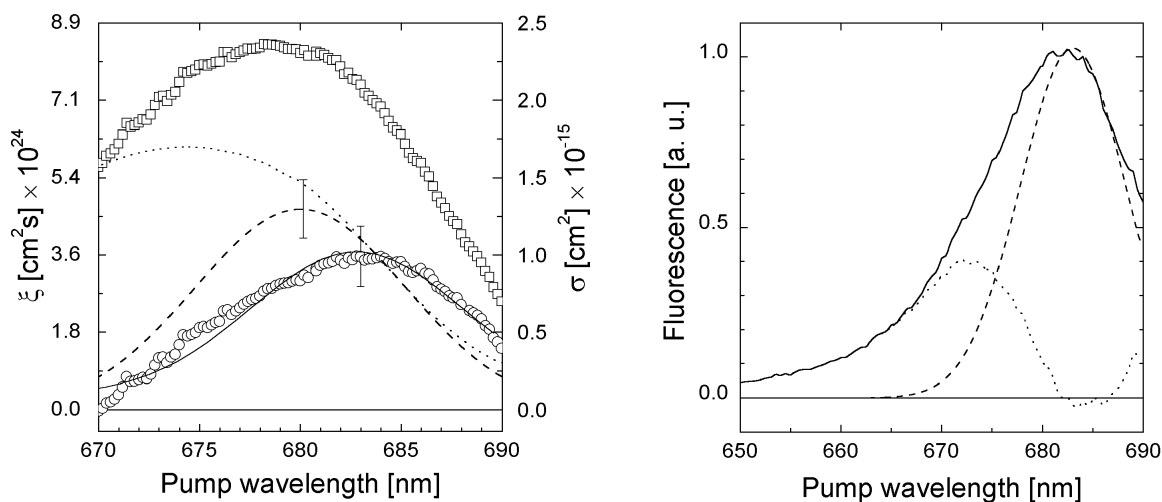**Figure 3.4.3 Left panel:** ξ-spectrum of trimeric LHCII constructed from the intensity dependent NLPF-spectra in the left panel of Fig. 3.4.2 (squares, left scale). The right scale (σ) is calculated from ξ by multiplication with the fluorescence-decay time 3.6 ns (corresponding to the case $N_A = 1$ in Eq. 33, see text). Subtracting σ^{abs} (dotted line) from the ξ-spectrum yields σ^{em} (circles) of the terminal acceptor. Bars indicate the total statistical error. σ^{em} can be fitted by a Gaussian (solid line) centered at 683(±1) nm with a FWHM of 260(±30) cm^{-1}. For comparison with the NLA results an absorption band with the same FWHM (260 cm^{-1}) and a maximum absorption cross section of 1.3$\cdot10^{-15}$ centered at 680 nm was simulated (dashed line). **Right panel:** Deconvolution of the fluorescence spectrum (solid line) between 670 and 690 nm into a Gaussian sub-band (dashed line) at 683 nm with a FWHM of 260 cm^{-1} (cp. left panel) and additional fluorescence band(s) with a maximum around 672 nm (dotted line).

Using this approach the number of acceptors can be determined. In Fig. 3.4.3 (left panel) the ξ-spectrum multiplied by $\gamma_{fd} = (3.6 \text{ ns})^{-1}$ is compared to $\sigma^{abs}(\omega_p)$ as approximated above (for γ_{fd} see [13]). This procedure corresponds to probing *one* acceptor per LHCII monomer, i.e. $N_A = 1$ in Eq. 33. The contribution of $\sigma^{em}(\omega_p)$ can be obtained as the difference of both spectra (see Fig. 3.4.3, left panel), resulting in a maximum value of $1.0(\pm 0.2) \cdot 10^{-15} \text{ cm}^2$ at 683 nm. However, applying the same procedure assuming $N_A = 2$ yields the unreasonably high value of $3.6 \cdot 10^{-15} \text{ cm}^2$ for $\sigma^{em}(\omega_p)$ at maximum. Therefore, one should conclude that only the case $N_A = 1$ is in agreement with the experimental data. The emission spectrum $\sigma^{em}(\omega_p)$ obtained from ξ-spectrum analysis is centered at $683(\pm 1)$ nm and can be approximated by a Gaussian with $260(\pm 30) \text{ cm}^{-1}$ FWHM (see Fig. 3.4.3, left panel). Notably, the fluorescence spectrum of LHCII has a broader width and a non-Gaussian shape. Deconvolution of the fluorescence spectrum considering one Gaussian as obtained from the ξ-spectrum suggests the existence of an additional fluorescence band centered at about 672 nm. This band contributes less than 40 % to the total fluorescence yield (see Fig. 3.4.3, right panel). The additional fluorescent species is completely lacking in the ξ-spectrum, since it originates from acceptor(s) with vanishing contributions at $\lambda_t = 685$ nm.

3.4.2 Discussing the derived transition probability with respect to excitonic coupling in LHCII

According to the used model, the result $N_A = 1$ implies that within a LHCII monomeric subunit only *one* state emits *at a given time* in the main fluorescence region above 680 nm. Hence, while one branch in the EET chain is obviously directed to an emitter centered at ≈ 672 nm, no further permanent branches appear to exist. A temporarily fluctuating acceptor (for example due to spectral shifts) cannot be excluded explicitly, if only one branch is active at the same time. In this case, however, the cross section as obtained by NLPF still corresponds to only one transition – the one with the lowest saturation threshold. The measured value of the maximum emission cross section at 683 nm of LHCII is 3.2 times that of monomeric Chl *a*. Moreover, a 4.2-fold increased absorption-cross section for a sub-band at the red edge of the Q_y-region was found in the NLA experiment. As illustrated in Fig. 3.4.3 (left panel), both increased cross sections most probably belong to the same electronic transition, in particular if a Stokes-shift similar to that observed for Chl *a* in solution is assumed. The remaining deviation in the cross sections as obtained by the two approaches is due to the experimental error, and the mean value suggests a $3.7(\pm 1)$-fold increased cross section as compared to Chl *a* in solution.

Reasonable explanations for the increased maximum cross section can be either line narrowing in the protein environment and/or size enhancement of the corresponding transition-dipole moment. The effect of line narrowing can be estimated by comparing the linewidth of the emitting sub-band of LHCII with that of the Q_y-(0-0) vibrational band of Chl *a* in solution (390 cm^{-1} FWHM; [49]). As illustrated in Fig. 3.4.3 (left

panel), the width of the emission band obtained by NLPF is 260($\pm$30) cm^{-1} (FWHM). This is slightly higher than the previously reported value of 220 cm^{-1} for the FWHM of sub-bands in the red absorption region of LHCII [55]. However, the FWHM as obtained there was estimated indirectly by deconvolution of the absorption spectrum into Gaussian sub-bands, the outcome of which depends strongly on the assumed substructure model. In order to account for the uncertainty of the linewidth, in the following calculations we employ an average value of 240 cm^{-1} with an error range of $\pm$40 cm^{-1}. Under this assumption a 2.3($\pm$0.8)-fold size enhancement of the transition-dipole strength can be derived. The most obvious reason for such an enhancement is redistribution of oscillator strength by excitonic interaction between Chl molecules, thus forming the terminal emitter in LHCII. The magnitude of redistribution depends thereby on the interacting Chl-species, the distance between them and the geometrical arrangement of their transition dipoles [64]. Hence, this coupling involves *at least* two Chls, assuming that all Q_y-oscillator strength of both molecules is redistributed to the lower exciton state.

In a recent study, Rogl and Kühlbrandt [37] reported the assignment of the lowest Chl *a* transition at around 680 nm to the Chl-binding site **a2.** Please note that the designation of Chl-binding sites in this paper refers to the original nomenclature of Kühlbrandt et al. [6]. These must not necessarily correspond to Chls *a* and *b*, since a few reassignments (see, e.g., [37]) had to be introduced recently. On the other hand, theoretical calculations of the Q_y-transition energies for Chls in LHCII considering their unique (binding-site dependent) environment resulted in a value of only 670 nm for Chl **a2** (14918 cm^{-1} for attachment to the Asparagin residue, see [32]). For that reason an additional mechanism - like excitonic coupling - must be responsible for the experimentally observed shift of Chl **a2** to about 680 nm. Furthermore, the existing structural model shows that the shortest center-to-center distance between two Chls in LHCII is that of Chl **a2** and **b2** with 8.3 Å [6]. Therefore, the size enhancement of the transition-dipole strength of the terminal emitter is discussed in the following section with respect to possible excitonic coupling of Chl **a2** to its nearest neighbors.

The 3D-structure allows the estimation of the mutual orientations of the corresponding Chl molecular planes, while the orientations of the transition dipoles within these planes are not determined, yet. Assuming that the dipole moments are oriented along the diagonals of their tetrapyrrole rings, a binary model for the orientations was developed by Gradinaru et al. [14]. Based on this, van Amerongen and van Grondelle [40] presented calculations of excitonic coupling strengths for all Chl sites, yielding the highest value of $V_{a2/b2}$ = 121 cm^{-1} for the Chl **a2/b2** pair (cp. Eq. 2, p. 18). This value, however, is insufficient for the formation of delocalized excitonic states. Kimura et al. [31] have outlined the approximate condition for exciton delocalization as $4V > 3\Gamma$, where V is the coupling strength and Γ is the homogeneous linewidth caused by dynamic disorder. For Γ = 185 cm^{-1} (cp. [55]) and $V_{a2/b2}$ = 121 cm^{-1} this condition is obviously not fulfilled. Hence, for the diagonal orientation of the transition dipoles within the tetrapyrrole ring a size enhancement by excitonic coupling cannot be explained. However, several attempts have been made to determine the exact

orientation of the Q_y- and Q_x-transition dipole moments of Chls within their molecular frames. Vrieze and Hoff [153] have described the orientation of the Q_y-transition in Chl a as to be rotated by about 20º out of the diagonal in the tetrapyrrole ring. A similar value was recently used by Simonetto et al. [154] for determination of the Chl orientations in the minor antenna complex CP29. Although the question remains whether this angle is conserved for Chls bound to a protein matrix, it provides four new reasonable configurations of the mutual dipole arrangement of the Chls **a2** and **b2**, which are worthy of investigation. As it turns out, one of these orientations increases the calculated dipole-dipole interaction energy considerably. In this configuration, the Q_y-transition dipoles of Chl **a2** and **b2** are oriented nearly in one plane with the center-to-center distance vector and enclose an angle of only 23°. Following the calculation procedure employed by van Amerongen and van Grondelle [40] (cp. Eq. 2, p. 18), this configuration results in a larger geometrical factor $\kappa = 1.38$ and thus yields $V_{a2/b2} = 181\ \text{cm}^{-1}$.

A value of $\lambda_c \approx 668\ \text{nm}$ for the Q_y-(0-0) transition band of Chl a in protein environment was experimentally determined in [155], which corresponds sufficiently to the calculation for Chl **a2** by Nishigaki et al. [32]. Assuming the same spectral shift, a value around 648 nm can be obtained for Chl b within the protein. Basing on the coupling and geometry as obtained above, these values yield in the calculation according to van Amerongen et al. [64] the following two excitonic sub-bands: One centered at 671 nm with 1.6-times the dipole strength of monomeric Chl a and another one at 645 nm with less than 0.4-times the dipole strength of Chl b. This model of an excitonically coupled Chl-a/b heterodimer fits the lower limit (1.5-fold) of the obtained size enhancement of the acceptor species. Nevertheless, the calculated shift by only 3 nm is not consistent with the experimental results – i. e. under the assumption of the uncoupled Chl-a transitions being centered at 668 nm.

At this point, it is interesting to note that the assignment of Chl a or Chl b to the distinct binding sites in the structural model has been made only tentatively, i.e. relying on the necessity of Chl a triplet-state quenching by carotenoids [6]. This assignment was confirmed for several binding sites by analyses of reconstituted complexes in which individual Chl-binding amino acid residues had been removed by site-directed mutagenesis [37]. On the other hand, population of site **b3** by Chl a was also verified therein. Remarkably, Chl **b2** is one of three chromophores in LHCII for which *no* Mg-coordinating amino-acid residue can be defined in the protein sequence. The presumed population with Chl b can thus not be checked by site-directed mutagenesis. Hence, in principle an alternative assignment of this chromophore to Chl a is conceivable. Excitonic calculations of a tentative Chl-a homodimer located at sites **a2** and **b2** with the favorable geometry as described above yields a coupling strength of 216 cm^{-1}. This would result in one transition at 678 nm with dipole strength of 1.9-times that of

monomeric Chl *a* and another one at 659 nm with less than 8 % of the dipole strength of Chl *a*.[*]

For both models, the homo- as well as the heterodimer, the dipole-dipole interaction fulfills the condition for exciton delocalization $4V > 3\Gamma$ using $\Gamma = 185$ cm^{-1} according to Zuchelli et al. [55]. Interestingly, this relation still holds for $\Gamma = 240$ cm^{-1}, a value that is higher than the maximum Γ consistent with the total FWHM of the sub-band (see above). On the other hand, the calculated coupling strength to further neighbors of Chl **a2** in the frame of the present structural model did not suffice to meet the delocalization criterion. For example, the Chl-**a2**/**a1** interaction amounts to only 26 cm^{-1}. Although at a first glance calculations assuming a homodimer fit the experimentally obtained values better than a heterodimer, one has to consider a possible hyperchromic effect redistributing oscillator strength from the Soret-band into the Q_y-band. Such an effect has been observed to accompany strong excitonic interaction between Chls *a* in aggregates as formed in 50 % aqueous DMSO (see Section 3.3.1). For this system, assumed to consist of dimeric subunits, redistribution of oscillator strength from the Soret- to the Q_y-band on the order of 30 % has been observed. Such hyperchromism has also been discussed for the highly related BChls, e.g. by Scherz and Parson [52]. A hyperchromic effect of comparable magnitude would further increase the calculated transition dipole of the lower excitonic state in the case of the heterodimer to a factor of about 2. Unfortunately, a quantitative calculation of hyperchromic oscillator strength redistribution is impossible without detailed knowledge about the energy levels in the Soret-region. Hence, we cannot reliably determine the type of the dimer in this study. Recent results obtained by evaluation of stepwise two-photon excited fluorescence from the B_x-state (Soret-band) gave strong hints for the existence of a Chl *a/b* heterodimer in LHCII - probably located at the sites **a2**/**b2** [61]. Under this assumption, the deviation in the exciton band position for the Chl *a/b* heterodimer as calculated above (671 nm) necessitates a larger spread of the original (molecular) transition energies due to pigment-protein interactions (cp. [32]).

3.4.3 Summarizing discussion

The findings of an enhanced absorber/emitter of excitonic origin at the red edge of the Q_y-absorption band are consistent with results from linear and circular dichroism measurements [53, 71]. In particular, the strongest features in CD spectra of LHCII appear between 676 and 685 nm. This may well indicate the existence of an excitonic band in this region. Any corresponding higher energetic excitonic transition was not identified yet due to the specific structure of the CD spectrum and probable superposition of several bands. In contrast to this, hole burning studies at low

---

[*] The assumption of Chl-*a* homodimers at site **a2**/**b2** became internally known as 'Malmö interpretation', since the idea was born during a one-week visit of W.J.D. Beenken at my temporary living place in Malmö.

temperature have not revealed the existence of a fluorescent excitonic state, which can be convincingly explained by the expected change of the final acceptor with increasing temperature (see Section 3.2.2). Interestingly, the first results from single-molecule spectroscopy applied to LHCII can be also interpreted in terms of a single emitter per LHCII monomer.[*] The photo-bleaching of single trimeric LHCII units occurs in mainly three steps, while the degree of polarization increases with each step to nearly one (see Fig. 3.4.4, left panel). Furthermore, LT emission spectra of monomeric LHCII are typically characterized by one fluorescence band, while trimeric units emit with three bands (see Fig. 3.4.4, right panel). Accordingly, only *one* major emitter per LHCII monomer can be expected *at one time*.
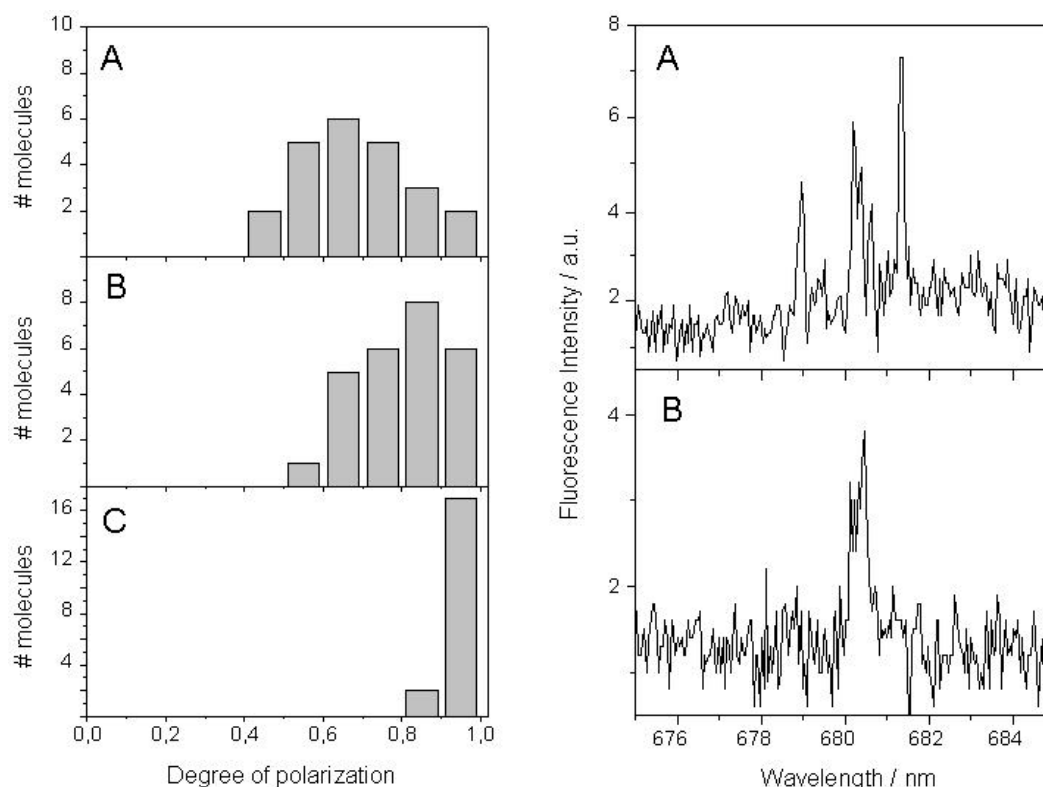

Figure 3.4.4 Left panel: Bleaching behavior of single LHCII trimers at room temperature. The histograms show distributions of the polarization degree before the third last step (**A**), the second last step (**B**), and the final step (**C**) of bleaching. **Right panel:** Typical emission spectra of a trimeric (**A**) and monomeric (**B**) LHCII at low temperature (T = 1.8 K). Both images were taken from [109] with kind authorization by Dr. C. Tietz (Stuttgart University).

The previous two sections have provided evidence for excitonic coupling of Chls in LHCII. In particular, a nearly in-line dimer was identified that forms the main fluorescence emitter by its lower exciton state. Moreover, the proposed Chl dimer can be related to Chl-binding sites **a2** and **b2** in the LHCII structure [6] by using the spectral assignment from Chapter 3.2. In this context, two alternatives of a Chl-*a/a* homodimer or Chl-*a/b* heterodimer are consistent with the experimental results. The distinction

---

[*] These data were obtained in the framework of a co-operation with the group of Prof. J. Wrachtrup (Stuttgart University). The author was involved as one of the project initiators and co-author in the resulting publication (see also Fig. 3.4.4).

between both cases is especially hampered by uncertainties in applicable theoretical calculations. Above all, the coupling strength in heterodimers would not be sufficient to explain red-shifts of the lower exciton band from 670 nm (as calculated for Chl **a2** in [32]) to 680 nm. However, this calculation assumed a refractive index of 1.6 (cp. [77]), while the correct estimation of the electric shielding between two very closely neighboring Chls is hard to assess. Moreover, recent studies by Knox [51] suggested higher transition-dipole moments for Chls than previously reported [49, 50]. Consequently, the split between exciton states in heterodimers would increase, thus matching much better the observed value of 680 nm. Recent observations of excitonic coupling between Chl *a* and *b* as obtained from two-photon excited fluorescence and NLPF in the Soret-region [41, 61] strongly support this idea. In addition, the evaluation of NLPF spectra in Chapter 3.5 will partly support this conclusion of a heterodimer.

The most important discrepancy to other results, i.e. fluorescence-quantum yield measurements, are also briefly discussed. Palacios et al. [156] have found only ~1.1-times increased transition-dipole moment(s) for the fluorescent state(s) in LHCII. Their calculations were based on an observed lower fluorescence quantum yield (~20%) and simultaneously decreased fluorescence lifetime (~3.5 ns) in LHCII when compared to Chl in solution (~30%, ~5.5 ns). In particular, the reduced lifetime is expected to be a direct result of fluorescence quenching at the emitting state(s). In contrast, a different picture must be drawn if both effects are assumed to have distinct origin. Certainly, the formation of excitonic states with increased transition probability reduces their fluorescence lifetime to the same extent, since the Einstein-coefficient is correspondingly increased. Hence, the fluorescence lifetime of 3.5 ns as observed in LHCII could be a direct result of about 1.6-fold transition probability in comparison to monomeric Chl in solution. If - simultaneously - the observed fluorescence quenching occurs predominantly at *different* Chl sites, the presumptions in [156] are not applicable. In this context, it is interesting to refer to other recent investigations studying carotenoid-driven Chl quenching in LHCII [157]. In this study, Chl **a1** was identified to perform the majority of (T_1)-triplet quenching. This observation indicates that both pigments are closely neighboring in LHCII and the resulting considerable interactions may lead to (S_1)-singlet quenching. Since the possible existence of mainly *one* effective S_1-quencher, i.e. at this binding site **a1**, cannot be excluded, the increased transition probability found in this thesis is not in contradiction to the experimental results reported in [156].

Finally, the determination of an enhanced excitonic transition revealed additional information that is required to understand the complicated sub-structure of the Q_y-absorption region of LHCII. This forms – together with the tentative sub-structure model obtained in Chapter 3.2 – a firm base to evaluate NLPF spectra of this complex in the following. The outcomes discussed in Chapter 3.3 and 3.4 were obtained by straightforward applications of nonlinear laser spectroscopic techniques. Accordingly, the achieved results are equally related to the topic of this thesis like the NLPF applications discussed below.

3.5 Refining the parameter model of LHCII: Discussion of the nonlinear polarization response

3.5.1 Certainties and uncertainties about the LHCII parameter model

The detailed analysis of multi-level absorption systems in Chapter 3.1 revealed that the comprehensive evaluation of their NLPF spectra includes a large number of relevant parameters. Consequently, substantial additional information – i.e. a basic absorption sub-structure model – is required to study such systems. Accordingly, this kind of information was gathered for the LHCII complex in previous Chapters 3.2-3.4 by different experimental approaches. Several model parameters were further investigated by other authors on the basis of either comparable or rather different methods. Hence, all results presented in the previous sections are shortly discussed at this point with respect to supplementary information in the literature.

The first issue refers to proper assignments of Chls *a* or *b* to the respective binding sites. Besides the mutation analysis described in Chapter 3.2, especially Remelli et al. [38] and Yang et al. [39] have studied Chl assignments in reconstituted LHCII. Their findings are rather similar to the results presented here except that mixed Chl *a* and *b* occupations were reported in both studies for certain binding sites. For example, Remelli et al. [38] observed a 50:50% occupation probability with Chl *a* and *b* at binding sites **a3** and **b3**. This outcome could not be confirmed by investigating a highly similar mutant as discussed in Chapter 3.2. In this context, it has to be repeated that the reconstitution conditions in both experiments varied considerably. In particular, a lower Chl *a*/*b* ratio during reconstitution is reported in [38]. The question whether the observed promiscuity is a result of *in-vitro* protein folding or a phenomenon also observable *in vivo* is therefore still a matter of debate. Consequently, mixed occupations were *not* considered in the following, since all NLPF experiments were performed by using native (isolated) LHCII. This assumption nicely fits to the observation of pure Chl *a* occupation at binding site **b3** in Chapter 3.2. Consequently, an assignment of site **a3** to Chl *b* becomes most likely: In this case, the explanation of promiscuity in [38] and [39] could originate from somehow co-operative binding of both closely neighboring Chls to the protein (Chl *b* at **a3** and Chl *a* at **b3**). Mutations at *one* binding site may thus result in losses of *both* Chl species, thus pretending mixed occupancy at both sites.

Finally, it should be noted that an assignment of binding site **b1** to Chl *a* as well as promiscuity for the sites **a6** and **a7** was also suggested in [38]. Nevertheless, indications for this are rather scare, since they originate from indirect interpretation of the mutation analysis. Above all, LHCII proteins exhibit no distinct binding sites (e.g., polar amino-acid residues) for the Chls **b1**, **b2** and **a7** that could be modified. Moreover, modification of binding site **a6** does not yield any changes in the pigment composition after protein folding. For that reason, the Chl assignment of all four sites was presumed unknown in the following simulations. This assumption includes also uncertainty about the origin of the excitonic transition centered at ~680 nm as a result of Chl-*a*/*a* or Chl-*a*/*b* coupling at binding site **a2**/**b2** (see Chapter 3.4). In contrast to the differences discussed above, the

assignments of all other binding sites seems to be properly verified according to similar results in [38] and Chapter 3.2. The corresponding Chl species at agreeably assigned binding sites are indicated by different colors in Fig. 3.5.1.

A second question concerns correct assignments of binding sites to distinct bands in the absorption sub-structure. In this context, good matches between results in Chapter 3.2 and [38] are obtained for the sites **a2**, **a5**, and **b6**. Within an error range of ±2 nm, the corresponding bands are located at λ_c = 680 nm, 672 nm, and 650 nm, respectively. Remelli et al. [38] have further obtained values for λ_c at the sites **a1** (679 nm), **a4** (674 nm), and **b5** (652 nm). These numbers corresponds well to certain bands in the absorption sub-structure model established in Chapter 3.2 (taking into account errors of ±2 nm; cp. Table 3.2.5 and Fig. 3.2.9, p. 76). The band with double amplitude centered at ~671 nm obviously represents a superposition of the bands from sites **a4** and **a5**. Since the Chls **a6**, **a7**, **b1** and **b2** are not accessible by site-directed mutagenesis studies, explicit assignments have not been obtained in these cases, yet.[*] Nevertheless, Chl **b2** can be related under the assumption of excitonic coupling between the Chls at binding site **a2/b2** to the observed band with $\lambda_c \approx 680$ nm (cp. Chapter 3.4). Ambiguity must be further assumed for the band corresponding to site **a3**. All accessible information about λ_c of the Q_y-bands at distinct binding sites in LHCII is summarized in Fig. 3.5.1. Following the remarks above, all determined wavelengths are adjusted to fit the model from Table 3.2.5 (p. 76).

The last parameters required to model the nonlinear response of the Q_y-region in LHCII are the Chl transition-dipole orientations. According to remarks in Chapter 1.2.1, two singular orientations ('0' and '1') can be presumed within the structural model proposed by Kühlbrandt et al. [6]. Several studies addressed the distinction between these two cases for each individual Chl. Gradinaru et al. [14] have used a combination of LD, CD, and transient-absorption spectra to determine transition-dipole orientations in LHCII. An additional study based on similar data was reported by Iseri and Gülen [73]. Nevertheless, the results of such simulations depend strongly on the presumed initial parameters. In particular, different assumptions about site occupation with either Chl *a* or *b* can result in considerably deviating simulations of the dichroism spectra or EET scheme. Since the assignment of binding sites **a3**, **a6**, **a7**, **b1**, **b2**, and **b3** turned out to be uncertain in these previous studies (see above), the results obtained there are also rather vague. For that reason, the orientation of Chl transition dipoles has been assumed unknown in all simulations of NLPF spectra in the following – with one exception. The observation of enhanced transition probability suggests nearly in-line arrangement of the Q_y-dipoles for Chl **a2** and **b2** in Chapter 3.4. Consequently, both dipoles were fixed to the corresponding '0'-orientation for sub-structure models considering this excitonic transition (cp. Table 1.2.1 and Fig. 1.2.5, pp. 9).

Figure 3.5.1 illustrates known and unknown Chl parameters, which are essentially required to understand EET processes among their first-excited states in LHCII. Despite

---

[*] Although transition wavelengths are reported for *each* binding site by Remelli et al., the parameter model obtained there is clearly incompatible with the total absorption spectrum of LHCII (cp. Fig. 3.2.1, p. 65).

of quite sufficient knowledge about several Chls, the remaining uncertainties cause still a high number of possible EET schemes, i.e. >30.000 possible combinations. Since the variation of one single parameter may change the EET scheme as well as resulting NLPF spectra significantly, experimental model verification becomes a difficult objective. Nevertheless, it turned out that some model parameters show less impact on the NLPF spectrum than others. For that reason, different parameter 'levels' are distinguished in the following to further improve the comprehensibility of the performed model evaluations.
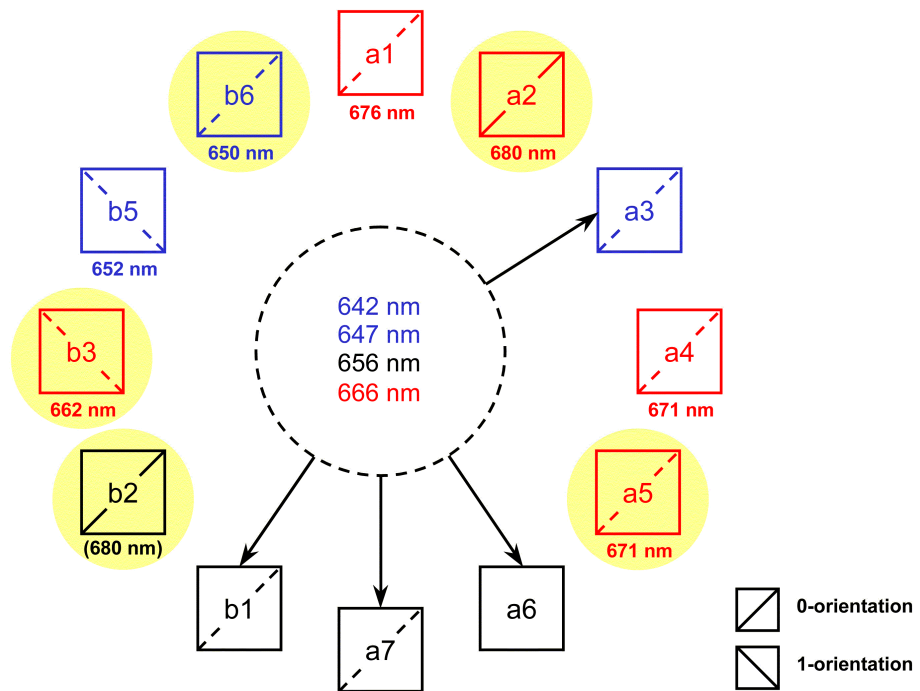
Figure 3.5.1 Summary of available structural and spectral information about the Chl binding sites in LHCII including Chl-assignments (Chl *a*: red, Chl *b*: blue, unknown: black). All λ_c of the Q_y-bands are in agreement with the sub-structure model from Table 3.2.5 (p. 76), but the remaining λ_c from the sub-structure model indicated in the center circle are not assigned yet. Diagonals indicate transition dipoles in orientation '0' or '1' (solid = fixed and dashed = variable for NLPF simulations). In the framework of this thesis, essential information could be obtained for the yellow-marked sites *before* evaluation of NLPF measurements (see Chapters 3.2-3.4). Additional parameters were taken from the literature as discussed in the text. In particular, the dipole orientations have been suggested in [14].

The first parameter level is related to the observation of enhanced transition probability as discussed in Chapters 3.3 and 3.4. Based on these results, the NLPF spectra should be also investigated with respect to possible dimer formation at the binding sites **a2**/**b2**. Three fundamental models can be discerned in this context, comprising either the existence of a Chl-*a*/*a* dimer, a Chl-*a*/*b* dimer, or no excitonic coupling at all. The first and last case can be directly evaluated by using the absorption sub-structure model obtained in Chapter 3.2 (see Table 3.2.5, p. 76). For that purpose, the two-fold increased absorption band with $\lambda_c \approx 671$ nm is separated into two transitions representing the absorption of Chl **a4** and **a5**. Furthermore, the second band with double amplitude ($\lambda_c \approx 680$ nm) is assumed as *one* excitonic transition to simulate the existence of a Chl-*a*/*a* dimer. Without coupling, the transition probability is separated into *two*

bands, which reflect the absorption of one Chl *a* at binding site **a2** and one Chl *a* at site **a6**, **a7**, **b1** or **b2**.

Concerning the third case of Chl *a/b* coupling at binding sites **a2/b2**, the sub-structure model from Table 3.2.5 (p. 76) is not directly compatible with the existence of such a heterodimer. In particular, the maximum transition probability of the lower exciton band is only ~1.6-fold increased when compared to monomeric Chl *a* (see Chapter 3.4). Accordingly, a slightly modified sub-structure model was obtained by reducing the relative area of the 680 nm band from 2.0 to 1.6. At the same time, one Chl *b* band must be swapped for Chl *a* by increasing its relative area in the model from 0.7 to 1.0 as applied to the band with the longest $\lambda_c = 656$ nm. These changes require further minor band shifts as summarized in Table 3.5.1 to fit the measured absorption spectrum (cp. initial values in Table 3.2.5 and Fig. 3.2.9, p. 76). Especially the two bands of Chl **a4** and **a5** are no longer identical but shift slightly apart to 671 and 674 nm, respectively. Nevertheless, all other characteristic features of the previous sub-structure model are conserved.

Table 3.5.1 Modified sub-structure model of the LHCII absorption spectrum considering formation of an 'in-line' heterodimer at binding sites **a2/b2** (see text). Eleven sub-bands (Voigt-profiles) are identified by λ_c [nm], Δ [nm], 2Γ [nm] and α [a.u.]. The Lorentzian in the first column with $\lambda_c = 618$ nm summarizes higher vibrational (0,1)-transitions of Chl *a* interfering with (0,0)-transitions of Chl *b*. The Voigt-profile in the second column ($\lambda_c \approx 648$ nm) reflects 0.5 Chl *b* unspecific bound per LHCII monomer.

λ_0	618.0	647.8	642.7	648.0	650.5	652.2	658.8	663.0	668.0	670.7	673.6	676.5	680.0
α	6.2	0.35	0.7	0.7	0.7	0.7	1	1	1	1	1	1	1.6
2Γ	50	12	11	10	10	12	12	11	9	9	9	8	8
Δ	-	14	5	5	5	5	5	5	5	5	5	5	5

The three coupling models were studied separately because of their differing absorption sub-structure. Based on this major distinction, the Chl assignment to binding sites **a6**, **a7**, **b1**, and **b2** comprises the second parameter level. Remaining uncertainties about the assignment of two Chl *a* and two Chl *b* in LHCII (see Fig. 3.5.1) allow different combinations as summarized in Table 3.5.2. All six combinations are possible, if excitonic coupling at site **a2/b2** is excluded. In contrast to this, the assumption of a Chl-*a/a* or Chl-*a/b* dimer restricts variations to the first and last three rows, respectively.

Combination of the three coupling cases with different Chl assignments from Table 3.5.2 results finally in a set of 12 basic models. Consequently, identification of the model that embodies the best LHCII representation can be seen as a key task of NLPF analyses in this work. In principle, each model had to be compared to measured NLPF spectra for all possible combinations of the two dipole orientations per individual Chl, which represent accordingly the third parameter level. It is essential to remember at this point that dipole orientations are reflected in NLPF spectra in two different ways. First, the geometrical factor g_{mn} in Eq. 22/23 (p. 37) directly relates the dipole directions of two transitions that are connected by either excitonic coupling or EET. Secondly, the orientation has an impact on EET rates itself according to Eq. 1 (p. 17). Hence, *each*

change of a Chl dipole orientation is reflected in both, the geometrical factor g_{mn} *and* the EET rate γ_{nm} (the latter via β_{mn} according to Eq. 21, p. 37).

Table 3.5.2 Six possible combinations of Chl occupation at different binding sites of the LHCII complex, which have not been evidently assigned yet (cp. Fig. 3.5.1).

a6	a7	b1	b2
Chl *a*	Chl *b*	Chl *b*	Chl *a*
Chl *b*	Chl *a*	Chl *b*	Chl *a*
Chl *b*	Chl *b*	Chl *a*	Chl *a*
Chl *a*	Chl *a*	Chl *b*	Chl *b*
Chl *a*	Chl *b*	Chl *a*	Chl *b*
Chl *b*	Chl *a*	Chl *a*	Chl *b*

Last but not least, the fourth level of variable parameters is formed by the yet unidentified assignments of four λ_c to certain Chl sites (see Fig. 3.5.1). This uncertainty increases the total number of possible models by a factor of 4, if the two shorter and two longer wavelengths in the sub-band model are implicitly assigned to Chl *b* and *a*, respectively. Nevertheless, the exchange of λ_c with differences of less than 10 nm shows only slight effects on NLPF spectra. Hence, this assignment was only used for final refinements of the best model fits to distinguish the two possible band assignments for Chl *a* and Chl *b*.

3.5.2 Obtaining basic LHCII parameters from NLPF spectra

In the previous section, separate levels of LHCII parameters are distinguished to enhance the clarity of NLPF simulations performed in the following. This approach resulted in a starting point of *twelve* models with deviating Chl occupations at certain binding sites and with or without dimeric coupling between the Chls at site **a2/b2**. In principle, a global analysis can be performed for each of these 12 models by fitting NLPF spectra for all possible orientation combinations in either '0' or '1' direction. To reduce the number of required calculations for this approach, an initial analysis addressed the significance of orientation variation for each individual Chl. As a general result, Chl *b* orientations had much less impact on NLPF spectra because of fast EET from Chl *b* to Chl *a* as discussed previously in Chapter 3.1.5. Hence, an initial series of NLPF fits was performed with fixed Chl *b* orientations ('0'-direction). This reduction yielded *one* set of best-fitting Chl *a* orientations for *each* of the 12 investigated models. (The differences were evaluated by using the global χ^2-value calculated during the fit procedure as described below.) These tentative models were then further analyzed with respect to Chl *b* directions. Nevertheless, the observable χ^2-variations are at least ten times lower for Chl *b* orientations when compared to Chl *a*.

Due to the above-mentioned impact of dipole orientations on EET rates and geometrical factors, each orientation model requires re-calculation of several matrix

elements g_{nm} and β_{nm}. To reduce the resulting calculation expenses, EET rates have been approximated by neglecting their exact dependence on λ_c. Strictly speaking, 'downhill' EET rates would be increased as compared to 'uphill' rates (see Chapter 1.3.1). However, equal overlap factors C_{AB} independently from λ_c have been assumed, since the differences between transition energies among one Chl species are rather moderate. EET between Chl a and Chl b was certainly weighted by the deviating overlap terms $C_{a,b}$ and $C_{b,a}$, respectively (cp. exact values on p. 18). These factors reflect good approximations of the underlying energetic differences in the thermal equilibrium.

Finally, the required number of calculations was executed under the assumptions above with reasonable time expenses. In particular, fits were performed for NLPF spectra recorded at ten different λ_t ranging from 645 to 690 in 5 nm steps. The fit procedure calculated total errors χ^2 between model simulation and measurement as the weighted sum of standard deviations for each single data point. All values obtained per individual spectrum are then averaged to a 'global' χ^2. Since different models were compared on the basis of this global χ^2, the procedure is referred to as 'global analysis' in the following. The first major consequence from global NLPF analyses of different LHCII models concerns excitonic coupling at binding sites **a2/b2**. According to the procedure described above, six different occupation models for the sites **a6**, **a7**, **b1** and **b2** (see Table 3.5.2) were tested under consideration of three possible coupling cases at sites **a2** and **b2**. In the resulting fits of NLPF spectra, all models presuming a Chl-a/a dimer resulted in global χ^2-values well above 2.0. In contrast, the other models considering either a Chl-a/b dimer or no coupling resulted in numbers well below 1.5 (see Fig. 3.5.2). Hence, the results of NLPF measurements are apparently incompatible with the existence of a Chl a homodimer at site **a2/b2** and corresponding formation of an excitonic transition with two-fold increased transition probability.

On the contrary, a distinction between heterodimer and uncoupled case on the basis of NLPF spectra turned out to be impossible. This is illustrated in Fig. 3.5.2, where the *best* three model fits are directly compared. These models (summarized in Table 3.5.3) resulted in the lowest global χ^2-values obtained in the framework of this study. Interestingly, model **A** does *not* consider excitonic coupling, while model **B** and **C** were based on the assumption of a Chl a/b dimer at sites **a2/b2**. (Please note that the underlying absorption sub-structure differs between both model types as discussed previously in Section 3.5.1.) The small remaining differences are indeed insignificant. For example, model **C** yields a lower χ^2-value than model **B,** if the first measurement at $\lambda_t = 645$ nm is neglected. On the other hand, model **A** has one additional degree of freedom according to the extra absorption band within this model, thus improving the fit results to some extent. However, these minor differences are ignorable in comparison to the remaining uncertainties about *exact* dipole orientations. Due to the achievable resolution of 3.4 Å in the structure analysis [6], average errors of ±10 ° for the two angles θ and φ could be expected (cp. Table 1.2.1, p. 9). Consideration of this additional variability would certainly result in better fits, but was omitted because of ambiguity.
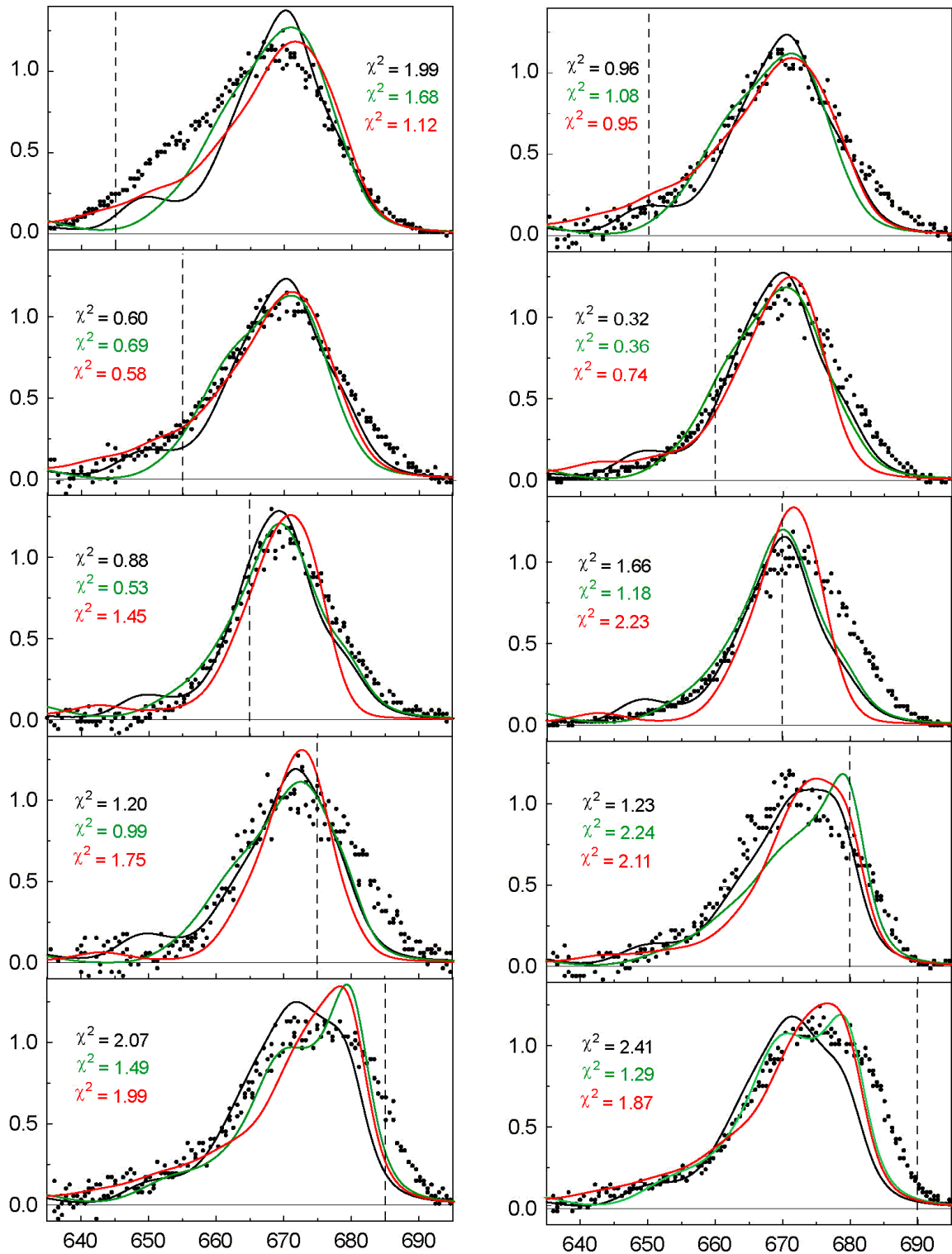
Figure 3.5.2 Results from global analyses of NLPF spectra of trimeric LHCII. In each graph the x-axis describes variations of λ_P, while the y-axis represents the corresponding (normalized) NLPF signal. Black dots indicate original NLPF data points and vertical dashed lines illustrate different λ_t. NLPF simulations are presented for three population models, which yielded the lowest global χ^2-values. The main characteristics of these models are: **A** (black) - no excitonic coupling, similar Chl occupation like model **B** with some different Chl orientations; **B** (green) - excitonic coupling at sites **a2/b2**, similar Chl occupation like model **A** with some different Chl orientations; **C** (red) - excitonic coupling at sites **a2/b2**, different Chl occupation at sites **a6/a7** and some different Chl orientations (for details see Table 3.5.3). The following global χ^2-values were obtained: 1.27 (model **A**), 1.32 (model **B**), and 1.38 (model **C**).

The next question concerns yet unidentified assignments of certain binding sites (**a6**, **a7**, **b1**, **b2**) to Chl *a* or *b*. From the best-fit models in Table 3.5.3 one can directly obtain a highly likely occupation of site **b1** with Chl *a* and site **b2** with Chl *b*. Nevertheless, an unambiguous assignment of the other two sites (**a6** and **a7**) to one remaining Chl *a* and one Chl *b* is nearly impossible. Even under consideration of the strong support for models **B** and **C** by the investigations in Chapter 3.3 and 3.4, this drawback remains evident. Consequently, the evaluation of NLPF spectra further clarifies the assignment of binding sites **b1** and **b2**, but reveals no clear information about the last unidentified sites **a6** and **a7**.

Table 3.5.3 Three LHCII parameter models yielding the lowest χ^2-values in global analyses of NLPF spectra. The numbers indicate Q_y-transition dipole orientations in either '0'- or '1'-direction, while their colors specify presumed site occupation with Chl *a* (red) or Chl *b* (blue). In addition, the formation of a Chl-*a*/*b* dimer at binding sites **a2**/**b2** was assumed for model **B** and **C**, while model **A** contains no excitonic interaction.

	a1	a2	a3	a4	a5	a6	a7	b1	b2	b3	b5	b6
Model A	0	0	1	1	1	1	1	1	0	0	1	0
Model B	0	0	1	1	1	0	1	1	0	0	0	1
Model C	0	0	0	1	0	1	0	0	0	0	0	0

These remaining uncertainties about Chl assignments hamper also the identification of individual transition-dipole orientations to some extent. Unequivocal conclusions can be drawn for the following Chl *a* orientations: **a1** = 0, **a2** = 0, **a4** = 1, and **b3** = 0. This outcome is especially confirmed by the simulation in Fig. 3.5.4 (left panel), where orientations of the mentioned sites are presumed in opposite direction (see further below). Besides this, dipole orientations **b2** = 0 and **b5** = 0 are indicated for these Chls *b*, but on a much lower confidence level (cp. the remarks about Chl *b* parameters above). Obviously, no orientation preference can be gained for the Chl *b* sites **b6** and **a3**. Dipole orientations of the remaining sites **a5**, **a6**, **a7**, and **b1** require a more detailed discussion. On one hand, the orientation at sites **a5**, **a7**, and **b1** is strongly favored in '1'-direction, if the assignment of site **a6** is fixed to Chl *b*. In particular, all global fits of NLPF spectra for either model **A** or **B** yield χ^2-values well above 2.0, if one (or more) of these sites is assumed in '0'-direction. On the contrary, the exchange of Chl assignments between **a6** and **a7** clearly supports '0'-orientation for the mentioned sites by an analogous motivation for model **C**. Hence, it can be concluded that the NLPF method provides a firm base for the determinations of dipole orientations in heterogeneous pigment-protein systems like LHCII, especially for Chl *a*. Unfortunately, the success of this approach is partly hindered by still uncertain Chl assignments for site **a6** and **a7**.

In this context, it should be briefly mentioned that the previously reported attempt to determine dipole orientations in LHCII [14] was based on certain, not explicitly verified Chl assignments. Hence, it should be emphasized that the incompleteness of determined Chl *a* orientations is a result of the actual uncertainty for Chl binding at sites **a6** and **a7**, but not an intrinsic drawback of the method. A different picture must be drawn in the case of Chl *b*. The observed weak dependence of NLPF spectra on Chl *b* orientations is

directly related to their effective EET towards Chl *a*. Following the discussion in Chapter 3.1, these fast EET rates reduce contributions from Chl *b* transition bands to the NLPF signal. For that reason, the significance of certain Chl *b* parameters in NLPF spectra is *indeed* lower as compared to Chl *a*.

This behavior strongly suggests a combined evaluation of time-resolved pump-probe spectra as described in [14] *and* NLPF measurements to determine dipole orientations without the shortcomings of each individual method. The first technique is highly sensitive to Chl *b* orientations, since these species show ultra-fast EET to the spectrally well resolved Chls *a*. At the same time, Chl *a* orientations are much harder to obtain from measured EET rates because of their extensive spectral overlap. This disadvantage could be compensated for by parallel evaluation of NLPF spectra in a combined fit on the basis of identical parameter models. Unfortunately, such a combined evaluation was impossible in the framework of this thesis. In particular, one finds different isolation procedures and detergent treatments for the employed LHCII samples in [14]. Up to now, a detailed influence of these factors on spectroscopic properties of LHCII has not been studied satisfactorily (but unpublished data of B. Voigt indicate considerable changes). For that reason, any comparison of data obtained with differently prepared samples is still beyond the level of adequate scientific understanding. Nevertheless, this experimental combination comprises in principle a highly promising approach for future investigations on the basis of identically treated preparations.

Finally, the most interesting features of the obtained results are discussed in more detail. At the first glance, one observes only small differences between all NLPF spectra of LHCII measured at different λ_t (cp. Fig. 3.5.2). These variations are to some extent lower than expected from the analytical simulations of NLPF signals in Chapter 3.1 (cp. particularly Fig. 3.1.19, p. 62). Nevertheless, it can be unequivocally demonstrated that this observation is a direct result of unique Chl dipole orientations in LHCII. For that purpose, Fig. 3.5.3 and 3.5.4 compare the NLPF spectra of different parameter models, which are closely related to model **B** from Table 3.5.3. To enable a comprehensive comparison of these spectra, the simulations of model **B** are initially summarized for five different λ_t in Fig. 3.5.3 (left panel). The spectra correspond directly to the green curves in Fig. 3.5.2 (left column). A first modification of model **B** (= model **E**) assumes all Q_y-transition dipoles in '1'- orientation as further indicated by the underlying parameter scheme in Table 3.5.4. The resulting NLPF spectra (Fig. 3.5.3, right panel) show a significantly increased λ_t-dependence.[*] Hence, these simulations evidently show that the low variance of recorded spectra results to a large extent from actual dipole orientations of the Chls in LHCII.

This observation is further corroborated by NLPF simulations for model **F** (cp. Table 3.5.4). According to the statements above, the orientations of Chls *a* at binding sites **a1**, **a2**, **a4**, and **b3** can be clearly determined by fitting NLPF spectra, and (weaker) indications can be found for the sites **b2** and **b5**. Consequently, model **F** assumes exactly

---

[*] These spectra are calculated again by considering different dipole orientations in *both* matrix elements g_{nm} and β_{nm} and reflect thus also corresponding changes in the underlying EET scheme.

these dipole orientations in opposite direction, while all other parameters are identical to model **B**. In this case, a remarkable change of the simulated NLPF spectra can be obtained from Fig. 3.5.4 (left panel). Accordingly, the observed alterations reveal again that strong or weak λ_t-dependence is directly related to the underlying orientation parameters of the Chl transition dipole moments.

Table 3.5.4 Two modified LHCII parameter schemes representing special modifications of model **B** from Table 3.5.3. The numbers indicate Q_y-transition dipole orientations in either '0'- or '1'-direction, while their colors specify presumed site populations with Chl *a* (red) or Chl *b* (blue). In addition, the formation of a Chl-*a/b* dimer is presumed at binding sites **a2/b2**.

	a1	a2	a3	a4	a5	a6	a7	b1	b2	b3	b5	b6
Model E	1	1	1	1	1	1	1	1	1	1	1	1
Model F	1	1	1	0	1	0	1	1	1	0	1	1
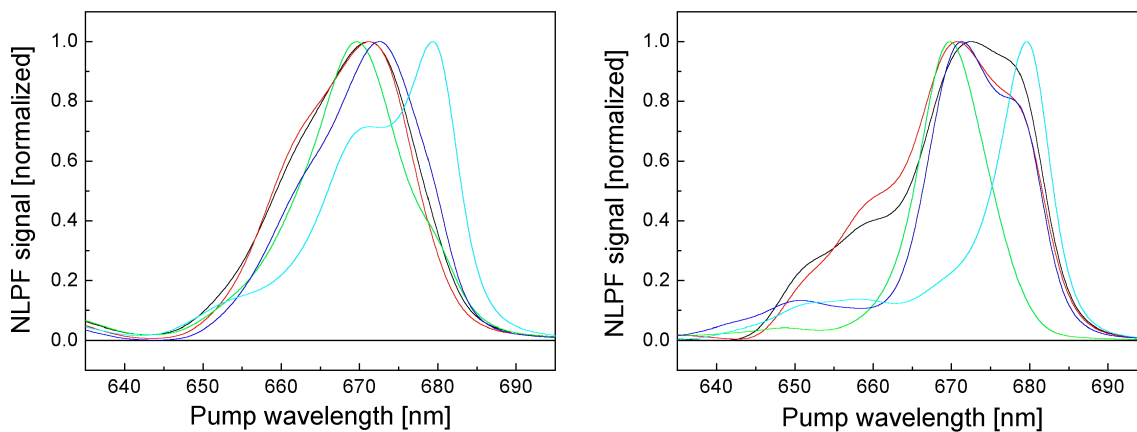
Figure 3.5.3 Simulated NLPF spectra for parameter model **B** from Table 3.5.3 (**left panel**) and **E** from Table 3.5.4 (**right panel**) at λ_t = 645 nm (black), 655 nm (red), 665 nm (green), 675 nm (dark blue) and 685 nm (light blue).
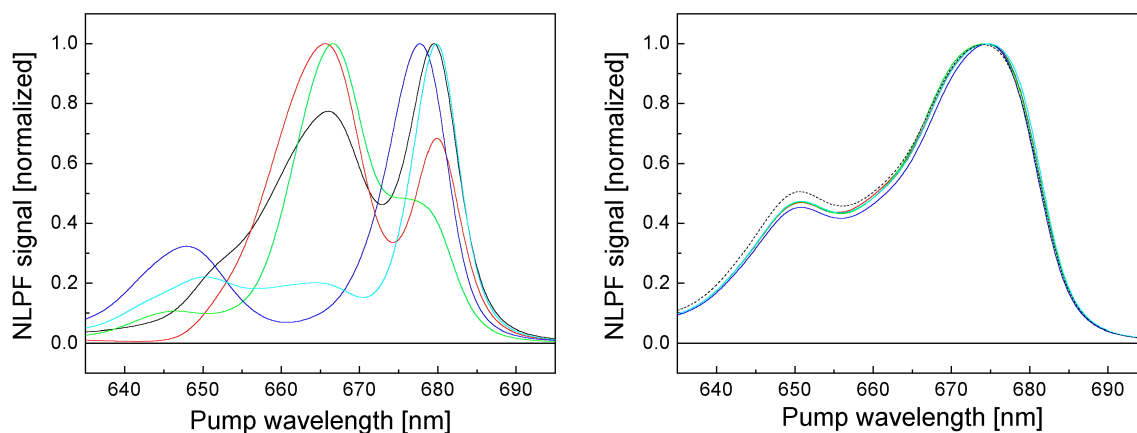
Figure 3.5.4 NLPF spectra simulated for two parameter models at λ_t = 645 nm (black), 655 nm (red), 665 nm (green), 675 nm (dark blue) and 685 nm (light blue). **Left panel:** Model **F** from Table 3.5.4. **Right panel:** Special modification of model **B** from Table 3.5.3: All geometrical factors are set to $g_{nm} = 1$, which corresponds to *parallel* transition-dipole orientations. However, all EET rates were kept similar to model **B** (see text). For better comparison, a squared absorption spectrum is added (dashed line).

This conclusion is further illustrated in Fig. 3.5.4 (right panel). Once more, NLPF spectra are simulated in this graph for a modified parameter scheme on the basis of model **B** from Table 3.5.3. In particular, all employed matrix elements β_{nm} (= EET rates) actually match the assumed dipole orientations from model **B**. In contrast to this, all geometrical factors were set to $g_{nm} = 1$, which corresponds to virtually *parallel* orientation of *all* Q_y-transition dipoles (cp. Eq. 22, p. 37). According to the discussion in Chapter 3.1.3 (see especially the left panel in Fig. 3.1.10, p. 50), the resulting NLPF spectra resemble in this case mainly a squared absorption spectrum. This behavior was related to considerably faster equilibration among the excited states as compared to their fluorescence lifetimes. In other words, the EET rates calculated for the orientations of model **B** actually result in excitation equilibration much faster than the fluorescence decay time in LHCII (~3.5 ns). Similar simulations ($g_{nm} = 1$, but EET rates according to the actual orientation model) resulted in almost identical spectra as shown Fig. 3.5.4 (right panel) for all models **A-F** (not shown). Consequently, the unique features of NLPF spectra originate to the largest extent from the different individual transition-dipole orientations.

Comparison of all models in Fig. 3.5.4 and Fig. 3.5.3 enables an intuitive explanation for the low variance among NLPF spectra measured at different λ_t for LHCII. In particular, the reduced λ_t-dependence can be directly related to the inherent structural arrangement of Chls in this antenna complex. Additionally, the simulations of model **F** offer a firm estimation of the experimental *significance* of the NLPF method when applied to such multi-pigment proteins. Under this point of view, this thesis provided basic understanding of the information content of NLPF spectra, which allowed indeed the determination of (otherwise hardly accessible) structural parameters.

Summary

In this chapter, NLPF spectra in the Q_y-absorption region of LHCII were analyzed to determine yet unidentified molecular parameters of the attached Chls. Especially, assignments of Chl *a* or *b* to different binding sites, Q_y-transition dipole orientations, and possible excitonic interaction have been studied. This evaluation was based on detailed investigations of NLPF spectra for heterogeneous absorption systems in Chapter 3.1 and the establishment of a sufficient sub-structure model in Chapter 3.2. The problem of excitonic coupling was further investigated with respect to previous findings in Chapter 3.3 and 3.4. In this context, the attempted corroboration of excitonic interaction at binding sites **a2/b2** differed from the picture drawn in Section 3.1.2. This analytical section was mainly addressed to universal features of the NLPF method. Accordingly, excitonic interactions in dimeric sub-units have been evaluated for general coupling cases, i.e. the formation of two transition bands with common ground state. In contrast to this, the discussion in Chapter 3.4 strongly suggested the formation of a nearly 'in-line' dimer with basically *one* excitonic transition (cp. Fig. 1.3.2, p. 19). In this case, NLPF spectra cannot reveal excitonic coupling by corresponding parameters in

the β-matrix (see Eq. 20, p. 37), but only via an *increased* transition probability within the absorption sub-structure.

With this approach, the existence of a Chl *a/a* homodimer with 'in-line' arrangement and correspondingly *two*-fold increased absorption at site **a2/b2** was adequately excluded. In contrast to this, the existence of a heterodimer could not be distinguished from the uncoupled case by *pure* evaluation of NLPF spectra. However, the combination of results obtained in this section and in Chapter 3.4 yields in the end satisfactory evidence for an excitonically coupled heterodimer in LHCII. These findings are further in good agreement to recent results obtained by NLPF experiments in the Soret-region of LHCII [41] or the homologue chlorophyll protein CP29 [131].

Hence, the assignment of Chl *b* to binding site **b2** is implicitly confirmed. Moreover, binding site **b1** could be adequately assigned to Chl *a* as previously suggested in [38]. Unfortunately, respective occupations of binding sites **a6** and **a7** with one Chl *a* and one Chl *b* could not be distinguished. This problem has further hampered the determination of several transition-dipole orientations. Nevertheless, unambiguous results with respect to the distinction between '0'- or '1'-orientation were gained for the Chls at sites **a1**, **a2**, **a4**, and **b3**. Additionally, a weak indication was found for the orientation of Chl **b5**, while the orientation for Chl **b2** is again implicitly obtained from the nearly 'in-line' heterodimer. These obtained dipole directions allow further the determination of corresponding inter-pigment EET rates (see Fig. 4.3.1 in Chapter 4.3). Finally, one can conclude that application of the NLPF technique on the intricate molecular system LHCII revealed indeed one part of the so far inaccessible parameter space. Under this point of view, it represents an ideal complement to the existing zoo of spectroscopic methods applied to biological systems, i.e. photosynthetic proteins.

3.5.3 NLPF studies at low temperature and supporting investigations

A major experimental development in the framework of this thesis was the application of NLPF measurements at cryogenic temperatures. These investigations were initiated to enable the comparison to results obtained by other techniques at LT, i.e. hole-burning [54, 110] and single-molecule spectroscopy [109]. NLPF measurements at LT are considerably complicated, since the solid-state phase transition induces strong tensions within the sample volume. The resulting additional birefringence interferes with the NLPF signal and reduces the sensitivity of the method. In principle, this drawback can be compensated for by applying increased pump intensities. However, intensities above the excited-state saturation level result in discrepancies between theoretical weak-field approximation and experimental conditions as discussed in Chapter 3.4 (see especially Fig. 3.4.2, p. 85). These deviations cannot be elucidated for NLPF pump spectra covering the whole Q_y-absorption range within the existing theoretical framework (cp. [1]). For that reason, the phenomenological description below is intended to provide intuitive comprehension for high-intensity effects. This approach enables a better evaluation of LT measurements and is in addition helpful to interpret the

impact of sample aggregation on NLPF spectra. Actually, aggregation effects cause a second difficulty in LT measurements. In most spectroscopic experiments, an amount of 67% glycerol is added to obtain transparent protein environments even at cryogenic temperatures. This sample treatment with glycerol can result in aggregation effects that has not been fully understood so far [158]. Accordingly, the sample preparation requires adequate adaptations to ensure the formation of trimeric LHCII species under RT and LT conditions (see further below).

High-intensity NLPF spectra at room temperature

NLPF spectra measured at varying pump intensities for two different λ_t are shown in Fig. 3.5.5. As the most striking feature, one can observe a general spectral shift to shorter wavelengths (blue-shift) with increasing pump intensity. This characteristic is induced by successive saturation of the fluorescent state(s) at the end of the EET chain, which usually dominate NLPF spectra at *low* pump intensities.
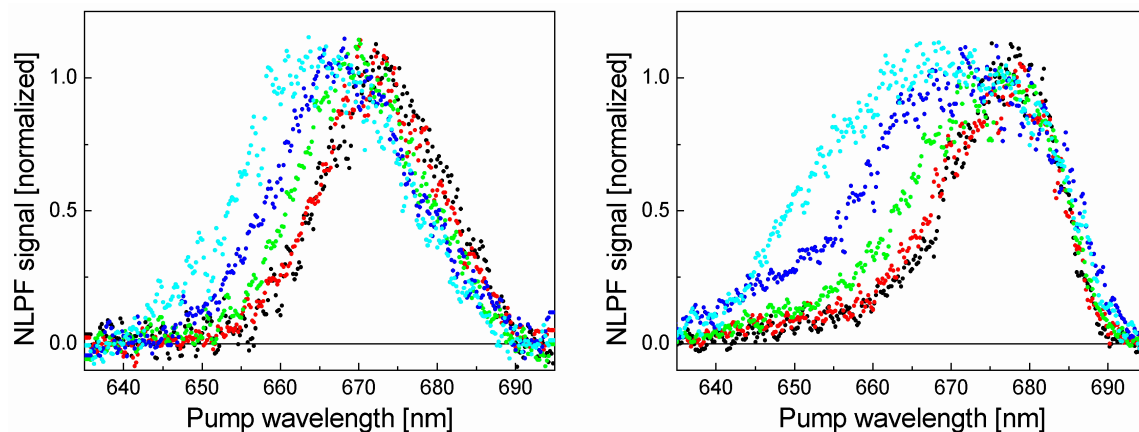
Figure 3.5.5 NLPF spectra of trimeric LHCII obtained for $\lambda_t = 665$ nm (**left panel**) and $\lambda_t = 685$ nm (**right panel**) at the following pump-field intensities [photons cm^{-2} s^{-1}]: $8.0 \cdot 10^{22}$ (black), $2.1 \cdot 10^{23}$ (red), $4.7 \cdot 10^{23}$ (green), $1.4 \cdot 10^{24}$ (dark blue), and $4.3 \cdot 10^{24}$ (light blue). Similar values were also used for the saturation curves in Chapter 3.4.1, which reveal the non-saturated intensity range (see text).

All employed pump intensities in Fig. 3.5.5 (right panel) are identical to intensities used for the quantitative saturation studies in Chapter 3.4.1. While the two corresponding graphs (Fig. 3.4.2, p. 85) reflect relative NLPF signal amplitudes, the illustration above contains normalized NLPF spectra. Both results can be directly compared, since they were obtained for equal $\lambda_t = 685$ nm. Obviously, saturation in Fig. 3.4.2 starts at pump intensities beyond the indicated value of $\xi^{-1} \approx 1.2 \cdot 10^{23}$ photons cm^{-2} s^{-1}. For that reason, the spectrum in Fig. 3.5.5 (right panel) recorded with $8.0 \cdot 10^{22}$ photons cm^{-2} s^{-1} (black dots) clearly represents unsaturated conditions. At intensities slightly above ξ^{-1}, i.e. $2.1 \cdot 10^{23}$ photons cm^{-2} s^{-1} (red dots), the spectral shape is still rather similar to non-saturated spectra. However, any further intensity increase results in expanding blue-shifts of the spectra. By direct comparison, these differences are now straightforwardly correlated to the saturation effects quantitatively described in Chapter 3.4.1. In particular, one can state that application of pump intensities above the specific saturation level ξ^{-1} causes increasingly blue-shifted NLPF spectra. This

phenomenological elucidation of NLPF intensity dependence allowed improved interpretations of spectra obtained at cryogenic temperatures further below. Besides this, the interpretation of aggregation effects in the next section benefits also from this improved understanding of the pump-intensity influence on NLPF spectra.

Aggregation effects and glycerol-induced aggregation

Disaggregation in LHCII samples is induced by detergent treatment, e.g. OG for the preparations used in this work. According to results reported in [159], 1.2% OG content is sufficient to achieve disaggregated, trimeric LHCII proteins in buffer/water solution. Lower amounts result in samples, which are still aggregated to some extent. In contrast to this, higher OG contents lead to partial monomerization of the LHCII proteins [92]. The application of NLPF measurements at LT requires further an addition of ~67% glycerol to the samples. Otherwise, the freezing process results in amorphous water environment, which increases light scattering well above the level of NLPF signals. However, a recent study revealed that glycerol treatment may induce protein aggregation when using the same amount of detergent as in pure buffer/water solutions [158]. Interestingly, NLPF measurements are highly sensitive to aggregation-induced changes of the Chls excited-state properties. Two main effects can be distinguished in this context. The left panel in Fig. 3.5.6 shows NLPF pump spectra of glycerol-free preparations containing only 0.5% OG. In comparison to the spectra of trimeric LHCII (cp. Fig. 3.1.1, right panel, p. 41), a general red-shift in combination with almost vanishing λ_t-selectivity can be observed. Both features have been previously reported in [159] and were related to probably non-photochemical quenching at a Chl *a* species absorbing around 670 nm after aggregation.
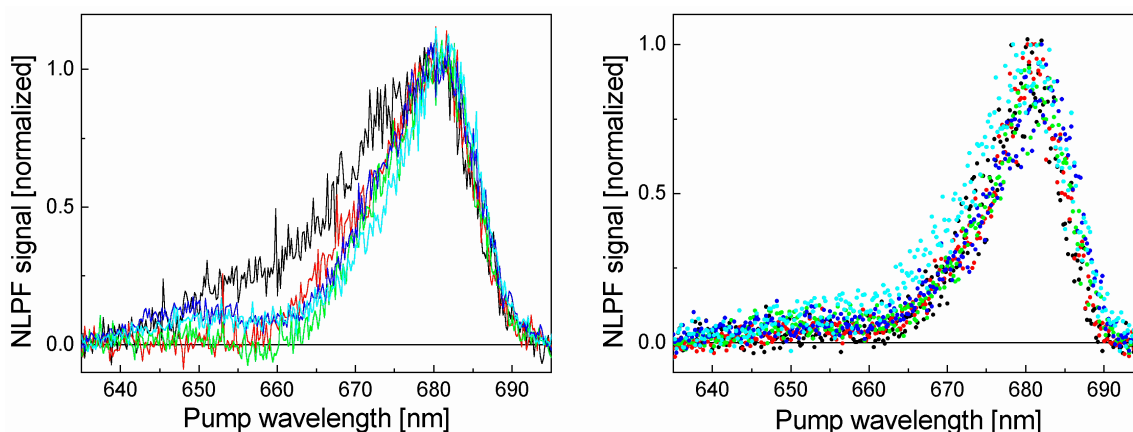

Figure 3.5.6 NLPF spectra of aggregated LHCII in buffer/water solution containing ~0.5% OG. **Left panel:** Variation of λ_t – 645 nm (black), 655 nm (red), 665 nm (green), 675 nm (dark blue), and 685 nm (light blue). **Right panel:** Variation of pump intensities – $8.0 \cdot 10^{22}$ (black), $2.1 \cdot 10^{23}$ (red), $4.7 \cdot 10^{23}$ (green), $1.4 \cdot 10^{24}$ (dark blue), and $4.3 \cdot 10^{24}$ (light blue).

Meanwhile, an other possible explanation became available by theoretical investigations concerning the bacterial light-harvesting complex LH2 [160]. In

particular, the prospective formation of excitation-trapping states at the contact area between two pigment-protein complexes was discussed with respect to expected pigment-pigment interactions. If such trap states would be formed in LHCII aggregates, the NLPF signal would be mainly determined by the corresponding spectral region, i.e. the red edge of Q_y-absorption. However, the intensity dependence of NLPF spectra makes such a trap-state formation in aggregated LHCII highly unlikely (Fig. 3.5.6, right panel). The spectra measured at different pump intensities ($\lambda_t = 685$ nm) reveal barely any saturation effect, while trimeric LHCII shows a strong intensity dependence (cp. Fig. 3.5.5, right panel). Since a *higher* intensity dependence must be expected in the case of trap-state formation (almost all excitations are concentrated there), this phenomenon can now be sufficiently excluded for LHCII aggregates. On the contrary, one can conclude that excitations in such aggregates are spread over numerous S_1-states located in distinct complexes shortly after initial photon absorption. The increased intensity-saturation level thus results from the corresponding orientation relaxation due to rather random protein orientations in each aggregate.

Unfortunately, an exact study of the detergent-concentration dependence on NLPF spectra includes several risks of potential errors. Main issues in this context are the initial detergent purity, temperature and pH-dependence of solubilization processes as well as probable cation impurities in the stock solution [92, 161, 162, 163]. Accordingly, a widespread investigation of detergent-dependent solubilization was omitted in this thesis. Nevertheless, evaluations of NLPF spectra obtained at different OG concentrations allow at least comparison to the results in [159] and monitoring of the disaggregation process. Three NLPF spectra obtained at different detergent concentrations are shown in Fig. 3.5.7 (left panel). The highest amount of 1.2% OG corresponds to the value required for complete solubilization into trimeric LHCII. A continuous red-shift of the NLPF spectra can be further observed for decreasing OG content. Below 0.5% OG, extreme light scattering originating from large aggregate sizes prevents NLPF measurements. Nevertheless, the accessible concentration range is sufficient to compare the results to glycerol-containing samples used for LT experiments.

In Fig. 3.5.7 (right panel), NLPF spectra of LHCII in buffer/water solution are compared to preparations using a 2:1 glycerol/water mixture as solvent. Most strikingly, glycerol-containing samples require a total amount of 1.8% OG to show a spectrum similar to trimeric LHCII. In contrast to this, preparations with glycerol and 1.2% OG result in spectra rather analogous to aggregated samples as prepared with 0.5% OG in pure buffer/water solution. Consequently, one can conclude that glycerol treatment changes the equilibrium of detergent-induced protein solubilization considerably. For that reason, all LT measurements have been performed with samples containing 1.8% OG in the 2:1 glycerol/water mixture. Nevertheless, Fig. 3.5.7 further reveals that the obtained NLPF spectra are not *completely* identical when using higher detergent amounts. This observation strongly indicates that LT measurements of glycerol-containing samples may be influenced by additional errors of so far unknown origin.
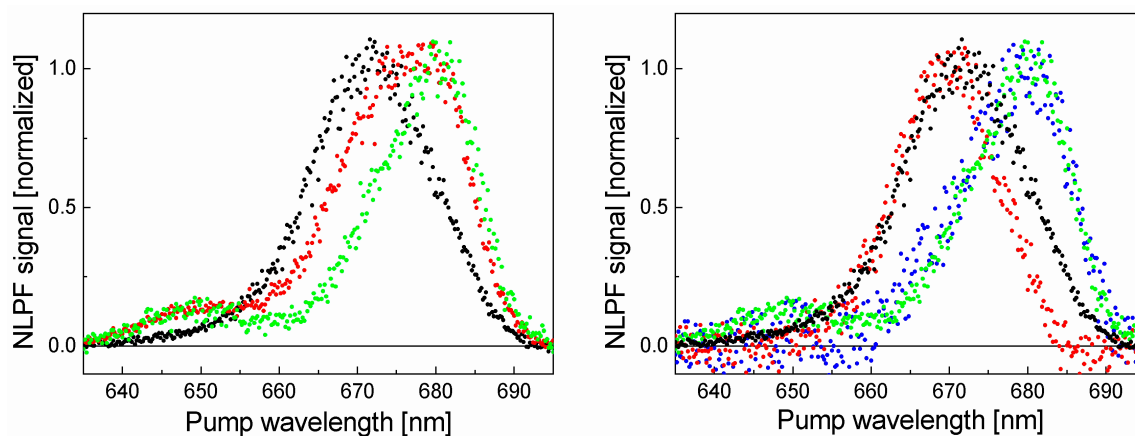
Figure 3.5.7 Left panel: NLPF spectra ($\lambda_t = 670$ nm) of LHCII samples prepared in buffer/water solution with different OG content: 1.2% (black), 0.85% (red), and 0.5% (green). Thus, the black spectrum corresponds to preparations used for all above reported measurements. **Right panel:** Comparison of the black and green spectrum from the left panel to samples prepared with 1.2% OG in 2:1 glycerol/water mixture (blue), and 1.8% OG in 2:1 glycerol/water mixture (red). Some curves were slightly smoothed (adjacent averaging) to enhance the comparability.

NLPF spectra at low temperatures

The first NLPF measurement of condensed matter at cryogenic temperature (77 K) was applied to LHCII samples [164]. It revealed a significant sub-structure with five distinct peaks and a slight shoulder indicating a sixth transition band (Fig. 3.5.8, right panel, and Table 3.5.5). Interestingly, these features are not observable in the squared absorption spectrum of LHCII at similar temperature (cp. Fig. 3.5.8, left panel). Following simulations on the basis of Eq. 18-21 (p. 36), excitonic interaction among several Chls provided the only consistent explanation for the observed spectrum. However, the corresponding calculations were partially hampered by an incompleteness of the theoretical description at that time, i.e. the exclusion of Chl transition dipole orientations. In addition, this analysis was complicated by the formerly unidentified absorption sub-structure of LHCII. Especially the dephasing times reported in [164] (cp. Table 3.5.5) might thus be influenced by the deficient sub-structure model. On the other hand, the general behavior of increased homogeneous linewidth at shorter wavelengths is in good agreement with the results obtained in Section 3.2.1. Moreover, all λ_c in Table 3.5.5 fit convincingly to the sub-structure model established in Section 3.2.1. In other words, the direct comparison of NLPF measurements at LT with results from the mutation analysis is highly consistent. This is especially important, since the theoretical basis is still inadequate to model the measured spectrum in Fig. 3.5.8 (right panel) quantitatively.

Table 3.5.5 Parameters obtained from fitting the NLPF spectrum from Fig. 3.5.8 under the assumption of six transitions according to Eq. 18-21. The fit also shown in Fig. 3.5.8 (right panel).

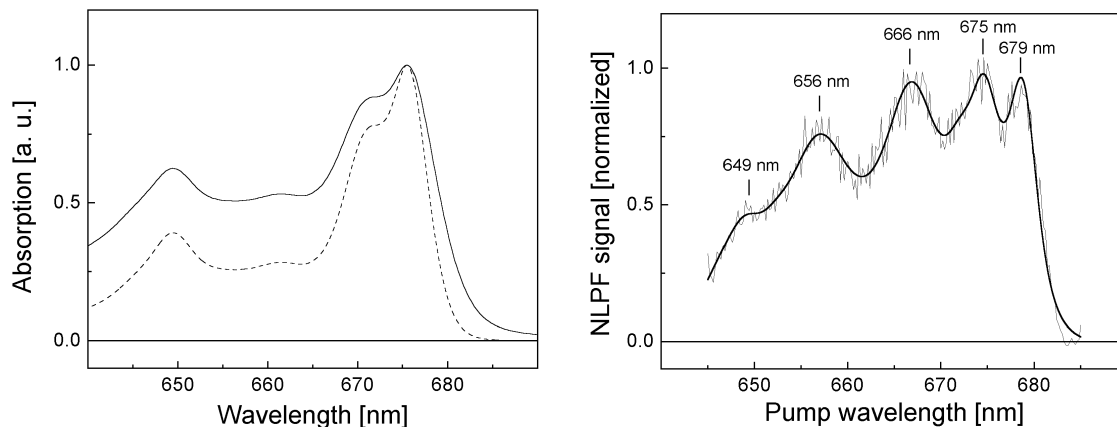| λ_c [nm]	648.6	657.0	666.8	672.4	674.8	678.9
T_2 [fs]	34	45	43	90	80	87

Figure 3.5.8 Left panel: Absorption spectrum of isolated LHCII at 77 K (solid line) and square module of the same spectrum (dashed line). **Right panel:** NLPF spectrum of isolated trimeric LHCII (thin line) measured at 77 K (λ_t = 675 nm; pump intensity: $2.3 \cdot 10^{23}$ photons cm^{-2} s^{-1}) and fit of the spectrum applying a heterogeneous sub-structure model according to Table 3.5.5 (thick line).

By now, theoretical difficulties concerning Chl dipole orientations has been solved in parallel studies by Beenken [132] as reflected in Eq. 22/23 (p. 37). Nevertheless, a further disadvantage of NLPF measurements at LT still prevents their proper theoretical modeling. Following the discussion above, pump intensities beyond the saturation level ξ^{-1} result in blue-shifted NLPF spectra, which cannot be simulated correctly. On one hand, the employed pump intensity of $2.3 \cdot 10^{23}$ photons cm^{-2} s^{-1} in [164] exceeds the estimated ξ^{-1}-level at 675 nm only moderately (~$1.25 \cdot 10^{23}$ photons cm^{-2} s^{-1}, cp. the ξ-value in the left panel of Fig. 3.4.3, p. 86). On the other hand, this saturation level estimated at RT might be decreased at cryogenic temperatures due to significantly reduced back transfer in the EET chain. A strong indication for such behavior can be obtained by comparison to more recent spectra, which could be measured at about ten times lower pump intensities ($1.8 \cdot 10^{22}$ photons cm^{-2} s^{-1}; Fig. 3.5.9).
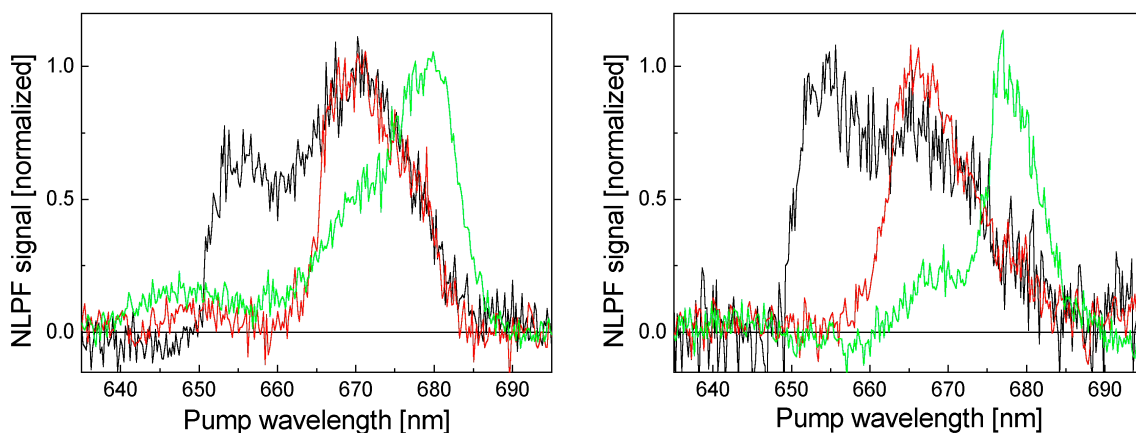

Figure 3.5.9 NLPF spectra of LHCII measured with pump intensities of $1.8 \cdot 10^{22}$ photons cm^{-2} s^{-1} at lower temperatures. **Left panel**: 120 K, λ_t = 650 nm (black), 665 nm (red), and 685 nm (green). **Right panel:** 77 K, λ_t = 650 nm (black), 663 nm (red), and 675 nm (green). The samples were prepared in 2:1 glycerol/water mixture with 1.8% OG.

Comparison between the two spectra measured at 77 K for λ_t = 675 nm (right panels in Figs. 3.5.8 and 3.5.9) indicates significantly increased short-wavelength contributions at higher pump intensity. As a direct result, most of the observed spectral features vanish

in low-intensity NLPF spectra. The origin of this unexpectedly strong intensity dependence at LT has not been fully understood yet. Undoubtedly, uphill EET from the Chl-*a* region >675 nm to shorter wavelengths is reduced at LT due to the smaller bandwidth, while downhill EET is less influenced because of additional spectral overlap between (0,1)-bands (cp. Section 1.3.1 and [165]). Hence, the saturation in NLPF experiments at LT starts at considerably lower pump intensities than in RT measurements. Furthermore, the actual distribution of excitation energy among fluorescent states at LT is still completely unknown. In this context, a probable change of the main fluorescence emitter in the temperature range around 100 K was discussed before in Section 3.2.1. Finally, one has to conclude that convenient simulations of NLPF spectra at LT are out of range at the present stage of investigation.

Although adequate evaluation of NLPF spectra obtained at cryogenic temperatures was omitted in this work because of increasing theoretical difficulties, one interesting feature of the results should be briefly highlighted. In contrast to NLPF measurements at RT in the previous section, the spectra in Fig 3.5.9 show a significant λ_t-dependence. This feature is again explainable by reduced back transfer from the lowest excited state(s) of the EET chain. In Section 3.1.3, an almost vanishing λ_t-selectivity was directly related to equilibration among several first-excited states (cp. Fig. 3.1.10, left panel). In conversion of this principle, increased λ_t-dependence has to be expected if excitation equilibration is prevented to a certain extent. Accordingly, all observed features in LT spectra convincingly aid the analytical discussion in Chapter 3.1. Since understanding of NLPF signals from heterogeneous sub-structures like LHCII was the major scope of this thesis, the LT measurements provided a further mosaic piece to this challenging puzzle. Furthermore, the technical feasibility of NLPF investigations at LT has been successfully demonstrated. Its future extension to even lower temperatures will facilitate direct comparison to results obtained with other techniques, e.g. non-photochemical hole-burning or single-molecule spectroscopy at 4 K.

4   Conclusions

Investigations in this thesis were primarily aimed at improving the understanding of nonlinear optical phenomena in pigment-containing proteins, i.e. photosynthetic antenna complexes. This approach was expected to provide new information about basic physical parameters of the examined system that is hard to obtain by other currently available methods. On this basis, improvements for the theoretical description of the light-harvesting function within the photosynthetic apparatus were anticipated. In other words, this work attempted to answer the following questions:

1) Do measurements of NLPF spectra convincingly reveal physical parameters of the investigated system in the case of a highly complicated system like LHCII?

2) Can the obtained results be employed to improve the understanding of the biological function of LHCII?

4.1   Experimental and theoretical developments

An extensive theoretical background for the compulsory physical description of pigment-protein complexes has been developed recently [29, 30, 31, 32, 33]. On this basis, general improvements in the NLPF theory could be achieved in parallel studies by Beenken [1]. This starting point enabled in this thesis indeed convenient simulations of NLPF signals from multi-pigment protein complexes. However, the highly complex correlation between the different molecular parameters complicates the understanding of NLPF experiments applied to such systems. For that reason, a detailed analysis in Chapter 3.1 depicts the different parameters influence on NLPF spectra (cp. especially the summarizing Fig. 3.1.19, p. 62). In this way, sufficient comprehension of the methods principle and sensitivity could be achieved without paying too much attention to mathematical equations.

The experimental evaluation was primarily directed to isolated trimeric LHCII, since well-defined isolation procedures and spectroscopic characterizations are available for this complex [40, 96]. Additionally, the LHCII structure was determined with the best resolution (3.4 Å) when compared to the minor antenna proteins in higher plants [6]. On the other hand, the necessary model for NLPF simulations includes a considerable number of so-far unknown parameters (cp. Chapter 1.2). This disadvantage required the extension of existing knowledge about certain LHCII parameters *before* NLPF simulations. Accordingly, intensity-dependent NLPF and NLA measurements were performed to study possible excitonic coupling between Chls in LHCII.

Actually, NLA with ps-pulses has been earlier employed to study excitonic interaction within the B850 ring of the bacterial antenna complex LH2 [65]. However, ultra-fast EET among Chls *a* in LHCII on the sub-ps timescale complicated the proper interpretation of similar experiments. In contrast, the use of fs-pulses reduced the theoretical expense for simulations and enabled thus the straightforward evaluation of

underlying absorption parameters (cp. Chapter 3.3). The application of *intensity-dependent* NLPF measurements represents an innovative extension of the original NLPF method and it allowed improved investigations of excitonic coupling in LHCII (cp. Chapter 3.4). Last but not least, applications of the NLPF technique at cryogenic temperatures has been firstly demonstrated in the framework of this thesis. A more qualitative evaluation of the results mainly indicates congruent results as compared to the mutagenesis analysis at LT in Chapter 3.2.

4.2   Basic improvements of the LHCII parameter model

The analytical description of NLPF spectra for heterogeneous systems in Chapter 3.1 revealed that the methods significance mainly depends on the establishment of a sufficient sub-structure model. For that purpose, supplementary examinations were initiated in co-operation with Dr. H. Rogl (MPI Frankfurt) to clarify the basic absorption sub-structure of LHCII. As a main result, it was shown in Chapter 3.2 more clearly than before [37, 38] that different transition bands can be assigned to individual Chl molecules located at distinct binding sites. In this way, a direct relation between structural parameters and the optical properties of LHCII has been established for at least four Chls. Furthermore, there were *no* features observable that would indicate a mixed occupancy of certain binding sites by Chl *a* and Chl *b* as reported by other authors [38]. Finally, a sub-structure model with a minimal set of spectral sub-bands could be established for LT and RT spectra, which provided the proper base to evaluate NLPF measurements in Chapter 3.5.

Considerable effort has been further made to study excitonic coupling among Chls in the LHCII complex, since this interaction is hardly accessible by other experimental techniques. Combination of intensity-dependent NLPF and NLA measurements using fs-pulses revealed in this context similar results, which were interpreted by dimer formation among Chls at binding site **a2/b2**. In addition, the excitonic state was identified to function as main fluorescence emitter in LHCII. This firstly reported evidence for excitonic coupling in LHCII [118] could be meanwhile aided by additional NLPF experiments in the Soret-band [41] as well as a two-photon excited fluorescence study [61]. The existence of mainly one fluorescent state per LHCII monomer was also confirmed by parallel investigations on single complexes [109].

Supplementary studies using site-directed mutagenesis and advanced nonlinear spectroscopic techniques resulted in a comprehensive model of basic absorption parameters. On this basis, convenient simulations of NLPF spectra of trimeric LHCII became available. As a main result, transition-dipole orientations could be determined for several Chls, in particular Chls *a*. These findings reflect the unique orientation dependence of NLPF spectra. Furthermore, the assignment of binding site **b1** to Chl *a* could be confirmed by comparison of different models as suggested earlier in [38]. The same time, an occupation of binding site **b2** with Chl *b* was implicitly concluded by combining results of NLPF simulations with investigations about excitonic coupling in

Chapter 3.3. Figure 4.2.1 provides an overview of physical parameters that were determined or confirmed in the framework of this thesis. Interestingly, relevant information could be gained for almost every Chl site.
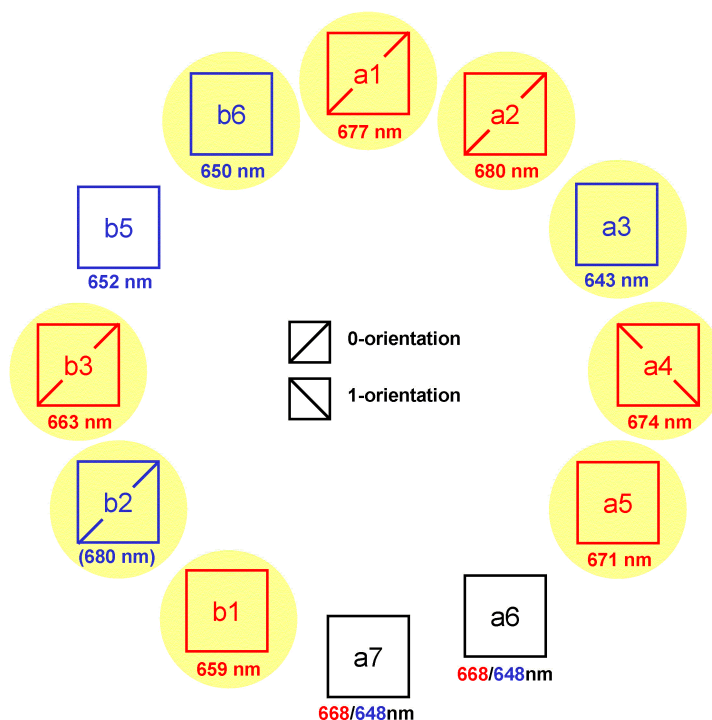

Figure 4.2.1 Summary of parameters obtained or confirmed in the framework of this thesis for the 12 Chl binding sites in LHCII. Chl-assignments are illustrated by the color (Chl *a*: red, Chl *b*: blue, unknown: black), their transition bands are characterized by λ_c, and dipole orientations are indicated by diagonals. For all yellow-marked sites, at least one parameter could be identified by the investigations in this thesis.

4.3 Implications for the light-harvesting function of LHCII

The combination of results obtained by NLPF and supplementary methods improves the understanding of light-harvesting mechanisms in LHCII, indeed. In particular, the resulting parameter model from Fig. 4.2.1 is appropriate to clarify some basic features within the EET scheme of Chl S_1-states in LHCII (see Fig. 4.3.1). However, several still unresolved parameters, especially Chl orientations, have hindered the establishment of a more complete scheme so far. Thus, numerous EET rates could not be estimated more accurate than reported before [40].

The proposed scheme of Fig. 4.3.1 reveals that EET rates among Chl S_1-states have been determined for at least three transfer channels. Moreover, the uncertainty could be substantially reduced for two further channels (connecting **a3**/**b3** and **a4**/**a5**). This result – including seven of the Chls, i.e. **a1-a5** and **b2**, **b3** – is far from a complete physical description for the overall EET scheme in LHCII. On the other hand, it describes satisfactorily the pathways at the *end* of the EET chain. In particular, the two Chls at site **a1** and **a2** were identified in this work as the mostly red-shifted absorption species (cp. Chapter 3.2). Furthermore, the structural data summarized in the introduction section

(Fig. 1.2.1-1.2.3) clearly indicate that Chl **a2**, **b2**, and **b3** are the outmost pigments of the LHCII complex in its trimeric form. Accordingly, inter-trimeric EET (which is most essential for the light-harvesting function of an extended antenna system) will most possibly occur between these molecules. Although all of these three pigments are connected to other Chl-*a* molecules, the connectivity of the **a2**/**b2**-dimer is considerably higher than for the Chl *a* at binding site **b3**. The average population time at this pigment will be further decreased due to a rather high energetic level of its Q_y-transition ($\lambda_c \approx 663$ nm). Accordingly, one can assume that binding site **a2**/**b2** plays a unique role for inter-trimeric EET.
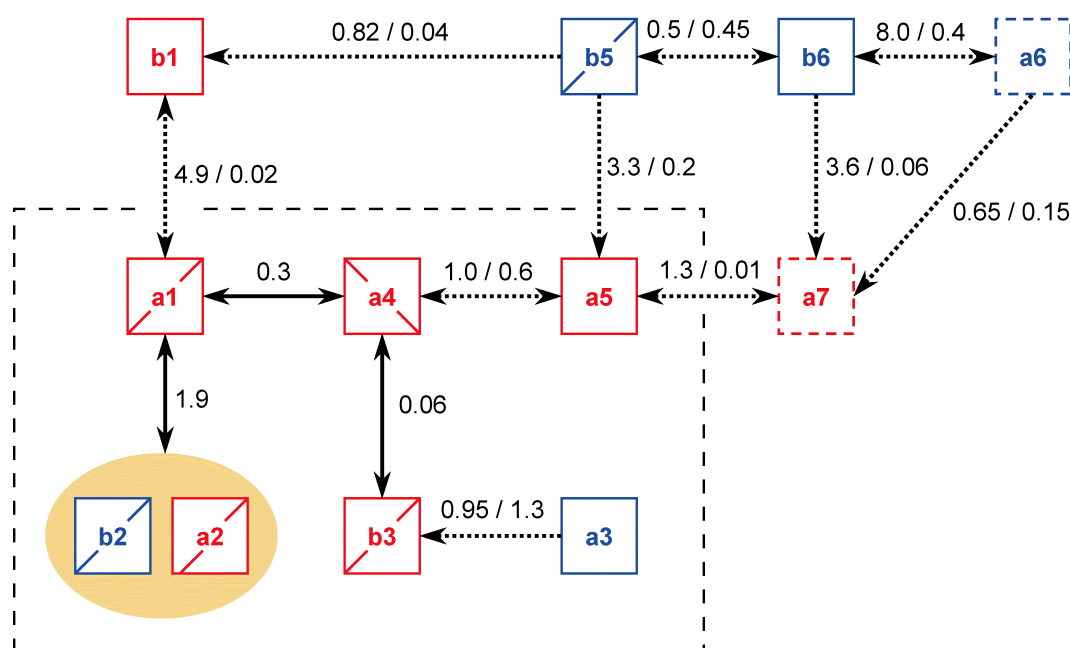
Figure 4.3.1 EET scheme (rates in ps^{-1}) for Chl S_1-excitations in LHCII as calculated for Förster-transfer between different binding sites according to model parameters obtained in this study (cp. Fig. 4.2.1). If two binding sites could be characterized by Chl assignment *and* dipole orientation, only *one* EET rate is calculated. In all other cases, a maximum and minimum value is indicated, which is in agreement to the established parameter model. Formation of a Chl-*a*/*b* heterodimer at binding sites **a2**/**b2** was illustrated by the yellow ellipse. The dashed square encircles those binding sites, which are connected by rather well-defined EET rates.

This observation nicely confirms early considerations about the inter-trimeric connectivity based on the first-obtained LHCII structure [166]. Furthermore, the determination of a key fluorescence emitter at binding sites **a2**/**b2** in Chapter 3.4 strongly suggests that most of the excitation energy is guided to this location. In other words, this unique state attracts most excitations to the LHCII outer surface. Accordingly, the dimer appears to function as *the* connecting site of the complex. In this context, the size enhancement of the transition dipole can potentially increase the connectivity of neighboring trimers, thus contributing to the formation of an extended PS II-antenna network. Hence, the fluorescent dimer at the end of the EET chain in LHCII can be expected to play a crucial role for the overall efficiency of higher plant photosynthetic energy conversion.

4.4   Outlook

In this work, it has been demonstrated that the NLPF method can provide new information on inherent physical parameters when applied to intricate heterogeneous systems like higher plant antenna proteins. Accordingly, the NLPF technique represents an ideal complement to the existing zoo of spectroscopic techniques commonly applied to these systems. Especially its unique orientation dependence allowed the estimation of several Chl (*a*) dipole orientations in LHCII. In contrast, the method revealed deficiencies in the elucidation of Chl *b* parameters for the most part. Consequently, a combined evaluation of time-resolved measurements (e.g., [14]) and NLPF spectra might provide in the end a sufficient approach to determine the *complete* set of orientation parameters. On this basis, the physical description of light-harvesting mechanisms by an overall EET scheme (cp. Fig. 4.3.1) could be improved to a large extend. However, at the present stage of investigation this combined evaluation is especially hampered by distinct preparation procedures and sample treatments, i.e. the use of different detergents.

Besides this, certain improvements of the NLPF method itself will also be suited to solve remaining questions about the structure-function relationship of EET phenomena in antenna proteins. Measurements of NLPF probe spectra with fixed λ_P and varying λ_t allow the relative normalization of NLPF spectra (cp. Chapter 3.1). In this way, the direct determination of EET rates by NLPF measurements becomes possible indeed (see especially Section 3.1.3). Furthermore, the splitting of λ_P and λ_t to different electronic transitions (i.e., Q_y and Soret) represents a promising extension of the method. First successful applications of this approach have revealed unique results for LHCII and the highly homologue antenna protein CP29 [41, 131]. Last but not least, it should be mentioned that the highly promising application of NLPF at 77 K can be further extended to even lower temperatures. Simultaneous studies of the temperature influence on excitation *back* transfer by time-resolved studies would further raise this application to an adequate level of quantitative evaluation.

5   Appendix

A1

LHCII complexes comprise the function of a quantum-optical OR-gate on the ps-time scale:

Binary logic of an OR-gate (On = state 1, Off = state 0):

Input A	Input B	Output C
0	0	0
0	1	1
1	0	1
1	1	1

Experimental realization:

Input A: State 1 - Laser pulse A on ($\lambda = 640$ nm, $\Delta = 100$ fs, FWHM: 10 nm)

State 0 - Laser pulse A off

Input B: State 1 - Laser pulse B on ($\lambda = 680$ nm, $\Delta = 100$ fs, FWHM: 10 nm)

State 0 - Laser pulse 2 off

Output C: Laser pulse C ($\lambda = 680$ nm, $\Delta = 100$ fs, FWHM: 10 nm) probes first-excited state excitations by ground-state bleaching and stimulated emission.

Excitations of the Chl-*b* region in LHCII at 640 nm are transferred within at least 3 ps to the absorption region of Chl *a* around 680 nm [40]. This wavelength can be probed with 3 ps delay after the two spectrally separated, but coincident input pulses via ground-state depletion and stimulated emission. Hence, an output signal can be detected after *i*) initial excitation at 640 nm only, *ii*) initial excitation at 680 nm only, or *iii*) initial excitations at both wavelengths. In the latter case, the two excitations meeting at the EET chain end undergo an ultra-fast excitation annihilation process. This results in only one remaining excitation (cp. Chapter 1.3).

A2

		a2 0	a2 1	a3 0	a3 1	a4 0	a4 1	a5 0	a5 1	a6 0	a6 1	a7 0	a7 1	b1 0	b1 1	b2 0	b2 1	b3 0	b3 1	b5 0	b5 1	b6 0	b6 1
a1	0	0.72	1.3	-	-	0.07	0.84	1.0	0.002	0.78	0.004	-	-	1.25	0.04	1.83	1.44	-	-	0.03	0.003	0.003	0.84
	1	0.62	0.38	-	-	0.86	0.21	0.005	1.18	1.11	2.13	-	-	0.23	1.57	0.09	1.12	-	-	0.002	1.64	1.44	0.79
a2	0			0.03	0.05	1.02	0.002	0.05	1.20	3.35	0.27	-	-	0.001	1.86	0.84	0.87	0.07	0.31	-	-	-	-
	1			0.02	3.67	0.01	1.08	1.23	0.01	0.003	0.008	-	-	0.09	0.02	0.71	0.34	1.48	1.84	-	-	-	-
a3	0					0.46	2.32	3.60	0.03	0.009	1.12	0.44	1.29	-	-	0.56	0.02	0.31	1.31	-	-	-	-
	1					0.09	1.39	0.001	0.001	1.12	0.04	0.72	0.11	-	-	2.10	1.38	0.44	0.50	-	-	-	-
a4	0							0.72	0.78	-	-	-	-	0.79	0.71	0.10	~0	-	-	2.12	1.12	-	-
	1							0.59	0.41	-	-	-	-	0.36	0.56	1.67	0.20	-	-	0.64	0.45	-	-
a5	0									0.03	0.03	0.88	0.19	0.26	0.001	-	-	-	-	0.94	0.05	0.12	0.53
	1									0.23	3.33	0.03	3.49	0.02	1.15	-	-	-	-	0.04	1.05	3.74	0.09
a6	0											0.42	0.19	0.02	0.51	-	-	-	-	0.39	0.27	0.07	1.43
	1											0.29	0.81	0.27	2.49	-	-	-	-	0.94	1.31	0.55	0.20
a7	0													0.75	0.63	-	-	-	-	1.59	0.12	0.78	2.13
	1													0.22	1.73	-	-	-	-	0.32	2.27	1.0	0.03
b1	0															-	-	-	-	0.64	0.03	0.05	1.76
	1															-	-	-	-	0.08	1.01	0.99	0.96
b2	0																	0.07	0.41	-	-	-	-
	1																	1.55	0.04	-	-	-	-
b3	0																			-	-	-	-
	1																			-	-	-	-
b5	0																					1.64	0.70
	1																					1.77	0.01

Table of geometrical factors κ^2 determining the mutual electronic interaction among Chls in LHCII (see Chapter 1.3.1). The values are calculated for all pairs separated by less than ~25 Å in the two possible orientations '0' and '1' (compare Chapter 1.2.1).

References

[1] Beenken, W.J.D. (2003): Theory of nonlinear polarization spectroscopy in the frequeny domain (NLPF) with applications to photosynthetic antennae, PhD Thesis, Institute of Physics, Humboldt University, Berlin.

[2] Renger, G. (1992): Energy transfer and trapping in photosystem II, Barber, J., The Photosystem Structure, Function and Molecular Biology pp. 45- 99, Elsevier Science Publishers B.V.

[3] Ruban, A.V. and Horton, P. (1995): Regulation of non-photochemical quenching of chlorophyll fluorescence in plants, Aust. J. Plant Physiol. (vol. 22), pp. 221-230.

[4] Niyogi, K.K. (1999): Photoprotection revisited: Genetic and molecular approaches, Annu. Rev. Plant Physiol. Plant Mol. Biol. (vol. 50), pp. 333-359.

[5] McDermott, G.; Prince, S.M.; Freer, A. A.; Hawthornthwaite-Lawless, A.M.; Papiz, M.Z.; Cogdell, R.J. and Isaacs, N.W. (1995): Crystal structure of an integral membrane light-harvesting complex from photosynthetic bacteria, Nature (vol. 374), pp. 517-521.

[6] Kühlbrandt, W.; Wang, D.N. and Fujiyoshi, Y. (1994): Atomic model of plant light-harvesting complex by electron crystallography, Nature (vol. 367), pp. 614-621.

[7] van Grondelle, R.; Dekker, J.P.; Gillbro, T. and Sundstrom, V. (1994): Energy transfer and trapping in photosynthesis, Biochim. Biophys. Acta (vol. 1187), pp. 1-65.

[8] Li, J.; Ambroise, A.; Yang, S.I.; Diers, J.R.; Seth, J.; Wack, C.R.; Bocian, D.F.; Holten, D. and Lindsey, J.S. (1999): Template-directed synthesis, excited-state photodynamics, and electronic communication in a hexameric wheel of porphyrins, J. Am. Chem. Soc. (vol. 121), pp. 8927-8940.

[9] Sun, L. C.; Akermark, B.; Hammarstrom, L. and Styring, S. (2003): Toward solar energy conversion into fuels: Design and synthesis of ruthenium-manganese supramolecular complexes to mimic the function of photosystem II, Utilization of Greenhouse Gases (vol. 852), pp. 219-244.

[10] Imahori, H.; Mori, Y. and Matano, Y. (2003): Nanostructured artificial photosynthesis, Journal of Photochemistry and Photobiology C-Photochemistry Reviews (vol. 4), No. 1, pp. 51-83.

[11] Bittner, T.; Irrgang, K.D.; Renger, G and Wasielewski, M.R. (1994): Ultrafast excitation energy transfer and exciton-exciton annihilation processes in isolated light harvesting complexes of photosystem II (LHC II) from spinach, J Phys Chem (vol. 98), pp. 11821-11826.

[12] Trinkunas, G.; Connelly, J.P.; Müller, M.G.; Valkunas, L. and Holzwarth, A. (1997): Model for the excitation dynamics in the light-harvesting complex II from higher plants, J. Phys. Chem. B (vol. 101), pp. 7313-7320.

[13] Connelly, J.P.; Müller, M.G.; Hucke, M.; Gatzen, G.; Mullineaux, C.W.; Ruban, A.V.; Horton, P. and Holzwarth, A. (1997): Ultrafast spectroscopy of trimeric light-harvesting complex II from higher plants, J. Phys. Chem. B (vol. 101), pp. 1902-1909.

[14] Gradinaru, C.C.; Özdemir, S.; Gülen, D.; van Stokkum, I.H.M.; van Grondelle, R. and van Amerongen, H. (1998): The flow of excitation energy in LHCII monomers: Implications for the structural model of the major plant antenna, Biophys. J. (vol. 75), No. 6, pp. 3064-3077.

[15] Sirringhaus, H.; Brown, P.J.; Friend, R.H.; Nielsen, M.M.; Bechgaard, K.; Langeveld-Voss, B.M.W.; Spiering, A.J.H; Janssen, R.A.J; Meijer, E.W.; Herwig, P. and de Leeuw, D.M. (1999): Two-dimensional charge transport in self-organized, high-mobility conjugated polymers, Nature (vol. 401), pp. 685-688.

[16] Li, M.; Schnablegger, H. and Mann, S. (1999): Coupled synthesis and self-assembly of nanoparticles to give structures with controlled organization, Nature (vol. 402), pp. 393-395.

[17] Ambroise, A.; Wagner, R.W.; Rao, P.D.; Riggs, J.A; Hascoat, P.; Diers, J.R.; Seth, J.; Lammi, R.K.; Bocian, D.F.; Holten, D. and Lindsey, J.S. (2001): Design and synthesis of porphyrin-based optoelectronic gates, Chem. Mater. (vol. 13), pp. 1023-1034.

[18] Ogawa, K.; Zhang, T.; Yoshihara, K. and Kobuke, Y. (2002): Large third-order optical nonlinearity of self-assembled supramolecular porphyrin oligomers, J. Am. Chem. Soc. (vol. 124), pp. 22-23.

[19] Allen, J.F. and Forsberg, J. (2001): Molecular recognition in thylakoid structure and function, Trends Plant Sci. (vol. 6), pp. 317-326.

[20] Jansson, S. (1994): The light-harvesting chlorophyll a/b-binding proteins, Biochim. Biophys. Acta (vol. 1184), pp. 1-19.

[21] Yakushevska, A.E.; Jensen, P.E.; Keegstra, W.; van Roon, H.; Scheller, H.V.; Boekema, E.J. and Dekker, J.P. (2001): Supermolecularorganization of photosystem II and its associated light-harvesting antenna in Arabidopsis thaliana, Eur. J. Biochem. (vol. 268), pp. 6020-6028.

[22] Yakushevska, A.E.; Keegstra, W.; Boekema, E.J.; Dekker, J.P.; Andersson, J.; Jansson, S.; Ruban, A. V. and Horton, P. (2003): The structure of photosystem II in Arabidopsis: Localization of the CP26 and CP29 antenna complexes, Biochemistry (vol. 42), pp. 608-613.

[23] Mullineaux, C.W.; Tobin, M.J. and Jones, G.R. (1997): Mobility of photosynthetic complexes in thylakoid membranes, Nature (vol. 390), pp. 421-424.

[24] Jansson, S. (1999): A guide to the Lhc genes and their relatives in Arabidopsis, Trends in Plant Science (vol. 4), No. 6, pp. 236-240.

[25] Jackowski, G. and Pielucha, K. (2001): Heterogeneity of the main light-harvesting chlorophyll a/b-protein complex of photosystem II (LHCII) at the level of trimeric subunits, J Photochem Photobiol B (vol. 64), pp. 45-54.

[26] Jackowski, G.; Kacprzak, K. and Jansson, S. (2001): Identification of Lhcb1/Lhcb2/Lhcb3 heterotrimers of the main light-harvesting chlorophyll a/b-protein complex of photosystem II (LHC II), Biochim. Biophys. Acta (vol. 1504), pp. 340-345.

[27] Walters, R.G. and Horton, P. (1999): Structural and functional heterogeneity in the major light-harvesting complexes of higher plants, Photosynth. Res. (vol. 61), pp. 77-89.

[28] Zer, H.; Vink, M.; Keren, N.; Dilly-Hartwig, H.G.; Paulsen, H.; Herrmann, R.G.; Andersson, B. and Ohad, I. (1999): Regulation of thylakoid protein phosphorylation at the substrate level: Reversible light-induced conformational changes expose the phosphorylation site of the light-harvesting complex II, Proc. Natl. Acad. Sci. USA (vol. 96), No. 14, pp. 8277-11649.

[29] Kühn, O. and May, V. (1994): Dissipative vibrational dynamics in a curve-crossing system, J. Chem. Phys. (vol. 101), pp. 10404-10415.

[30] Peterman, E.J.; Pullerits, T.; van Grondelle, R. and van Amerongen, H. (1997): Electron-phonon coupling and vibronic fine structure of light-harvesting complex II of green plants: temperature dependent absorption and high-resolution fluorescence spectroscopy, J. Phys. Chem. B (vol. 101), pp. 4448-4457.

[31] Kimura, A.; Kakitani, T. and Yamato, T. (2000): Theory of excitation energy transfer in the intermediate coupling case. II. Criterion for intermediate coupling excitation energy transfer mechanism and application to the photosynthetic antenna system, J. Phys. Chem. B (vol. 104), No. 9276-9287.

[32] Nishigaki, A.; Ohshima, S.; Nakayama, K.; Okada, M. and Nagashima, U. (2001): Application of molecular orbital calculations to interpret the chlorophyll spectral forms in pea photosystem II, Photochem. Photobiol. (vol. 73), No. 3, pp. 245-248.

[33] Zucchelli, G.; Jennings, R.C.; Garlaschi, F. M.; Cinque, G.; Bassi, R. and Cremones, O. (2002): The calculated in vitro and in vivo chlorophyll a absorption bandshape, Biophys. J. (vol. 82), pp. 378-390.

[34] Damjanovic, A.; Ritz, T. and Schulten, K. (2000): Excitation transfer in the Peridinin-chlorophyll-protein of Amphidinium carterae, Biophys. J. (vol. 79), pp. 1695-1705.

[35] Croce, R.; Remelli, R.; Varotto, C.; Breton, J. and Bassi, R. (1999): The neoxanthin binding site of the major light harvesting complex (LHCII) from higher plants, FEBS Lett. (vol. 456), pp. 1-6.

[36] Croce, R.; Weiss, S. and Bassi, R. (1999): Carotenoid-binding sites of the major light-harvesting complex II of higher plants, J. Biol. Chem. (vol. 274), No. 42, pp. 29613-29623.

[37] Rogl, H. and Kühlbrandt, W. (1999): Mutant trimers of light-harvesting complex II exhibit altered pigment content and spectroscopic features, Biochemistry (vol. 38), No. 49, pp. 16214-16222.

[38] Remelli, R.; Varotto, C.; Sandona, D.; Croce, R. and Bassi, R. (1999): Chlorophyll binding to monomeric light-harvesting complex. A mutation analysis of chromatophore-binding residues, J. Biol. Chem. (vol. 274), No. 47, pp. 33510-12788.

[39] Yang, C.; Kosemund, K.; Cornet, C. and Paulsen, H. (1999): Exchange of pigment-binding amino acids in light-harvesting chlorophyll a/b protein, Biochemistry (vol. 38), No. 49, pp. 16205-16213.

[40]   van Amerongen, H. and van Grondelle, R. (2001): Understanding the energy transfer function of LHCII, the major light-harvesting complex of green plants, J. Phys. Chem. (vol. 105), pp. 604-617.

[41]   Krikunova, M.; Voigt, B. and Lokstein, H. (2002): Direct evidence for excitonically coupled chlorophylls a and b in LHCII of higher plants by nonlinear polarization spectroscopy in the frequency domain, Biochim. Biophys. Acta (vol. 1556), pp. 1-5.

[42]   Schödel, R.; Irrgang, K.-D.; Voigt, J. and Renger, G. (1998): Rate of carotenoid triplet formation in solubilized light-harvesting complex II (LHCII) from spinach, Biophys. J. (vol. 75), No. 6, pp. 3143-3153.

[43]   Lokstein, H.; Tian, L.; Polle, J. and DellaPenna, D. (2002): Xanthophyll biosynthetic mutants of *Arabidopsis thaliana*: Altered nonphotochemical quenching of chlorophyll fluorescence is due to changes in photosystem II antenna size and stability, Biochim. Biophys. Acta (vol. 1553), pp. 93-103.

[44]   Härtel, H.; Reinhardt, I. and Grimm, B. (1998): Relationship between energy-dependent fluorescence quenching and xanthophyll-cycle-pigments in transgenic chlorophyll-deficient tobacco grown under different light intensities, Photochem. Photobiol. B: Biology (vol. 43), pp. 136-145.

[45]   Bassi, R. and Caffarri, S. (2000): Lhc proteins and the regulation of photosynthetic light harvesting function by xanthophylls, Photosynth. Res. (vol. 64), pp. 243-256.

[46]   Fragata, M.; Norden, B. and Kurucsev, T. (1988): Linear Dichroism (250-700 Nm) of Chlorophyll-a and Pheophytin-a Oriented in a Lamellar Phase of Glycerylmonooctanoate H2o - Characterization of Electronic-Transitions, Photochemistry and Photobiology (vol. 47), No. 1, pp. 133-143.

[47]   Schödel, R.; Irrgang, K.-D.; Voigt, J. and Renger, G. (1999): Quenching of chlorophyll fluorescence by triplets in solubilized light-harvesting complex II (LHCII), Biophys. J. (vol. 76), No. 4, pp. 2238-2248.

[48]   Cho, H.S.; Song, N. W.; Kim, Y. H; Jeoung, S.C.; Hahn, S.; Kim, D.; Kim, S.K.; Yoshida, N. and Osuka, A. (2000): Ultrafast energy relaxation dynamics of directly linked porphyrin arrays, J. Phys. Chem. A (vol. 104), pp. 3287-3298.

[49]   Shipman, L.L. (1977): Oscillator and dipole strengths for chlorophyll and related molecules, Photophem. Photobiol. (vol. 26), pp. 287-292.

[50]   Sauer, K.; Lindsay Smith, J.R. and Schultz, A.J. (1966): The dimerization of chlorophyll a, chlorophyll b, and bacteriochlorophyll in solution, J. Amer. Chem. Soc. (vol. 88), No. 12, pp. 2681-2688.

[51]   Knox, R. S. (2003): Dipole and oscillator strengths of chromophores in solution, Photochemistry and Photobiology (vol. 77), No. 5, pp. 492-496.

[52]   Scherz, A. and Parson, W. W. (1984): Exciton interactions in dimers of bacteriochlorophyll and related molecules, Biochim. Biophys. Acta (vol. 766), pp. 666-678.

[53]   Nussberger, S.; Dekker, J.P.; Kühlbrandt, W.; van Bolhuis, B.M. ; van Grondelle, R. and van Amerongen, H. (1994): Spectroscopic characterization of three different monomeric forms of the main chlorophyll a/b binding protein from chloroplast membranes, Biochemistry (vol. 33), pp. 14775-14783.

[54]   Reddy, N.R.S.; van Amerongen, H.; Kwa, S.L.S.; van Grondelle, R. and Small, G.J. (1994): Low-energy exciton level structure and dynamics in light harvesting complex II trimers from the Chl a/b antenna complex of photosystem II, J. Phys. Chem. (vol. 98), pp. 4729-4735.

[55]   Zucchelli, G.; Garlaschi, F.M. and Jennings, R.C. (1996): Thermal broadening analysis of the light harvesting complex II absorption spectrum, Biochemistry (vol. 35), pp. 16247-16254.

[56]   Jennings, R.C.; Bassi, A; Garlaschi, F.M.; Dainese, P and Zucchelli, G. (1993): Distribution of the chlorophyll spectral forms in the chlorophyll-protein complexes of photosystem II antenna, Biochemistry (vol. 32), pp. 3203-3210.

[57]   Leupold, D.; Lokstein, H. and Hoffmann, P. (1999): Structure-function relationships in the higher plant photosynthetic antenna complex LHC II as revealed by non-linear laser spectroscopy - the problem of "chlorophyll forms", Trends Photochem. Photobiol. (vol. 6), pp. 43-52.

[58]   Croce, R.; Cinque, G.; Holzwarth, A. and Bassi, R. (2000): The soret absorption properties of carotenoids and chlorophylls in antenna complexes of higher plants, Photosynth. Res. (vol. 64), pp. 221-231.

[59] Cinque, G.; Croce, R. and Bassi, R. (2000): Absorption spectra of chlorophyll a and b in Lhcb protein environment, Photosynth. Res. (vol. 64), pp. 233-242.

[60] Shipman, L.L.; Cotton, T.M.; Norris, J.R. and Katz, J.J. (1976): An analysis of the visible absorption spectrum of chlorophyll a monomer, dimer, and oligomers in solution, J. Amer. Chem. Soc. (vol. 98), No. 25, pp. 8222-8230.

[61] Leupold, D.; Teuchner, K.; Ehlert, J.; Irrgang, K.-D.; Renger, G. and Lokstein, H. (2002): Two-photon excited fluorescence from higher electronic states of chlorophylls in photosynthetic antenna conplexes: A new approach to detect strong excitonic chlorophyll *a/b* coupling, Biophys. J. (vol. 82), pp. 1580-1585.

[62] Förster, T. (1948): Zwischenmolekulare Energiewanderung und Fluoreszenz, Ann. Phys. (vol. 2), pp. 55-67.

[63] Scholes, G.D.; Jordanides, X J. and Fleming, G.R. (2001): Adapting the Förster theory of energy transfer for modeling dynamics in aggregated molecular assemblies, J. Phys. Chem. B. (vol. 105), No. 8, pp. 1640-1651.

[64] van Amerongen, H.; Valkunas, L. and van Grondelle, R. (2000): Photosynthetic excitons, World Scientific Publishing, Singapore.

[65] Leupold, D.; Stiel, H.; Teuchner, K.; Nowak, F.; Sandner, W.; Ücker, B. and Scheer, H. (1996): Size enhancement of transition dipoles to one- and two-exciton bands in a photosynthetic antenna, Phys. Rev. Lett. (vol. 77), No. 22, pp. 4675-4678.

[66] Pullerits, T.; Chachisvilis, M. and Sundström, V. (1996): Exciton delocalization length in the B850 antenna of Rhodobacter sphaeroides, J. Phys. Chem. B (vol. 100), pp. 10787-10792.

[67] Tietz, C.; Chekhlov, O.; Dräbenstedt, A.; Schuster, J. and Wrachtrup, J. (1999): Spectroscopy on single light-harvesting complexes at low temperature, J. Phys. Chem. B (vol. 103), pp. 6328-6333.

[68] Dahlbom, M.; Pullerits, T.; Mukamel, S. and Sundström, V. (2001): Exciton delocalization in the B850 light-harvesting complex: Comparison of different measures, J. Phys. Chem. B (vol. 105), pp. 5515-5524.

[69] Hu, X. and Schulten, K. (1998): Model for the light-harvesting complex I (B875) of Rhodobacter sphaeroides, Biophys. J. (vol. 75), pp. 683-694.

[70] Brüggemann, B.; Herek, J.L.; Sundström, V.; Pullerits, T. and May, V. (2001): Microscopic theory of excitation annihilation: application to the LH2 antenna system, J. Phys. Chem. B (vol. 105), pp. 11391-11394.

[71] Hemelrijk, P.W.; Kwa, S.L.S.; van Grondelle, R. and Dekker, J.P. (1992): Spectroscopic properties of LHC-II, the main light-harvesting chlorophyll a/b protein complex from chloroplast membranes, Biochim. Biophys. Acta (vol. 1098), pp. 159-166.

[72] Gülen, D.; van Grondelle, R. and van Amerongen, H. (1997): Structural information on the light-harvesting complex II of green plants that can be deciphered from polarized absorption characteristics, J. Phys. Chem. B. (vol. 101), pp. 7256-7261.

[73] Iseri, E.I. and Gülen, D. (2001): Chlorophyll transition dipole moment orientations and pathways for flow of excitation energy among the chlorophylls of the major plant antenna, LHCII, Eur. Biophys. J. (vol. 30), pp. 344-353.

[74] Tetenkin, V.L. (2003): Stuctural-functional organization of the main light-harvesting complex and photosystem 2 of higher plants, Biochemistry (Moscow) (vol. 68), pp. 810-827.

[75] Cinque, G.; Croce, R.; Holzwarth, A. and Bassi, R. (2000): Energy transfer among CP29 chlorophylls: Calculated Förster rates and experimental transient absorption at room temperature, Biophys. J. (vol. 79), pp. 1706-1717.

[76] Knox, R. S. and van Amerongen, H. (2002): Refractive index dependence of the Forster resonance excitation transfer rate, Journal of Physical Chemistry B (vol. 106), No. 20, pp. 5289-5293.

[77] Kleima, F.J.; Hofmann, E.; Gobets, B.; van Stokkum, I.H. M.; van Grondelle, R.; Diederichs, K. and van Amerongen, H. (2000): Förster excitation energy transfer in peridinin-chlorophyll-a-protein, Biophys. J. (vol. 78), No. 1, pp. 344-2154.

[78] Shipman, L.L.; Norris, J.R. and Katz, J.J. (1976): Quantum mechanical formalism for computation of the electronic spectral properties of chlorophyll aggregates, J. Phys. Chem. (vol. 80), No. 8, pp. 877-882.

[79]   Novoderezhkin, V.; Salverda, J. M.; van Amerongen, H. and van Grondelle, R (2003): Exciton modeling of energy-transfer dynamics in the LHCII complex of higher plants: A redfield theory approach, J. Phys. Chem. B (vol. 107), pp. 1893-1912.

[80]   Jennings, R.C.; Zucchelli, G.; Garlaschi, F.M. and Vianelli, A. (1992): A comparison of the light-induced, non-reversible fluorescence quenching in photosystem II with quenching due to open reaction centres in terms of the chlorophyll emission spectral forms, Biochim. Biophys. Acta (vol. 1101), pp. 79-83.

[81]   Gruszecki, W.I.; Grudzinski, W.; Matula, M.; Kernen, P. and Krupa, Z. (1999): Light-induced excitation quenching and structural transition in light-harvesting complex II, Photosynth. Res. (vol. 59), pp. 175-185.

[82]   Horton, P.; Ruban, A.V. and Wentworth, M. (2000): Allosteric regulation of the light-harvesting system of photosystem II, Phil. Trans. R. Soc. Lond. B (vol. 355), pp. 1361-1370.

[83]   Li, X.-P.; Björkman, O.; Shih, C.; Grossman, A.R.; Rosenquist, M.; Jansson, S. and Niyogi, K.K. (2000): A pigment-binding protein essential for regulation of photosynthetic light harvesting, Nature (vol. 403), pp. 391-395.

[84]   Lokstein, H. ; Härtel, H. and Hoffmann, P. (1994): The role of light-harvesting complex II in excess excitation dissipation: An in-vivo fluorescence study on the origin of high-energy quenching, J. Photochem. Photobiol. B: Biol. (vol. 26), pp. 175-184.

[85]   Härtel, H.; Lokstein, H.; Grimm, B. and Rank, B. (1996): Kinetic studies on the xantophyll cycle in barley leaves: Influence of antenna size and relations to nonphotochemical chlorophyll fluorescence quenching, Plant Physiol. (vol. 110), pp. 471-482.

[86]   Ruban, A.V. and Horton, P. (1994): Spectroscopy of non-photochemical and photochemical quenching of chlorophyll fluorescence in leaves; evidence for a role of the light harvesting complex of Photosystem II in the regulation of energy dissipation, Photosynth. Res. (vol. 40), pp. 181-190.

[87]   Buschmann, C. (1999): Photochemical and non-photochemical quenching coefficients of the chlorophyll fluorescence: Comparison of variation and limits, Photosynthetica (vol. 37), No. 2, pp. 217-224.

[88]   Walters, R.G. and Horton, P. (1991): Resolution of components of non-photochemical chlorophyll fluorescence quenching in barley leaves, Photosynth. Res. (vol. 27), pp. 121-133.

[89]   Ruban, A.V.; Wentworth, M. and Horton, P. (2001): Kinetic analysis of nonphotochemical quenching of chlorophyll fluorescence. 1. Isolated chloroplasts, Biochemistry (vol. 40), pp. 9896-9901.

[90]   Laisk, A. and Oja, V. (2000): Alteration of photosystem II properties with non-photochemical excitation quenching, Phil. Trans. R. Soc. Lond. B (vol. 355), pp. 1405-1418.

[91]   Mullineaux, C.W.; Pascal, A.; Horton, P. and Holzwarth, A. (1993): Excitation-energy quenching in aggregates of the LHC II chlorophyll-protein complex: a time-resolved fluorescence study, Biochim. Biophys. Acta (vol. 1141), pp. 23-28.

[92]   Vasilev, S.; Irrgang, K.D.; Schrötter, T.; Bergmann, A.; Eichler, H.-J. and Renger, G (1997): Quenching of chlorophyll a fluorescence in the aggregates of LHCII: Steady state fluorescence and picosecond relaxation kinetics, Biochemistry (vol. 36), No. 24, pp. 7503-7512.

[93]   Niyogi, K.K.; Bjorkman, O. and Grossman, A.R. (1997): The roles of specific xanthophylls in photoprotection, Proc. Natl. Acad. Sci. USA (vol. 94), No. 25, pp. 14162-14167.

[94]   Hoffmann, P. (1998): Oxygenic photosynthesis - a photon driven hydrogen generator - the energetic / entropic basis of life, Photosynthetica (vol. 35), No. 1, pp. 1-11.

[95]   Allen, J.F. (1983): Chloroplast protein phosphorylation couples plastoquinone redox state to distribution of excitation energy between photosystems, Nature (vol. 291), pp. 25-29.

[96]   Krupa, Z.; Huner, N. P. A.; Williams, J. P.; Maissan, E. and James, D. R. (1987): Development at cold-hardening temperatures, PLant Physiol (vol. 84), pp. 19-24.

[97]   Lichtenthaler, H.K. (1987): Chlorophylls and carotenoids: Pigments of photosynthetic biomembranes, Methods in Enzymology (vol. 148), pp. 350-382.

[98]   Wellburn, A.R. (1994): The spectral determination of chlorophylls a and b, as well as total carotenoids, using various solvents with spectrophotometers of different resolution, J. Plant. Physiol. (vol. 144), pp. 307-313.

[99] Eads, D.D.; Castner, E.W.; Alberte, R.S.; Mets, L. and Fleming, G.R. (1989): Direct observation of energy transfer in a photosynthetic membrane: Chlorophyll b to chlorophyll a transfer in LHC, J Phys Chem B (vol. 93), No. 26, pp. 8271-8275.

[100] Kwa, S.L.S.; van Amerongen, H. ; Lin, S.; Dekker, J.P.; van Grondelle, R. and Struve, W.S. (1992): Ultrafast energy transfer in LHC-II trimers from the Chl a/b light-harvesting antenna of photosystem II, Biochim. Biophys. Acta (vol. 1102), pp. 202-212.

[101] Du, M.; Xie, X.; Mets, L. and Fleming, G.R. (1994): Direct observation of ultrafast energy transfer processes in light harvesting complex II, J. Phys. Chem. B (vol. 98), pp. 4736-4741.

[102] Gradinaru, C.C.; Stokkum, I.H.M.; Pascal, A.; van Grondelle, R. and van Amerongen, H. (2000): Identifying the pathways of energy transfer between carotenoids and chlorophylls in LHCII and CP29. A multicolor, femtosecond pump-probe study, J. Phys. Chem. B (vol. 104), pp. 9330-9342.

[103] Barzda, V.; Mustardy, L. and Garab, G. (1994): Size dependency of circular dichoism in macroaggregates of photosynthetic pigment-protein complexes, Biochemistry (vol. 33), pp. 10837-10841.

[104] Barzda, V.; Vengris, M.; Valkunas, L.; van Grondelle, R. and van Amerongen, H. (2000): Generation of fluorescence quenchers from the triplet states of chlorophyll in the major light-harvesting complex II from green plants, Biochemistry (vol. 39), pp. 10468-10477.

[105] Pieper, J.; Schödel, R; Irrgang, K.D.; Voigt, J. and Renger, G. (2001): Electron-phonon coupling in solubilized LHC II complexes of green plants investigated by line-narrowing and temperature-dependent fluorescence spectroscopy, J. Phys. Chem. B (vol. 105), pp. 7115-7124.

[106] Ruban, A.V.; Horton, P. and Robert, B. (1995): Resonance raman spectroscopy of the photosystem II light-harvesting complex of green plants: A comparison of trimeric and aggregated states, Biochemistry (vol. 34), pp. 2333-2337.

[107] Pascal, A.; Wacker, U.; Irrgang, K.D.; Horton, P.; Renger, G. and Robert, B. (2000): Pigment binding site properties of two photosystem II antenna proteins. A resonance raman investigation, J. Biol. Chem. (vol. 275), No. 29, pp. 22031-22036.

[108] Tietz, C.; Gerken, U.; jelezko, F. and Wrachtrup, J. (2000): Polarization measurements on single pigment-protein complexes, Single Mol. (vol. 1), No. 1, pp. 67-72.

[109] Tietz, C.; Jelezko, F.; Gerken, U.; Schuler, S.; Schubert, A.; Rogl, H. and Wrachtrup, J. (2001): Single molecule spectroscopy on the light-harvesting complex II of higher plants., Biophys. J. (vol. 81), p. 556–562.

[110] Pieper, J.; Rätsep, M.; Jankowiak, R.; Irrgang, K.-D.; Voigt, J.; Renger, G. and Small, G.J. (1999): Q_y-level structure and dynamics of solubilized light-harvesting complex II of green plants: Pressure and hole burning studies, J. Phys. Chem. A (vol. 103), pp. 2412-2421.

[111] Yang, M. and Fleming, G. R. (1999): Two-color three-pulse photon echoes as a probe of electronic coupling in molecular complexes, J. Chem. Phys. (vol. 110), pp. 2983-2990.

[112] Agarwal, R.; Krueger, B.P.; Scholes, G.D.; Yang, M.; Yom, J.; Mets, L. and Fleming, G.R. (2000): Ultrafast energy transfer in LHC-II revealed by three-pulse photon echo peak shift measurements, J. Phys. Chem. B (vol. 104), pp. 2908-2918.

[113] Jordanides, X.J.; Lang, M.J.; Song, X. and Fleming, G. R. (1999): Solvation dynamics in protein environments studied by photon echo spectroscopy, J. Phys. Chem. B (vol. 103), pp. 7995-8005.

[114] Louwe, R.J.W.; Vrieze, J.; Hoff, A.J. and Aartsma, T.J. (1997): Toward and integral interpretation of the optical steady-state spectra of the FMO-complex of Prosthecochloris aestuarii. 2. Exciton simulations, J. Phys. Chem. B (vol. 101), pp. 11280-11287.

[115] Stiel, H.; Leupold, D.; Teuchner, K.; Nowak, F.; Scheer, H. and Cogdell, R.J. (1997): One- and two-exciton bands in the LH2 antenna of rhodopseudomonas acidophila, Chem. Phys. Lett. (vol. 276), pp. 62-69.

[116] Stiel, H.; Becker, W. and Teuchner, K. (1991): Spectrometer for non-linear absorption measurements using a software-controlled signal analyzer, Exp. Techn. Physik (vol. 39), No. 1, pp. 15-24.

[117] Stiel, H.; Teuchner, K.; Leupold, D.; Oberländer, S.; Ehlert, J. and Jahnke, R. (1991): Computer aided laser-spectroscopic characterization and handling of molecular excited states, Intelligent Instruments & Computers, pp. 79-88.

[118] Schubert, A.; Beenken, W.; Stiel, H.; Voigt, B.; Leupold, D. and Lokstein, H. (2002): Excitonic coupling of chlorophylls in the plant light-harvesting complex LHC-II, Biophysical Journal (vol. 82), pp. 1030-1039.

[119] Zadoyan, R. S.; Zheludev, N. I. and Meysner, L. B. (1985): Nonlinear Polarization Spectroscopy of Ions Interaction Potential in Alkali-Halide Crystals, Solid State Communications (vol. 55), No. 8, pp. 713-715.

[120] Gancheryonok, II (1992): Conception of Normal Waves in Nonlinear Polarization Spectroscopy, Japanese Journal of Applied Physics Part 1-Regular Papers Short Notes & Review Papers (vol. 31), No. 12A, pp. 3862-3868.

[121] Wieman, C. and Hänsch, T.W. (1976): Doppler-free laser polarization spectroscopy, Phys. Rev. Lett. (vol. 36), pp. 1170-1173.

[122] Siese, M. and Tiemann, E. (1989): Combination of Doppler-Free Polarization Spectroscopy and Magnetic Rotation for the Example of Ibr, Applied Physics B-Photophysics and Laser Chemistry (vol. 49), No. 3, pp. 245-250.

[123] Song, J.J.; Lee, J.H. and Levenson, M.D. (1978): Picosecond relaxation measurements by polarization spectroscopy in condensed phases, Phys. Rev. A (vol. 17), No. 4, pp. 1439-1447.

[124] Trebino, R. and Siegman, A. E. (1983): Subpicosecond Relaxation Study of Malachite Green Using a 3-Laser Frequency-Domain Technique, Journal of Chemical Physics (vol. 79), No. 8, pp. 3621-3626.

[125] Voigt, B.; Nowak, F. and Beenken, W. (1999): A new set-up for nonlinear polarization spectroscopy in the frequency domain: experimental examples and theoretical background, Meas. Sci. Technol. (vol. 10), pp. N7-N11.

[126] Voigt, B.; Nowak, F.; Ehlert, J.; Beenken, W.J.D.; Leupold, D. and Sandner, W. (1997): Substructures and different energy relaxation time within the first electronic transition of pinacyanol, Chem. Phys. Lett. (vol. 278), pp. 380-390.

[127] Saikan, S. and Sei, J. (1983): Experimental studies of polarization spectroscopy in dye solutions, J. Chem. Phys. (vol. 79), No. 9, pp. 4146-4153.

[128] Marcano, A.; Marquez, L.; Aranguren, L. and Salazar, M. (1990): Polarization Spectra of Homogeneously and Inhomogeneously Broadened 2-Level Systems, Journal of the Optical Society of America B-Optical Physics (vol. 7), No. 11, pp. 2145-2149.

[129] Neef, E. and Mory, S. (1991): Content of information of nonlinear polarization spectroscopy, Exp. Techn. Phys. (vol. 39), No. 4/5, pp. 385-388.

[130] Leupold, D.; Voigt, B.; Beenken, W. and Stiel, H. (2000): Pigment-protein architecture in the light-harvesting antenna complexes of purple bacteria: does the crystal structure reflect the native pigment-protein arrangement?, FEBS Lett (vol. 480), pp. 73-78.

[131] Voigt, B.; Irrgang, K.-D.; Ehlert, J.; Beenken, W.; Renger, G.; Leupold, D. and Lokstein, H. (2002): Spectral substructure and excitonic interacitons in the minor photosystem II antenna complex CP29 as revealed by nonlinear polarization spectroscopy in the frequency domain, Biochemistry (vol. 41), pp. 3049-3056.

[132] Beenken, W. and Ehlert, J. (1998): Subband analysis of molecular electronic transitions by nonlinear polarization spectroscopy in the frequency domain, J. Chem. Phys. (vol. 109), No. 23, pp. 10126-10137.

[133] Marcano, A. and Golding, F. G. (1985): Power Effects in Polarization Spectroscopy on a Water Solution of Malachite Green, Journal of Chemical Physics (vol. 82), No. 3, pp. 1242-1245.

[134] Beenken, W. and May, V. (1997): Strong-field theory of nonlinear polarization spectroscopy. Fundamentals and the low-level system, J. Opt. Soc. Am. B (vol. 14), No. 11, pp. 2804-2810.

[135] Barzda, V.; Gulbinas, V.; Kananavicius, R.; Cervinskas, V.; van Amerongen, H.; van Grondelle, R. and Valkunas, L. (2001): Singlet-singlet annihilation kinetics in aggregates and trimers of LHCII, Biophys. J. (vol. 80), No. 5, pp. 2409-2421.

[136] Jackowski, G. and Jansson, S. (1998): Characterization of photosystem II antenna complexes separated by non-denaturing isoelectric focusing, Z Naturforsch (vol. 53c), pp. 841-848.

[137] Krawczyk, S.; Krupa, Z. and Maksymiec, W. (1993): Stark spectra of chlorophylls and carotenoids in antenna pigment-proteins LHC-II and CP-II, Biochim. Biophys. Acta (vol. 1143), pp. 273-281.

[138] Zucchelli, G.; Dainese, P.; Jennings, R.C.; Breton, J.; Garlaschi, F.M. and Bassi, R. (1994): Gaussian decomposition of absorption and linear dichroism spectra of outer antenna complexes of photosystem II, Biochemistry (vol. 33), No. 30, pp. 8982-8990.

[139] Plumley, F.G. and Schmidt, G.W. (1987): Reconstitution of chlorophyll a/b light-harvesting complexes:xanthophyll-dependent assembly and energy transfer, Proc. Natl. Acad. Sci. USA (vol. 84), pp. 146-150.

[140] Hobe, S.; Prytulla, S.; Kühlbrandt, W. and Paulsen, H. (1994): Trimerization and crystallization of reconstituted light-harvesting chlorophyll a/b complex, EMBO J (vol. 13), No. 15, pp. 3423-3429.

[141] Schmid, V. H. R.; Thome, P.; Rühle, W.; Paulsen, Harald; Kühlbrandt, W. and Rogl, H. (2001): Chlorophyll b is involved in long-wavelength spectral properties of light-harvesting complexes LHC I and LHC II, FEBS Lett (vol. 24932), pp. 1-5.

[142] Rogl, H.; Schödel, R.; Lokstein, H.; Kühlbrandt, W. and Schubert, A. (2002): Assignment of spectral substructures to pigment-binding sites in higher plant light-harvesting complex LHC-II, Biochemistry (vol. 41), pp. 2281-2287.

[143] Rogl, H.; Kosemund, K.; Kühlbrandt, W. and Collinson, I. (1998): Refolding of Escherichia coli produced membrane protein inclusion bodies immobilised by nickel chelating chromatography, FEBS Lett. (vol. 432), pp. 21-26.

[144] Bassi, R.; Croce, R.; Cugini, D. and Sandona, D. (1999): Mutational analysis of a higher plant antenna protein provides identification of chromophores bound into multiple sites, Proc. Natl. Acad. Sci. USA (vol. 96), pp. 10056-10061.

[145] Kleima, F.J.; Hobe, S.; Calkoen, F.; Urbanus, M.L.; Peterman, E.J.; van Grondelle, R. ; Paulsen, H. and van Amerongen, H. (1999): Decreasing the chlorophyll a/b ratio in reconstituted LHCII: Structural and functional consequences, Biochemistry (vol. 38), pp. 6587-6596.

[146] Peterman, E.J.G.; Hobe, S.; Calkoen, F.; van Grondelle, R.; Paulsen, H. and van Amerongen, H. (1996): Low-temperature spectroscopy of monomeric and trimeric forms of reconstituted light-harvesting chlorophyll a/b complex, Biochim. Biophys. Acta (vol. 1273), pp. 171-174.

[147] Bittner, T.; Wiederrecht, G.P.; Irrgang, K.D.; Renger, G and Wasielewski, M.R. (1995): Femtosecond transient absorption spectroscopy on the light-harvesting Chl a/b protein complex of PS II at room temperature and 12 K, Chem. Phys. (vol. 194), pp. 311-322.

[148] Schubert, A.; Krikunova, M. A.; Stiel, H.; Ehlert, J.; Leupold, D. and Lokstein, H. (1998): Determination of the aggregate size in chlorophyll a oligomers by non-linear absorption spectroscopy on the ps and fs timescale, Garab, G., Photosynthesis: Mechanisms and Effects (vol. 1) pp. 325-329, Kluwer Acaddemic Publishers.

[149] Uehara, K.; Shibata, K.; Nakamura, H. and Tanaka, M. (1982): Aggregation of chlorophyll a in aqueous dimethyl solfoxide, Chemistry Letters, pp. 1445-1448.

[150] Uehara, K.; Mimuro, M. and Tanaka, M. (1991): Spectroscopic studies of chlorophyll a aggregates formed by aqueous dimethyl sufoxide, Photochem. Photobiol. (vol. 53), No. 3, pp. 371-377.

[151] Iriyama, K.; Ogura, N. and Takamiya, A. (1974): Simple Method for Extraction and Partial-Purification of Chlorophyll from Plant Material, Using Dioxane, Journal of Biochemistry (vol. 76), No. 4, pp. 901-904.

[152] Teuchner, K.; Stiel, H.; Leupold, D.; Katheder, I. and Scheer, H. (1994): From Chlorophyll-a Towards Bacteriochlorophyll-a - Excited-State Processes of Modified Pigments, Journal of Luminescence (vol. 60-1), pp. 520-522.

[153] Vrieze, J. and Hoff, A. J. (1995): The orientation of the triplet axes with respect to the optical-transition moments in (bacterio)chlorophylls, Chem. Phys. Lett. (vol. 237), pp. 493-501.

[154] Simonetto, R.; Crimi, M.; Sandona, D.; Croce, R.; Cinque, G.; Breton, J. and Bassi, R. (1999): Orientation of chlorophyll transition moments in the higher plant light harvesting complex CP 29, Biochemistry (vol. 38), pp. 12974-12983.

[155] Kleima, F.J.; Wendling, M.; Hofmann, E.; Peterman, E.J.; van Grondelle, R. and van Amerongen, H. (2000): Peridinin chlorophyll a protein: Relating structure and steady-state spectroscopy, Biochemistry (vol. 39), pp. 5184-5195.

[156] Palacios, M.A.; de Weerd, F.L.; Ihalainen, J. A.; van Grondelle, R. and van Amerongen, H. (2002): Superradiance and exciton (de)localization in light-harvesting complex II from green plants ?, J. Phys. Chem. B (vol. 106), pp. 5782-5787.

[157] Formaggio, E.; Cinque, G. and Bassi, R. (2001): Functional architecture of the major light-harvesting complex from higher plants, Journal of Molecular Biology (vol. 314), No. 5, pp. 1157-1166.

[158] Vasilev, S.; Schrötter, T.; Bergmann, A.; Irrgang, K.D.; Eichler, H.-J. and Renger, G (1997): Cryoprotectant-induced quenching of chlorophyll a fluorescence from light-harvesting complex 2 in vitro: time-resolved fluorescence and steady state spectroscopic studies, Photosynthetica (vol. 33), No. 3-4, pp. 553-561.

[159] Lokstein, H.; Schubert, A.; Leupold, D. and Voigt, B. (1998): Direct resolution of spectral fine-structure and ultrafast exciton dynamics in plant LHC II by non-linear polarization spectroscopy in the frequency domain, Garab, G., Photosynthesis: Mechanisms and Effects (vol. 1) pp. 293-296, Kluwer Academic Publishers.

[160] Polivka, T.; Pullerits, T.; Herek, J.L. and Sundström, V. (2000): Exciton relaxation and polaron formation in LH2 at low temperature, J. Phys. Chem. B (vol. 104), pp. 1088-1096.

[161] Bassi, R.; Silvestri, M.; Dainese, P.; Moya, I. and Giacometti, G.M. (1991): Effects of non-ionic detergent on the spectral properties and aggregation state of the light-harvesting chlorophyll a/b protein complex (LHCII), J. Photochem. Photobiol. B: Biology (vol. 9), pp. 335-354.

[162] Barzda, V.; de Grauw, C.J.; Vroom, J.; Kleima, F.J.; van Grondelle, R.; van Amerongen, H. and Gerritsen, H.C. (2001): Fluorescense lifetime heterogeneity in aggregates of LHCII revealed by time-resolved microscopy, Biophys J (vol. 81), pp. 538-546.

[163] Kirchhoff, H.; Hinz, H.-J. and Rösgen, J. (2003): Aggregation and fluorescence quenching of chlorophyll a of the light-harvesting complex II from spinach in vitro, BBA (vol. 1606), pp. 105-116.

[164] Schubert, A.; Voigt, B.; Leupold, D.; Beenken, W.; Ehlert, J.; Hoffmann, P and Lokstein, H. (1997): Direct observation of spectral substructure in the Qy-absorption band of light-harvesting complex II by nonlinear polarization spectroscopy in the frequency domain at low temperature, Biochem. Biophys. Acta (vol. 1321), pp. 151-155.

[165] Kleima, F.J.; Gradinaru, C.C.; Calkoen, F.; van Stokkum, I.H.M. ; van Grondelle, R. and van Amerongen, H. (1997): Energy transfer in LHCII monomers at 77K studied by sub-picosecond transient absorption spectroscopy, Biochemistry (vol. 36), pp. 15262-15268.

[166] Kühlbrandt, W. (1994): Structure and function of the plant light-harvesting complex, LHC-II, Current Opinion in Structural Biology (vol. 4), pp. 519-528.

Acknowledgement

Curriculum vitae

Name: Axel Schubert

geboren am: 15.03.1970 in Jena

Staatsangehörigkeit: Deutsch

Familienstand: unverheiratet

07/1986	Mittlere Reife, POS 'A. Reichwein', Jena; Präd. 'Ausgezeichnet'
07/1988	Abitur, EOS 'J. R. Becher', Jena; Prädikat 'Sehr gut'
11/1988-07/1989	Grundwehrdienst (NVA)
10/1989-09/1990	Studienfach Physik, Technische Hochschule Leuna-Merseburg
10/1990-02/1992	Studienfach Physik, Friedrich-Schiller-Universität Jena
03/1992-07/1995	Studienfach Physik, Universität Hannover
07/1995	Diplom (Dipl. Phys.), Universität Hannover; Prädikat 'Sehr gut'
08/1995-01/2000	Doktorand, HU Berlin (Lehrst. Pflanzenphys.) / MBI Berlin
02/2000-03/2002	Wiss. Mitarbeiter, Chemical Center, Lund University (Sweden)
04/2002-06/2003	Mitarbeiter im elterlichen Unternehmen (Saale-Apotheke Jena)
11/2003-	Wiss. Mitarbeiter (F&E), Pentapharm GmbH München

Eidesstattliche Erklärung

Hiermit erkläre ich, die vorliegende Dissertation selbständig und ohne unzulässige fremde Hilfe angefertigt zu haben. Ich habe keine anderen als die angeführten Quellen und Hilfsmittel benutzt und sämtliche Textstellen, die wörtlich oder sinngemäß aus veröffentlichten oder unveröffentlichten Schriften entnommen wurden, als solche kenntlich gemacht. Ebenfalls sind alle von anderen Personen bereitgestellten Materialen oder erbrachten Dienstleistungen als solche gekennzeichnet.

Ich habe mich anderwärts nicht um einen Doktorgrad beworben und besitze einen entsprechenden Doktorgrad nicht. Ich erkläre weiterhin die Kenntnisnahme der dem Verfahren zugrunde liegenden Promotionsordnung der Mathematisch-Naturwissenschaftlichen Fakultät I der Humboldt-Universität zu Berlin.

Ort, Datum   Unterschrift